

# Tuning palladium selective oxidation catalysts via mesoporous supports

A thesis for the degree of  
Doctor of Philosophy in Chemistry

Cardiff University

School of Chemistry

2012

Christopher M.A. Parlett

## Abstract

Surfactant templating provides a facile route to mesoporous materials with tuneable architectures, whilst simultaneously allowing control over complementary macro and micro porosity. The impact of these varying physical properties, on both catalyst synthesis and during catalytic reactions, was one principal area of investigation. Catalyst series were prepared on mesoporous SBA-15, SBA-16 and KIT-6, meso-macroporous SBA-15, true liquid crystal templated SBA-15 and a commercial low surface area silica support. Additionally two mesoporous alumina series, with mesoporosity akin to SBA-15, were produced. The catalytic activity of the materials was screened for the selective oxidation of allylic alcohols, which represents a class of industrially relevant chemical upgrading reactions. Nano-particulate palladium is widely recognised as an able catalytic species, although the active site nature is still debated with both metallic and oxidic surfaces proposed. Further insight into the active species was another major area of investigation.

Extensive characterisation confirmed successful support synthesis and mesopore stability after palladium impregnation. Irrespective of support, decreasing metal loading elevates dispersion (particle sizes are typically less than 2nm), which correlates with the increase of surface PdO content. In relation to the silica supports these trends escalate via support transition in the order of: Pd/low surface area commercial silica < Pd/true liquid crystal templated SBA-15 < Pd/SBA-15 < Pd/mesomacroporous SBA-15 < Pd/KIT-6  $\approx$  Pd/SBA-16. Initially increasing support surface area is critical and later rising mesopore accessibility dictates. Catalytic activity, for cinnamyl and crotyl alcohol selective oxidation, reveals significant rate-enhancements with PdO content, with turnover frequencies providing compelling proof of a PdO active species. Alumina supports, even with lower surface areas than equivalent silicas, allow further gains in metal dispersion, surface oxidation state and resulting catalytic activity. In conclusion, tuning the physical and chemical properties of the support is paramount if highly active catalysts are to be produced.

## Acknowledgements

To start I would like to thank my supervisors, Professor Adam F. Lee and Dr Karen Wilson, for allowing me the opportunity to carry out this research and for their invaluable advice, motivation and guidance. For this I am truly grateful.

To our collaborators at The University of York; Professor Duncan W. Bruce and Dr Stephen G. Wainwright I am deeply thankful for their expert input, both practical and theoretical. Many thanks are also bestowed on Dr Nicole S. Hondow (University of Leeds) and Dr Lisa S. Karlsson (University of Oxford) for the acquisition of invaluable STEM/TEM images. Professor Wuzong Zhou (University of St. Andrews) and Dr Mark A. Newton (ESRF, France), are also thanked for their contribution to TEM imaging and XAS characterisation respectively. To the technicians, at both The University of York and Cardiff University, I am thankful, especially for making the relocation to Cardiff an almost enjoyable experience.

I am extremely appreciative for the support and friendship of the Surface, Materials and Catalysis Group and the Cardiff Catalysis Institute members, both past and present. Individually I would like to thank Dr Simon F. J. Hackett, for his guidance at the start of my PhD, and Miss Pooja Keshwalla for being an ideal supervisee and her resulting contribution to this thesis.

Thanks too, to the EPSRC, as without their generous funding this work would not have been possible.

Last but by no means least I would like to thank my family and friends. Without your support and encouragement I am sure I would not be where I am today. Special recognitions are made to both Mr Bryan R. D. Parlett, for being a more than capable proof-reader, and Miss Catherine V. Flood, for putting up with me and convincing me not to give up when everything seemed to be going wrong.

This work is dedicated in memory of Mrs Winifred F. Cullen (1911-2010) and Mr James (Townie) E. Richardson (1985-2008).

## Acronyms

<b>AAS</b>	-	Atomic adsorption spectroscopy
<b>BET</b>	-	Brunauer, Emmett and Teller Adsorption Theory
<b>BJH</b>	-	Barrett, Joyner and Halenda Pore Size Distribution Method
<b>CrOH</b>	-	Crotyl alcohol
<b>CrAld</b>	-	Crotonaldehyde
<b>CinnOH</b>	-	Cinnamyl alcohol
<b>CinnAld</b>	-	Cinnamaldehyde
<b>DRIFTS</b>	-	Diffuse reflectance infra red fourier transform spectroscopy
<b>EXAFS</b>	-	Extended x-ray absorption fine structure
<b>HAADF</b>	-	High angle annular dark field
<b>ICP-OES</b>	-	Inductively coupled plasma optical emission spectroscopy
<b>MS</b>	-	Mass spectrometry
<b>PGM</b>	-	Platinum group metals
<b>ppm</b>	-	parts per million
<b>Selox</b>	-	Selective oxidation
<b>SEM</b>	-	Scanning electron microscope
<b>STEM</b>	-	Scanning transmission electron microscope
<b>TEM</b>	-	Transmission electron microscope
<b>TOF</b>	-	Turnover frequency
<b>TPD</b>	-	Temperature programmed desorption
<b>XANES</b>	-	X-ray absorption near edge structure
<b>XAS</b>	-	X-ray absorption spectroscopy
<b>XPS</b>	-	X-ray photoelectron spectroscopy
<b>XRD</b>	-	X-ray diffraction
<b>XRF</b>	-	X-ray florescence spectroscopy

## Table of Contents

Abstract.....	i
Acknowledgement.....	ii
Declaration .....	iii
Acronyms .....	iv
<i>Chapter 1 Introduction</i>	
1.1 Introduction .....	6
1.1.1 Selective oxidation of alcohols.....	8
1.1.2 Catalytic selox of allylic/benzyl alcohols .....	9
1.1.2.1 Homogeneous palladium catalysts.....	9
1.1.2.2 Heterogeneous palladium catalysts .....	11
1.1.2.3 Mechanism of heterogeneously catalysed palladium selox .....	13
1.1.2.4 Heterogeneous palladium active site.....	15
1.1.2.5 Heterogeneous palladium selectivity .....	16
1.1.2.6 Heterogeneous palladium deactivation .....	18
1.1.3 Catalyst support .....	19
1.1.3.1 Ordered mesoporous silicas .....	21
1.1.3.2 Ordered mesoporous alumina .....	24
1.2 Thesis aims .....	25
1.3 References .....	26
<i>Chapter 2 Experimental</i>	
2.1 Catalyst preparation.....	33
2.1.1 SBA-15 synthesis .....	33
2.1.2 SBA-16 synthesis .....	33
2.1.3 KIT-6 synthesis.....	33
2.1.4 Macro-mesoporous SBA-15 synthesis .....	34
2.1.5 TLCT-SBA-15 synthesis .....	34
2.1.6 Mesoporous alumina.....	35
2.1.7 SBA-15 with an alumina grafted surface (Al-SBA-15) .....	35
2.1.8 Palladium incipient wetness impregnation (all supports).....	36
2.2 Support and catalyst characterisation .....	36
2.2.1 Elemental analysis .....	36
2.2.2 Powder X-Ray diffraction .....	38

2.2.3 Nitrogen porosimetry .....	40
2.2.4 Electron microscopy .....	43
2.2.5 Carbon monoxide chemisorption.....	44
2.2.6 Diffuse reflection infrared fourier transform spectroscopy - in-situ carbon monoxide chemisorption .....	46
2.2.7 X-ray photoelectron spectroscopy .....	48
2.2.8 X-ray adsorption spectroscopy – X-ray adsorption near edge structure and Extended x-ray adsorption fine structure.....	50
2.3 Selox reactions.....	51
2.3.1 Alcohol selective oxidation (standard conditions) .....	51
2.3.2 Mass transfer limitations.....	52
2.3.3 Heterogeneity of the active site - hot filtration test .....	52
2.3.4 Role of oxygen on cinnamyl alcohol selox .....	53
2.3.5 Role of in-situ reduction pre-treatment.....	53
2.3.6 Recycle testing.....	53
2.3.7 Reduced catalyst mass for cinnamyl alcohol selox .....	53
2.3.8 Effect of reaction temperature on cinnamyl alcohol selox .....	54
2.4 References .....	54
<i>Chapter 3 The selective oxidation of allylic alcohols over palladium supported on mesoporous silicas – the role of mesopore architecture</i>	
3.1 Introduction .....	57
3.2 Results and discussion .....	58
3.2.1 Characterisation of parent silica supports.....	58
3.2.1.1 Powder X-Ray diffraction .....	58
3.2.1.2 Nitrogen porosimetry .....	59
3.2.1.3 Transmission electron microscopy.....	68
3.2.2 Characterisation of Pd impregnated silicas supports .....	69
3.2.2.1 Inductively coupled plasma optical emission spectroscopy / X-Ray Fluorescence Spectroscopy .....	69
3.2.2.2 Powder X-Ray diffraction .....	70
3.2.2.3 Nitrogen porosimetry .....	75
3.2.2.4 Carbon monoxide chemisorption .....	83
3.2.2.5 Diffuse reflectance infrared fourier transform .....	84
3.2.2.6 Scanning transmission electron microscopy .....	87

3.2.2.7 X-ray photoelectron spectroscopy.....	89
3.2.2.8 X-ray adsorption spectroscopy.....	95
3.2.3 Allylic alcohol selox.....	100
3.2.3.1 Crotyl alcohol selox.....	100
3.2.3.2 Cinnamyl alcohol selox.....	107
3.2.3.3 Role of oxygen on cinnamyl alcohol selox.....	119
3.2.3.4 Role of reductive pre-treatment.....	123
3.2.3.5 Recycle testing.....	125
3.2.4 Alternative alcohol selox.....	129
3.3 Conclusion.....	131
3.4 References.....	132
<i>Chapter 4 The selective oxidation of allylic alcohols over palladium supported on SBA-15 – the role of complementary pore architectures</i>	
4.1 Introduction.....	136
4.2 Results and discussion.....	136
4.2.1 Characterisation of polystyrene spheres.....	136
4.2.1.1 Scanning electron microscopy.....	136
4.2.2 Characterisation of parent silica supports.....	137
4.2.2.1 Powder X-Ray diffraction.....	137
4.2.2.2 Nitrogen porosimetry.....	139
4.2.2.3 Scanning electron microscopy.....	144
4.2.2.4 Transmission electron microscopy.....	145
4.2.3 Characterisation of Pd impregnated silicas supports.....	146
4.2.3.1 Inductively coupled plasma optical emission spectroscopy.....	146
4.2.3.2 Powder X-Ray diffraction.....	147
4.2.3.3 Nitrogen porosimetry.....	150
4.2.3.4 Carbon monoxide chemisorption.....	154
4.2.3.5 Scanning transmission electron microscopy.....	155
4.2.3.6 X-ray photoelectron spectroscopy.....	157
4.2.4 Allylic alcohol selox.....	161
4.2.4.1 Crotyl alcohol selox.....	161
4.2.4.2 Cinnamyl alcohol selox.....	166
4.3 Conclusion.....	173
4.4 References.....	174

*Chapter 5 The selective oxidation of allylic alcohols over palladium supported on mesoporous alumina*

5.1 Introduction .....	177
5.2 Results and discussion .....	178
5.2.1 Characterisation of parent silica supports .....	178
5.2.1.1 Powder X-Ray diffraction .....	178
5.2.1.2 Nitrogen porosimetry .....	180
5.2.1.3 X-ray photoelectron spectroscopy .....	184
5.2.1.4 Scanning electron microscopy .....	189
5.2.1.5 Transmission electron microscopy .....	190
5.2.2 Characterisation of Pd impregnated alumina supports .....	190
5.2.2.1 Inductively coupled plasma optical emission spectroscopy / Atomic adsorption spectroscopy .....	191
5.2.2.2 Powder X-Ray diffraction .....	191
5.2.2.3 Nitrogen porosimetry .....	193
5.2.2.4 Carbon monoxide chemisorption .....	196
5.2.2.5 Scanning transmission electron microscopy .....	197
5.2.2.6 X-ray photoelectron spectroscopy .....	199
5.2.3 Allylic alcohol selox .....	203
5.2.3.1 Crotyl alcohol selox .....	203
5.2.3.2 Cinnamyl alcohol selox .....	204
5.2.3.3 Effect of reaction temperature on cinnamyl alcohol selox .....	211
5.3 Conclusion .....	213
5.4 References .....	214

*Chapter 6 Summary*

6.1 Conclusion .....	217
6.2 References .....	220

# *Chapter 1*

## *Introduction*

## 1.1 Introduction

The aspiration to further understand the bearing that catalyst support materials, especially their physical assets, impart on supported catalytic sites was the stimulus for this work. Recent advances in materials synthesis allows these considerations to be explored through the use of templated mesoporous silicas with uniquely differing pore architectures, to support Pd nanoparticles. The effect of their varying pore network on the physio-chemical nature of the Pd sites and their inherent catalytic performance towards the selective oxidation (selox) of allylic alcohol was the primary focus.

A catalyst, in the broadest sense, increases the rate at which a chemical reaction occurs, without itself being consumed. This is possible by providing a new reaction route that proceeds via an alternative mechanism, with a distinct transition state possessing a lower activation energy barrier. The process has no command on overall equilibrium, only the rate at which it is reached.<sup>[1]</sup> Due to this commendable quality catalysts are employed in a wide range of applications spanning large scale petrochemical processes e.g. crude oil cracking over zeolites,<sup>[2]</sup> to fine chemical synthesis such as olefin metathesis via Grubbs' catalyst<sup>[3]</sup> and, probably the most widely recognised, the catalytic convertor used for the after-treatment of internal combustion engine emission gases.<sup>[4]</sup>

Further motivation comes from increasing environmental and economical concerns that are dictating the reduction in use of waste-inefficient harmful/toxic stoichiometric reactants<sup>[5, 6]</sup> such as permanganates and chromates ( $\text{KMnO}_4$ ,  $\text{K}_2\text{Cr}_2\text{O}_7$  and  $\text{Na}_2\text{Cr}_2\text{O}_7$ ), well known oxidation reagents.<sup>[7, 8]</sup> Therefore within research laboratories, both academic and industrial, the replacement of these archaic methodologies with modern catalytic species is an active area of research.<sup>[9]</sup> Ideal systems would be highly active, allowing reactions at ambient temperature and pressure, and solely selective to the desired product, without ever deactivating, that is neither of these desirable characteristics would decrease. Obviously this is no superficial matter and a great challenge for catalyst design.

Catalysis can be divided into two subdivisions. First, homogeneous where the catalysts and reaction phases are identical, soluble metal complexes in liquid phase reactions being the most common. This discipline has, and continues to be,

extensively investigated for a wide range of catalysts and reactions with umpteen reviews focusing solely on alcohol oxidations.<sup>[10-15]</sup> Active and selective homogeneous catalysts are frequently investigated, with improvements via careful tuning of their structure (ligands) and the auxiliary chemicals used. While the transpiring ‘single-site’ catalyst is a desired property,<sup>[16]</sup> unfortunately their use is far from ideal: from an industrial point their recovery and reuse is problematic often resulting in loss of the catalytically active component. They can also contaminate the final product; an intolerable outcome especially in the pharmaceutical industry, due to tight quality controls and concerns over their toxicity. Additionally their synthesis can be complex with multiple steps and reagents. This, combined with the necessity of auxiliaries/co-catalysts, can dictate their large scale use to be environmentally and economical unjustified.<sup>[9]</sup>

The second branch is heterogeneous catalysis, with contrast between the reaction phase and catalyst, e.g. a solid catalyst for liquid or gas phase reactions. Generally this is more attractive as the segregation of the two components, and thus recovery of the precious active component, is facilitated. Furthermore the synthetic route to these can be relatively simple, aiding to reduce their environmental and economic impact. Unfortunately the nature of the active sites are usually less well understood, as studying the actual site of action and subsequent catalyst deactivation, specifically under operating conditions, is formidably demanding. Surface sensitive techniques, operating either in-situ or more ideally in operando conditions are utilised to try to shed light on these reactions.<sup>[17-22]</sup> The use of computational chemistry is also applied to strengthen our understanding of structure-performance relationships in catalysis.<sup>[21, 23]</sup> Our ability to study working catalysts has been expanded by the novel combination of multiple time resolved analytical methodologies. Simultaneous product formation, surface species and active site characterisation have been reported, although these are far from commonplace as synchrotron radiation is often imperative.<sup>[24-29]</sup> Even with these limitations numerous catalytic methodologies have been developed that are capable of executing a wide range of reactions.<sup>[10]</sup> Furthermore, various reviews devoted, at least partially, to the heterogeneous catalytic alcohol oxidations exist.<sup>[17, 30-33]</sup>

### 1.1.1 Selective oxidation of alcohols

Selective oxidation reactions find application in the synthesis of a wide range of organic compounds including alcohols, carbonyl species, carboxylic acids, epoxides and esters.<sup>[9]</sup> They are commonplace in the fine/speciality chemical sector, in particular pharmaceutical and agrochemical production.<sup>[5]</sup> The current use of stoichiometric reagents needs replacing with catalytic systems. New developments have produced positive results,<sup>[34]</sup> although often under harsh driving conditions e.g. elevated temperature, extreme oxygen/air pressures or the use of peroxides as an oxygen source.<sup>[5]</sup> Superior understanding of the active species is thus needed if calculated improvements are to be made.

The selox of alcohols to desirable carbonyl species is one of the most important classes of organic transformations,<sup>[13, 35]</sup> with the utilisation of air/oxygen as the oxidant making this an atom efficient route.<sup>[15, 33]</sup> To date extensive research has shown catalytic chemistry, both homogeneous and heterogeneous ordinarily based on transition metals, to be rich for the conversion of primary and secondary alcohols, diols and polyols.<sup>[10-15, 30-33, 36]</sup> For relatively reactive alcohols, such as benzylic and allylic alcohol, these can be achieved under gentle conditions, without auxiliaries, over heterogeneous catalysts, while utilising air/molecular oxygen as the oxidant.

The oxidation of primary alcohols to their corresponding aldehyde is chemically demanding.<sup>[31]</sup> Other functional groups within the alcohol can greatly influence the resultant selox activity. Heteroatoms, in particular sulphur or nitrogen, can vastly reduce reactivity possibly via the poisoning of the active site.<sup>[31]</sup> Allylic and benzylic alcohols, which exhibit similar  $\alpha,\beta$  unsaturation, are routinely more active than their unsaturated equivalents over heterogeneous catalysts. Good reactivity towards the desired aldehyde formation has been observed,<sup>[36]</sup> and an upshot is that the selox of benzyl alcohol is one of the most commonly studied reactions for heterogeneous systems.<sup>[31, 33]</sup> In contrast, over certain homogeneous Pd complexes allylic and benzylic alcohols can lead to deactivation or poisoning via complexing of the metal to the alkene moiety.<sup>[11]</sup> Fine tuning of the auxiliaries and/or ligands used can overcome this issue.<sup>[10, 12, 13, 15, 37]</sup>

For heterogeneous systems the formation of ketones, from secondary alcohols, is persistently slower than aldehyde productions, possibly arising due to steric effects.

Beneficially, ketone selectivity and yields can be raised relative to aldehydes due to the elimination of possible alcohol overoxidation.<sup>[31]</sup> Once more  $\alpha,\beta$  unsaturation dramatically enhances reaction rates.<sup>[36]</sup> As with primary alcohols, the activity of homogeneous Pd sites is dependent on the catalyst structure and reaction conditions.<sup>[37]</sup>

### 1.1.2 Catalytic selox of allylic/benzylic alcohols

The selox of allylic alcohols to allylic aldehydes/ketones, as illustrated in **Figure 1.1**, is a reaction of great importance to the fine chemical and food industries. They find widespread application and are implemented either directly as a final product or as valuable intermediates. In particular, crotonaldehyde exhibits anti-termite characteristics whilst also presenting as a valuable precursor to sorbic acid, an important food preservative.<sup>[38]</sup> In a similar fashion cinnamaldehyde is widely used to confer a cinnamon aroma in the food and fragrance sectors whilst also being observed to bear insecticidal properties for the control of mosquito larvae.<sup>[39]</sup>

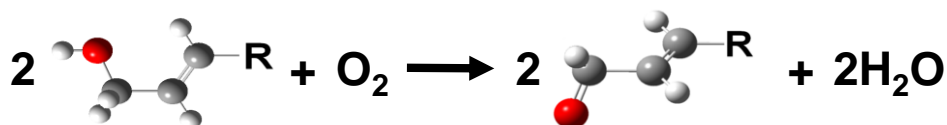


**Figure 1.1** – Selective oxidation of allylic alcohols (crotyl alcohol R = methyl, cinnamyl alcohol R = phenyl)

Homogeneous systems capable of allylic and/or benzylic alcohol selox (remembering their similarity) include Pd, OsO<sub>4</sub>/Cu, Ru, Cr and Cu.<sup>[10-12, 15, 37]</sup> Likewise heterogeneous active selox catalysts based on a range of active metals including Pt, Pd, Au, Ag and Ru as surfactant or support stabilised nanoparticles are reported.<sup>[10, 30-33]</sup> Due to the wide range of possible catalytic materials and the areas investigated within this project, the introduction will focus on Pd catalysis, predominately heterogeneous.

#### 1.1.2.1 Homogeneous palladium catalysts

The first example of an aerobic homogeneous Pd catalyst for selox was reported by Blackburn in 1977.<sup>[40]</sup> This used palladium(II) chloride, with oxygen, for the conversion of aliphatic secondary alcohols to their corresponding ketones.<sup>[11] [40]</sup>

Since then prominent advancements have been made, with numerous detailed reviews including, but not exclusive to, the ones by Sheldon et al,<sup>[10]</sup> Choudary et al,<sup>[11]</sup> Zhan & Thompson,<sup>[12]</sup> Stahl,<sup>[13]</sup> and Muzart <sup>[14, 15]</sup> covering catalyst development, reaction conditions optimisation and reaction mechanisms. An example of reaction control is demonstrated for palladium(II) acetate. The use of dimethyl sulfoxide and sodium carbonate as auxiliaries allows the oxidation of olefinic and benzylic alcohol,<sup>[12, 13]</sup> replacing these with pyridine and toluene, enables aliphatic primary and secondary alcohols to be oxidised.<sup>[10, 13]</sup> The use of Pd(II) species are extensively reported although Pd(0) catalysts are also known.<sup>[15]</sup>

The main obstacle reported for Pd, relative to other metals, is low turnover frequency (TOF) which thus increased reaction length <sup>[10]</sup> amplifying deactivation via Pd agglomeration.<sup>[11]</sup> Successful elevations of catalyst reactivity have been made though, with TOFs rising 20 fold, up to  $\sim 80 \text{ h}^{-1}$ , from 2000 to 2004.<sup>[12]</sup> As already discussed these systems are affected by the customary problems faced by homogeneous catalysis.

Homogeneous catalyst reaction mechanisms vary depending on the catalysts, ancillary reagents and reactants used.<sup>[12, 14]</sup> Two generic mechanisms are suggested from observations of selox over metalloenzymes,<sup>[13]</sup> biological molecules that are looked to for inspiration during the development of homogeneous species.<sup>[12]</sup> The first, over oxygenases, is an oxygen insertion mechanism typical when oxygen is absent from the starting material. This is a type of atom transfer reaction utilising either molecular oxygen or air as an oxygen donor.<sup>[13, 41, 42]</sup> The second route, oxidase, corresponds to reactions where molecular oxygen insertion does not occur, e.g. dehydrogenation reactions resulting in alcohol oxidation, the reaction of interest here, and alkene dehydrogenation. Again use of molecular oxygen is common,<sup>[12]</sup> although hydrogen acceptors have also been reported,<sup>[11]</sup> it proceeds via hydrogen transfer from the alcohol to an acceptor. The precise mechanism of this second route is an area of contention with two hypothesised workings, see **Figure 1.2**.<sup>[10, 12-14, 43]</sup> The first occurs via a hydroperoxy complex (*b*), formed by molecular oxygen insertion into a Pd-H bond (*a*), and maintains the Pd(II) oxidation state throughout. The other sees cycling of the Pd oxidation state, between (II) and (0), and occurs via a peroxypalladium complex (*c*). It is theorised that the nature of the ligands dictate which routes a catalyst takes.<sup>[14]</sup>

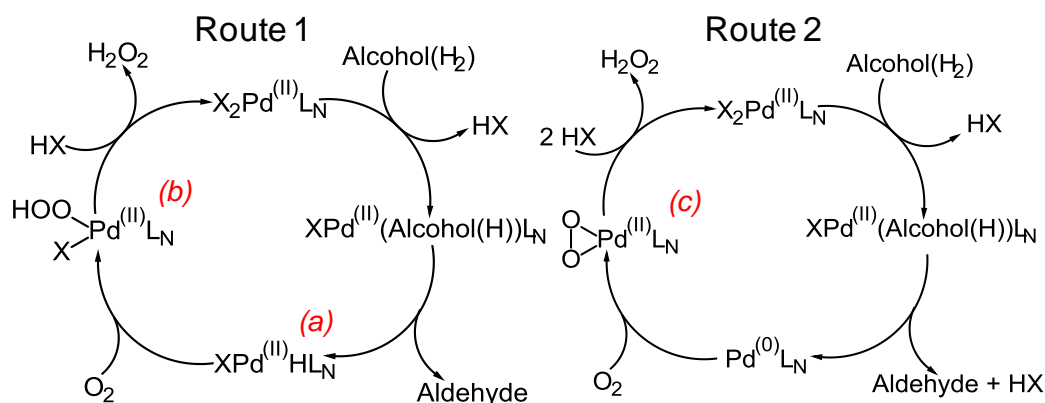


**Figure 1.2** – The major proposed reaction mechanisms (simplified) for aerobic oxidations alcohols via the hydrogen transfer mechanism <sup>[14, 43]</sup>

Tethering of Pd complexes to solid supports, known as heterogenisation, is one method of overcoming some of their shortfalls.<sup>[15, 34]</sup> This aids catalyst recovery by economically and environmentally desirable methods, including filtration, centrifugation or decantation. Further to this, product contamination can be eradicated/reduced, thus possibly offering a route for high-end chemical sector use. Increased catalyst recyclability is possible, via increased recovery and reduced sintering (agglomeration)<sup>[11, 44, 45]</sup> although metal leaching,<sup>[10, 31]</sup> possibly via the tethering species cleavage,<sup>[16]</sup> has been noted. Further issues arise from the continued requirement for auxiliary species and multiplied synthesis complexity.<sup>[12, 15, 45]</sup> Finally this methodology can cause a loss of catalyst reactivity,<sup>[10]</sup> due to either the modification of the catalytically active site<sup>[31, 34]</sup> or because it can result in reactions proceeding under mass transfer limited conditions within porous supports.<sup>[46]</sup> Heterogenisation of stoichiometric reagents is also achievable. Both permanganate and chromate on alumina show activity towards carbonyl species formation, including allylic aldehydes, without overoxidation, although these are still limited due to their stoichiometric mode of action.<sup>[9, 34]</sup>

### 1.1.2.2 Heterogeneous palladium catalysts

Precise control over synthetic conditions in conjunction with surface coordinated capping agents/stabilisers allow the formation of mono-dispersed shape and size selective Pd nanoparticles, which is an attractive route to prepare well defined heterogeneous Pd catalysts.<sup>[15, 30, 31, 47]</sup> These are capable of exhibiting a range of

common facets ((100), (110) and (111)), with varying relative concentrations achievable,<sup>[48, 49]</sup> of the face centred cubic Pd crystal structure. This packing results in a Pd coordination number of 12 in the bulk although this is significantly lower at the surface. The control of particle size regulates the bulk to surface ratio with a direct relationship observed, generally a beneficial phenomenon.<sup>[16, 50, 51]</sup> Additionally this also dictates the low co-ordination edge and corner sites to terrace ratio.<sup>[52, 53]</sup> These are quasi-homogeneous systems, a term coined as a result of the two ways by which the catalyst can be envisaged. This being either as large ‘soluble’ molecules and thus homogeneous, or as discrete solids and thus heterogeneous,<sup>[50]</sup> are shown to selectively oxidise benzyl alcohol.<sup>[54, 55]</sup> Regrettably, a noteworthy limitation does materialize due to the necessity of a capping agent, frequently comprised of a large chain surfactant. The co-ordination of this onto the metal surface restricts, to a degree, the accessibility of the active site.<sup>[50]</sup> This can curb reactivity below its feasible maximum as reactions can end up occurring under mass transfer limited conditions.<sup>[54]</sup> One must not forget the capping agent is essential to prevent particle growth/sintering during synthesis/catalytic reactions; therefore a trade-off between the two is necessary.

A major obstacle still not alleviated by these is their complete recovery from the reaction solution. This is a repercussion of their nanometre size range which complicates retrieval by filtration, although centrifugal methods are still applicable. Yet again supporting these active sites, as with the homogeneous species, can help to overcome this issue.<sup>[56, 57]</sup> The likelihood of leaching with these regrettably increases because the support metal interaction is weakened,<sup>[19]</sup> due to the presence of the capping agent. High temperature treatments can promote interaction, via removal of the capping agent, although this can induce shape and size modifications.<sup>[49, 58]</sup> In contrast to supporting these active species a porous protective shell, conventionally silica, can be synthesised around them with the capping agent able to act as a pore template,<sup>[59]</sup> a technically beautiful piece of chemistry which overcomes Pd agglomeration whilst still allowing active site accessibility.

An alternative to supporting preformed catalysts, either anchored homogeneous systems or deposited quasi-homogeneous species, is to generate the active sites in-situ, either in the presence of a porous support or during its formation.<sup>[30, 60, 61]</sup> This permits a simplistic strategy for the production of heterogeneous catalysts.

Frequently used classical techniques to afford these composites included; wet impregnation,<sup>[62-74]</sup> ion exchanging,<sup>[74-82]</sup> adsorption method (commonly on functionalised surfaces),<sup>[46, 83, 84]</sup> and deposition precipitation.<sup>[85-87]</sup> All have been utilised when a support has been preformed and are achieved by inducing an interaction between an active site precursor, e.g. a Pd salt or simple common complex, and the support. In the case of metal nanoparticle active sites this is often followed by high temperature treatments to convert the precursor into the desired active species. Alternatively a catalyst precursor can be introduced during support synthesis, so called co-precipitation.<sup>[68, 88, 89]</sup> This has led to greatly dispersed metal nanoparticles although their accessibility can be hindered if they are embedded in the support and can also compromise the support's physical qualities.<sup>[88, 89]</sup> Careful tailoring of synthetic parameters has permitted the production of mesoporous silicas containing metal nanoparticles within a mesopore network, thus reducing/overcoming the issue of metal accessibility whilst maintaining the desired support physical properties.<sup>[90, 91]</sup> These rudimentary avenues of catalyst preparation can lessen their environmental impact and economic cost, although support synthesis, especially for intricate high surface area supports, should not be overlooked when evaluating this. As stated earlier recovery of supported active species is straightforward, assuming support size is sufficient to allow filtration.<sup>[9]</sup> The major limitations of these methods are their reduced control over active site particle size and morphology. As a result the active species are consistently less well defined than supported homogeneous and quasi-homogeneous systems.<sup>[50]</sup> Even so, examples of the use of these catalysts in allylic and benzyl alcohol selox are widespread,<sup>[46, 63, 64, 69-71, 77-79, 83, 84]</sup> a likely result of their simplistic preparation.

### **1.1.2.3 Mechanism of heterogeneously catalysed palladium selox**

The reactivity of Pd towards selox reactions originates from its ability to activate alcohols and molecular oxygen at close to ambient temperatures.<sup>[17, 31]</sup> The popular consensus is that this progresses via the oxidative dehydrogenation route.<sup>[30, 31]</sup> The classic explanation proceeds via an alkoxy species adsorbed on the metal surface. This forms during alcohol adsorption as a result of the cleaving of the hydrogen from the alcohol moiety, with the hydrogen also adsorbing onto the surface.<sup>[17, 22]</sup> The alkoxy species loses a further hydrogen atom, again adsorbing on the surface, preferentially from the  $\beta$ -carbon (oxygen assigned as the  $\alpha$  species) due to

destabilisation of this bond by the electron withdrawing effect imparted by the oxygen.<sup>[17, 22]</sup> The presence of hydrogen at the  $\beta$ -carbon results in the heightened activity towards primary and secondary alcohols over tertiary alcohols, as hydrogen attached to  $\gamma$ -carbons are less destabilised. The scission of the second hydrogen is acknowledged as the rate determining step, with carbonyl desorption completing the catalytic cycle. Dissociatively adsorbed oxygen is proposed to react with the liberated hydrogen producing water, which desorbs and drives the equilibrium toward carbonyl formation, as illustrated in **Figure 1.3**.<sup>[30, 31, 92]</sup>

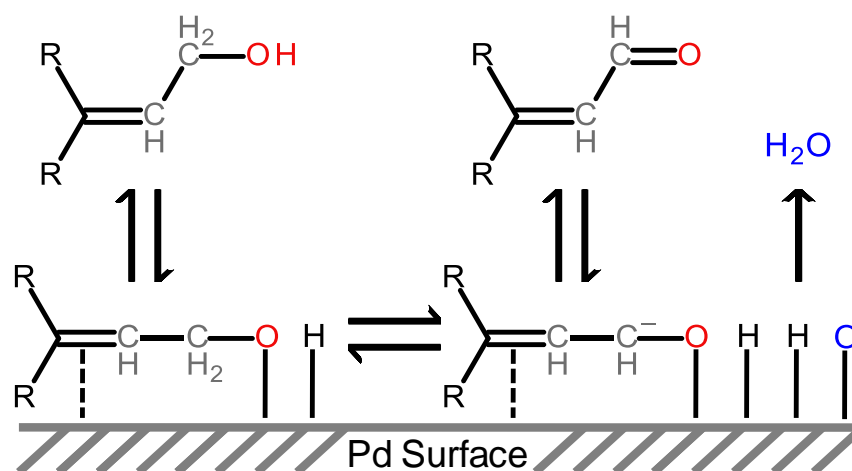


**Figure 1.3** – Classic alcohol oxidative dehydrogenation mechanism<sup>[30, 31]</sup>

This mechanism is supported by the following observations:-

- Oxygen can be substituted with hydrogen acceptors, e.g. olefins, without oxidation ceasing thus oxygen insertion does not occur.<sup>[31]</sup>
- XAS indicated a metallic active site.<sup>[20, 29, 31, 92-94]</sup> More recently an oxide (surface species) appears critical.<sup>[18, 24, 33, 63, 69, 95, 96]</sup>
- Hydrogenation and hydrogenolysis side reactions are observed which are known to occur on metallic surfaces.<sup>[17, 31]</sup>
- Intermediate Pd-O bond strength (adsorbed alkoxy) minimises C-O bond breakage. Stronger metal-O bonds (Mo) enhance C-O scission.<sup>[17]</sup>
- $^{18}O$  studies show no incorporation into hydrocarbon products.<sup>[22, 30]</sup>
- Comparable mechanism, beta-hydride elimination, to homogeneous systems.<sup>[10]</sup>

A modification of this mechanism, in which oxygen assists desorption of products, is also proposed.<sup>[20, 31, 97]</sup> Side reactions generate CO and hydrocarbons which leads to coking of the surface if they are not removed. More important is desorption of the desired aldehyde, which decreases the likelihood of it reacting further via decomposition.<sup>[18, 24, 63, 95]</sup> Thus at least a partial oxide covering of the surface is essential to maintain catalytic activity.

#### **1.1.2.4 Heterogeneous palladium active site**

As alluded to above, the active site in Pd catalysed selox is an area of widespread interest and debate. A metallic Pd active site has been suggested,<sup>[93, 94]</sup> due to the greater activity of bulk metallic Pd over bulk Pd oxide.<sup>[92]</sup> More recently the importance of at least a partial oxide surface for good catalyst reactivity and selectivity has been indicated.<sup>[18, 20, 24, 31, 95-97]</sup> This revelation suggests that the action of adsorbed oxygen is not solely to react with the hydrogen liberated, but is actually involved in product desorption, both desired and undesired.

Two proposals have been put forwards regarding the oxide surface. First it promotes Pd surface cleaning by assisting desorption of carbonaceous species, and thus regenerates a metallic active surface.<sup>[20, 31, 97]</sup> This is supported by in-situ XAS/ATR-IR which indicates that Pd is inactive until reduced.<sup>[92]</sup> It is worth highlighting that the Pd would look predominately metallic by XAS if it consisted of relatively large nanoparticles (in excess of 2nm), a feature of the majority of samples studied, with only a surface covering of oxide. Additionally, assignment of products from ATR-IR is severely limited as this probes surface species, not liquid phase components.

Another hypothesised role is that an oxide surface is more active for oxidative dehydrogenation, with a metallic surface readily poisoned by decomposition products. In-situ XAS results clearly indicate that activity decreases as the catalyst becomes more metallic.<sup>[96]</sup> Supported by drastically lower reactivity after in-situ pre-reduction, sintering from the pre-treatment was not apparent. The combination of XAS, DRIFTS and MS further verifies this conclusion,<sup>[24]</sup> the additional ability to monitor the products released from the surface being crucial. An oxide surface is vital for the formation and desorption of the desired aldehyde, whereas a metallic surface only forms the aldehyde with desorption inhibited. Rapid poisoning ensues

unless an oxide surface is restored. This has been confirmed by an in-situ surface sensitive XPS study.<sup>[18]</sup> Both revealed decomposition is favourable over a metallic surface. In fact the attributed catalyst activity in the XAS/ATR-IR experiment,<sup>[92]</sup> due to observed surface aldehyde, can be explained by the same reasoning. This could indicate catalyst poisoning by the aldehyde rather than a true catalytic cycle. The lack of observed aldehyde on the oxide surface, at the beginning of the reaction, could be due to a lower coverage resulting from its steady state desorption. Finally the synthesis of well dispersed catalysts, on alumina supports, revealed the merit of the Pd(II) oxidation state for allylic alcohol selox.<sup>[63, 64]</sup> Mesoporous alumina elevated dispersion to produce atomically dispersed Pd(II) species,<sup>[63]</sup> which exhibit exceptional TOFs ( $\sim 7000 \text{ h}^{-1}$  and  $4400 \text{ h}^{-1}$  for crotyl and cinnamyl alcohol respectively). No induction period was observed, so the high oxidation state surface must be active, as in-situ reduction is not essential. This highlights the importance of oxidation state in heterogeneously catalysed Pd selox, revealing similarities between these and homogeneous complexes which are routinely Pd(II) species.<sup>[13, 15, 43]</sup>

### 1.1.2.5 Heterogeneous palladium selectivity

Ideally reactions would be 100 % selective towards the desired product.<sup>[5]</sup> Regrettably, in the real world, this is rarely the case. So as important as activity is, selectivity of a catalytic system can be a greater deciding factor on whether it is implemented on an industrial scale.<sup>[98]</sup> The overall selectivity of a given catalyst, under a set of reaction conditions, is dictated by the relative occurrence of various possible reaction pathways. The formation of alternative products rather than the desired one, from identical or differing transition states, is detrimental.<sup>[22]</sup> Activation energy barriers of by-product formation must be similar to the favourable product, graphically depicted in **Figure 1.4**, with the degree to which they form being relative to how close they are.<sup>[51]</sup> This occurs due to the multitude of reaction pathways that an adsorbed intermediate can take and is responsible for the simultaneous formation of side products. Any modification of the active surface, chemically or physically, over the course of the reaction will result in changes to the activation energy barriers towards possible products, and thus shift selectivity.<sup>[51]</sup> Controlling desired product selectivity will often require a varied approach to enhance activity because the rate determining step might not necessarily be the step that decides selectivity.

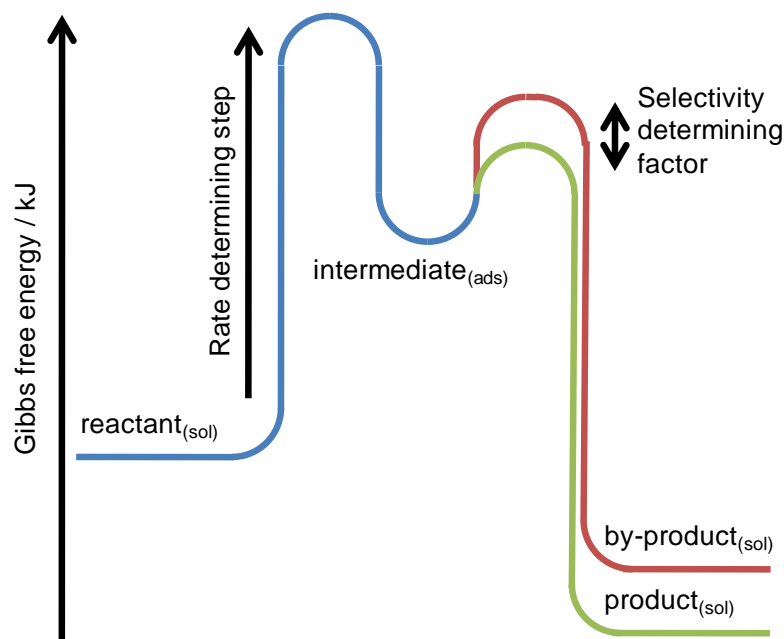


**Figure 1.4** – Potential-energy plot of product formation <sup>[22]</sup>

Consecutive reactions, in which the major product can further react to form more thermodynamically stable product(s) is also disconcerting. The use of a catalyst that will form only the desired product but not unwanted by-products, i.e. kinetic control, can help mediate this issue.<sup>[22]</sup> These selectivity influencing factors are manipulated by experimental and molecular factors including; surface structure, adsorbate induced restructuring, reaction intermediates and surface composition e.g. oxidation state.<sup>[51]</sup>

The select of cinnamyl alcohol<sup>(a)</sup> to cinnamaldehyde<sup>(b)</sup> over heterogeneous Pd systems can result in the formation of a multitude of products,<sup>[20, 31]</sup> shown in **Figure 1.5**, for a 5 wt% Pd alumina catalyst (65 °C, 1 bar air). The major by-products result from the hydrogenation of the olefinic moiety<sup>(c)</sup>, in particular the alcohol, this being indicative of the presence of surface hydrogen. This is further hinted at from the observed hydrogenolysis<sup>(d)</sup> of the carbon-oxygen bond. Decarbonylation<sup>(e)</sup> is also observed and is a route towards deactivation, as discussed above, via CO poisoning of the catalytic surface. Reaction conditions, such as temperature, oxygen/air flow rate and batch versus flow reactor design, can notably affect product distribution.<sup>[51]</sup> The addition of flowing oxygen through the reaction can emphatically escalate selectivity towards the desired carbonyl product.<sup>[71]</sup>

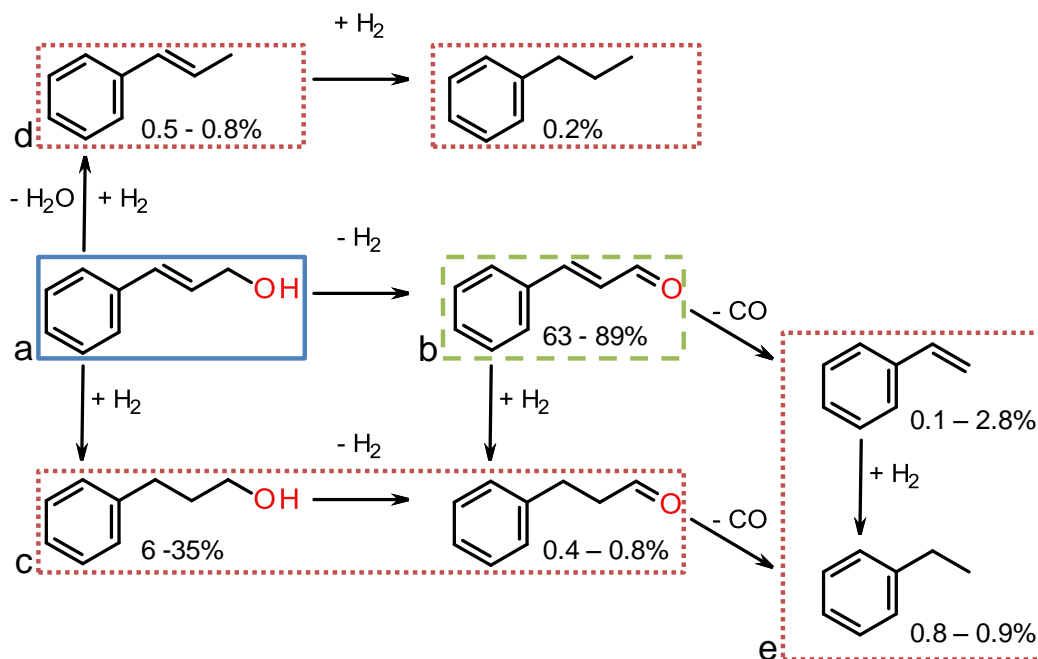


**Figure 1.5** – Product distribution for cinnamyl alcohol selox over Pd <sup>[20, 31]</sup>

### 1.1.2.6 Heterogeneous palladium deactivation

Catalyst deactivation can be categorised into six generic types; <sup>[99, 100]</sup>

- 1) poisoning by strongly bound chemisorbed species;
- 2) coking of the active site and/or support by carbon species;
- 3) solid state transformation;
- 4) leaching of the active species either in solution or by volatilisation;
- 5) thermal degradation such as sintering; or
- 6) mechanical degradation.

For Pd catalysis types 1-5 are the most common, <sup>[101]</sup> with poisoning, <sup>[92]</sup> coking <sup>[18, 102]</sup> and solid state transformation (reduction of surface oxidation state) <sup>[24, 96]</sup> having been reported during dehydrogenation reactions. The level and rate to which these occur is very sensitive to reaction conditions.

The types of deactivation postulated for liquid phase alcohol selox include overoxidation of the catalyst surface, leading to oxygen surface poisoning. <sup>[92, 103]</sup> This is however suggested in the context of the metallic sites being the active species. The level of dissociated oxygen present on the Pd surface is reported to be critical; too little and the surface becomes coked up, whereas too high leads to surface poisoning. In contrast, where an oxidic active site is hypothesised, oxygen

availability is critical in maintaining the active site.<sup>[63, 64]</sup> In-situ and operando experiments confirm this via decreased catalyst reactivity and selectivity under oxygen starved circumstances.<sup>[18, 24, 95, 96]</sup> This leads to decomposition reactions, over a metallic surface, leaving a carbon rich surface that does not desorb, i.e. a coked surface. The presence of this could be a cause of decarbonylation,<sup>[102, 104]</sup> as this is preferential over a carbon covered Pd surface. The low temperatures, typically less than 100 °C, and organic solvents commonly used in these reactions impede both sintering and leaching of the active species.<sup>[31, 45, 63, 64, 70, 71, 77, 97]</sup>

### 1.1.3 Catalyst supports

Straightforward catalyst recovery, attainable via a metamorphosis of a homogeneous or quasi-homogeneous to a heterogeneous catalytic system, is just one of the prime benefits that catalyst supports can afford. Likewise in-situ generated nanoparticles, either on preformed materials or during support synthesis, are also afforded this desirable property. Common support materials investigated include silica, alumina, titania, ceria, zirconia and mixtures of these such as alumina silicates or carbon based species.<sup>[33, 58, 60]</sup> Due to their varying chemical nature, which can influence supported metal nanoparticles; factors such as metal support interaction and acidity/basicity require consideration.<sup>[58, 105, 106]</sup> Physical properties are fundamentally more tuneable via controlled synthetic conditions.<sup>[2, 107-111]</sup> Surface areas, porosity including architecture, particle size and morphology are all controllable. As a result active species dispersion, sinter resistance qualities, ease of internal mass diffusion, and superior selectivity can all be dictated.

The term ‘strong metal support interaction’ was coined by Tauster, after observations made regarding Pd supported on TiO<sub>2</sub>.<sup>[105]</sup> High temperature reduction at 500 °C decreased the level of CO and H<sub>2</sub> that adsorbed on the Pd surface relative to the same material reduced at 400 °C. Sintering was eliminated as being the sole cause for this with altered electronic and geometric properties being advocated.<sup>[51, 106]</sup> Electron donation from the support to the metal is one explanation, although this only occurs over very short distances,<sup>[106]</sup> the nearest few neighbouring atoms. Geometric alterations have also been recognised with metal nanoparticles ‘spreading’ to form raft-like morphologies. This increases the metal support synergy and thus could enhance the likelihood of electronic alterations occurring.<sup>[105, 106]</sup> Alternatively

support migration has also been declared with it resulting in active site capping, either completely or by discreet islands. <sup>[105, 106]</sup> This being the reported reason for the loss of CO and H<sub>2</sub> adsorption in the original Tauster report. <sup>[105]</sup> Strong interactions are only observed for reducible supports such as TiO<sub>2</sub> and CeO<sub>2</sub>, <sup>[106, 112]</sup> and occur only after sufficiently high reduction processes, greater than 400 °C for Pd on CeO<sub>2</sub>. <sup>[112]</sup> This can impact greatly on catalytic activity and selectivity. <sup>[51, 105, 106, 112]</sup> Weak metal support interactions are also acknowledged, with this accredited to Van der Waals forces, typical of non-reducible support e.g. SiO<sub>2</sub> and Al<sub>2</sub>O<sub>3</sub> <sup>[105, 113]</sup> although relative to silica, alumina asserts a greater support interplay with Pd. <sup>[58, 113]</sup>

Acidic supports draw electron density from very small metal clusters inducing positively charged species; larger metal nanoparticles are capable of delocalising this charge across their vast number of atoms. <sup>[58]</sup> This influence originates from the interplay between metal clusters with Brønsted or Lewis acid sites, an effect common in zeolites which can beneficially restrain nanoparticle growth within their micropore domains. Brønsted acidity is associated with the donation, at least partially, of hydrogen from the support whereas Lewis acidity covers the ability of the support to accept electrons. Alumina silicate zeolites exhibit both acidity types. <sup>[58]</sup> Al<sup>3+</sup> substitution of Si<sup>4+</sup> within the solid framework induces Brønsted acidity, depicted in **Figure 1.6** <sup>[111]</sup> with the negative charge associated with this substitution counteracted by proton addition to the bridging oxygen. Lewis acidity arises from the existence of extra framework alumina inducing positive charged sites. <sup>[111]</sup>

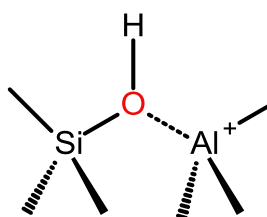


**Figure 1.6** - Brønsted acidity in Zeolites (alumina silicates)

A support surface area increase, through the introduction of internal porosity is common, although control over particle size can also be significant. Elevating surface area confers an increase in active site dispersion, <sup>[16]</sup> especially when metal nanoparticles are deposited on preformed catalyst supports. Porosity is classified

into 3 types; microporosity (pore diameters less than 2nm), mesoporosity (pore diameter between 2-50 nm) and macroporosity (pores greater than 50nm).<sup>[110]</sup> The lower surface areas of macroporous materials hinders active site dispersion, whilst the small pore size of microporous supports can result in internal mass transfer limitations during reactions.<sup>[9, 107, 114]</sup> The development of templated mesoporous supports is a promising solution to overcome these limitations.<sup>[107]</sup> By controlling the surfactant composition pore diameter and architecture can be tuned, resulting in interpenetrating and non-interpenetrating ordered and disordered systems.<sup>[110, 114, 115]</sup> Increasing pore size and interconnectivity was expected<sup>[116, 117]</sup> and recently shown to overcome interpore mass transfer restrictions.<sup>[69, 118]</sup> In addition enhanced metal dispersion,<sup>[63]</sup> reduced sintering<sup>[83]</sup> and lower coking<sup>[119]</sup> have all been reported for interconnected mesoporous supports relative to non-interconnected materials. Recent combination of dual porosity, involving macroporosity and mesoporosity in silica, has displayed elevated activity for bio-fuel production over pure mesoporous equivalents, with this attributed to enhanced mass diffusion of bulky substrate.<sup>[120]</sup> Size controlled product selectivity is achievable by the confinement of reactions within microporous/small mesopores, although often at the expense of operating under mass transfer limited conditions;<sup>[2, 111, 121]</sup> i.e. the rate of reactant diffusion to the active site is the controlling kinetic factor.<sup>[122-124]</sup> Dual meso and microporous zeolites is thus an area of great interest,<sup>[125-127]</sup> with the utilisation of dual porosity structural directing agents representing an elegant route to such materials.<sup>[128]</sup>

### 1.1.3.1 Ordered mesoporous silicas

Ordered mesoporous silicas were first reported in the early 1990s after the versatility of templating methodologies were first realised.<sup>[129, 130]</sup> This provided the blueprint for pore architectures, ordering and size distribution manipulation, and led to the M41S family, an important bridge in extending the range of porous support from the micro to mesopore domain.<sup>[121]</sup> Since then diverse mesoporous silicas have been reported, with their synthesis, properties and possible applications covered in numerous reviews including the ones by Corma,<sup>[114, 121]</sup> Wan,<sup>[107, 115]</sup> Meynen,<sup>[110]</sup> Schuth<sup>[125]</sup> and Viswanathan.<sup>[131]</sup> The high surface areas, tuneable pore structures and thermal/chemical stability<sup>[16]</sup> of the SBA family,<sup>[116, 117]</sup> in particular SBA-15/16, and KIT-6<sup>[132, 133]</sup> make them choice support materials. These exhibit a variety of pore architectures; including 2-D non-interconnected hexagonal *p6mm*

(SBA-15) and 3-D interconnected systems  $Im\bar{3}m$  (SBA-16) and  $Ia\bar{3}d$  (KIT-6). These architectural variations combined with their chemical inertness,<sup>[134]</sup> relative to reducible supports, and weak metal interactions,<sup>[105, 113]</sup> are beneficial when probing the role of support physical properties.

Synthesis of these materials requires the presence of a cationic, anionic or non-ionic surfactant, as a structure directing agent. Non-ionic surfactants are becoming more attractive due to their low toxicity, biodegradability and wide range of assembly geometries.<sup>[107]</sup> Originally it was proposed that templating occurred around a preformed micelle liquid crystal structure.<sup>[130]</sup> More recently a cooperative self-assembly mechanism was proposed for the low surfactant concentration (~5 %) used, which is widely accepted.<sup>[107, 121]</sup> Entropy driven surfactant micelle formation occurs as a result of the removal water of crystallisation that forms around individual surfactant molecules. Electrostatic interaction and/or hydrogen bonding between the silica, silicate ion (anion or cation pH dependent), and surfactant micelles follows. Common reagents and corresponding interactions include;<sup>[107, 121]</sup>

- ionic surfactant (S) and silicate (I) with opposite charge e.g.  $S^+I^-$
- ionic surfactant and silicate with matching charge in the presence of a counter ion such as halogen, nitrate or sulphate e.g.  $S^+XI^-$
- A nonionic surfactant, silicate and acid e.g.  $S^0H^+XI^+$
- A nonionic surfactant and hydrated silicate e.g.  $S^0I^0$

Silica polymerisation at the interface ensues from this interaction, with this stage believed to result in self-assembly leading to mesopore architecture,<sup>[135, 136]</sup> via the coalescing of these silicate surfactant species. Precipitation accompanies this step with further polymerisation and condensation resulting in the formation of the silica walls.<sup>[107]</sup> True liquid crystal templating (TLCT) represents an alternative synthetic pathway.<sup>[137]</sup> Notably high (~50 %) surfactant concentrations result in lyotropic ( $H_1$  normal phase) liquid crystal phase formation,<sup>[138]</sup> around which silica can be templated. An analogous method to this is the evaporation induced self-assembly strategy. This is used to form silica films and membranes, and where slowing the rate of inorganic precursor hydrolysis is desired, such as titania<sup>[110]</sup> or alumina.<sup>[139-141]</sup> Production of inorganic oligomers, by controlled polymerisation in volatile polar protic solvent, facilitates enhanced assembly at the surfactant interface.<sup>[107, 115]</sup> During solvent evaporation further inorganic species polymerisation occurs

combined with liquid crystalline phase formation, due to increasing surfactant concentration, around which the material is templated.

The choice of structure directing agent can impact on multiple mesopore properties. First, pore shape, which subsequently effects pore architecture, and is predictable.<sup>[107, 115]</sup> The ratio of hydrophilic to hydrophobic moieties in nonionic triblock copolymer surfactants, used to produce SBA-15/16 and KIT-6, is the influential factor. High ratios favour spherical surfactant micelles; the larger hydrophilic region being capable of fully encapsulating the hydrophobic section; whereas lower ratios favour less curved geometries, disks that congregate into rods. This, combined with how these surfactant structures pack together, determine the difference between SBA-15 and SBA-16. The interpenetrating bicontinuous '3D' structure of KIT-6, which is synthesised from the same structure directing agent as SBA-15, occurs due to the addition of 1-butanol. It has been put forward that during the final condensation of the silica, after precipitation, butanol at the water surfactant interface causes an initial hexagonal phase to restructure to the *Ia3d* structure of KIT-6.<sup>[142]</sup> Surfactant phase diagrams allow the prediction of the resulting pore network prior to its production when using the TLCT method.<sup>[137]</sup> Structural directing agents also influence pore diameter; increasing the length of the alkyl chain of ionic surfactants or increasing the molecular weight of the hydrophobic moiety in non-ionic surfactants increases mesopore diameter. For quaternary ammonium surfactants, used for MCM-41 production, an increase in chain length from C<sub>8</sub> to C<sub>22</sub> increases pore diameter from 1.6 to 4.2 nm.<sup>[107]</sup> Further increases are possible using swelling agents, organic molecules such as 1,3,5-trimethylbenzene or hexane, preferentially dissolve in the hydrophobic surfactant region swelling the micelles.<sup>[107, 121, 143]</sup> Finally, increasing the duration and temperature of the hydrothermal treatments can also provoke increases.<sup>[116, 132, 144, 145]</sup> The hydrolysis and cross linking of the inorganic species continues during this step allowing pore diameters to be influenced.

Significant mesopore interconnectivity, due to the presence of complementary microporosity, is reported for SBA-15.<sup>[144, 146-151]</sup> This is theorised to arise from the interaction between the more hydrophilic ethylene oxide region and the silica framework. Significant interpenetration of the ethylene oxide chains into the inorganic layer is the precursor to microporosity, which can lead to mesopore

interconnections.<sup>[151]</sup> Increasing hydrothermal temperature decreases microporosity although there is not a general consensus on why. Deprotonation<sup>[144]</sup> or dehydration<sup>[150]</sup> of the ethylene oxide lowers its hydrophilic nature and thus interaction at the inorganic interface. Alternatively high hydrothermal temperature induces swelling of the micropores into mesopores, which avoid detection in microporosity calculations.<sup>[151]</sup> Evaporation induced self-assembly results in decreased microporosity, due to the rapid formation of the solid structure with this also the reason for the result less uniform mesopore structure.<sup>[107, 115]</sup> Further connections between two neighbouring mesopores, due to presence of looping mesopore channels at pore openings, has been observed by SEM.<sup>[152]</sup>

Although not widespread, high temperature aqueous recrystallisation (100-150 °C for up to a week) prior to surfactant removal can amplify long range pore order.<sup>[115]</sup> While the reason behind this is ambiguous, it only affects materials in which the surfactant is still present and that are not washed after recovery. Thus trace levels of acid or/base from the synthesis are vital.

Removal of the structure directing template is most commonly achieved through calcination.<sup>[116, 130]</sup> Slow ramp rates are required to avoid localised overheating, which is detrimental, with temperature maxima being greater than that required to totally remove the surfactant, without damaging the support, typically 500-550 °C. The drawback to calcination is the loss of the surfactant template. Template extraction in organic solvents such as ethanol can overcome this, although complete triblock copolymer removal is not achievable; approximately 4 % remains. Stepwise removal of the template by decomposition in concentrated H<sub>2</sub>SO<sub>4</sub> (generating mesoporosity) with subsequent calcination at 200 °C to remove the remaining template (yielding complementary micropores) has also been shown.<sup>[146, 147]</sup>

### **1.1.3.2 Ordered mesoporous alumina**

Alumina has found wide catalysts support applications in industry.<sup>[108]</sup> As a result improvements to their physical properties, porosity in particular, is highly beneficial. In 1996 Vaudry published the first mesoporous alumina synthesis, this employed carboxylic acids as structure directing agents.<sup>[153]</sup> This fabricated materials with low long range pore order; only one broad low angle XRD peak was observed, and small mesopore/large micropore diameters. Additionally low thermal stability could result

in pore ordering losses accompanied by support wall crystallisation and pore collapse.<sup>[108, 109]</sup>

Recently synthetic routes via the evaporation induced self-assembly pathway have employed the same triblock copolymer utilised in SBA-15 and SBA-16.<sup>[141, 154]</sup> This extended long range pore order and increased pore diameters, up to ~7 nm. Irrespective of whether Pluronic P123 and F127, structure directing agents for SBA-15 and SBA-16 respectively, is used the same 2-D non-interconnected hexagonal (*p6mm*) networks is formed. Whilst these lack the high level of complementary microporosity, present in equivalent mesoporous silica, complementary macropores can be introduced using a comparable hard templating method to silicas.<sup>[139]</sup>

Not long after the discovery of the M41S family it was shown that an alumina precursor could be co-precipitated during MCM-41 synthesis at varying ratios;<sup>[155, 156]</sup> a procedure which introduces Brønsted and Lewis acidity into the support. At low alumina incorporation the materials show well ordered porosity throughout, unfortunately at high alumina content catastrophic loss or pore order occurs.<sup>[157]</sup> Alternatively alumina can be grafted onto mesoporous silicas, which results in a highly ordered thermally stable material.<sup>[158]</sup> This is also witnessed to exhibit acidity, especially at low alumina contents less than ~10 wt%.<sup>[159-163]</sup>

## 1.2 Thesis aims

The principle aims of this investigation are:

- To explore the influence that mesoporous silica support architectures can impart to supported Pd nanoparticles; including their consequence on Pd impregnation and the resulting physio-chemical properties of the supported Pd nanoparticles.
- To study these materials as catalysts for allylic alcohol selenylation; the role of support structure in relation to internal mass transfer limitations, if they arise, and to gain a further understanding of the active species responsible for these catalytic transformations and their subsequent deactivation mechanism.

## 1.3 References

1. Atkins, P., *The Elements of Physical Chemistry*. 3rd ed. 2001, Oxford: Oxford University Press.
2. Vermeiren, W. and J.P. Gilson, *Topics in Catalysis*, 2009. **52**: p. 1131.
3. Vougioukalakis, G.C. and R.H. Grubbs, *Chemical Reviews*, 2010. **110**: p. 1746.
4. Koltsakis, G.C. and A.M. Stamatelos, *Progress in Energy and Combustion Science*, 1997. **23**: p. 1.
5. Clark, J.H., *Green Chemistry*, 1999. **1**: p. 1.
6. Clark, J.H., *Green Chemistry*, 2005. **8**: p. 17.
7. Lee, D.G. and U.A. Spitzer, *Journal of Organic Chemistry*, 1970. **35**: p. 3589.
8. Prabhakaran, P.V., S. Venkatachalam, and K.N. Ninan, *European Polymer Journal*, 1999. **35**: p. 1743.
9. Clark, J.H. and D.J. Macquarrie, *Chemical Society Reviews*, 1996. **25**: p. 303.
10. Sheldon, R.A., I. Arends, and A. Dijkstra, *Catalysis Today*, 2000. **57**: p. 157.
11. Choudary, B.M., K.M. Lakshmi, and S.P. Lakshmi, *Catalysis Today*, 2000. **57**: p. 17.
12. Zhan, B.Z. and A. Thompson, *Tetrahedron*, 2004. **60**: p. 2917.
13. Stahl, S.S., *Angewandte Chemie-International Edition*, 2004. **43**: p. 3400.
14. Muzart, J., *Chemistry-an Asian Journal*, 2006. **1**: p. 508.
15. Muzart, J., *Tetrahedron*, 2003. **59**: p. 5789.
16. Polshettiwar, V. and R.S. Varma, *Green Chemistry*, 2010. **12**: p. 743.
17. Weldon, M.K. and C.M. Friend, *Chemical Reviews*, 1996. **96**: p. 1391.
18. Lee, A.F., Z. Chang, P. Ellis, S.F.J. Hackett, and K. Wilson, *Journal of Physical Chemistry C*, 2007. **111**: p. 18844.
19. Marx, S., F. Krumeich, and A. Baiker, *Journal of Physical Chemistry C*, 2011. **115**: p. 8195.
20. Keresszegi, C., T. Brugi, T. Mallat, and A. Baiker, *Journal of Catalysis*, 2002. **211**: p. 244.
21. Liu, X.Y., R.J. Madix, and C.M. Friend, *Chemical Society Reviews*, 2008. **37**: p. 2243.
22. Zaera, F., *Catalysis Letters*, 2003. **91**: p. 1.
23. Pang, S.H. and J.W. Medlin, *Acs Catalysis*, 2011. **1**: p. 1272.
24. Lee, A.F., C.V. Ellis, J.N. Naughton, M.A. Newton, C.M.A. Parlett, and K. Wilson, *Journal of the American Chemical Society*, 2011. **133**: p. 5724.
25. Newton, M.A., *Topics in Catalysis*, 2009. **52**: p. 1410.
26. Bando, K.K., T. Wada, T. Miyamoto, K. Miyazaki, S. Takakusagi, Y. Koike, Y. Inada, M. Nomura, A. Yamaguchi, and T. Gott, *Journal of Catalysis*, 2012. **286**: p. 165.
27. Ferri, D., M.S. Kumar, R. Wirz, A. Eyssler, O. Korsak, P. Hug, A. Weidenkaff, and M.A. Newton, *Phys. Chem. Chem. Phys.*, 2010. **12**: p. 5634.
28. Newton, M.A. and W. van Beek, *Chemical Society Reviews*, 2010. **39**: p. 4845.
29. Mondelli, C., D. Ferri, J.-D. Grunwaldt, F. Krumeich, S. Mangold, R. Psaro, and A. Baiker, *Journal of Catalysis*, 2007. **252**: p. 77.
30. Besson, M. and P. Gallezot, *Catalysis Today*, 2000. **57**: p. 127.
31. Mallat, T. and A. Baiker, *Chemical Reviews*, 2004. **104**: p. 3037.
32. Kaneda, K., K. Ebitani, T. Mizugaki, and K. Mori, *Bulletin of the Chemical Society of Japan*, 2006. **79**: p. 981.

33. Vinod, C.P., K. Wilson, and A.F. Lee, *Journal of Chemical Technology and Biotechnology*, 2011. **86**: p. 161.
34. Rafelt, J.S. and J.H. Clark, *Catalysis Today*, 2000. **57**: p. 33.
35. Wang, X.L., R.H. Liu, Y. Jin, and X.M. Liang, *Chemistry-a European Journal*, 2008. **14**: p. 2679.
36. Uozumi, Y. and Y.M.A. Yamada, *Chemical Record*, 2009. **9**: p. 51.
37. Schultz, M.J., S.S. Hamilton, D.R. Jensen, and M.S. Sigman, *Journal of Organic Chemistry*, 2005. **70**: p. 3343.
38. Hattori, T., Y. Suzuki, O. Uesugi, S. Oi, and S. Miyano, *Chemical Communications*, 2000: p. 73.
39. Cheng, S.S., J.Y. Liu, K.H. Tsai, W.J. Chen, and S.T. Chang, *Journal of Agricultural and Food Chemistry*, 2004. **52**: p. 4395.
40. Blackburn, T.F. and J. Schwartz, *J. Chem. Soc., Chem. Commun.*, 1977: p. 157.
41. Zhou, M. and R.H. Crabtree, *Chemical Society Reviews*, 2011. **40**: p. 1875.
42. Punniyamurthy, T., S. Velusamy, and J. Iqbal, *Chemical Reviews*, 2005. **105**: p. 2329.
43. Popp, B.V. and S.S. Stahl, *Chemistry-a European Journal*, 2009. **15**: p. 2915.
44. Yang, H.Q., X.J. Han, Z.C. Ma, R.Q. Wang, J. Liu, and X.F. Ji, *Green Chemistry*, 2010. **12**: p. 441.
45. Karimi, B., A. Zamani, S. Abedia, and J.H. Clark, *Green Chemistry*, 2009. **11**: p. 109.
46. Chen, Y.T., H.M. Lim, Q.H. Tang, Y.T. Gao, T. Sun, Q.Y. Yan, and Y.H. Yang, *Applied Catalysis a-General*, 2010. **380**: p. 55.
47. Cushing, B.L., V.L. Kolesnichenko, and J.O.C. Charles, *Chemical Reviews*, 2004. **104**: p. 3893.
48. Xiong, Y., H. Cai, J. Benjamin, J. Wang, M.J. Kim, and Y. Xia, *Journal of the American Chemical Society*, 2007. **129**: p. 3665.
49. Tao, A.R., S. Habas, and P. Yang, *Small*, 2008. **4**: p. 310.
50. Jia, C.-J. and F. Schüth, *Physical Chemistry Chemical Physics*, 2011. **13**: p. 2457.
51. Somorjai, G.A. and J.Y. Park, *Angewandte Chemie-International Edition*, 2008. **47**: p. 9212.
52. Crespo-Quesada, M., A. Yarulin, M.S. Jin, Y.N. Xia, and L. Kiwi-Minsker, *Journal of the American Chemical Society*, 2011. **133**: p. 12787.
53. Zhou, X., N.M. Andoy, G. Liu, E. Choudhary, K.S. Han, H. Shen, and P. Chen, *Nature Nanotechnology*, 2012.
54. Hou, W.B., N.A. Dehm, and R.W.J. Scott, *Journal of Catalysis*, 2008. **253**: p. 22.
55. Biffis, A. and L. Minati, *Journal of Catalysis*, 2005. **236**: p. 405.
56. Demel, J., J. Cejka, S. Bakardjieva, and P. Stepnicka, *Journal of Molecular Catalysis a-Chemical*, 2007. **263**: p. 259.
57. Nadgeri, J.M., M.M. Telkar, and C.V. Rode, *Catalysis Communications*, 2008. **9**: p. 441.
58. Stakheev, A.Y. and L.M. Kustov, *Applied Catalysis a-General*, 1999. **188**: p. 3.
59. Joo, S.H., J.Y. Park, C.K. Tsung, Y. Yamada, P.D. Yang, and G.A. Somorjai, *Nature Materials*, 2009. **8**: p. 126.
60. White, R.J., R. Luque, V.L. Budarin, J.H. Clark, and D.J. Macquarrie, *Chemical Society Reviews*, 2009. **38**: p. 481.
61. Toebes, M.L., J.A. van Dillen, and Y.P. de Jong, *Journal of Molecular Catalysis a-Chemical*, 2001. **173**: p. 75.
62. Abate, S., P. Lanzafame, S. Perathoner, and G. Centi, *Catalysis Today*, 2011. **169**: p. 167.

63. Hackett, S.E.J., R.M. Brydson, M.H. Gass, I. Harvey, A.D. Newman, K. Wilson, and A.F. Lee, *Angewandte Chemie-International Edition*, 2007. **46**: p. 8593.
64. Lee, A.F., S.F.J. Hackett, J.S.J. Hargreaves, and K. Wilson, *Green Chemistry*, 2006. **8**: p. 549.
65. Arbiol, J., A. Cabot, J.R. Morante, F. Chen, and M. Liu, *Applied Physics Letters*, 2002. **81**: p. 3449.
66. Lee, S.S., H.I. Park, B.K. Park, and S.H. Byeon, *Materials Science and Engineering: B*, 2006. **135**: p. 20.
67. Li, J.J., X.Y. Xu, Z. Jiang, Z.P. Hao, and C. Hu, *Environmental Science & Technology*, 2005. **39**: p. 1319.
68. Wu, Y., L. Zhang, G. Li, C. Liang, X. Huang, Y. Zhang, G. Song, J. Jia, and C. Zhixiang, *Materials Research Bulletin*, 2001. **36**: p. 253.
69. Parlett, C.M.A., D.W. Bruce, N.S. Hondow, A.F. Lee, and K. Wilson, *Acs Catalysis*, 2011. **1**: p. 636.
70. Li, B., W.Z. Weng, Q. Zhang, Z.W. Wang, and H.L. Wan, *Chemcatchem*, 2011. **3**: p. 1277.
71. Yasu-eda, T., R. Se-ike, N.O. Ikenaga, T. Miyake, and T. Suzuki, *Journal of Molecular Catalysis a-Chemical*, 2009. **306**: p. 136.
72. Chilukoti, S., F. Gao, B.G. Anderson, J.W.H. Niemantsverdriet, and M. Garland, *Phys. Chem. Chem. Phys.*, 2008. **10**: p. 5510.
73. Ghedini, E., F. Menegazzo, M. Signoretto, M. Manzoli, F. Pinna, and G. Strukul, *Journal of Catalysis*, 2010. **273**: p. 266.
74. Bassil, J., A. AlBarazi, P. Da Costa, and M. Boutros, *Catalysis Today*, 2011. **176**: p. 36.
75. Jiao, L. and J.R. Regalbuto, *Journal of Catalysis*, 2008. **260**: p. 342.
76. Yuranov, I., P. Moeckli, E. Suvorova, P. Buffat, L. Kiwi-Minsker, and A. Renken, *Journal of Molecular Catalysis a-Chemical*, 2003. **192**: p. 239.
77. Li, C.L., Q.H. Zhang, Y. Wang, and H.L. Wan, *Catalysis Letters*, 2008. **120**: p. 126.
78. Li, F., Q.H. Zhang, and Y. Wang, *Applied Catalysis a-General*, 2008. **334**: p. 217.
79. Wu, H.L., Q.H. Zhang, and Y. Wang, *Advanced Synthesis & Catalysis*, 2005. **347**: p. 1356.
80. Cabilla, G.C., A.L. Bonivardi, and M.A. Baltanas, *Catalysis Letters*, 1998. **55**: p. 147.
81. Joyal, C.L.M. and J.B. Butt, *Journal of the Chemical Society-Faraday Transactions I*, 1987. **83**: p. 2757.
82. Okumura, K., K. Kato, T. Sanada, and M. Niwa, *The Journal of Physical Chemistry C*, 2007. **111**: p. 14426.
83. Ma, Z.C., H.Q. Yang, Y. Qin, Y.J. Hao, and G.A. Li, *Journal of Molecular Catalysis a-Chemical*, 2010. **331**: p. 78.
84. Chen, Y.T., L.L. Bai, C.M. Zhou, J.M. Lee, and Y.H. Yang, *Chemical Communications*, 2011: p. 6452.
85. Agostini, G., R. Pellegrini, G. Leofanti, L. Bertinetti, S. Bertarione, E. Groppo, A. Zecchina, and C. Lamberti, *The Journal of Physical Chemistry C*, 2009. **113**: p. 10485.
86. Soomro, S.S., F.L. Ansari, K. Chatziapostolou, and K. Kohler, *Journal of Catalysis*, 2010. **273**: p. 138.
87. Melada, S., F. Pinna, G. Strukul, S. Perathoner, and G. Centi, *Journal of Catalysis*, 2005. **235**: p. 241.
88. Wang, L.C., C.Y. Huang, C.Y. Chang, W.C. Lin, and K.J. Chao, *Microporous and Mesoporous Materials*, 2008. **110**: p. 451.
89. Han, P., X.M. Wang, X.P. Qiu, X.L. Ji, and L.X. Gao, *Journal of Molecular Catalysis a-Chemical*, 2007. **272**: p. 136.

90. Danks, M.J., H.B. Jervis, M. Nowotny, W.Z. Zhou, T.A. Maschmeyer, and D.W. Bruce, *Catalysis Letters*, 2002. **82**: p. 95.
91. Amos, K.E., N.J. Brooks, N.C. King, S. Xie, J. Canales-Vazquez, M.J. Danks, H.B. Jervis, W. Zhou, J.M. Seddon, and D.W. Bruce, *Journal of Materials Chemistry*, 2008. **18**: p. 5282.
92. Grunwaldt, J.D., M. Caravati, and A. Baiker, *The Journal of Physical Chemistry B*, 2006. **110**: p. 25586.
93. Caravati, M., D.M. Meier, J.D. Grunwaldt, and A. Baiker, *Journal of Catalysis*, 2006. **240**: p. 126.
94. Grunwaldt, J.D., C. Keresszegi, T. Mallat, and A. Baiker, *Journal of Catalysis*, 2003. **213**: p. 291.
95. Naughton, J., A. Pratt, C.W. Woffinden, C. Eames, S.P. Tear, S.M. Thompson, A.F. Lee, and K. Wilson, *Journal of Physical Chemistry C*, 2011. **115**: p. 25290.
96. Lee, A.F. and K. Wilson, *Green Chemistry*, 2004. **6**: p. 37.
97. Keresszegi, C., D. Ferri, T. Mallat, and A. Baiker, *Journal of Physical Chemistry B*, 2005. **109**: p. 958.
98. Somorjai, G.A. and K. McCrea, *Applied Catalysis a-General*, 2001. **222**: p. 3.
99. Bartholomew, C.H., *Applied Catalysis A: General*, 2001. **212**: p. 17.
100. Moulijn, J.A., A.E. Van Diepen, and F. Kapteijn, *Applied Catalysis A: General*, 2001. **212**: p. 3.
101. Albers, P., J. Pietsch, and S.F. Parker, *Journal of Molecular Catalysis A: Chemical*, 2001. **173**: p. 275.
102. Bowker, M., L. Cookson, J. Bhanoo, A. Carley, E. Hayden, L. Gilbert, C. Morgan, J. Counsell, and P. Yaseneva, *Applied Catalysis A: General*, 2011. **391**: p. 394.
103. Keresszegi, C., J.-D. Grunwaldt, T. Mallat, and A. Baiker, *Journal of Catalysis*, 2004. **222**: p. 268.
104. Bowker, M., L. Gilbert, J. Counsell, and C. Morgan, *The Journal of Physical Chemistry C*, 2010. **114**: p. 17142.
105. Tauster, S.J., *Accounts of Chemical Research*, 1987. **20**: p. 389.
106. Hayek, K., R. Kramer, and Z. Paal, *Applied Catalysis a-General*, 1997. **162**: p. 1.
107. Wan, Y. and D. Zhao, *Chemical Reviews*, 2007. **107**: p. 2821.
108. Marquez-Alvarez, C., N. Zilkova, J. Perez-Pariente, and J. Cejka, *Catalysis Reviews-Science and Engineering*, 2008. **50**: p. 222.
109. Cejka, J., *Applied Catalysis a-General*, 2003. **254**: p. 327.
110. Meynen, V., P. Cool, and E.F. Vansant, *Microporous and Mesoporous Materials*, 2009. **125**: p. 170.
111. Corma, A., *Chemical Reviews*, 1995. **95**: p. 559.
112. Tsubaki, N. and K. Fujimoto, *Topics in Catalysis*, 2003. **22**: p. 325.
113. Dropsch, H. and M. Baerns, *Applied Catalysis a-General*, 1997. **158**: p. 163.
114. Corma, A., *Topics in Catalysis*, 1997. **4**: p. 249.
115. Wan, Y., Y. Shi, and D. Zhao, *Chemical Communications*, 2007: p. 897.
116. Zhao, D.Y., Q.S. Huo, J.L. Feng, B.F. Chmelka, and G.D. Stucky, *Journal of the American Chemical Society*, 1998. **120**: p. 6024.
117. Zhao, D.Y., J.L. Feng, Q.S. Huo, N. Melosh, G.H. Fredrickson, B.F. Chmelka, and G.D. Stucky, *Science*, 1998. **279**: p. 548.
118. Chen, Y.T., Z. Guo, T. Chen, and Y.H. Yang, *Journal of Catalysis*, 2010. **275**: p. 11.

119. Huirache-Acuna, R., B. Pawelec, E. Rivera-Munoz, R. Nava, J. Espino, and J.L.G. Fierro, *Applied Catalysis B: Environmental*, 2009. **92**: p. 168.
120. Dhainaut, J., J.P. Dacquin, A.F. Lee, and K. Wilson, *Green Chemistry*, 2010. **12**: p. 296.
121. Corma, A., *Chemical Reviews*, 1997. **97**: p. 2373.
122. Hoek, I., T.A. Nijhuis, A.I. Stankiewicz, and J.A. Moulijn, *Chemical engineering science*, 2004. **59**: p. 4975.
123. Hájek, J. and D.Y. Murzin, *Industrial & Engineering Chemistry Research*, 2004. **43**: p. 2030.
124. Lee, A.F., J.J. Gee, and H.J. Theyers, *Green Chemistry*, 2000. **2**: p. 279.
125. Schüth, F. and W. Schmidt, *Advanced Materials*, 2002. **14**: p. 629.
126. Petushkov, A., G. Merilis, and S.C. Larsen, *Microporous and Mesoporous Materials*, 2011. **143**: p. 97.
127. Choi, M., H.S. Cho, R. Srivastava, C. Venkatesan, D.H. Choi, and R. Ryoo, *Nature Materials*, 2006. **5**: p. 718.
128. Choi, M., K. Na, J. Kim, Y. Sakamoto, O. Terasaki, and R. Ryoo, *Nature*, 2009. **461**: p. 246.
129. Kresge, C.T., M.E. Leonowicz, W.J. Roth, J.C. Vartuli, and J.S. Beck, *Nature*, 1992. **359**: p. 710.
130. Beck, J.S., J.C. Vartuli, W.J. Roth, M.E. Leonowicz, C.T. Kresge, K.D. Schmitt, C.T.W. Chu, D.H. Olson, E.W. Sheppard, S.B. McCullen, J.B. Higgins, and J.L. Schlenker, *Journal of the American Chemical Society*, 1992. **114**: p. 10834.
131. Viswanathan, B. and B. Jacob, *Catalysis Reviews*, 2005. **47**: p. 1.
132. Kim, T.W., F. Kleitz, B. Paul, and R. Ryoo, *Journal of the American Chemical Society*, 2005. **127**: p. 7601.
133. Kleitz, F., S.H. Choi, and R. Ryoo, *Chemical Communications*, 2003: p. 2136.
134. Gucci, L., A. Beck, and Z. Paszti, *Catalysis Today*, 2012. **181**: p. 26.
135. Flodstrom, K., H. Wennerstrom, and V. Alfredsson, *Langmuir*, 2004. **20**: p. 680.
136. Flodstrom, K., C.V. Teixeira, H. Amenitsch, V. Alfredsson, and M. Linden, *Langmuir*, 2004. **20**: p. 4885.
137. Attard, G.S., J.C. Glyde, and C.G. Goltner, *Nature*, 1995. **378**: p. 366.
138. Wanka, G., H. Hoffmann, and W. Ulbricht, *Macromolecules*, 1994. **27**: p. 4145.
139. Dacquin, J.P., J. Dhainaut, D. Duprez, S. Royer, A.F. Lee, and K. Wilson, *Journal of the American Chemical Society*, 2009. **131**: p. 12896.
140. Yuan, X., S. Xu, J. Lu, X. Yan, L. Hu, and Q. Xue, *Microporous and Mesoporous Materials*, 2011. **138**: p. 40.
141. Niesz, K., P. Yang, and G.A. Somorjai, *Chemical Communications*, 2005: p. 1986.
142. Ruthstein, S., J. Schmidt, E. Kesselman, R. Popovitz-Biro, L. Omer, V. Frydman, Y. Talmon, and D. Goldfarb, *Chemistry of Materials*, 2008. **20**: p. 2779.
143. Johansson, E.M., J.M. Cordoba, and M. Oden, *Microporous and Mesoporous Materials*, 2010. **133**: p. 66.
144. Kruk, M., M. Jaroniec, C.H. Ko, and R. Ryoo, *Chemistry of Materials*, 2000. **12**: p. 1961.
145. Kim, T.W., R. Ryoo, M. Kruk, K.P. Gierszal, M. Jaroniec, S. Kamiya, and O. Terasaki, *Journal of Physical Chemistry B*, 2004. **108**: p. 11480.
146. Yang, C.M., H.A. Lin, B. Zibrowius, B. Spliethoff, F. Schüth, S.C. Liou, M.W. Chu, and C.H. Chen, *Chemistry of Materials*, 2007. **19**: p. 3205.
147. Yang, C.M., B. Zibrowius, W. Schmidt, and F. Schüth, *Chemistry of Materials*, 2003. **15**: p. 3739.

148. Silvestre-Albero, A., E.O. Jardim, E. Bruijn, V. Meynen, P. Cool, A. Sepulveda-Escribano, J. Silvestre-Albero, and F. Rodriguez-Reinoso, *Langmuir*, 2009. **25**: p. 939.
149. Sonwane, C.G. and P.J. Ludovice, *Journal of Molecular Catalysis a-Chemical*, 2005. **238**: p. 135.
150. Galarneau, A., H. Cambon, F. Di Renzo, and F. Fajula, *Langmuir*, 2001. **17**: p. 8328.
151. Galarneau, A., H. Cambon, F. Di Renzo, R. Ryoo, M. Choi, and F. Fajula, *New Journal of Chemistry*, 2002. **27**: p. 73.
152. Che, S., K. Lund, T. Tatsumi, S. Iijima, S.H. Joo, R. Ryoo, and O. Terasaki, *Angewandte Chemie International Edition*, 2003. **42**: p. 2182.
153. Vaudry, F., S. Khodabandeh, and M.E. Davis, *Chemistry of Materials*, 1996. **8**: p. 1451.
154. Yuan, Q., A.X. Yin, C. Luo, L.D. Sun, Y.W. Zhang, W.T. Duan, H.C. Liu, and C.H. Yan, *Journal of the American Chemical Society*, 2008. **130**: p. 3465.
155. Zhao, X.S., a. Gq Lu, and G.J. Millar, *Industrial & Engineering Chemistry Research*, 1996. **35**: p. 2075.
156. Wu, Z.Y., H.J. Wang, T.T. Zhuang, L.B. Sun, Y.M. Wang, and J.H. Zhu, *Advanced Functional Materials*, 2008. **18**: p. 82.
157. Ribeiro Carrott, M.M.L., F.L. Conceicao, J.M. Lopes, P.J.M. Carrott, C. Bernardes, J. Rocha, and F. Ramoa Ribeiro, *Microporous and Mesoporous Materials*, 2006. **92**: p. 270.
158. Landau, M.V., E. Dafa, M.L. Kaliya, T. Sen, and M. Herskowitz, *Microporous and Mesoporous Materials*, 2001. **49**: p. 65.
159. Venezia, A.M., R. Murania, V. La Parola, B. Pawelec, and J.L.G. Fierro, *Applied Catalysis a-General*, 2010. **383**: p. 211.
160. Kanda, Y., T. Aizawa, T. Kobayashi, Y. Uemichi, S. Namba, and M. Sugioka, *Applied Catalysis B: Environmental*, 2007. **77**: p. 117.
161. Baca, M., E. de la Rochefoucauld, E. Ambroise, J.M. Krafft, R. Hajjar, P.P. Man, X. Carrier, and J. Blanchard, *Microporous and Mesoporous Materials*, 2008. **110**: p. 232.
162. Iengo, P., M. Di Serio, A. Sorrentino, V. Solinas, and E. Santacesaria, *Applied Catalysis A: General*, 1998. **167**: p. 85.
163. Bhangé, P., D.S. Bhangé, S. Pradhan, and V. Ramaswamy, *Applied Catalysis A: General*, 2011. **400**: p. 176.

# *Chapter 2*

## *Experimental*

## 2.1 Catalyst Preparation

### 2.1.1 SBA-15 synthesis

Pure silica SBA-15 was synthesised using the method of Zhao and co-workers.<sup>[1]</sup> The structure directing agent, Pluronic P123 (10 g) was dissolved in water (75.5 cm<sup>3</sup>) and hydrochloric acid (2 M, 291.5 cm<sup>3</sup>) with stirring at 35 °C. Tetramethoxysilane (15.5 cm<sup>3</sup>) was added and left for 20 h with agitation. The resulting gel was hydrothermally treated under sealed conditions for 24 h at 80 °C without agitation. The solid was filtered, washed with water (1000 cm<sup>3</sup>) and dried at room temp before calcination at 500 °C for 6 h in air (ramp rate 1 °C min<sup>-1</sup>). This yielded approximately 7.0 g of white solid.

### 2.1.2 SBA-16 synthesis

The synthesis of silica SBA-16 was carried out using the protocol of Zhao and co-workers, under parallel conditions to SBA-15 with three exceptions; a different structural directing agent, a reduced synthesis temperature and an increased hydrothermal treatment length. Pluronic F127 surfactant (10 g) was dissolved in water (75.5 cm<sup>3</sup>) and hydrochloric acid (2 M, 291.5 cm<sup>3</sup>) with stirring at 25 °C. Tetramethoxysilane (15.5 cm<sup>3</sup>) was added and left for 20 h with agitation. The resulting gel was aged under sealed conditions for 48 h at 80 °C without agitation. The solid was filtered, washed with water (1000 cm<sup>3</sup>) and dried at room temperature before calcination at 500 °C for 6 h in air (ramp rate 1 °C min<sup>-1</sup>). The yield was approximately 7.0 g.

### 2.1.3 KIT-6 synthesis

Silica KIT-6 was produced using the procedure reported by Kim and co-workers.<sup>[2]</sup> Pluronic P123 (10 g) was dissolved in water (361.6 cm<sup>3</sup>), Butan-1-ol (12.3 cm<sup>3</sup>) and hydrochloric acid (35 %, 16.7 cm<sup>3</sup>) with stirring at 35 °C. Tetramethoxysilane (15.6 cm<sup>3</sup>) was added and left for 20 h with agitation. The resulting gel was aged under sealed conditions for 24 h at 80 °C without agitation. The solid was filtered, washed with water (1000 cm<sup>3</sup>) and dried at room temperature before calcination at 500 °C for 6 h in air (ramp rate 1 °C min<sup>-1</sup>). This produced approximately 7.0 g of white solid.

### 2.1.4 Macro-mesoporous SBA-15 synthesis

Macro-mesoporous SBA-15 silica (MM-SBA-15) was synthesised via a modified route which included a hard macropore template of polystyrene spheres. The work regarding this support and corresponding catalysts series was carried out Miss Pooja Keshwalla, under the supervision of the author.

Polystyrene sphere were synthesised using the emulsion polymerisation method of Vandreuil and co-workers.<sup>[3]</sup> Potassium persulfate (0.16 g) was dissolved in distilled water (12 cm<sup>3</sup>) at 70 °C. In a separate 500 cm<sup>3</sup> three-necked round bottomed flask distilled water (377 cm<sup>3</sup>) was purged under N<sub>2</sub> (10 cm<sup>3</sup> min<sup>-1</sup>) at 70 °C. Styrene (50 cm<sup>3</sup>) and divinylbenzene (9.5 cm<sup>3</sup>) were each washed three times with sodium hydroxide solution (0.1 M, 1:1 vol/vol) followed by three washings with distilled water (1:1 vol/vol) to remove the polymerisation inhibitors. The washed organic phases were added to the purged water phase followed by the potassium persulfate solution. The mixture was left to stir under N<sub>2</sub> (10 cm<sup>3</sup> min<sup>-1</sup>) for 15 h, filtered and washed three times with distilled water (100 cm<sup>3</sup>) and then three times with ethanol (100 cm<sup>3</sup>). The final bead yield was in the region of 45 g.

The silica support was produced using the methodology published by Dhainaut and co-workers.<sup>[4]</sup> Pluronic P123 (10 g) was dissolved in water (75 cm<sup>3</sup>) and hydrochloric acid (2 M, 290 cm<sup>3</sup>) with stirring at 35 °C. Polystyrene beads (45 g) were added to the solution and left to stir for 1 h. Tetramethoxysilane (15.0 cm<sup>3</sup>) was then added and left for 20 h with agitation. The resulting gel was aged under sealed conditions for 24 h at 80 °C under static conditions. The solid was filtered, washed with water (1000 cm<sup>3</sup>) and dried at room temp before calcination at 550 °C for 6 h in air (ramp rate 0.5 °C min<sup>-1</sup>). This yielded approximately 7.0 g of white solid.

### 2.1.5 TLCT-SBA-15 synthesis

True liquid crystal templated mesoporous silica SBA-15 (TLCT-SBA-15) was synthesised using an adapted protocol of Attard et al,<sup>[5]</sup> by Dr Stephen G. Wainwright, working under the supervision of Professor Duncan W. Bruce at the University of York. Pluronic P123 (0.5 g) was mixed with hydrochloric acid acidified water (pH 2, 0.5 g) and sonicated at 40 °C to produce a homogeneous gel. The sol-gel was predicted to,<sup>[6]</sup> and subsequently did <sup>[7]</sup> exhibit a hexagonal mesophase. Tetramethoxysilane (1.02 cm<sup>3</sup> 1:4 mole ratio to H<sub>2</sub>O) was then added

and mixed to form a homogeneous liquid. The evolved methanol was removed under a light vacuum (0.12 bar) at 40 °C to form a viscous gel. The gel was exposed to the atmosphere at room temperature for 24 h to complete condensation before calcination at 500 °C for 6 h in air (ramp rate 3 °C min<sup>-1</sup>). This yielded approximately 0.5 g of solid material.

### 2.1.6 Mesoporous alumina

Mesoporous alumina was prepared using the procedure of Yuan and colleagues,<sup>[8]</sup> using Pluronic P123 as the mesopore template. Pluronic P123 (3 g) was dissolved in anhydrous ethanol (60 cm<sup>3</sup>) under vigorous agitation. Concentrated nitric acid (65 wt%, 4.5 cm<sup>3</sup>) and aluminium isopropoxide (6.2 g) were added and the solution was covered and stirred until dissolved. After 5 h evaporation induced self-assembly was triggered by the slow removal of the solvent at 60 °C under static conditions. After 96 h the resulting yellow solid was ground to a powder and calcined at 600 °C for 3 h (ramp rate 0.4 °C min<sup>-1</sup>) under flowing O<sub>2</sub> (50 cm<sup>3</sup> min<sup>-1</sup>). In the order of 3 g of solid material was produced from this protocol.

### 2.1.7 SBA-15 with an alumina grafted surface (Al-SBA-15)

A mesoporous silica core alumina surface SBA-15 (Al-SBA-15) was assembled using the method of Landau and co-workers,<sup>[9]</sup> with the exception that SBA-15 was used instead of MCM-41. SBA-15 was produced using the procedure outlined above, with an increased hydrothermal treatment of 100 °C being the only difference. Consecutive grafting cycles were carried out using an identical protocol each time with adjustments to the quantities to maintain the initial ratios. Aluminium-tri-*sec*-butoxide (14.5 g) was dissolved in anhydrous toluene (100 cm<sup>3</sup>) at 85 °C with stirring. Triethylamine (2.1 cm<sup>3</sup>) was added to the solution followed by dried SBA-15 (1 g). After 6 h stirring at 85 °C the solution was filtered under vacuum (~0.1 bar) to recover the solid, which was washed three times in toluene (100 cm<sup>3</sup>). The alumina surface was hydrolysed in ethanol (318 cm<sup>3</sup>) containing water (1.6 cm<sup>3</sup>) for 24 h at 25 °C. The solid product was recovered by filtration under vacuum (~0.1 bar) and washed with ethanol (300 cm<sup>3</sup>) before drying under vacuum (0.25 bar) at 50 °C on a rotary evaporator. The solid was further dried at 120 °C in air before a three step calcination sequence. The material was initially heated to 250 °C for 1 h, then 400 °C for 1h and finally 500 °C for 4h (constant ramp rate 1 °C min<sup>-1</sup>).

### **2.1.8 Palladium incipient wetness impregnation (all supports)**

All supports were impregnated using the incipient wetness methodology.<sup>[10]</sup> Solely mesoporous silicas; SBA-15, TLCT-SBA-15, SBA-16 and KIT-6 supports (1.5 g) were wetted with aqueous tetraammine palladium(II) nitrate solution (12 cm<sup>3</sup> with Pd precursor concentrations adjusted to achieve nominal metal loadings of 0.05-5 wt% for SBA-15, TLCT-SBA-15 and KIT-6 and 0.05-2.5 wt% for SBA-16). Resulting slurries were stirred for 18 h at room temperature before heating to 50 °C. After ~5 h, agitation ceased and the solids were left at 50 °C for 24 h to dry to a powder. The powders were calcined at 500 °C for 2 h in air (ramp rate 1 °C min<sup>-1</sup>) prior to reduction at 400 °C for 2 h (ramp rate 10 °C min<sup>-1</sup>) under flowing H<sub>2</sub> (10 cm<sup>3</sup> min<sup>-1</sup>). MM-SBA-15 (1.0 g) was likewise wetted with aqueous tetraammine palladium(II) nitrate solution (10 cm<sup>3</sup> with varying Pd precursor levels to span 0.05-2.5 wt% nominal loadings). The slurries were treated as for the mesoporous supports (dried, calcined and reduced). A fumed commercial silica (1.5 g Sigma, 220 m<sup>2</sup>g<sup>-1</sup>) was similarly impregnated with aqueous tetraammine palladium(II) nitrate solution (8 cm<sup>3</sup> with differing Pd concentrations to span 0.05-3 wt% nominal loadings). The resulting slurries were processed as for the other silica materials (dried, calcined and reduced). Mesoporous Alumina (1.5 g) and Al-SBA-15 (0.3 g) were saturated with aqueous tetraammine palladium(II) nitrate solution (1.5 cm<sup>3</sup> with Pd precursor concentrations adjusted so that nominal Pd loadings spanned 0.05-5 wt% for mesoporous alumina and to obtain a 1 wt% desired loading for Al-SBA-15 support). Again the resulting slurries were treated as before (dried, calcined and reduced).

## **2.2 Support & Catalyst Characterisation**

### **2.2.1 Elemental analysis**

Bulk Pd loadings for the SBA-15, SBA-16, KIT-6, MM-SBA-15, and TLCT-SBA-15 series and the single Al-SBA-15 catalyst were determined by MEDAC Analytical and Chemical Consultancy Service LTD. Samples were digested in hydrofluoric acid prior analysis on a Varian Vista MPX ICP-OES. The commercial silica series was analysed by XRF spectroscopy on a Horiba XGT-7000 x-ray analytical microscope fitted with a rhodium x-ray tube operating at 50 kV, with a nickel filter and spot size of 1.2 mm and a silicon detector.

Bombardment of a sample with sufficiently high energy x-rays facilitates ejection of a core electron. The rendered ‘hole’ in the lower energy shell decreases atomic stability, which is overcome by the relegation of a high energy shell electron to the hole.<sup>[11]</sup> To allow this demotion, energy loss, emitted as an energetically characteristic secondary x-ray photon, is compulsory. The secondary x-ray is described by the electron shell transition, i.e. a  $L \rightarrow K$  is  $K\alpha$  whereas a  $M \rightarrow K$  is a  $K\beta$ . In essence, fluorescence is the phenomenon of radiation adsorption followed by emission at a different energy, the basic principle is shown in **Figure 2.1**.

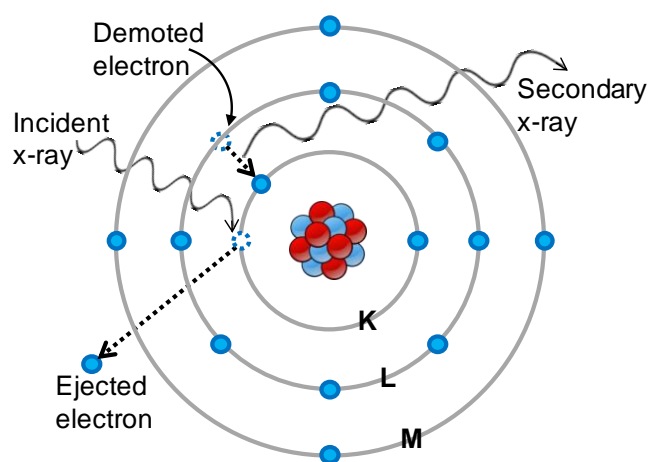


**Figure 2.1** – Illustrative representation of x-ray fluorescence

Actual Pd loadings for the mesoporous alumina series and levels of Pd leaching from hot filtration tests were verified by flame AAS. Analysis was carried out on a Varian SpectrAA 55B AAS with an air acetylene flame, fitted with a Pd hollow cathode lamp emitting light at 244.8 nm; relaxation after excitation of the Pd (cathode) generates this distinctive photon. The optimum Pd concentration range under these conditions is 0.1 – 15 ppm. An aerosol of the analyte solution, generated by its passage through a nebuliser, is sprayed into the flame. Atomised Pd absorbs the characteristic wavelength light due to excitation of the Pd atoms, with the level of absorption relative to Pd concentration.<sup>[11]</sup>

Varying amounts of the Pd doped mesoporous alumina series were digested in concentrated nitric acid (65 wt% 5-0.5 cm<sup>3</sup>) and diluted with distilled water (100-10 cm<sup>3</sup>) to give nominal Pd concentrations of 5 ppm. To minimise interference from Pd ionisation, lanthanum chloride 5000 ppm (0.5-0.05 g), an ionisation reagent, was

added. A calibration curve, Pd concentration range of 0.1-10 ppm with an  $R^2$  greater than 0.99, was produced from commercial Pd AAS solution (Aldrich 1.000 g/L Pd,  $\sim 2.3 \text{ cm}^3/\text{L HNO}_3$ ). Lanthanum chloride and nitric acid concentrations were adjusted to match the mesoporous alumina samples. Analysis was carried out in triplicate and averaged. The hot filtrate solutions were evaporated to dryness under a vacuum ( $\sim 0.1 \text{ bar}$ ) at  $60^\circ\text{C}$ , before digestion in concentrated nitric acid ( $65 \text{ wt}\% \text{ } 0.5 \text{ cm}^3$ ) and diluted with distilled water ( $9.5 \text{ cm}^3$ ) with lanthanum chloride ( $0.05 \text{ g}$ ) added. Leaching of  $\sim 0.5 \%$  ( $0.1 \text{ Pd ppm}$ ) of total Pd was the detection limit.

### 2.2.2 Powder X-Ray diffraction

XRD patterns were recorded on either a Panalytical X'pertPro diffractometer fitted with an X'celerator detector, or a Bruker D8 Advance diffractometer fitted with a LynxEye high-speed strip detector, both using  $\text{Cu K}_\alpha$  ( $1.54\text{\AA}$ ) sources with a nickel filter, calibrated against either Si (Panalytical) or  $\text{SiO}_2$  (Bruker) standards. Low angle patterns were recorded over a range of  $2\theta = 0.3\text{-}8^\circ$  (step size  $0.01^\circ$ , scan speed  $0.014^\circ \text{ s}^{-1}$ ) and wide angle patterns over a range of  $2\theta = 25\text{-}75^\circ$  (step size  $0.02^\circ$ , scan speed  $0.020^\circ \text{ s}^{-1}$ ).

$\text{Cu K}_\alpha$  ( $1.54\text{\AA}$ ,  $8.04 \text{ keV}$ ) x-ray photons, generated via the demotion of a high energy shell electron to a lower vacancy (in a copper anode), are fired at a homogeneous powder sample, their sufficiently energy allowing bulk characterisation. Sample homogeneity guarantees that for a powder sample, which organise randomly, a degree will be in the correct orientation to allow constructive interference,<sup>[12]</sup> from either crystal planes or ordered pore walls. This arises from elastic scattering of the photons which if in-phase, as shown in **Figure 2.2**, results in constructive interference, i.e. they reinforce rather than cancel out. This gives rise to characteristic diffraction patterns unique to individual materials.<sup>[12, 13]</sup> Constructive interference, for set refraction angles, is observed only if the distance between scatterers is equal to an integer multiplied by the x-ray wavelength, Bragg's Law.

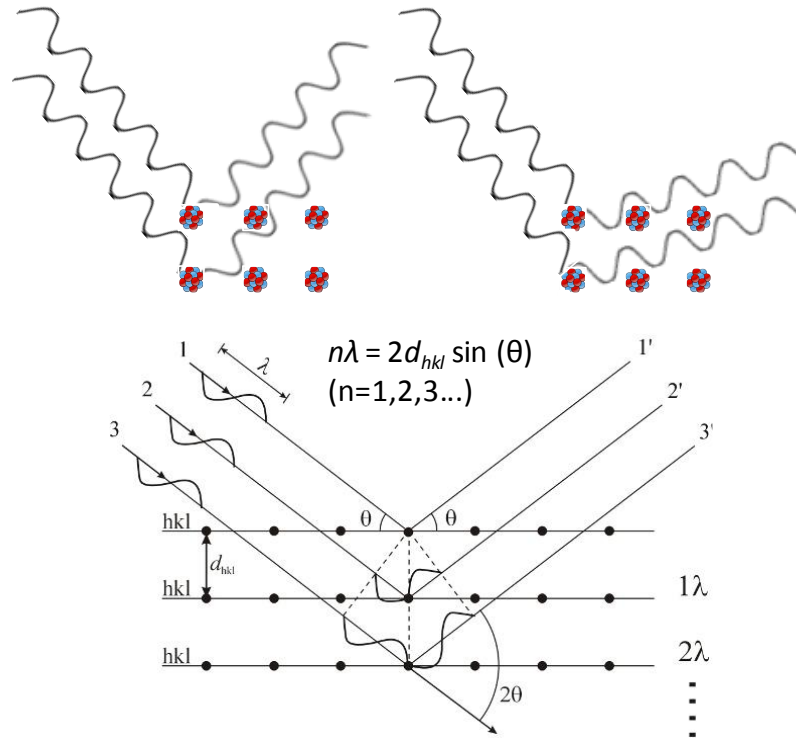


**Figure 2.2** – Simplified constructive (left) and deconstructive (right) interference (top) and its relation to lattice spacing (bottom)<sup>[14]</sup>

Lattice and pore spacing were determined for cubic systems from the relationship between Bragg's law and Miller indices (**Equation 2.1**). For the hexagonal mesopore architectures, the use of the  $d(10)$  simplifies the equation, although this does not result in the pore spacing and multiplication by 1.15 ( $2/\sqrt{3}$ ) is required.

$$a = \frac{\lambda \sqrt{h^2 + k^2 + l^2}}{2 \sin \theta} \quad \text{Equation 2.1}$$

$a$  = lattice parameter;  $\lambda$  = Wavelength of Cu  $K_\alpha$  radiation (0.1541nm);  $h, k, l$  = Miller indices;  $\theta$  = Diffraction angle

Selection rules exist which accounts for the absence of certain peaks.<sup>[13]</sup> Body centered cubic structures (SBA-16, Fe) do not exhibit  $d(100)$  and  $d(111)$  peaks, or any peak whose sum of its Miller indices is odd, due to the presence of pores, or atoms, at  $\frac{1}{2}$  Miller indices. This produces refractions that are  $180^\circ$  out of phase and thus cancel each other completely. In face centered cubic structures (Pd) peaks are only present if indices are either all odd or all even. Furthermore, diffraction peaks

only occur if long range order is present (crystalline materials or ordered porosity), with a minimum detectable crystallite size of ~2 nm.<sup>[15]</sup> Peak width increases with decreasing particle size,<sup>[13]</sup> due to incomplete cancelling of scattered x-rays close to the peak maxima. This arises because the refraction from the next lattice plane, when just off the maxima, is only slightly out of phase and cancels weakly. In large crystals the combination of multiple refractions overcome this, whereas the limited number of lattice planes in small crystals diminished this effect.<sup>[12]</sup> Beneficially this is utilised for particle size evaluation by the Scherrer Equation (**Equation 2.2**)<sup>[16]</sup>

$$PS_{av} = \frac{k\lambda}{\left(\sqrt{(B^2 - S^2)} \cos\theta\right)} \quad \text{Equation 2.2 – Scherrer equation}$$

$PS_{ave}$  = Particle size (Å); B = FWHM of diffraction peak; S = 0.15 (systematic broadening caused by diffractometer); k = 0.9 (constant)

### 2.2.3 Nitrogen porosimetry

N<sub>2</sub> porosimetry was undertaken on a Quantachrome Nova 1200 porosimeter using NovaWin v2.2 analysis software. Samples were degassed at 120 °C for 2 h prior to N<sub>2</sub> adsorption. Adsorption/desorption isotherms were recorded at -196 °C. BET surface areas were calculated over the relative pressure range 0.05-0.2 where a linear relationship was observed. Microporosity was assessed using the t-plot method, over the relative pressure of 0.2-0.5 which displayed a linear correlation. Mesopore diameters were calculated applying the BJH method to the desorption branch.

Adsorption, at constant temperature and pressure, results in a decrease in system entropy, thus enthalpy of adsorption must be negative (exothermic)<sup>[17]</sup> if they are to occur (Gibbs free energy).<sup>[18, 19]</sup> Gas surface collisions are either elastic, with no interaction, or inelastic, the latter being exothermic via energy transfer from the adsorbate to the adsorbent. If the energy loss is sufficient to forbid spontaneous desorption yet no further energy loss occurs, via chemical bond formation, adsorption is classed as physisorption. Due to the weak enthalpy of adsorption (low in magnitude), of N<sub>2</sub> physisorption, it only occurs at temperatures below the adsorbate boiling point.<sup>[18]</sup> This permits multilayer adsorption, as the enthalpy of vaporisation (condensation) from adsorbate adsorbate interactions is close in value to the enthalpy of adsorption, and non-selectivity to the sites of physisorption.<sup>[20]</sup>

Adsorbate attractions to both the surface, and each other in multilayer adsorption, arises due to Van der Waals forces (dipole to dipole attractions).<sup>[17, 18]</sup> N<sub>2</sub> adsorption, recorded at liquid N<sub>2</sub> temperature, result from London forces,<sup>[18]</sup> which occur from spontaneous variations in electron distribution (induced temporary dipoles). Isotherms are generated by the static volumetric technique,<sup>[20]</sup> N<sub>2</sub> is incrementally dosed and the amount adsorbed (under dynamic equilibrium with rate of adsorption = rate of desorption) at a given pressure and constant temperature recorded. The isotherm type, its shape, divulges information regarding the adsorbents. There are six classifications of isotherm, depicted in **Figure 2.3**.<sup>[21]</sup> type I represents microporous materials where a strong interactions between adsorbate and adsorbent occurs from their close proximity within micropores; type II is typical for either nonporous or macroporous materials; the unusual type III occurs when adsorbate interactions are greater than those with the surface; hysteresis observed in types IV and V is indicative of mesoporous supports; and type VI indicates consecutive adsorbate layer formation due to uniform surface.

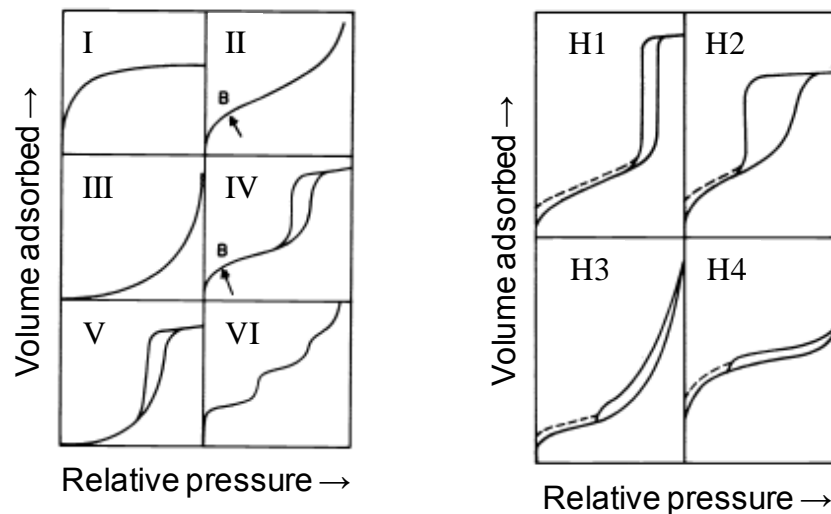


**Figure 2.3** – Common adsorption isotherms and hysteresis types<sup>[22]</sup>

Hysteresis, witness in isotherm types IV and V, presents as four types, as shown in **Figure 2.3**. It occurs due to differences in condensation (adsorption) and evaporation (desorption) within mesopores.<sup>[20]</sup> Adsorption occurs from the pore wall inwards. The close proximity between adsorbate and pore wall enhances the attractive interaction, with this accounting for the sharp increase in the volume of gas

adsorbed (capillary condensation) relative to non-mesoporous materials. The strength of this effect increases as pore diameters reduce. In contrast desorption occurs from the liquid surface, present at pore openings, with this interaction being stronger than that present during adsorption where hysteresis presents (mesoporous and macroporous materials).<sup>[20]</sup> This lowers the pressure that gas evaporation occurs relative to the condensation process. Hysteresis shape reveals further information; type H1 is witnessed for uniform pore sizes, whereas H2 represents non-uniformity ink bottle pore shapes. Slit shaped pores produce H3 and H4.<sup>[21]</sup>

Total surface areas were calculated by the BET equation (**Equation 2.3**).<sup>[23]</sup> It is a development of the Langmuir theory to accommodate multilayer formation via an additional parameter C. This accounts for differences between mono and multilayer interactions, with a low value indicating a stronger interaction between adsorbate species than adsorbate adsorbent and vice versa for high values.<sup>[21]</sup> Surface areas are determined from the monolayer volume assuming N<sub>2</sub> molecules close pack and each occupies 0.162 nm<sup>2</sup> (**Equation 2.4**).<sup>[18, 20, 21]</sup>

$$\frac{P}{V_a(P_0-P)} = \frac{1}{V_m C} + \frac{C-1}{V_m C} \left( \frac{P}{P_0} \right) \quad \text{Equation 2.3 – BET (linear)}$$

$$V_m = \frac{1}{(\text{Gradient} + \text{Intercept})}$$

$$C = \left( \frac{\text{Gradient}}{\text{Intercept}} \right) + 1$$

$$sa = \frac{V_m \sigma N_a}{mv} \quad \text{Equation 2.4}$$

P = pressure; P<sub>0</sub> = saturation pressure; V<sub>a</sub> = volume adsorbed; V<sub>m</sub> = monolayer volume; C = multilayer adsorption parameter; sa = surface area; σ = N<sub>2</sub> area (0.162 nm<sup>2</sup>); N<sub>a</sub> = Avogadro number; m = sample mass; v = gas molar volume

Microporosity was assessed using the t-plot method, this assumes for a known monolayer volume subsequent adsorbate layer volumes can be calculated.<sup>[20]</sup> Computer modelled expected multi-layer thickness, using parameters for a non-porous reference, is plotted against the actual volume adsorbed for corresponding pressures. Extrapolation to the y-axis, which dissects at zero if monolayer accessibility is unrestricted, allows micropore volume to be determined.

The BJH method allowed mesopore diameters to be deduced. This applies the Kelvin equation (**Equation 2.5**),<sup>[20]</sup> which predicts the pressure at which the adsorbate will spontaneously evaporate for a given pore diameter. Calculations at each pressure change allow pore size distribution to be determined.

$$\ln\left(\frac{P}{P_0}\right) = -\left(\frac{2\gamma v \cos\theta}{RT r_m}\right) \quad \text{Equation 2.5 – Kelvin equation}$$

$P/P_0$  = relative pressure of vapor in equilibrium with condensed gas meniscus;  $\gamma$  = liquid surface tension;  $v$  = condensed adsorbate molar volume;  $\cos\theta$  = adsorbate surface contact angle (0 for  $N_2$  thus  $\cos\theta = 1$ );  $R$  = gas constant;  $T$  = temperature;  $r_m$  = mean radius of condensed gas meniscus

## 2.2.4 Electron microscopy

SEM images were recorded on a Carl Zeiss Evo-40 SEM operating at 10 kV. Samples were mounted on aluminium stubs using adhesive carbon tape and gold sputter coated to reduce charging. High resolution TEM/STEM(HAADF) images were recorded on either a FEI Tecnai TF20 FEG TEM operating at 200 kV equipped with a Gatan Orius SC600A CCD camera or a JEOL JEM-3000F FEGTEM operating at 200 kV fitted with a 1k Gatan 794 MultiScan (MSC) camera and two annular dark field detectors with analysis carried out at the University of Leeds and University of Oxford. Samples were prepared by dispersion in methanol and drop-casting onto a copper grid coated with a holey carbon support film (Agar Scientific Ltd). Images were analysed using ImageJ 1.41.

The wavelength of electrons (~12.3 pm at 10 kV decreasing to 2.5 pm at 200 kV) is significantly shorter than both visible and x-ray radiation, enhancing microscope resolution to an atomic level under high resolution TEM/STEM conditions.<sup>[24]</sup> An electron beam is focused, through a series of electromagnetic lens, onto the sample with interaction occurring in multiple ways. SEM images are formed by detection of secondary electrons that result from the displacement of a k orbital (1s) electron.<sup>[24]</sup> The low energy, ~50 eV, of the secondary electrons provokes the surface sensitivity of the technique as their escape from the bulk is impeded. Scanning coils within the SEM configuration facilitate the electron beam to raster over a sample. Image contrast is generated from the 3-D morphology of the sample; surfaces at right angles to the beam are brightest with increasingly darker regions observed as surfaces tilt

towards being parallel to the beam. This property combined with the technique's surface nature produces a 3-D image. For TEM, the electron beam that is transmitted through the sample, with and without interaction, is of interest as this generates the image.<sup>[24]</sup> All images are 2-D representation of the sample. Variations in thickness, atomic mass and density all contribute to the degree of interaction (diffraction) between beam and sample. STEM can be envisaged as a combination of the two, allowing a converged electron beam to raster across the sample, generating HAADF images, commonly referred to as Z contrast. Images are produced from high angle scattering of the beam by the atoms nucleus, with the higher the atomic mass of the element the stronger it diffracts and thus appears brighter.<sup>[25]</sup> High resolution of heavier elements, even very small clusters on lower molecular weight substrates is possible, although, where specimen thickness is great, high angle scattering from low atomic mass species escalates due to multiple scattering processes.<sup>[25]</sup>

### **2.2.5 Carbon monoxide chemisorption**

Pd dispersions were assessed by CO chemisorption using a Quantachrome ChemBET 3000. Samples were outgassed at 150 °C under flowing He (20 cm<sup>3</sup> min<sup>-1</sup>) for 1 h, then reduced at 100 °C under flowing H<sub>2</sub> (20 cm<sup>3</sup> min<sup>-1</sup>) for 1 h before analysis at room temperature. The mild protocol was to eliminate artefacts associated with sintering. CO (0.05 cm<sup>3</sup>) was injected into a flowing helium stream (80 cm<sup>3</sup> min<sup>-1</sup>) which passed over the sample. CO that did not adsorb was detected in real time. Consecutive injections were carried out until three equivalent detector responses were measured, with CO volume calculated retrospectively.

Chemisorption processes exhibit significantly higher enthalpies of adsorptions relative to physisorption, although this is site specific.<sup>[17]</sup> As a result, the requirement of analysis at temperatures below adsorbate boiling point is eliminated. This limits adsorption to a monolayer and induces adsorption site selectivity. The former is due to the enthalpy of vaporisation being significant lower than the enthalpy of adsorption, whereas the latter is a result of difference in enthalpies of adsorption at different sites, chemical or physical. The high enthalpies of adsorption arise from a chemical bond formation, via an additional energy loss from the adsorbate to the adsorbent.<sup>[18]</sup> The bond, formed by charge redistribution, is either covalent or ionic in character,<sup>[17]</sup> and results in lowering the surface energy of the

metal.<sup>[13]</sup> The stronger bonding increases thermal stability of the adsorbate (either un-dissociated or dissociated), which increase residence time.<sup>[18]</sup>

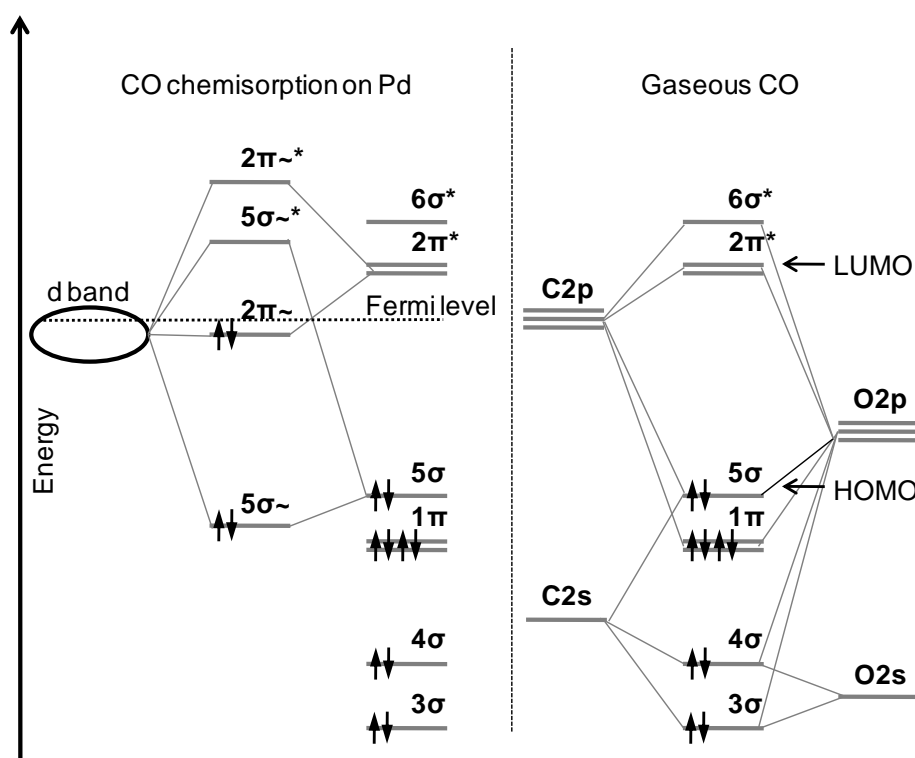


**Figure 2.4** – Molecular orbital diagrams for CO on Pd and free gaseous CO

One way for visualising CO bonding on a Pd surface is to consider the Pd (100) face.<sup>[13, 18]</sup> A dative bond (both electrons from the same atom) forms from the non-bonding orbital (associated with carbon) with the empty perpendicular  $d_{z^2}$  orbital. This is accompanied by a second interaction between the filled  $d_{zx}$  and  $d_{yz}$  orbitals and the CO  $\pi$  orbitals. This strengthens the Pd carbon bond whilst weakening the carbon oxygen bond. The weakening effect on the carbon oxygen escalates with the Pd atoms the CO associates with. The CO Pd interaction, and its resulting effects, can be further clarified using molecular orbital theory between the metal surface d-band and adsorbed CO, illustrated in **Figure 2.4**.<sup>[13, 17]</sup> The Pd d-band, a result of the large number of orbitals from an array of atoms with similar energy, interacts with the highest occupied and lowest unoccupied molecular orbitals of CO, the  $5\sigma$  non-bonding orbital (associated with carbon) and the  $2\pi^*$  anti-bonding orbital. The interaction generates two bonding adsorption orbitals,  $5\sigma\sim$  and  $2\pi\sim$ , and corresponding anti-bonding adsorption orbitals,  $5\sigma\sim^*$  and  $2\pi\sim^*$ . The  $5\sigma\sim$  orbital

lying below the Fermi level (valence band of Pd) is filled and the corresponding anti bonding orbital lying above the Fermi level is empty. This indicates the filled  $5\sigma$  non-bonding molecular orbital of CO is emptied into  $5\sigma^*$  adsorption orbital during chemisorption. This occurs via a process called sigma donation and results in forming the adsorption sigma bond. The  $2\pi^*$  adsorbate orbital, also lying below the Fermi level, is filled with the charge transferred to the  $2\pi^*$  anti-bonding molecular orbital of CO, in a process called pi back donation. Overall this forms a strong Pd carbon bond whilst simultaneously weakening the carbon oxygen bond of CO.<sup>[17]</sup> The Fermi level dictates the chemisorption bond strength with a higher Fermi level, e.g. Au or Ag, decreasing it via partial filling of the anti-bond adsorbate orbitals.<sup>[13]</sup>

CO Pd chemisorption bonds are covalent in nature and occurring vertical to the Pd surface at terminal, bridging and three-fold sites without dissociation.<sup>[13, 26]</sup> The multiplicity of sites results in the Pd CO stoichiometry requiring consideration. A stoichiometry of 2:1 was used throughout, as at saturation (standard temperature and pressure) bridging sites dominate.<sup>[17, 27, 28]</sup> Also, a maximum  $\frac{1}{2}$  monolayer coverage is reported for Pd(100) at 25 °C,<sup>[15, 17, 18, 29]</sup> due to lowering enthalpies of adsorption from repulsive interactions between adsorbed species. Pd dispersions and average particle sizes were calculated using **Equation 2.6**,<sup>[17]</sup> and **Equation 2.7**.<sup>[15]</sup>

$$D_m = \left( \frac{\text{mol}_{\text{COads}} S_{av}}{\text{mol}_{\text{Pd}}} \right) \times 100 \quad \text{Equation 2.6 – metal dispersion}$$

$D_m$  = Metal dispersion;  $\text{mol}_{\text{COAds}}$  = moles CO adsorbed;  $S_{av}$  = average stoichiometry;  $\text{mol}_{\text{Pd}}$  = total number of moles of Pd

$$PS_{ave} = \frac{5 C_m f_m}{2.7e^{12} S_{av} d_m V_g} \quad \text{Equation 2.7 – average particle size}$$

$PS_{ave}$  = particle size (nm);  $C_m$  = metal surface density (atoms  $\text{cm}^{-1}$ );  $f_m$  = metal loading ( $\text{g}_{\text{met}}/\text{g}_{\text{cat}}$ );  $S_{av}$  = stoichiometry;  $d_m$  = metal density ( $\text{g}_{\text{met}} / \text{cm}^3$ );  $V_g$  = chemisorbed gas volume ( $\text{cm}^3 / \text{g}_{\text{cat}}$ )

## 2.2.6 Diffuse reflection infrared fourier transform spectroscopy - in-situ carbon monoxide chemisorption

In-situ CO adsorption, monitored by DRIFTS, allowed Pd facets and bonding sites to be investigated. This was performed on a Nicolet Avatar 370 MCT with Smart Collector accessory, ever-glo mid/near infrared source and mercury cadmium

telluride (MCT-A) photon detector at  $-196\text{ }^{\circ}\text{C}$ . A temperature programmable, gold-coated in-situ cell, interfaced to electronic mass flow controllers via a gas manifold permitted the following treatment. Samples were dried at  $150\text{ }^{\circ}\text{C}$  under flowing  $\text{N}_2$  ( $20\text{ cm}^3\text{ min}^{-1}$ ), prior to reduction at  $100\text{ }^{\circ}\text{C}$  under flowing  $\text{H}_2$  ( $20\text{ cm}^3\text{ min}^{-1}$ ) for 1 h. CO adsorption was conducted under flowing CO ( $10\text{ cm}^3\text{ min}^{-1}$ ) at  $100\text{ }^{\circ}\text{C}$  until the gas phase peaks indicated the cell was saturated. The cell was subsequently purged with  $\text{N}_2$  for  $\sim 20\text{-}30$  min prior to collection of chemisorbed CO spectra. Spectra were measured from  $4000$  to  $400\text{ cm}^{-1}$  wavenumbers with a resolution of 4.

Diffuse reflectance orientation focuses infrared radiation onto the sample. Photons are partially reflected by the sample, the remaining being transmitted through it, in a multitude of directions. Reflected signal originates from the surface and bulk, the latter by reflection of photons that transmits through the surface. Random orientation in powder sample induces multiple scattering angles so a parabolic mirror is used to focus the reflected beam maximising detection.<sup>[13]</sup>

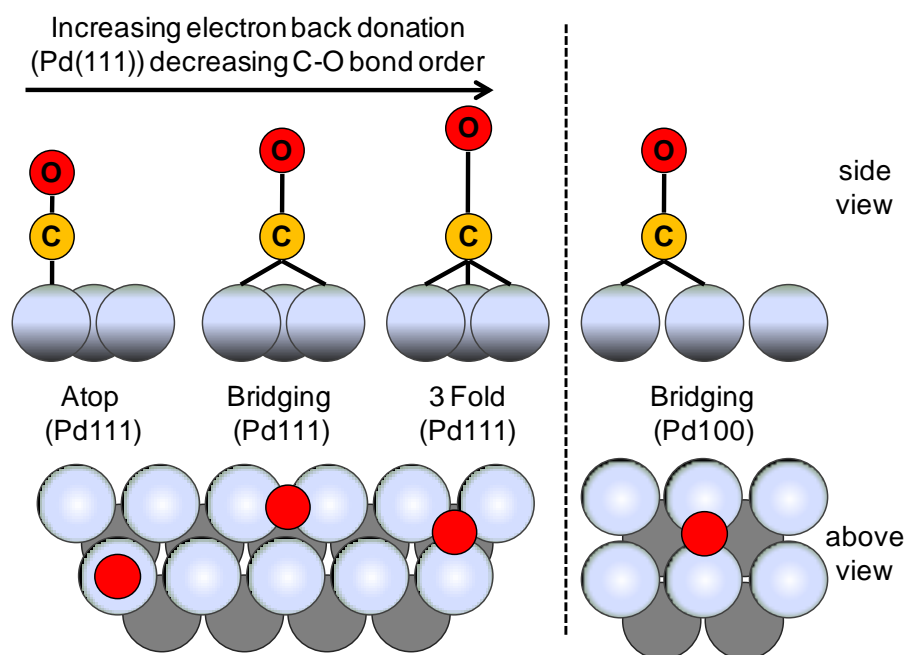


**Figure 2.5** – CO adsorption atop, bridging and three fold Pd(111) (left) and bridging Pd(100) (right) (only O of CO shown for clarity)

Molecular vibrations, either stretching or bending, are excited by the adsorption of photons of an appropriate energy, causing the dipole moment of the molecule to pulse. CO adsorption on Pd, on varying facets and by differing bonding type, is

evaluated from shifts in the carbon oxygen bond stretching frequency. Increasing electron back donation shifts adsorption to lower wavenumbers (less energetic due to reducing bond order),<sup>[18]</sup> and allows atop, bridging and three fold sites to be differentiated, depicted in **Figure 2.5**, whilst simultaneously discriminating different surface facets due to varying surface Pd coordination number.<sup>[26, 28, 30]</sup> Increasing coverage, from below  $\frac{1}{3}$  to  $\frac{1}{2}$  monolayer, shifts stretching frequencies to higher wavenumber from decreased back donation to individual molecules,<sup>[18]</sup> with preferential adsorption switching from three-fold to bridging.

### 2.2.7 X-ray photoelectron spectroscopy

XPS was performed on a Kratos Axis HSi X-ray photoelectron spectrometer fitted with a charge neutraliser and magnetic focusing lens employing Al  $K_{\alpha}$  monochromated radiation (1486.6 eV). Spectral fitting was performed in CasaXPS version 2.3.14. Binding energies were charge corrected to the Si 2p at 103.4 eV and cross checked to adventitious C 1s at 284.6 eV. Pd 3d XP spectra were fitted using a common asymmetric peak shape determined from a PdO standard. Errors were estimated by varying a Shirley background across reasonable limits.

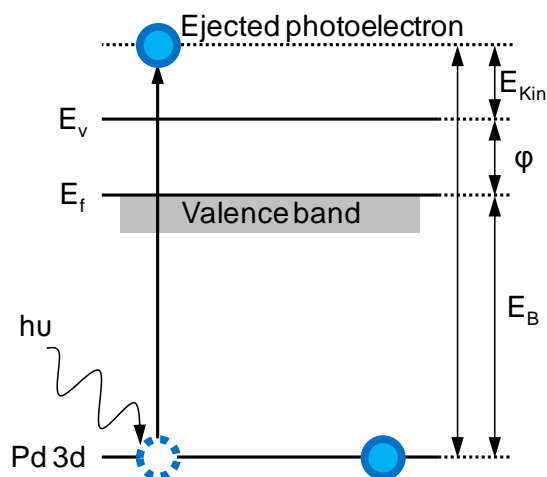


**Figure 2.6** – Schematic depiction of photoionisation ( $E_{kin}$  = Photoelectron kinetic energy;  $h\nu$  = photon energy (Planck’s constant multiplied by frequency);  $E_b$  = electron binding energy;  $\phi$  = work function;  $E_f$  = Fermi level;  $E_v$  = vacuum level)

XPS gives information on elemental composition, oxidation state and local elemental environment of the sample. X-rays routinely employed are Mg  $K_{\alpha}$

(1253.6 eV) and Al K $\alpha$  (1486.6 eV) which due to their low energy, relative to XAS, are classed as soft x-rays.<sup>[31]</sup> This eliminates the necessity for synchrotron radiation, under general conditions, increasing accessibility of the technique. XPS is intrinsically surface sensitive, due to the short distance that an electron can escape from (1-3 nm), its escape depth, rather than the x-ray energy, which can travel far into a material. The low escape depth is due to interactions between the ejected photoelectron and electrons of other atoms imparting short electron mean free path values over the electron energy range of 0-1000 eV.<sup>[32]</sup> Following adsorption of the x-ray photon, is the ejection of a core electron if adequate energy is supplied,<sup>[17, 31]</sup> this is schematically represented in **Figure 2.6**.<sup>[13, 32]</sup>

The ejected photoelectron possesses a discrete kinetic energy, which is characteristic of the element and its environment. Quantification of this, and the intensity of photoelectrons at said energy, produces an XPS spectrum. Typically spectra are plotted as a function of the binding energy which is deduced from the following relationship (**Equation 2.8**).

$$E_{kin} = h\nu - E_b - \varphi_{sp} \quad \text{Equation 2.8}$$

$E_{kin}$  = Photoelectron kinetic energy;  $h\nu$  = photon energy;  $E_b$  = electron binding energy;  $\varphi_{sp}$  = spectrometer work function

Work function relates to the energy required to eject an electron at the Fermi level into the vacuum, i.e. it relates to ionisation potential.<sup>[13]</sup> For conducting samples, an electrical connection between the sample and spectrometer aligns their Fermi levels, but their work function still vary with the difference related to the spectrometer work function. For insulating samples, e.g. silica, charge referencing is required.<sup>[13]</sup> This is achieved by systematically shifting binding energies, by a common value, so that a known peak is aligned at its correct value. This accounts for uniform shifts in binding energies, to higher values, due to an increasing positive charge at the analyte surface. Charge neutralisers can help to compensate for this.

Oxidation state and sample composition, the local elemental environment, influence subtle shifts in photoelectron binding energy of an element.<sup>[13, 32]</sup> Binding energy of Pd(II) is ~1.5 eV<sup>[33]</sup> higher than Pd(0), a direct consequence of the greater attractive force of the nucleus felt by 44 electrons over 46. Substituting Br with Cl in

PdBr<sub>2</sub> increases Pd binding energy by ~0.7 eV,<sup>[33]</sup> Cl being more electronegative. Generally the outermost filled electron shell is probed as it experiences the greatest effect of these changes and thus gives the greatest resolution. Electron ejected from orbitals which boast angular momentum ( $l > 0$ , i.e. p, d and f orbitals) are affected by spin coupling between orbital angular momentum ( $l$ ) and electron spin ( $m_s$ ) magnetic fields, with the sum of the two giving total angular momentum ( $j$ ). This interaction is either favourable or not, as  $m_s$  is either anti-clockwise (+1/2) or clockwise (-1/2) and thus two values for  $j$  exist. A product of spin coupling is peak doublets (spin orbital splitting),<sup>[13]</sup> with predetermined ratios equal to  $2j + 1$ . For d orbitals the intensity ratio is 3:2, as  $l = 2$  and thus  $j = 5/2$  and  $3/2$ . Favourable coupling increases binding energy and occurs when forces oppose,  $j = 3/2$ . A lack orbital angular momentum in s orbitals prohibits this effect. Asymmetric peak broadening towards higher binding energies is witnessed for d shell electrons,<sup>[13]</sup> an upshot of energy donation from an escaping photoelectron to another bound electron. This lowers the measured kinetic energy value of the escaping photoelectron and thus artificially inflates its reported binding energy. Receiving electrons are either promoted to an unoccupied state, known as shake up, or escapes from the atom, referred to as shake off. The loss of kinetic energy also rationalises the inherent stepped background of an XPS spectra, as photoelectrons generated further from the surface lose a greater degree of energy, via multiple interactions.

### **2.2.8 X-ray adsorption spectroscopy – X-ray adsorption near edge structure and extended x-ray adsorption fine structure**

XAS measurements were performed at BM23 of the European Synchrotron Radiation Facility (ESRF, Grenoble France), using a Si(111) double crystal fixed exit monochromator, with fluorescence spectra collected on a 13-element Ge detector. Pd (24350 eV) K-edge spectra were acquired of the powder catalyst samples mounted in a stainless steel washer. XANES and EXAFS spectra were normalised, background subtracted, and fitted, using the Athena and Artemis components of the IFEFFIT software suite respectively. PdO and Pd foil were recorded as standards.

In a similar manner to XPS, XAS also involves the generation of photoelectrons but instead of evaluating these directly the technique assess their influence on the adsorption of subsequent x-ray photons. Simply, the technique is an x-ray photon in

x-ray photon out measurement, which eliminates the need for ultra-high vacuum systems. Therefore permitting characterisation of materials under atmospheric conditions and more attractively the option of in-situ/operando investigations.<sup>[34]</sup>

Adsorption of an x-ray photons bearing sufficient energy (greater than the binding energy of the electron) ejects an electron as a photoelectron.<sup>[32]</sup> Electrons from a shell close to the nucleus are generally targeted, which results in increasingly energetically demanding transformations. For Pd the K-edge (1s electrons) is commonly studied with adsorption occurring at 24350 eV. After photoelectron discharged, the atom is excited by virtue of the unfilled electron orbital and affects subsequent x-ray photon adsorption. This excited state can be partially stabilised by fluorescence, 'electron hole' shifting or alternatively through adsorption of scattered photoelectrons, including backscattering of the original. The scattering of photoelectron by their neighbouring atoms induces a multitude of effects, both constructive or deconstructive in regards to subsequent photon adsorption.<sup>[13]</sup> Spectra attained comprise bulk information regarding both electronic and local geometric information, even where sample periodicity is absent.<sup>[31]</sup>

Typically photon energies are tuned from ~300 eV below to ~1000 eV above the adsorption edge, this being the minimum energy at which x-ray photon adsorption occurs (photoelectron generation). The first 100 eV or so after the adsorption edge, the XANES region, divulges oxidation state information,<sup>[13, 32]</sup> due to photoelectrons and valence electron interactions. A result of the relatively low photoelectron kinetic energy which arises due to the close proximity between incident x-rays and electron binding energy. The EXAFS region pursues and continues for ~1000 eV or as far as oscillations are observable. Photoelectrons here possess higher kinetic energy, on the grounds of the increasing incident x-ray energy, which allow them to propagate further. Single and multiple scattering of the photoelectrons by the surrounding atoms result and allow local geometry to be scrutinised.

## **2.3 Selox reactions**

### **2.3.1 Alcohol selective oxidation (standard conditions)**

All catalyst screening was performed using a Radleys Starfish carousel batch reactor on a 10 cm<sup>3</sup> scale at 90 °C under atmospheric air pressure. Catalyst (50 mg

unless stated otherwise) was added to a reaction mixture of 8.4 mmol crotyl (0.603 g) or cinnamyl (1.123 g) alcohol, mesitylene (0.1 cm<sup>3</sup>) and toluene (10 cm<sup>3</sup>) at 90 °C under stirring at sufficient rates so that external reagent diffusion was eliminated. Blank reactions, using bare supports and in their absence, were conducted in parallel. Reactions were sampled (0.25 cm<sup>3</sup>) at regular intervals (0, 10, 20, 30 and 40 min and 1, 3, 6, 22 and 24 h) and diluted (~1.75 cm<sup>3</sup>) with dichloromethane (crotyl alcohol) or toluene (cinnamyl alcohol) for the acquisition of activity and selectivity profiles. Samples were analysed, in triplicate, with values averaged, on either a Varian 3900GC with CP-8400 autosampler fitted with a CP-Sil5 CB column (15 m x 0.25 mm x 0.25 µm). Reactions were run for 24 h with initial rates calculated over the initial linear region (initial 0.5-1 h). Selectivity and overall mass balances were evaluated from GC calibrations for reactants and products with reported conversion and selectivity values subject to ±3 % error.

### **2.3.2 Mass transfer limitations**

The role of stirring rate was studied for each silica support series.<sup>[35, 36]</sup> Standard reaction protocol was followed with stirring rates varied (150-1200 RPM). Sampling frequency doubled and reaction length decreased to 0.5 h. Varying the catalyst alcohol ratio and O<sub>2</sub> flow rates verified external mass diffusion limitations were overcome. Common reaction conditions were used with the following exceptions; varying catalyst mass (50-100 mg 0.89 wt% Pd/SBA-15 and 12.5-50 mg 0.44 wt% Pd MesoAl<sub>2</sub>O<sub>3</sub> and 0.77 wt% Pd Al-SBA-15) and O<sub>2</sub> flow rates (0-5 cm<sup>3</sup> min<sup>-1</sup>). Sampling frequency doubled and reaction length decreased to 0.5 h.

### **2.3.3 Heterogeneity of the active site - hot filtration test**

The hot filtration test was utilised to confirm the heterogeneity of the active species.<sup>[37]</sup> The standard protocol was followed for the initial 30 min. At this time point the catalyst was removed by filtration of the hot solution under vacuum (~0.1 bar). The filtrate was returned to standard reaction conditions and sampled as for the standard protocol.

### 2.3.4 Role of oxygen on cinnamyl alcohol selox

A high and low metal loading (2.22 and 0.05 wt%) on KIT-6 and all alumina supported catalysts were investigated under standard conditions with the exception that O<sub>2</sub> (5 cm<sup>3</sup> min<sup>-1</sup>) flowed through the reaction solution.

### 2.3.5 Role of in-situ reduction pre-treatment

The catalyst (50 mg, 0.46 wt% Pd KIT-6) was reduced under flowing H<sub>2</sub> (10 cm<sup>3</sup> min<sup>-1</sup>) in toluene (5 cm<sup>3</sup>) at 90 °C for 1 h. The reaction was then purged with N<sub>2</sub> (10 cm<sup>3</sup> min<sup>-1</sup>) for 30 min prior to initiating the reaction by the addition of 8.4 mmol cinnamyl alcohol (1.123 g), mesitylene (0.1 cm<sup>3</sup>) and toluene (5 cm<sup>3</sup>), N<sub>2</sub> flow ceased from this point. A parallel reaction was performed flowing O<sub>2</sub> (5 cm<sup>3</sup> min<sup>-1</sup>) through the reaction solution immediately after the reaction started. Control reactions were performed using N<sub>2</sub> instead of H<sub>2</sub> during the reduction pre-treatment.

### 2.3.6 Recycle testing

Catalyst recyclability was assessed for 3 consecutive reactions. The catalyst was reactivated by calcination at 500 °C for 2 h in air (ramp rate 1 °C min<sup>-1</sup>) prior to reduction at 400 °C for 2 h (ramp rate 10 °C min<sup>-1</sup>) under flowing H<sub>2</sub> (10 cm<sup>3</sup> min<sup>-1</sup>) after each reaction. The standard protocol including catalyst substrate ratio was maintained by scaling the initial reaction so that the catalyst (100 mg 0.42 wt% Pd SBA-16) was added to reaction mixtures containing 16.8 mmol of cinnamyl alcohol (2.246 g), mesitylene (0.2 cm<sup>3</sup>) and toluene (20 cm<sup>3</sup>) at 90 °C. The first recycle was carried out with catalyst (70 mg), 11.7 mmol of cinnamyl alcohol (1.572 g), mesitylene (0.14 cm<sup>3</sup>) and toluene (14 cm<sup>3</sup>). The second recycle test used catalyst (35 mg), 5.9 mmol of cinnamyl alcohol (0.786 g), mesitylene (0.07 cm<sup>3</sup>) and toluene (7 cm<sup>3</sup>).

### 2.3.7 Reduced catalyst mass for cinnamyl alcohol selox

All alumina supported catalysts (5 mg Pd loading 4.11-1.75 wt%, 10 mg Pd loading 0.77-0.44 wt% and 20 mg Pd loadings 0.07-0.05 wt%) were screened as described for standard reaction conditions except for the reduced catalyst mass used.

### 2.3.8 Effect of reaction temperature on cinnamyl alcohol selox

A mesoporous alumina supported catalyst (50 mg 0.74 wt% Pd mesoAl<sub>2</sub>O<sub>3</sub>) and the Al-SBA-15 supported catalyst (50 mg 0.77 wt % Pd Al-SBA-15) were screened for selective oxidation of cinnamyl alcohol (1.123 g) with mesitylene (0.1 cm<sup>3</sup>) and toluene (10 cm<sup>3</sup>) under flowing O<sub>2</sub> (5 cm<sup>3</sup> min<sup>-1</sup>) at temperatures of 75 and 55 °C.

## 2.4 References

1. Zhao, D.Y., Q.S. Huo, J.L. Feng, B.F. Chmelka, and G.D. Stucky, *Journal of the American Chemical Society*, 1998. **120**: p. 6024.
2. Kim, T.W., F. Kleitz, B. Paul, and R. Ryoo, *Journal of the American Chemical Society*, 2005. **127**: p. 7601.
3. Vaudreuil, S., M. Bousmina, S. Kaliaguine, and L. Bonneviot, *Advanced Materials*, 2001. **13**: p. 1310.
4. Dhainaut, J., J.P. Dacquin, A.F. Lee, and K. Wilson, *Green Chemistry*, 2010. **12**: p. 296.
5. Attard, G.S., J.C. Glyde, and C.G. Goltner, *Nature*, 1995. **378**: p. 366.
6. Wanka, G., H. Hoffmann, and W. Ulbricht, *Macromolecules*, 1994. **27**: p. 4145.
7. Wainwright, S.G., *True Liquid Crystal Templating of Nanoparticle-doped Mesoporous Silica*, in *Chemistry*. 2011, University of York: York. p. 212.
8. Yuan, Q., A.X. Yin, C. Luo, L.D. Sun, Y.W. Zhang, W.T. Duan, H.C. Liu, and C.H. Yan, *Journal of the American Chemical Society*, 2008. **130**: p. 3465.
9. Landau, M.V., E. Dafa, M.L. Kaliya, T. Sen, and M. Herskowitz, *Microporous and Mesoporous Materials*, 2001. **49**: p. 65.
10. White, R.J., R. Luque, V.L. Budarin, J.H. Clark, and D.J. Macquarrie, *Chemical Society Reviews*, 2009. **38**: p. 481.
11. Hollas, M.J., *Modern spectroscopy*. 4th ed. 2003, Chichester: Wiley and Sons.
12. Hammond, C., *Basics of Crystallography and Diffraction*. 2nd ed. 2001, New York: Oxford University Press.
13. Niemantsverdriet, J.W., *Spectroscopy in Catalysis: An introduction*. 2nd ed. 2007, Darmstadt: Wiley-VCH.
14. Katholieke Universiteit Leuven Nuclear solid state group, 2010. **X-ray diffraction – Bruker D8 Discover**: p. [online] Available at: <<http://fys.kuleuven.be/iks/nvsf/experimental>>.
15. Pernicone, N., *Cattech*, 2003. **7**: p. 196.
16. Scherrer, P., *Göttinger Nachrichten*, 1918. **2**: p. 98.
17. Somorjai, G.A. and Y. Li, *Introduction to surface chemistry and catalysis*. 2nd ed. 2010, Hoboken: John Wiley & Sons Inc.
18. Gasser, R.P.H., *An introduction to chemisorption and catalysis by metals*. 1985, New York: Oxford University Press.
19. Atkins, P., *The Elements of Physical Chemistry*. 3rd ed. 2001, Oxford: Oxford University Press.
20. Webb, P.A. and C. Orr, *Analytical Methods in Fine Particle Technology*. *Journal of the Chemical Society-Faraday Transactions II*. 1997, Norcross: Micromeritics.

21. Rouquerol, F., J. Rouquerol, and K.S.W. Sing, *Adsorption by powders & porous solids: principles, methodology and applications*. 1999, Bodmin: Academic Press.
22. Everett, D.H., R.A.W. Haul, L. Moscou, R.A. Pierotti, J. Rouquerol, and T. Siemieniowska, *Pure Appl. Chem*, 1985. **57**: p. 603.
23. Brunauer, S., P.H. Emmett, and E. Teller, *Journal of the American Chemical Society*, 1938. **60**: p. 309.
24. Rochow, T.G. and P.A. Tucker, *Introduction to microscopy by means of light, electrons, X rays, or acoustics*. 2nd ed. 1994, New York: Springer.
25. Keyse, R.J., A.J. Garratt-Reed, P.J. Goodhew, and G.W. Lorimer, *Introduction to scanning transmission electron microscopy*. 1998, Guilford: Bios Scientific Publishers.
26. Cabilla, G.C., A.L. Bonivardi, and M.A. Baltanas, *Catalysis Letters*, 1998. **55**: p. 147.
27. Dropsch, H. and M. Baerns, *Applied Catalysis a-General*, 1997. **158**: p. 163.
28. Guerrero-Ruiz, A., S.W. Yang, Q. Xin, A. Maroto-Valiente, M. Benito-Gonzalez, and I. Rodriguez-Ramos, *Langmuir*, 2000. **16**: p. 8100.
29. Canton, P., F. Menegazzo, S. Polizzi, F. Pinna, N. Pernicone, P. Riello, and G. Fagherazzi, *Catalysis Letters*, 2003. **88**: p. 141.
30. Marx, S., F. Krumeich, and A. Baiker, *Journal of Physical Chemistry C*, 2011. **115**: p. 8195.
31. Richards, R., ed. *Surface and Nanomolecular Catalysis*. Surface and Nanomolecular Catalysis. 2006, CRC Press: Boca Ranton.
32. Chorkendorff, I. and J.W. Niemantsverdriet, *Concepts of modern catalysis and kinetics*. 2003, Mörlenbach: Wiley-VCH.
33. NIST X-Ray Photoelectron spectroscopy database, 2003. *NIST Standard Reference Database 20, Version 3.5.*: p. [online] Available at: < <http://srdata.nist.gov/xps/>> [Accessed January 2012].
34. Newton, M.A. and W. van Beek, *Chemical Society Reviews*, 2010. **39**: p. 4845.
35. Hájek, J. and D.Y. Murzin, *Industrial & Engineering Chemistry Research*, 2004. **43**: p. 2030.
36. Lee, A.F., J.J. Gee, and H.J. Theyers, *Green Chemistry*, 2000. **2**: p. 279.
37. Corma, A., D. Das, H. García, and A. Leyva, *Journal of Catalysis*, 2005. **229**: p. 322.

## *Chapter 3*

*The selective oxidation of  
allylic alcohols over  
palladium supported on  
mesoporous silicas – the  
role of mesopore  
architecture*

### 3.1 Introduction

**Chapter 1** highlighted the debate surrounding the nature of the active site responsible for Pd catalysed selective oxidation (selox) of allylic alcohols. The principal question concerns whether metallic<sup>1,2</sup> or electron-deficient<sup>3-9</sup> Pd species are responsible for controlling the rate-determining step.

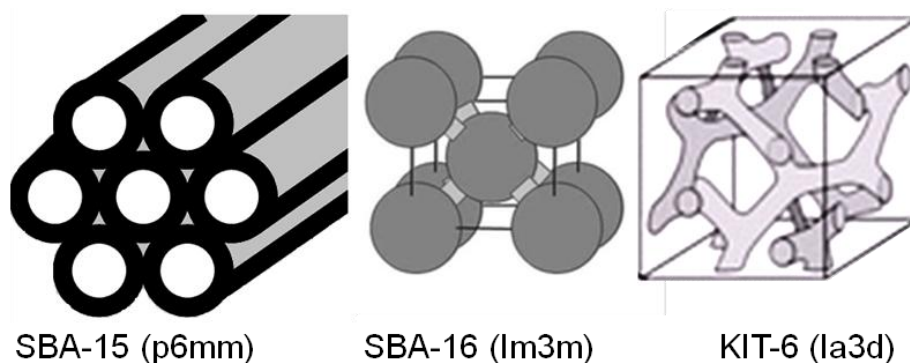


**Diagram 3.1** – Schematic of 2-dimensional SBA-15 and interconnected 3-dimensional SBA-16 and KIT-6 mesoporous silica architectures

This chapter exploits three distinct mesoporous silica supports possessing different pore architectures, graphically represented in **Diagram 3.1**. The aim is to explore their effects in allylic alcohol selox, including possible mass transfer effects and their role in stabilising catalytically active Pd species that catalyse the reactions of interest. To this end, 3D interconnecting versus 2D non-interconnecting mesoporous silicas have been compared. SBA-15 comprises hexagonally close-packed, parallel channels without connecting mesopores.<sup>10</sup> In contrast, SBA-16 and KIT-6 possess three-dimensionally interconnected mesopores: SBA-16 exhibits body centred cubic close-packed spherical pores, each connected to 8 nearest neighbours;<sup>10</sup> while KIT-6 is composed of two pore networks arranged in an ordered, interpenetrating, bicontinuous structure.<sup>11</sup> This study represents one of a handful of such systematically exploring the effect of mesopore interconnectivity on catalysis.<sup>12, 13</sup>

## 3.2 Results and discussion

### 3.2.1 Characterisation of parent silica supports

The three mesoporous silicas, SBA-15, SBA-16, and KIT-6, were prepared via the methods of Zhao <sup>10</sup> and Ryoo <sup>11</sup> respectively. The successful synthesis has been confirmed via a range of characterisation techniques. For comparison, a commercially silica (SiO<sub>2</sub>) support (Sigma Aldrich) has also been investigated.

#### 3.2.1.1 Powder X-Ray diffraction

Low angle powder XRD is employed to confirm the successful formation of the associated pore structures of SBA-15 (*p6mm*), SBA-16 (*Im3m*)<sup>10</sup> and KIT-6 (*Ia3d*)<sup>11</sup> via indexing of at least three peaks. **Figure 3.1** shows a stacked plot for the three mesoporous supports, with minor reflections positions reported. Reflections observed at the low angles used in these measurements are a consequence of the well-ordered mesopore structures, and not due to framework crystallinity.

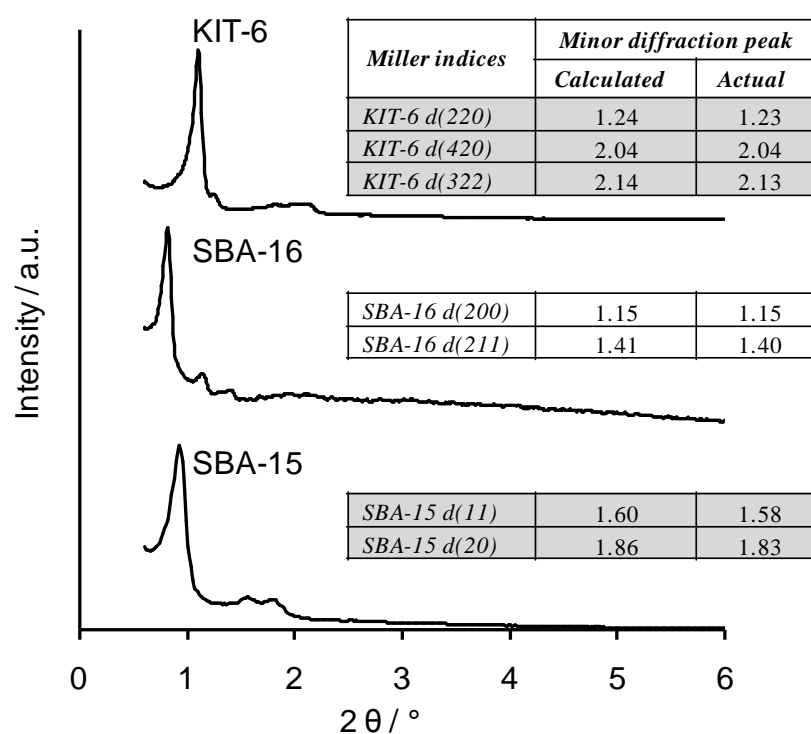


**Figure 3.1** - Stacked low angle XRD patterns of KIT-6, SBA-16 and SBA-15

The position of the most intense peak is used to calculate the associated cell parameter using Bragg's Law (**Chapter 2 Equation 2.1**); the resulting values are

presented in **Table 3.1**, and are in good agreement with literature for comparable synthesis conditions. The expected positions of weaker peaks for each space group are subsequently calculated from the strongest reflection, good agreement between this and the actual value confirms synthesis of the correct pore network (reported in **Figure 3.1**). For SBA-15, the strongest peak is indexed as the d(10) reflection, with the two smaller peaks assigned as the d(11) and d(20) peaks respectively, features of the hexagonally packed  $p6mm$  space group. For SBA-16, expected  $Im\bar{3}m$  space group, the main peak is indexed as the d(110) reflection, with the d(200) and d(211) reflections also visible. The  $Ia\bar{3}d$  space group of KIT-6 exhibits a major d(211) peak, a smaller shoulder from the d(220) reflection, and a broad feature from the d(420) and d(322) reflection. All are present in the parent KIT-6 sample. The commercial silica, used as a non-meso-structured reference support, exhibits no low angle reflections, indicative of either disordered mesoporosity or its absence.

**Table 3.1** - Textural properties of parent silica supports.

<i>Sample</i>	<i>Surface area / m<sup>2</sup> g<sup>-1(a)</sup></i>	<i>Micropore surface area / m<sup>2</sup> g<sup>-1(b)</sup></i>	<i>Mesopore Diameter / nm<sup>(c)</sup></i>	<i>Cell parameter / nm<sup>(d)</sup></i>
<i>SiO<sub>2</sub></i>	207 (± 21)	38 (± 4)	<i>n/a</i>	<i>n/a</i>
<i>SBA-15</i>	950 (± 95)	465 (± 47)	5.7	9.4 (± 0.2)
<i>SBA-16</i>	820 (± 82)	524 (± 52)	3.5	13.7 (± 0.2)
<i>KIT-6</i>	936 (± 94)	502 (± 50)	5.8	19.3 (± 0.2)

<sup>(a)</sup> N<sub>2</sub> BET, <sup>(b)</sup> N<sub>2</sub> t-plot, <sup>(c)</sup> BJH desorption branch of isotherm, <sup>(d)</sup> Low angle XRD

### 3.2.1.2 Nitrogen porosimetry

N<sub>2</sub> porosimetry allows further evaluation of support textural properties. The three mesoporous silicas, SBA-15, SBA-16 and KIT-6, display Type IV isotherms with hysteresis,<sup>14</sup> shown in **Figure 3.2**, characteristic of mesoporous materials. The sharp increase in N<sub>2</sub> adsorption over the relative pressure range of 0.4-0.8 is a consequence of capillary condensation within mesopores. Hysteresis is also common for mesoporous supports,<sup>14</sup> due to the differing condensation and evaporation processes during adsorption and desorption respectively. SBA-15 and KIT-6 exhibit type H1 hysteresis, signifying pore shapes with constant diameter throughout. SBA-16 differ however displays type H2 hysteresis, a consequence of its ink-bottle pore openings. In contrast, commercial silica exhibits a Type II isotherm with no observed capillary condensation, indicative of negligible mesoporosity in this reference material.

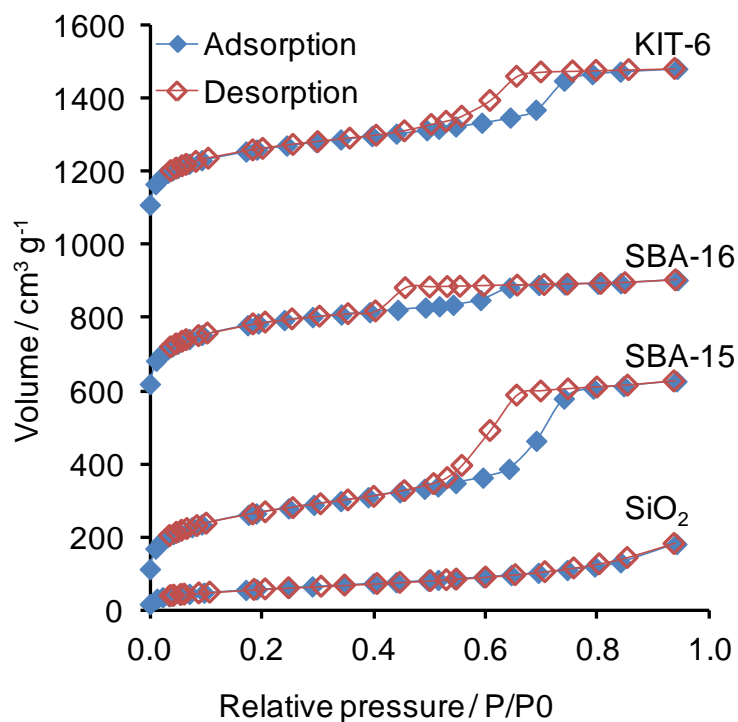


**Figure 3.2** – Stacked isotherm plot of KIT-6 (offset by  $1000 \text{ cm}^3 \text{ g}^{-1}$ ), SBA-16 (offset by  $500 \text{ cm}^3 \text{ g}^{-1}$ ), SBA-15 (offset by  $100 \text{ cm}^3 \text{ g}^{-1}$ ) and commercial silica

The surface areas and pore diameters, determined via the respective BET<sup>15</sup> and BJH<sup>16</sup> methods, are revealed in **Table 3.1** and are consistent with the literature for analogous samples analysed under comparable conditions. The BET surface area for all three mesoporous supports is significantly higher than the commercial silica due to their intrinsic ordered mesopore networks. The average pore sizes and the pore size distributions of SBA-15 and KIT-6 are similar, likely reflecting their common surfactant and hydrothermal synthesis conditions. In contrast, the mean BJH value of SBA-16 is significantly smaller than both, presumably a consequence of the different tri-block copolymer employed in its synthesis, resulting in the spherical pore structure and ink bottle pore openings. It is worth noting that concerns have been expressed regarding use of the BJH method for these types of structures, with reports indicating that it underestimates pore diameters by up to 2-3nm.<sup>17, 18</sup> In any event, the BJH pore size distributions of the three mesoporous supports, shown in **Figure 3.3**, indicate narrow pore size distributions.

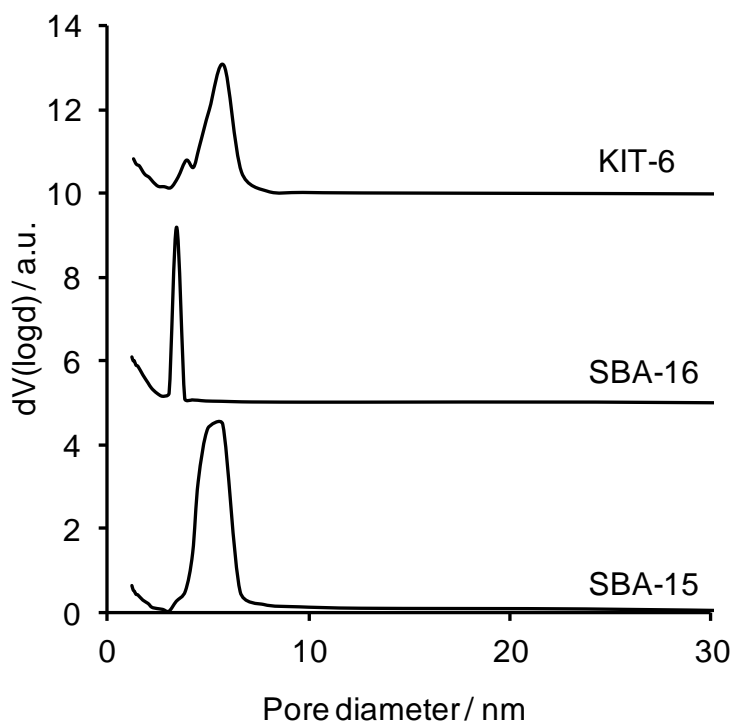


**Figure 3.3** – Stacked BJH pore size distributions for the mesoporous silica supports. (KIT-6 and SBA-16 offset by 10 and 5 respectively)

Microporosity, a feature that has been reported for SBA-15,<sup>19-22</sup> was also investigated using the t-plot method<sup>23</sup> with the resulting values reported in **Table 3.1**. This indicates that approximately 50-60 % of the surface areas of SBA-15, SBA-16 and KIT-6 occur within micropores. This value drops to only 19 % for the commercial silica, suggesting it is largely non-porous with a significant external surface area (recalling its Type II isotherm indicates the absence of mesoporosity). Low relative pressure N<sub>2</sub> porosimetry (pressure of initial data point ~0.6 Pa compared to ~100 Pa for standard porosimetry) was utilised to monitor the micropore filling process. The raw isotherm data was computationally fitted to isotherms of known standards, with fitting errors not exceeding 1 %, enabling the both micro and mesopore size distributions to be extracted. These results and the corresponding fitted plots are shown in **Figure 3.4**. To validate this method as a means to resolve microporosity within mesoporous silicas, MCM-41, which contains no micropores<sup>22</sup> was also analysed. For SBA-15, SBA-16 and KIT-6 it is evident that all contain a significant proportion of micro and small mesopores. The calculated micropore surface areas of 379, 492 and 533 m<sup>2</sup> g<sup>-1</sup> for SBA-15, SBA-16 and KIT-6

respectively, agree with the t-plot results. The commercial silica support also exhibits some micro and a small degree of mesoporosity. Again there is good agreement between the calculated micropore surface area of  $35 \text{ m}^2 \text{ g}^{-1}$  using this technique, and the t-plot measurement. In contrast, MCM-41 exhibits no microporosity by either method.

It is also possible to extract information regarding the pore diameters from **Figure 3.4**. The plot for SBA-15 clearly exhibits two peaks. The first, a broad peak centred at 1.2 nm, is attributed to micropores within the silica walls. A second sharp peak at 6.4 nm is a consequence of the mesopores, and is in good agreement with BJH predictions. For SBA-16, the fitted data reveals a tri-modal pore size distribution. The first peak at 1.4 nm can again be attributed to micropores as in SBA-15, and the second and third peaks at 2.4 nm and 5.9 nm both correspond to mesopores; the associated BJH mesopore diameter, of 3.4 nm, lies between these two values. Taking into the account the reported discrepancies observed from the BJH method discussed above, in conjunction with the reported average pore openings of 2.3 nm for SBA-16,<sup>17, 18, 24</sup> it seems reasonable to assign the 2.4 nm peak to the SBA-16 pore entrances and the 5.9 nm peak as the actual mesopore diameter. The KIT-6 plot exhibits a greater range of microporosity and small mesopores than SBA-15, with the main 6.6 nm peak attributed to mesopores in accordance with the BJH value. The commercial silica plot displays only a single broad peak at 2.3 nm, indicating both micro and mesoporosity, although the level of such porosity is significantly lower than the other three synthetic supports.

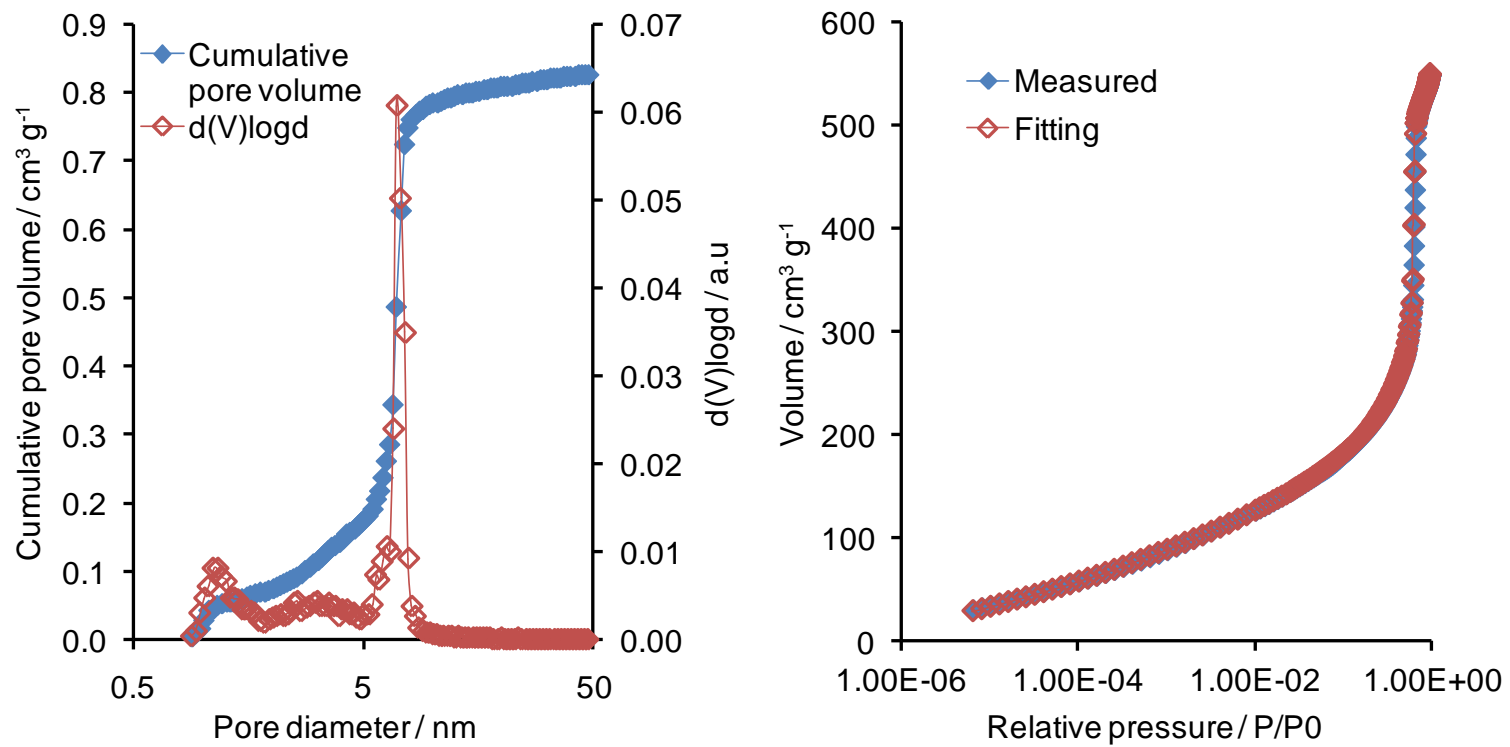


**Figure 3.4 (a)** – Pore size distribution and fitting plots for SBA-15 (fitting error 0.6 %)

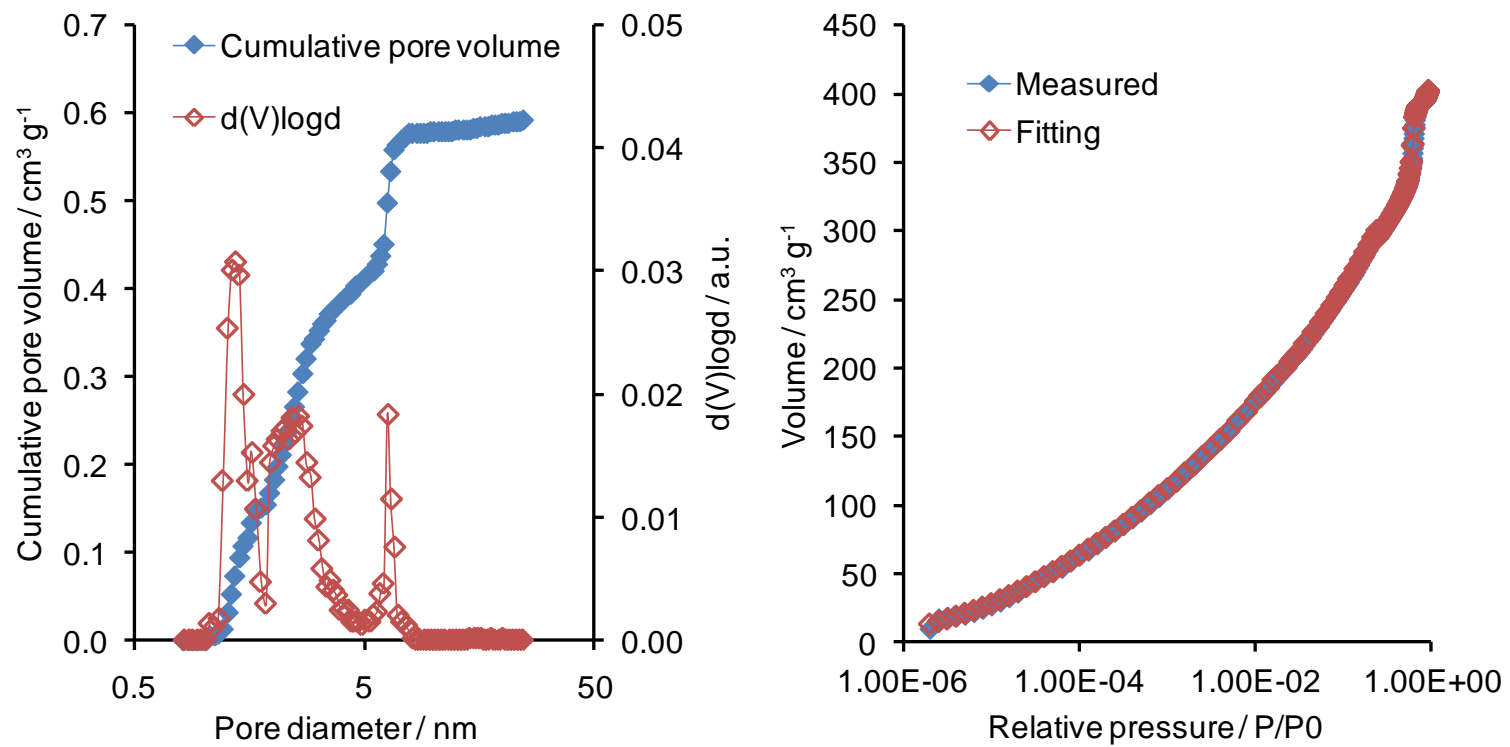


**Figure 3.4 (b)** – Pore size distribution and fitting plots for SBA-16 (fitting error 0.2 %)

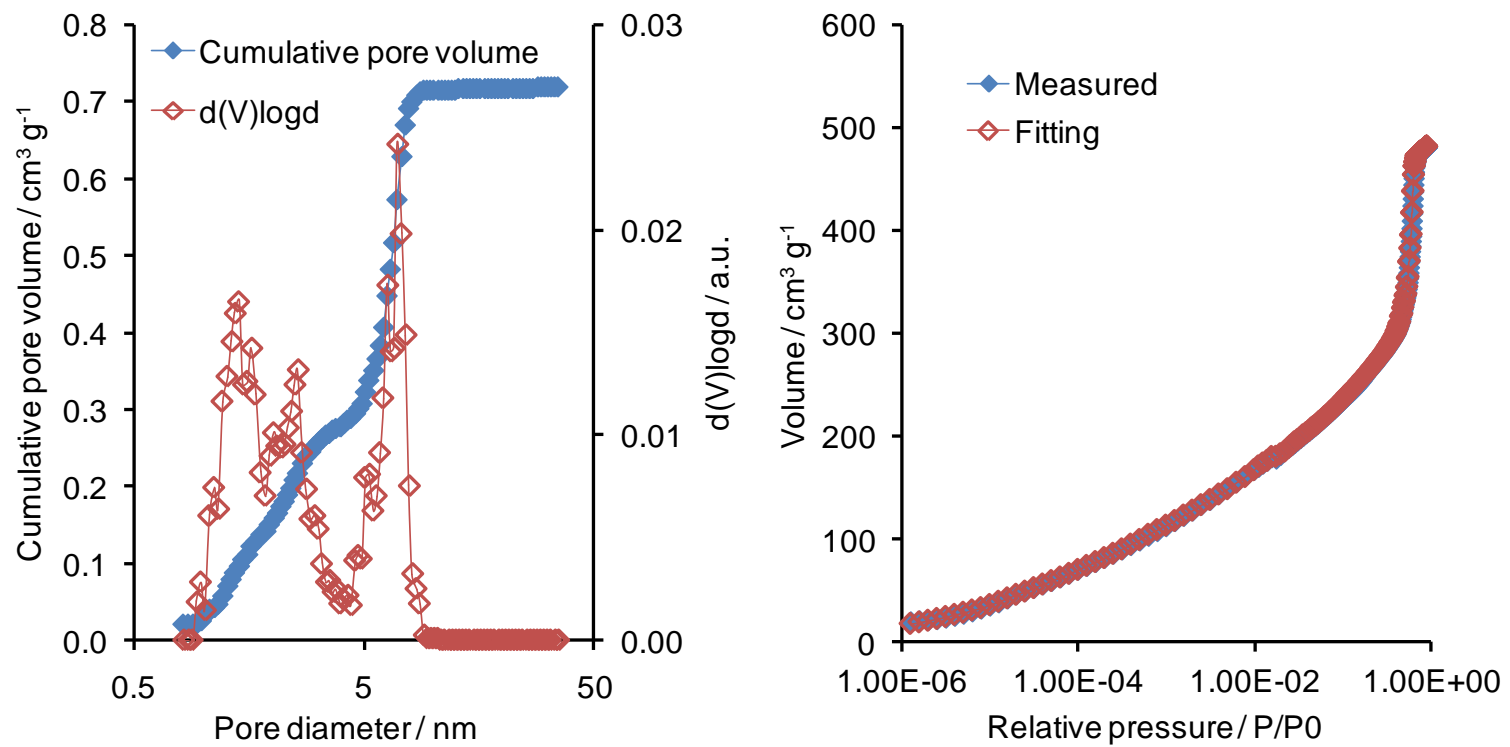


**Figure 3.4 (c)** – Pore size distribution and fitting plots for KIT-6 (fitting error 0.3 %)

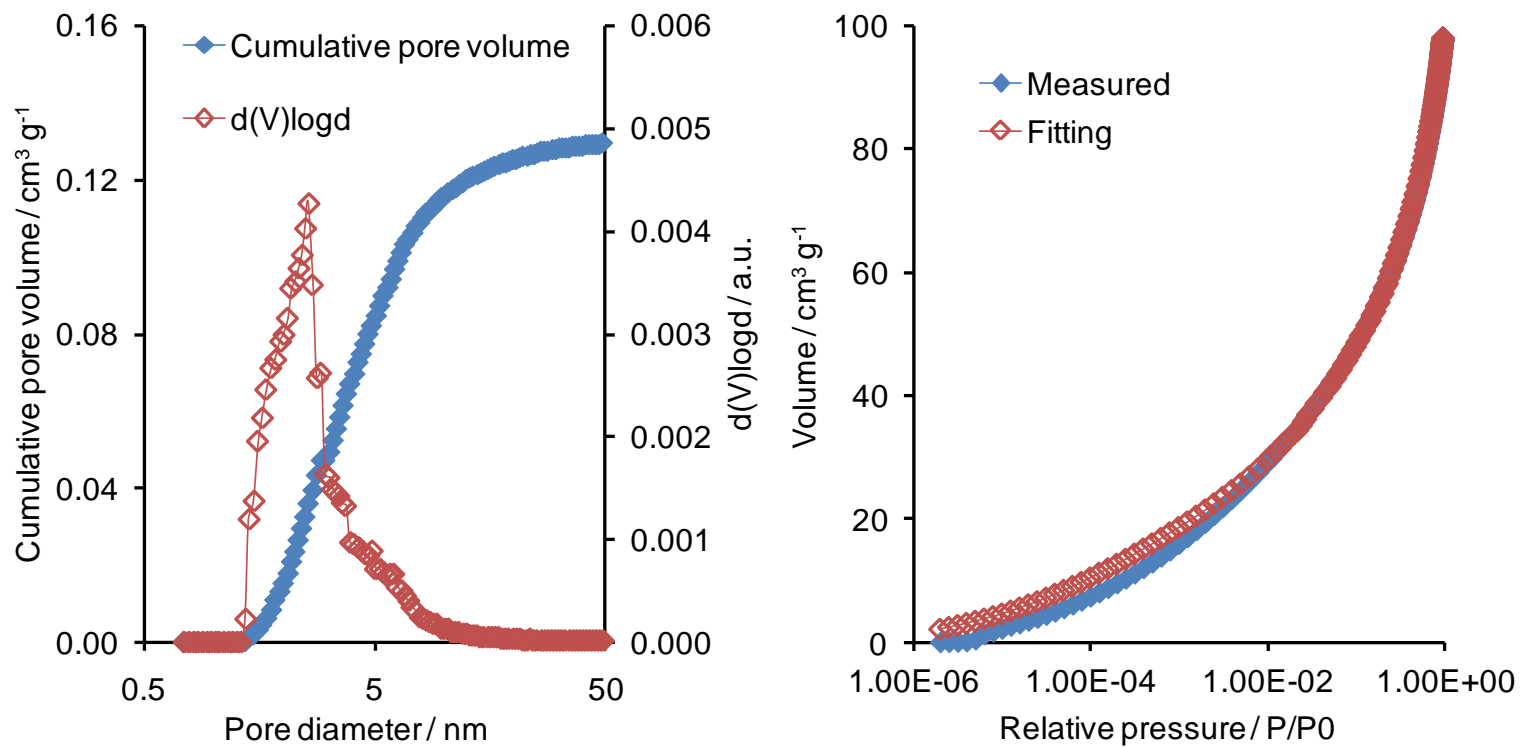


**Figure 3.4 (d)** – Pore size distribution and fitting plots for commercial silica (fitting error 1.0 %)

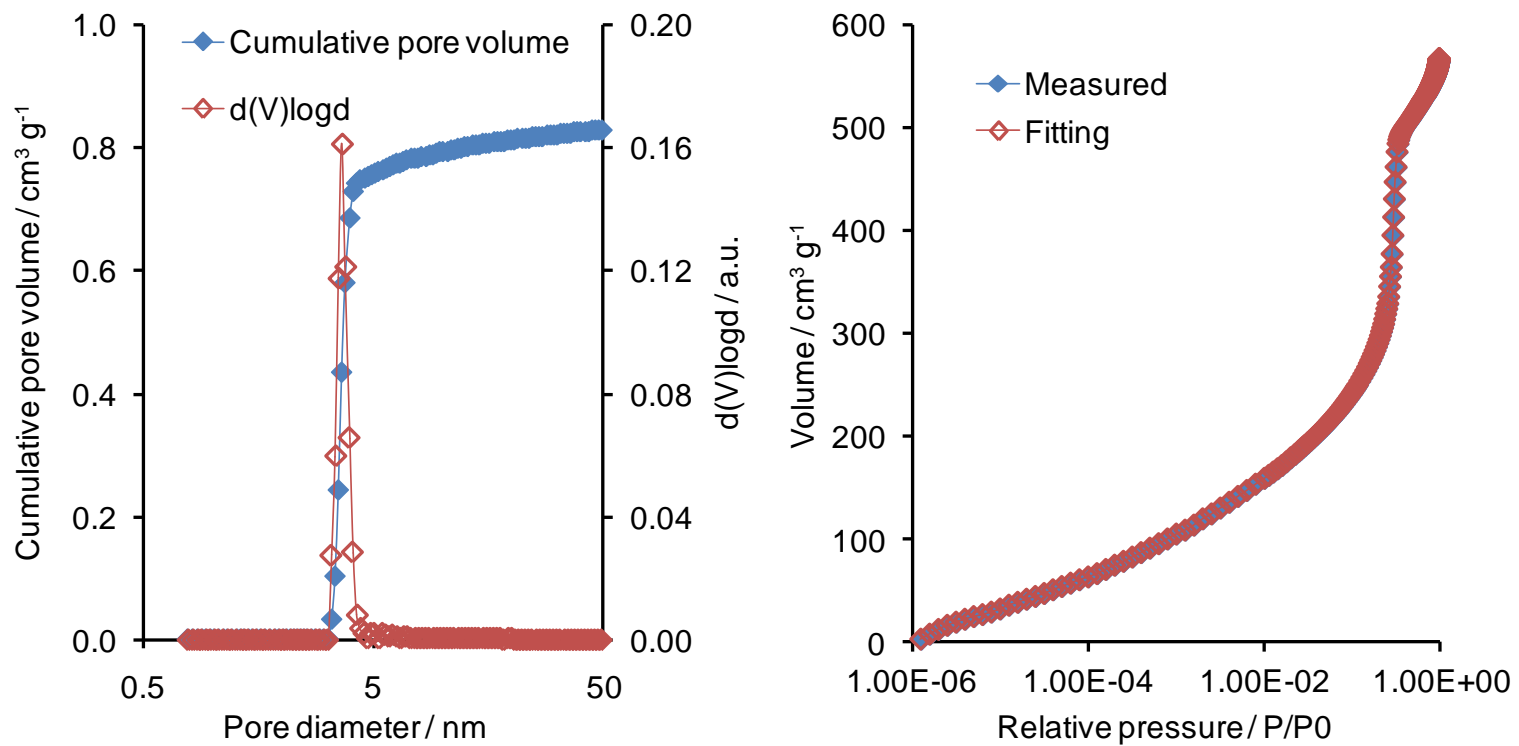


**Figure 3.4 (e)** – Pore size distribution, and fitting plots for MCM-41 (Fitting error 0.7 %)

### 3.2.1.3 Transmission electron microscopy

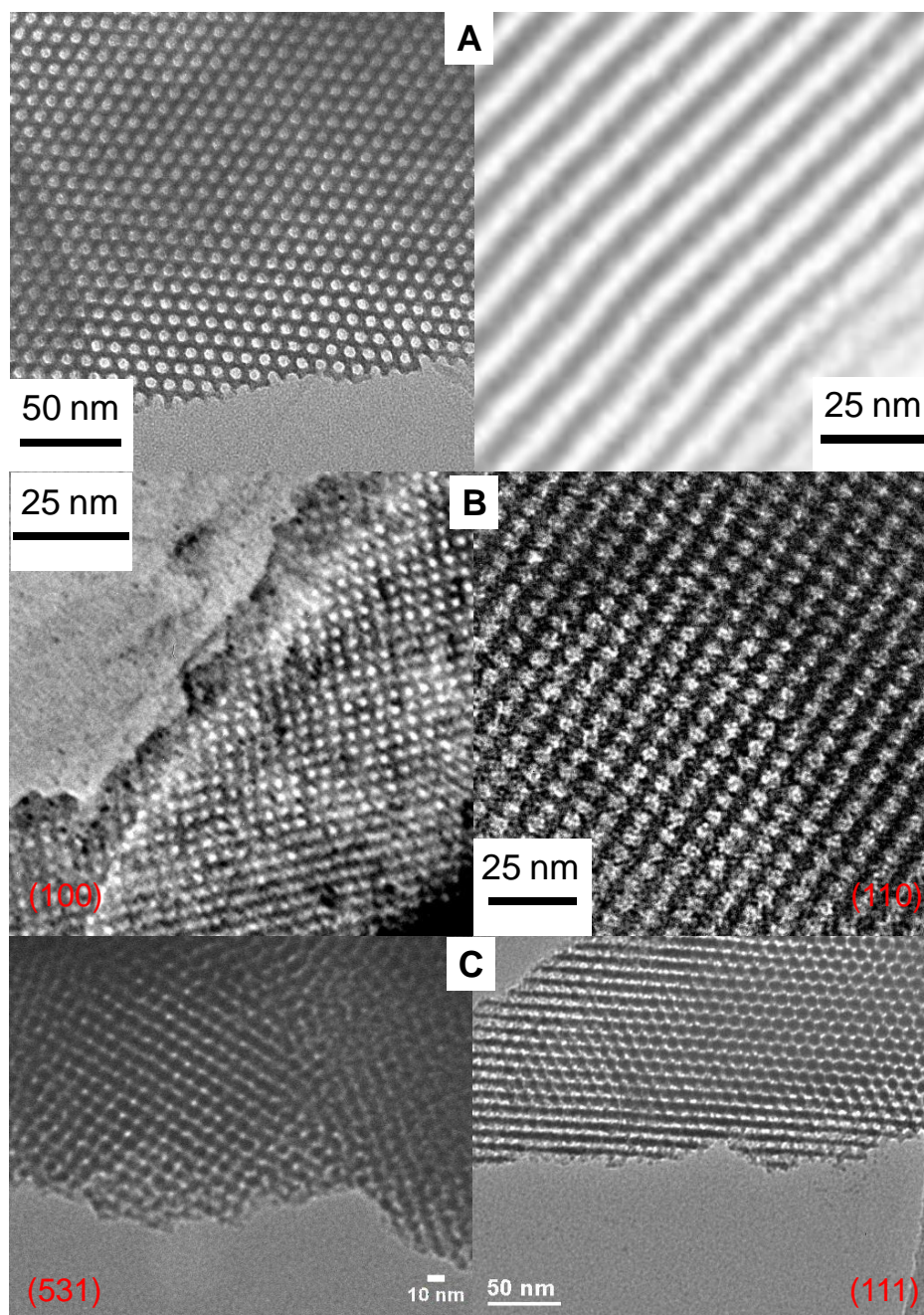


**Figure 3.5** – Bright field TEM images of (A) SBA-15, (B) SBA-16 and (C) KIT-6 (directions of incident is indicated in red for the cubic structures)

**Figure 3.5** depicts representative TEM images of the three mesoporous supports. SBA-15 clearly exhibits both the hexagonal packing and channel structures associated with the  $p6mm$  space group of these materials.<sup>10</sup> SBA-16 and KIT-6 exhibit cubic pore structures of the appropriate space groups;  $Im\bar{3}m$  for SBA-16<sup>10</sup>

and  $Ia\bar{3}d$  for KIT-6.<sup>11</sup> The measured pore spacing/cell parameter for all three supports concurs with values determined from low angle XRD. Average pore diameters, measured over ~100 pores, yield values of 6.3 ( $\pm$  0.4 nm), 6.5 ( $\pm$  0.5 nm), and 6.0 nm ( $\pm$  0.4 nm) for SBA-15, KIT-6 and SBA-16 respectively. For SBA-15 and KIT-6, these are in good agreement with both porosimetry methodologies. For SBA-16, the TEM value coincides only with the fitted data, supporting the BJH interpretation regarding the influence of ink bottle pore structures.

### 3.2.2 Characterisation of Pd impregnated silicas supports

Impregnation of the four silica supports was carried out by the incipient wetness method, with targeted bulk Pd loadings ranging from 0.05-2.5/5 wt%.

#### 3.2.2.1 Inductively coupled plasma optical emission spectroscopy / X-Ray Fluorescence Spectroscopy

**Table 3.2** – Comparison of desired and actual bulk metal loadings

<i>Support</i>	<i>Target loading / wt%</i>	<i>Measured loading / wt%</i>
<i>SiO<sub>2</sub><sup>(a)</sup></i>	2.5	3.13
<i>SiO<sub>2</sub><sup>(a)</sup></i>	1	1.03
<i>SiO<sub>2</sub><sup>(a)</sup></i>	0.5	0.53
<i>SiO<sub>2</sub><sup>(a)</sup></i>	0.1	0.11
<i>SiO<sub>2</sub><sup>(a)</sup></i>	0.05	0.05
<i>SBA-15<sup>(b)</sup></i>	5	4.14
<i>SBA-15<sup>(b)</sup></i>	2.5	2.17
<i>SBA-15<sup>(b)</sup></i>	1	0.89
<i>SBA-15<sup>(b)</sup></i>	0.5	0.45
<i>SBA-15<sup>(b)</sup></i>	0.1	0.08
<i>SBA-15<sup>(b)</sup></i>	0.05	0.05
<i>SBA-16<sup>(b)</sup></i>	2.5	2.28
<i>SBA-16<sup>(b)</sup></i>	1	0.89
<i>SBA-16<sup>(b)</sup></i>	0.5	0.42
<i>SBA-16<sup>(b)</sup></i>	0.1	0.10
<i>SBA-16<sup>(b)</sup></i>	0.05	0.05
<i>KIT-6<sup>(b)</sup></i>	5	3.84
<i>KIT-6<sup>(b)</sup></i>	2.5	2.22
<i>KIT-6<sup>(b)</sup></i>	1	0.78
<i>KIT-6<sup>(b)</sup></i>	0.5	0.46
<i>KIT-6<sup>(b)</sup></i>	0.1	0.13
<i>KIT-6<sup>(b)</sup></i>	0.05	0.05

<sup>(a)</sup> XRF, <sup>(b)</sup> ICP-OES

ICP-OES, after hydrogen fluoride digestion, was carried out by Medac analytical services Ltd to determine the accurate bulk Pd loadings for the three Pd/mesoporous silicas. Bulk compositions of the commercial Pd/silicas were determined via XRF, calibrated using the ICP-OES characterised Pd/SBA-15 series as standards. **Table 3.2** shows good agreement between the desired and actual loadings for all four series.

### 3.2.2.2 Powder X-Ray diffraction

Low angle XRD indicates that the impregnation process has no detrimental effect on the long-range pore order, as highlighted in **Figure 3.6**. For all three mesoporous supports, the same peaks can be indexed as observed for their equivalent parent material. Furthermore no sign of a systematic shift of the major peaks is witnessed and thus no noteworthy contractions or expansions of the mesopore unit cells occur.

Wide angle XRD provided information on crystalline Pd phase and size. Sharp reflections are only observed for highly ordered crystalline structures, which occur at higher  $2\theta$  values due to the closer packing of atoms compared to ordered mesopores. **Figure 3.7** shows the corresponding patterns for all impregnated silicas. The tail of a broad silica reflection, at less than  $35^\circ$ , is typical of amorphous silica<sup>25</sup> and is clear in all samples indicating a disordered frameworks. At bulk Pd loadings  $>3$  wt%, reflections at  $39.9^\circ$ , characteristic of Pd(111) reflection in Pd metal, and an additional peak at  $46.5^\circ$ , assigned to the Pd(200) reflection demonstrate the presence of metallic nanoparticles; the absence of these peaks at lower loadings suggest they comprise sub-2 nm nanoparticles.<sup>26</sup> Particle sizes were estimated using the Scherrer Equation<sup>27</sup> (**Chapter 2 Equation 2.2**) and the resulting values reported in **Table 3.3**. These suggest Pd particle size decreases with increasing support surface area and mesopore interconnectivity.

**Table 3.3** –Pd particle size determined from the Pd(100) reflection

<i>Support</i>	<i>Pd Loading / wt%</i>	<i>Pd Particle Size / nm</i>
<i>SiO<sub>2</sub></i>	<i>3.13</i>	<i>3.0 (<math>\pm 0.2</math>)</i>
<i>SBA-15</i>	<i>4.14</i>	<i>2.8 (<math>\pm 0.2</math>)</i>
<i>KIT-6</i>	<i>3.84</i>	<i>2.4 (<math>\pm 0.2</math>)</i>

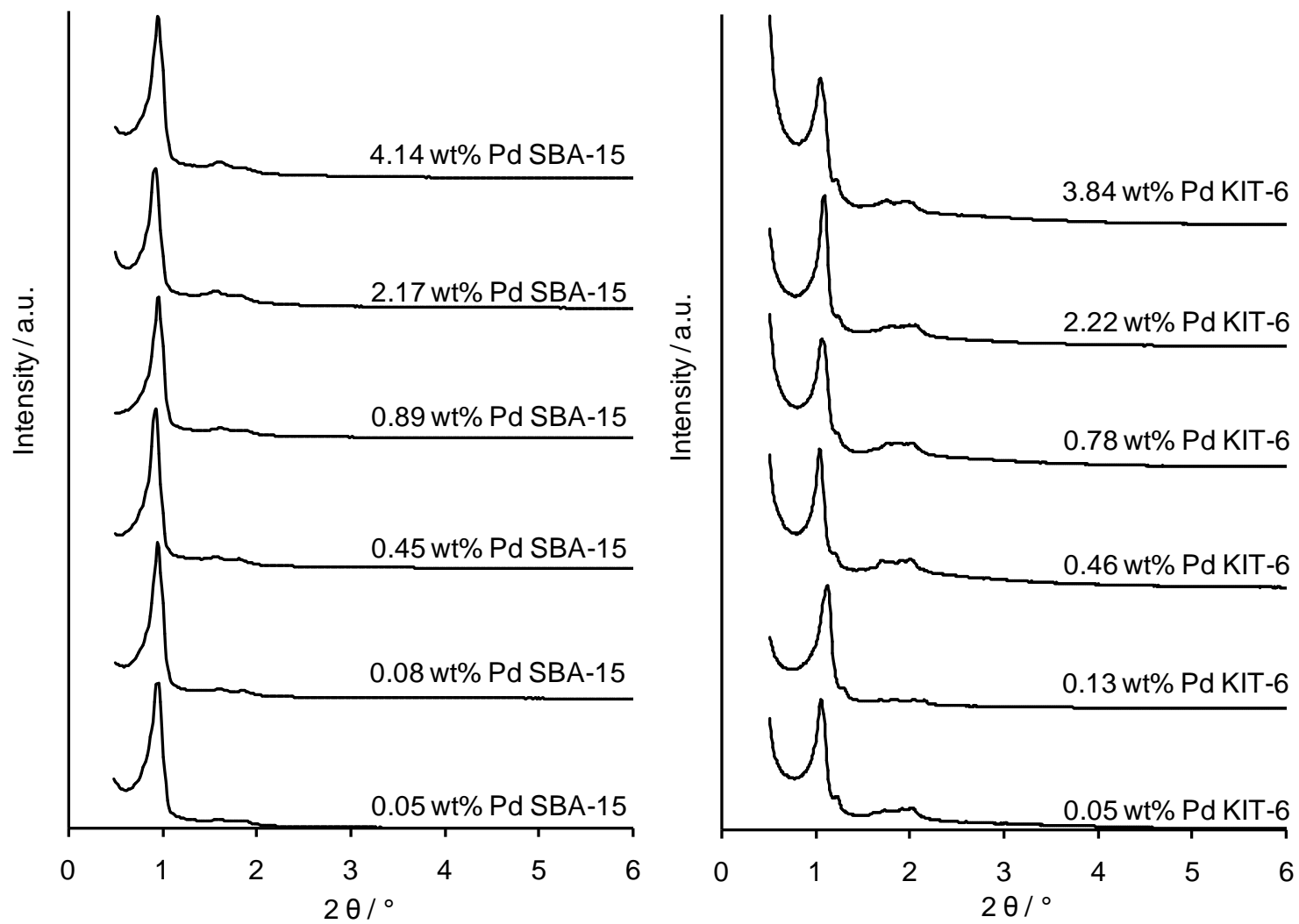


**Figure 3.6 (a)** - Stacked low angle XRD plots for Pd/SBA-15 and Pd/KIT-6

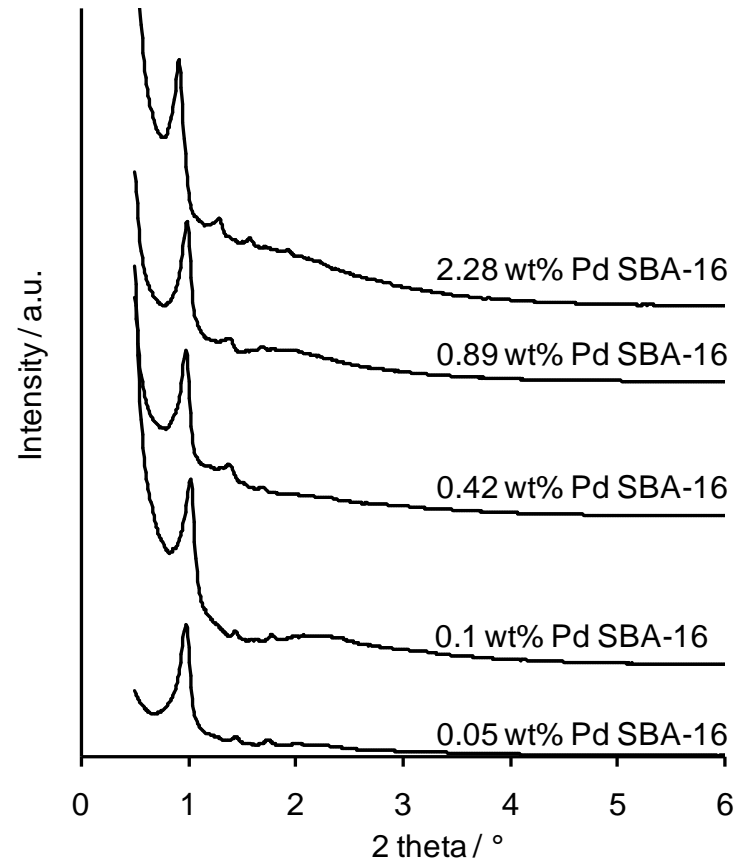


**Figure 3.6 (b)** – Stacked low angle XRD plots for Pd/SBA-16 series

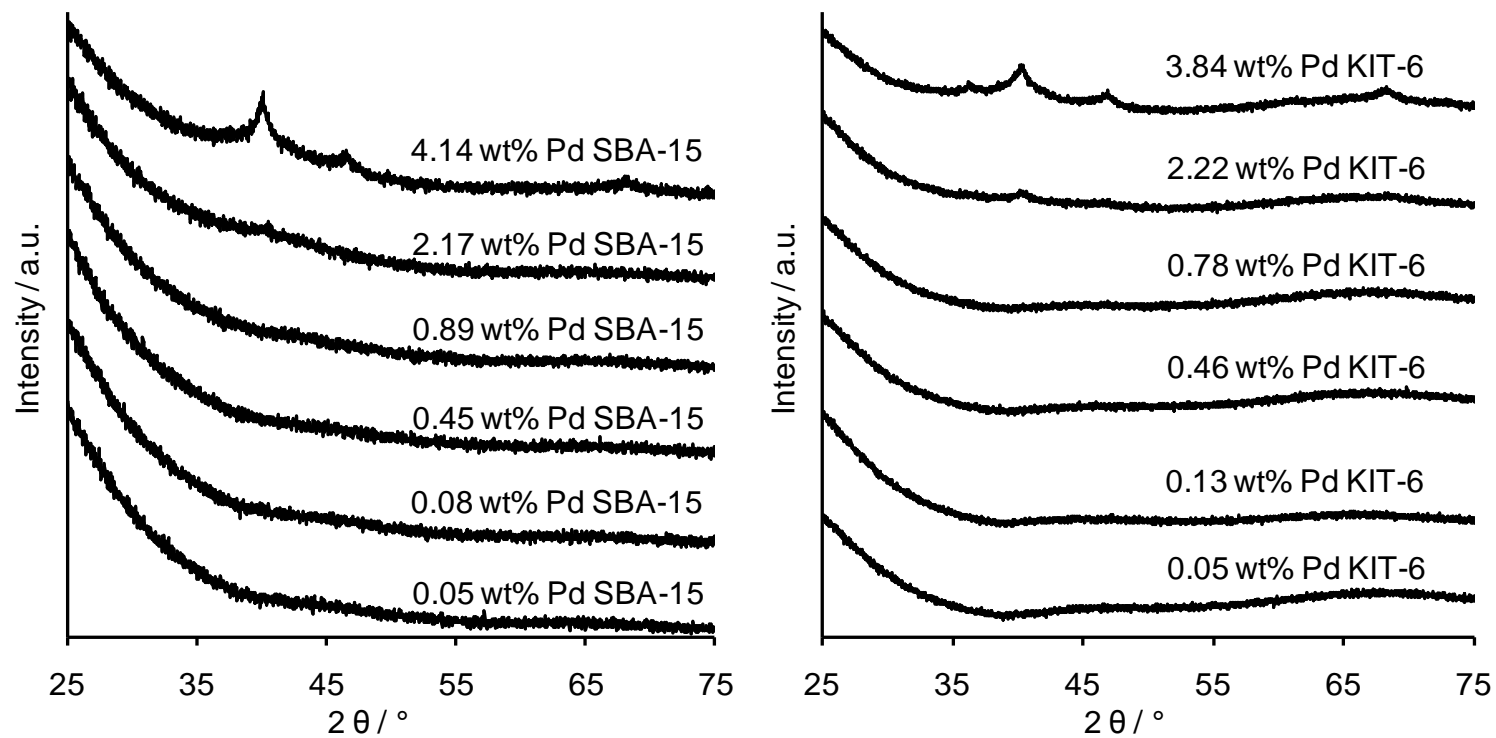


**Figure 3.7 (a)** - Stacked wide angle XRD plots for Pd/SBA-15 and Pd/KIT-6

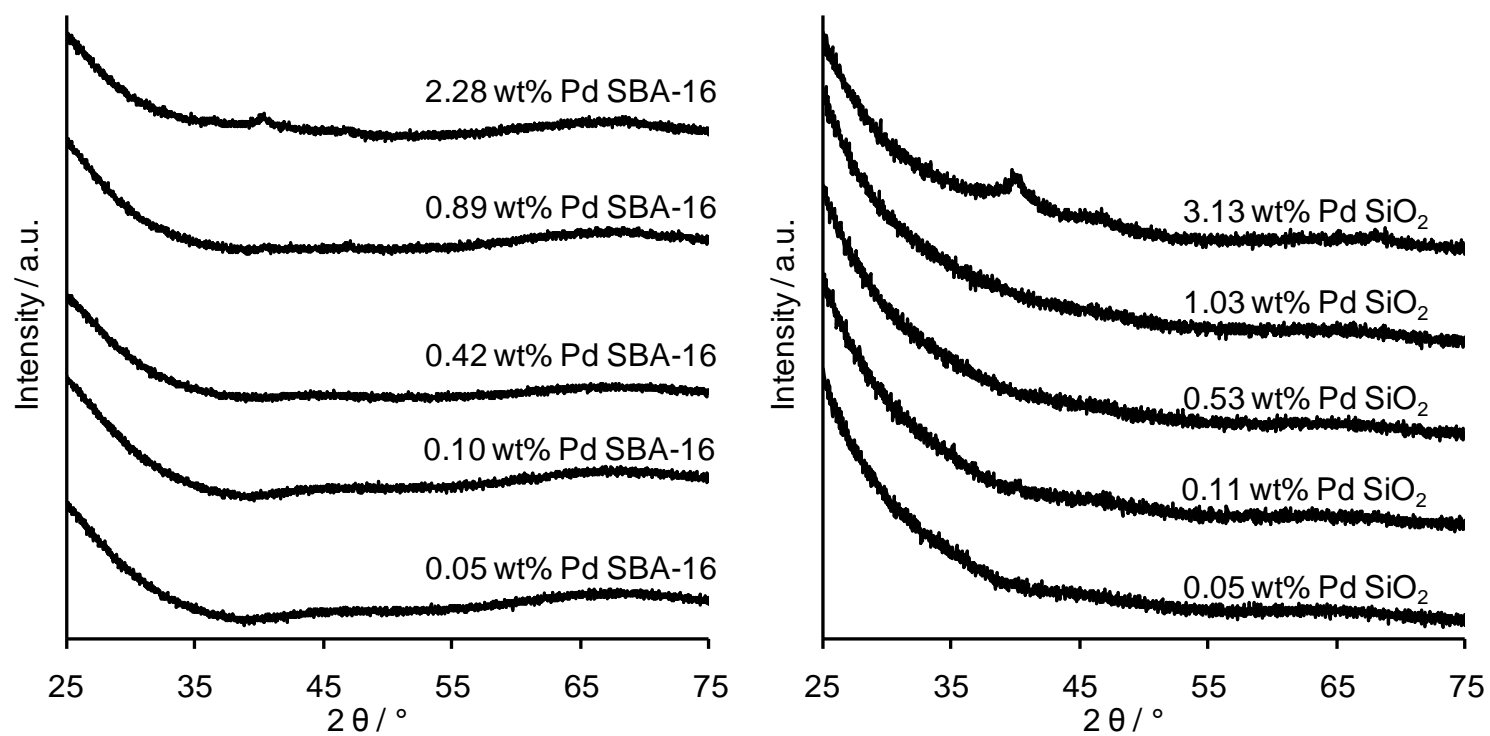


**Figure 3.7 (b)** – Stacked wide angle XRD plots for Pd/SBA-16 and Pd/commercial silica

### 3.2.2.3 Nitrogen porosimetry

Figure 3.8 shows the N<sub>2</sub> isotherms for all four Pd silica series.

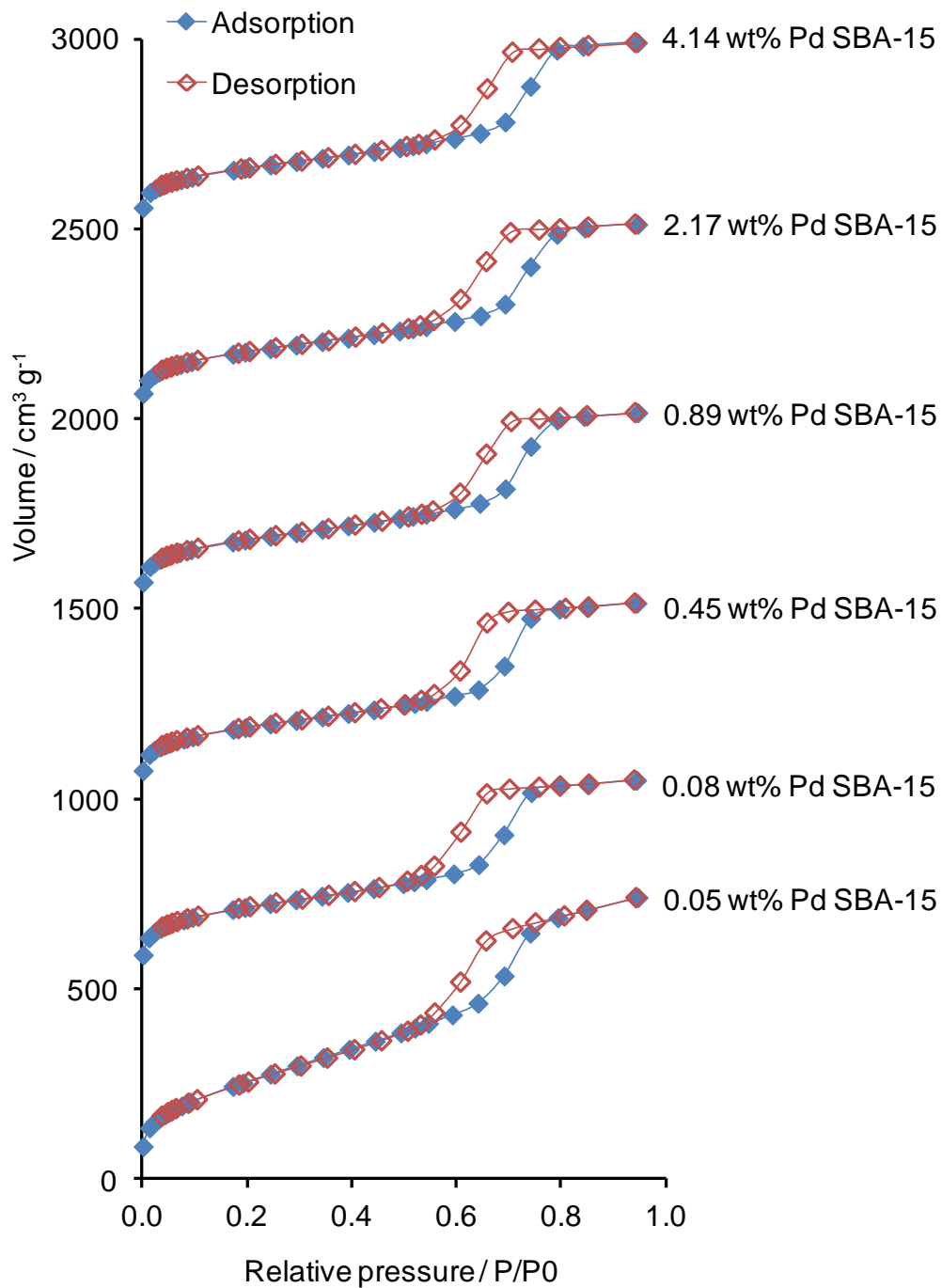
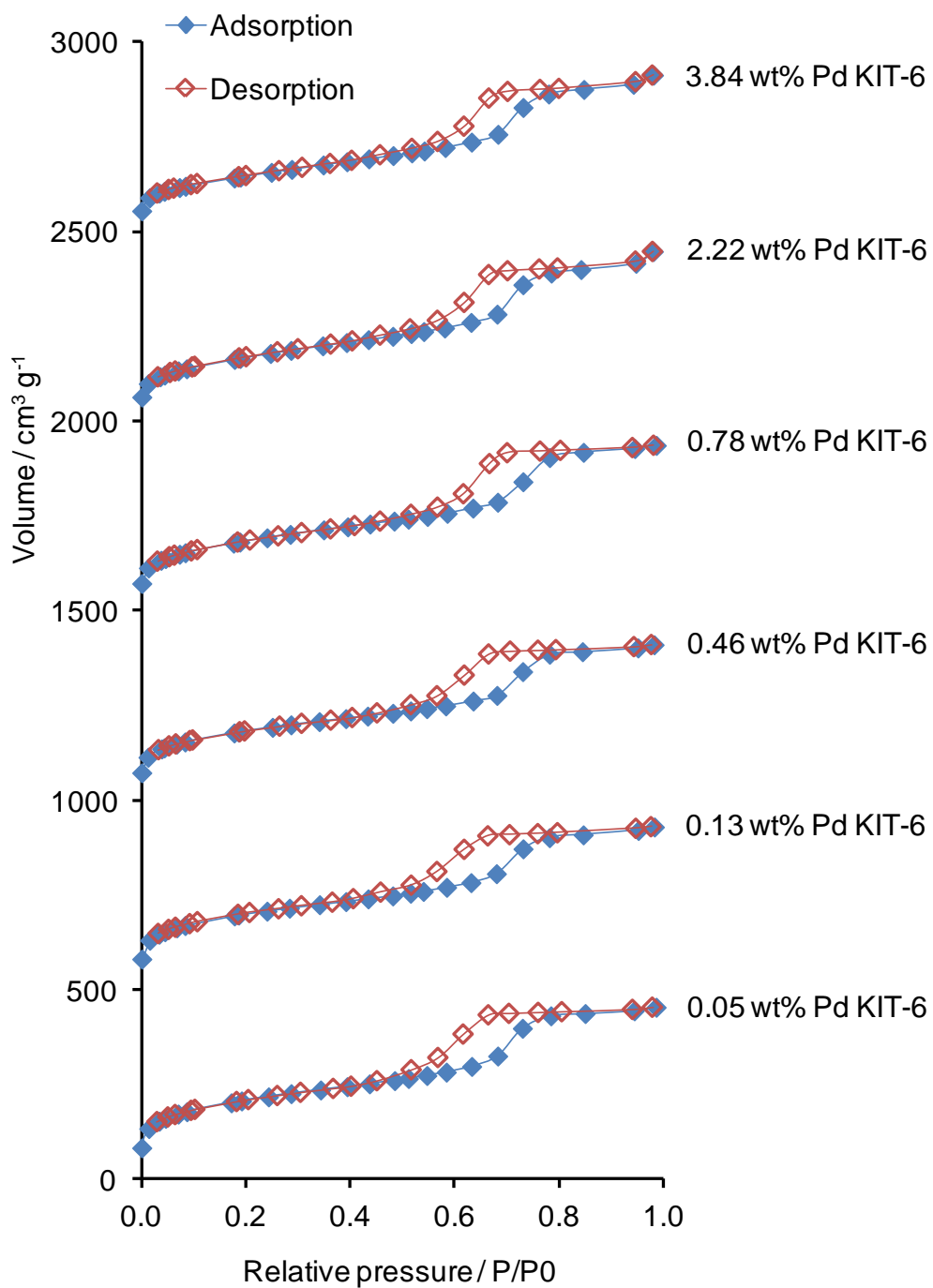
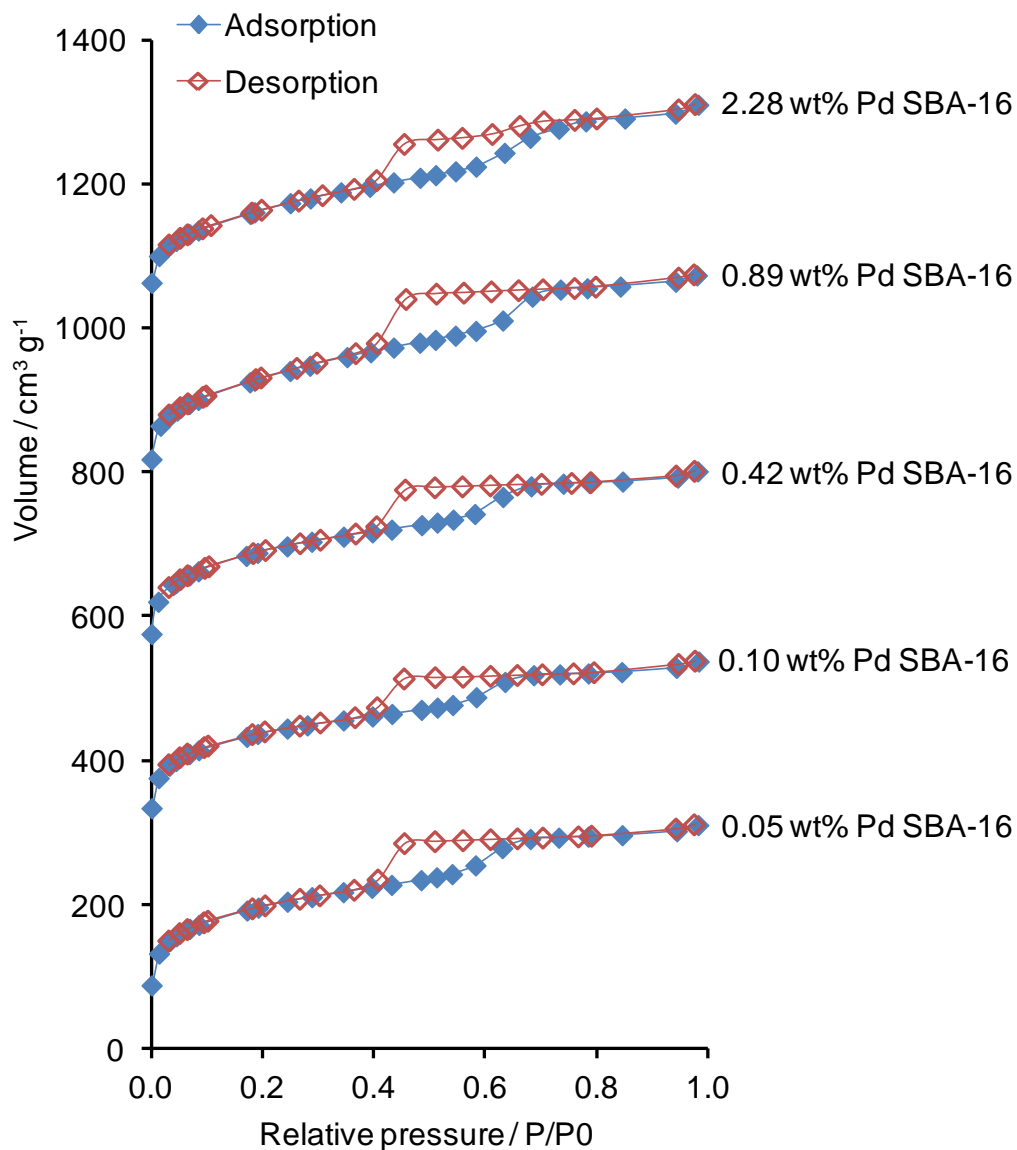


Figure 3.8 (a) - Stacked isotherm plots for Pd/SBA-15 (samples consecutively offset by 500 cm<sup>3</sup> g<sup>-1</sup> with each increase in metal loading)



**Figure 3.8 (b)** - Stacked isotherm plots for Pd/KIT-6 (samples consecutively offset by 500 cm<sup>3</sup> g<sup>-1</sup> with each increase in metal loading)



**Figure 3.8 (c)** - Stacked isotherm plot for Pd/SBA-16 (samples consecutively offset by 250 cm<sup>3</sup> g<sup>-1</sup> with each increase in metal loading)

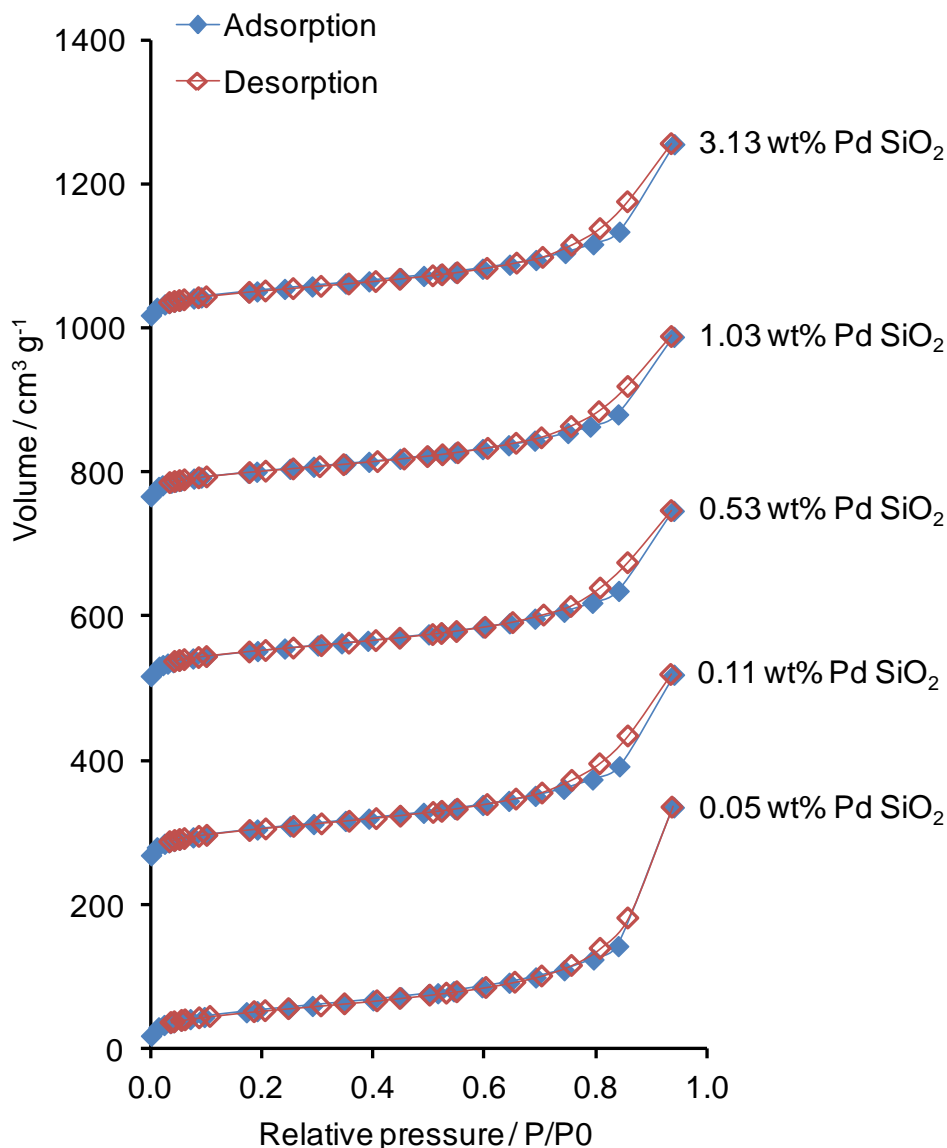


**Figure 3.8 (d)** - Stacked isotherm plots for Pd/commercial silica (samples consecutively offset by  $250 \text{ cm}^3 \text{ g}^{-1}$  with each increase in metal loading)

The isotherms (and, where present, hysteresis loops) are identical to their parent supports, providing further evidence that support architectures are preserved post-impregnation. As a result of silica's high stability, mesoporous silicas are a common choice for the grafting of other oxide coatings to thereby generate stable mesoporous alumina, ceria and zirconia supports.<sup>28-30</sup>

The principal textural effect of Pd impregnation is the decrease in BET support surface area with loading, as illustrated in **Figure 3.9**. This is more pronounced for the mesoporous silicas, and may result from pore blockage within the meso and/or

micropores, although all three silicas behave similarly. If mesopores were selectively blocked, then one might expect the non-interconnected SBA-15 to be more affected by Pd incorporation than SBA-16 and KIT-6 (significant surface area would be lost if long, parallel mesopore channels were blocked at both ends; in contrast to interconnected mesopore architectures where pores can be accessed from multiple routes). The commercial silica shows little change in surface area following impregnation, suggesting a high level of external surface decoration by Pd nanoparticles.

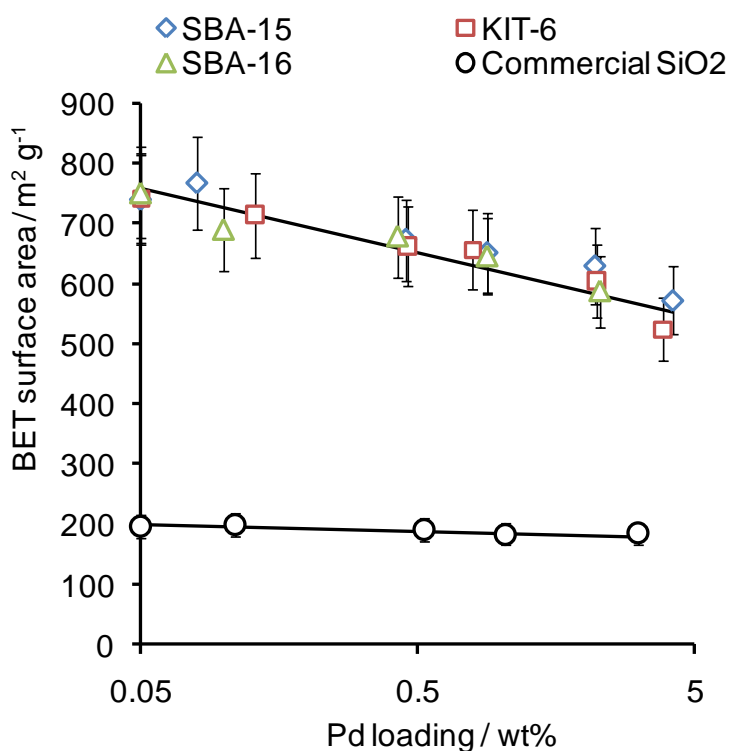


**Figure 3.9** - Effect of metal loading on BET support surface area

More detailed analysis, probing the effect of Pd on both micropore and mesopore surface areas via the t-plot method, can shed further insight into this aspect with the results shown in **Figure 3.10**.

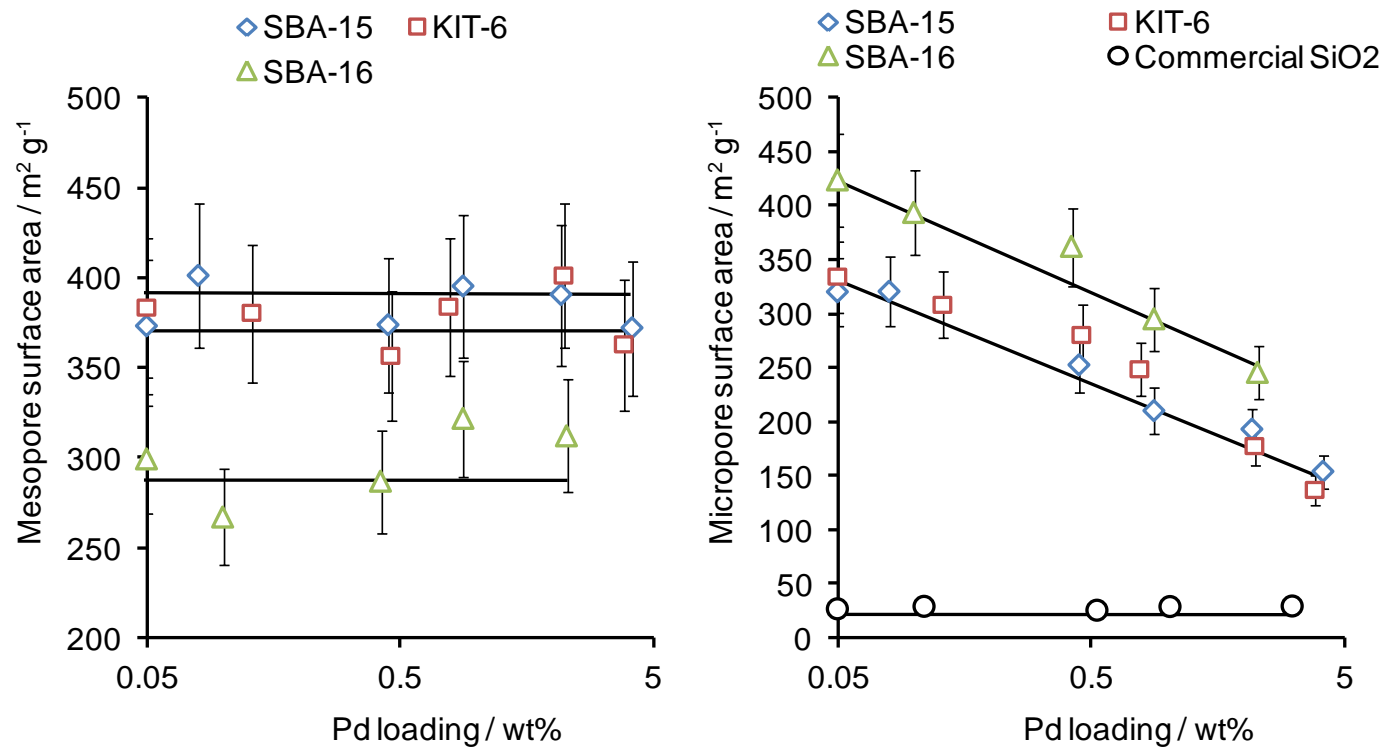


**Figure 3.10** - Effect of metal loading on mesopore (left) and micropore (right) surface area

This shows little change in mesopore surface area with Pd loading for SBA-15, SBA-16 and KIT-6, suggesting that minimal mesopore blockage occurs. In fact the mesopore surface areas closely match those of each parent support (427, 408 and 266  $\text{m}^2 \text{g}^{-1}$  for SBA-15 KIT-6 and SBA-16 respectively). The reverse is true of the micropore surface areas for the Pd/meso-silicas, which all exhibit an inverse relation between micropore surface area and Pd loading, suggesting this is the origin of the analogous trend in BET areas, i.e. Pd impregnation specifically blocks micropores and not mesopores. The commercial silica micropore surface area remains constant, confirming the majority of Pd nanoparticles reside at the external surfaces of this amorphous support.

Detailed inspection of the BJH pore size distribution plots, presented in **Figure 3.11**, shows no change in average pore sizes with Pd loading.

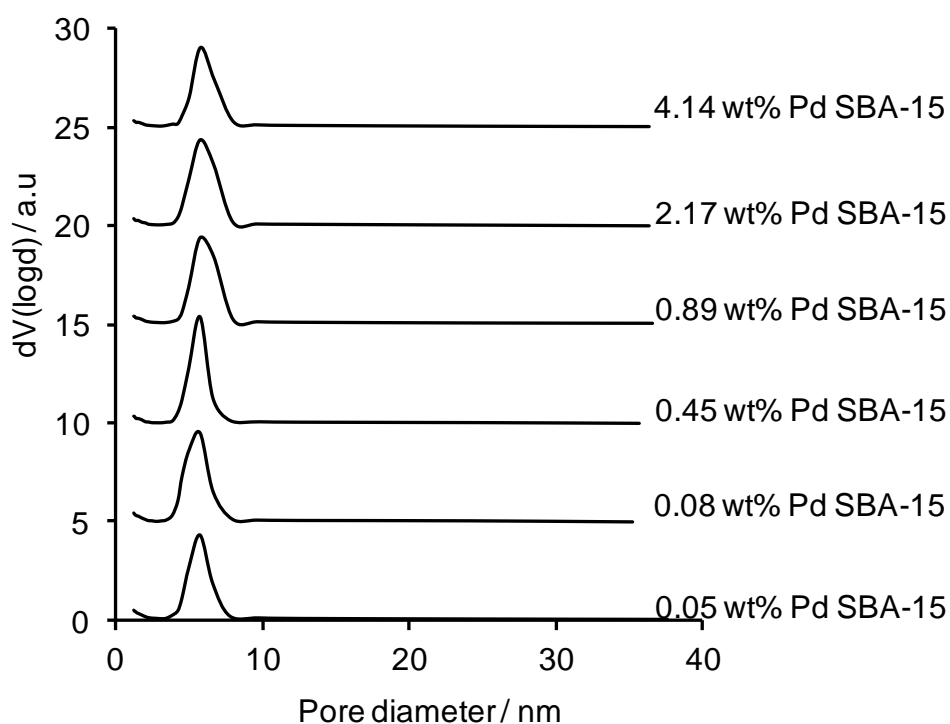


**Figure 3.11 (a)** – Stacked BJH size distribution plots for Pd/SBA-15 (samples consecutively offset by 5 with each increase in loading)

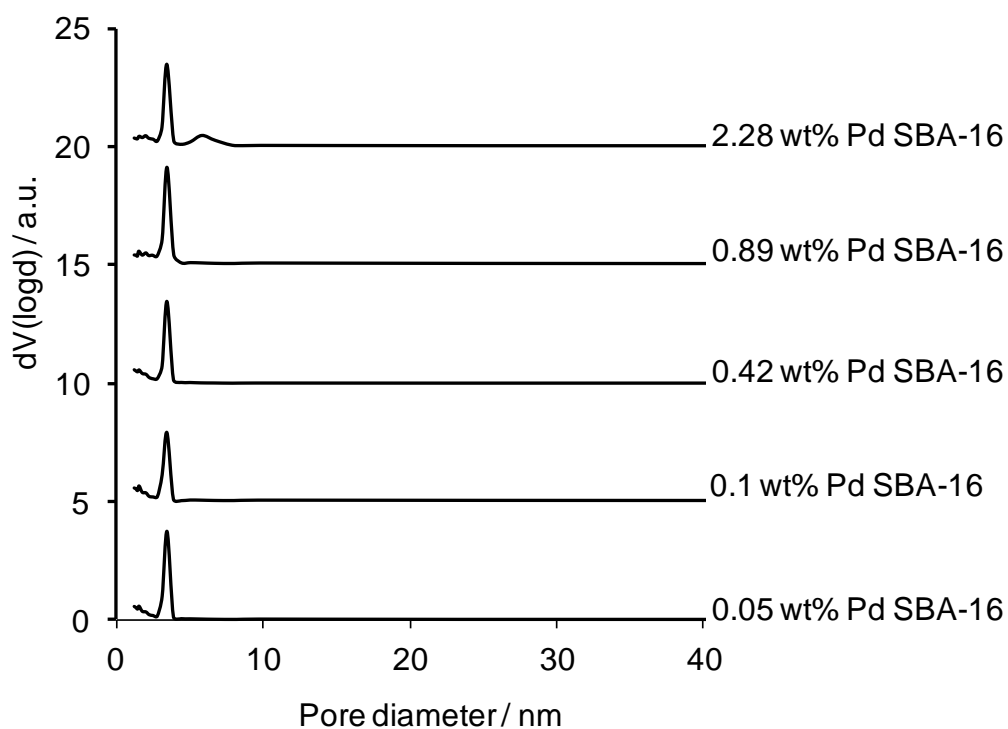
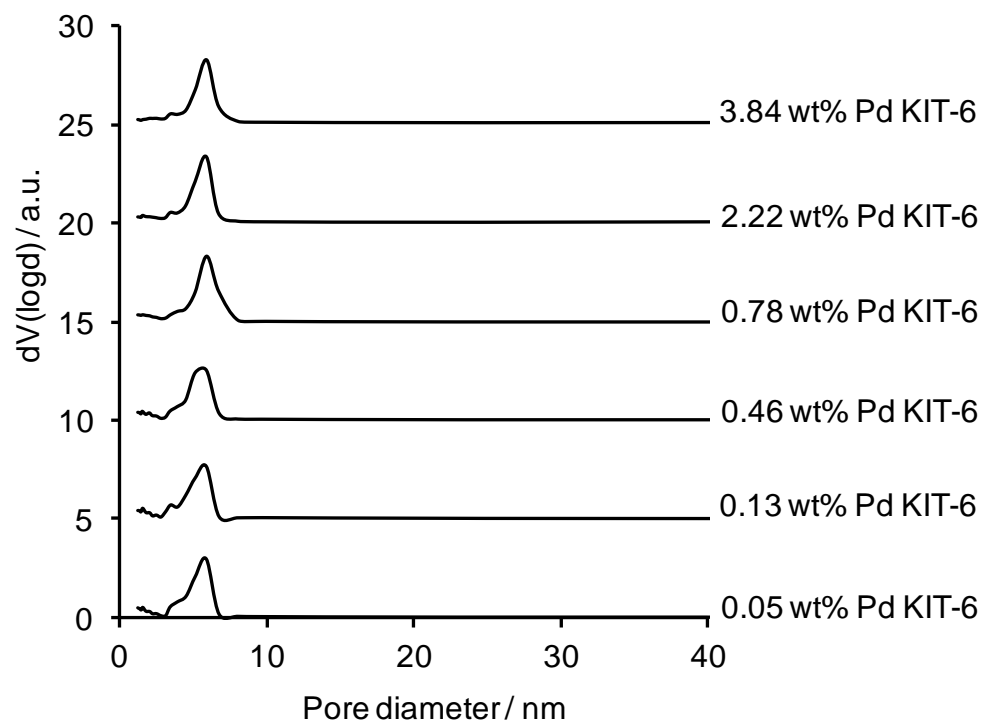


**Figure 3.11 (b)** – Stacked BJH size distribution plots for Pd/KIT-6 and Pd/SBA-16 (samples consecutively offset by 5 with each increase in loading)

### 3.2.2.4 Carbon monoxide chemisorption

**Table 3.4** – Dispersion and average Pd particle size from CO titrations

<i>Support</i>	<i>Loading / wt%</i>	<i>Dispersion / %</i>	<i>Average particle size / nm</i>
<i>SiO<sub>2</sub></i>	<i>3.13</i>	<i>28 (± 1)</i>	<i>3.4 (± 0.1)</i>
<i>SiO<sub>2</sub></i>	<i>1.03</i>	<i>40 (± 1)</i>	<i>2.8 (± 0.1)</i>
<i>SiO<sub>2</sub></i>	<i>0.53</i>	<i>44 (± 1)</i>	<i>2.5 (± 0.1)</i>
<i>SiO<sub>2</sub></i>	<i>0.11</i>	<i>56 (± 1)</i>	<i>1.9 (± 0.1)</i>
<i>SiO<sub>2</sub></i>	<i>0.05</i>	<i>67 (± 3)</i>	<i>1.6 (± 0.1)</i>
<i>SBA-15</i>	<i>4.14</i>	<i>37(± 1)</i>	<i>2.9 (± 0.1)</i>
<i>SBA-15</i>	<i>2.17</i>	<i>43 (± 1)</i>	<i>2.6 (± 0.1)</i>
<i>SBA-15</i>	<i>0.89</i>	<i>52 (± 1)</i>	<i>2.3 (± 0.1)</i>
<i>SBA-15</i>	<i>0.45</i>	<i>56 (± 1)</i>	<i>1.9 (± 0.1)</i>
<i>SBA-15</i>	<i>0.08</i>	<i>64 (± 1)</i>	<i>1.7 (± 0.1)</i>
<i>SBA-15</i>	<i>0.05</i>	<i>78 (± 4)</i>	<i>1.4 (± 0.1)</i>
<i>SBA-16</i>	<i>2.28</i>	<i>64 (± 1)</i>	<i>1.7 (± 0.1)</i>
<i>SBA-16</i>	<i>0.89</i>	<i>71 (± 1)</i>	<i>1.6 (± 0.1)</i>
<i>SBA-16</i>	<i>0.42</i>	<i>79 (± 1)</i>	<i>1.4 (± 0.1)</i>
<i>SBA-16</i>	<i>0.1</i>	<i>82 (± 2)</i>	<i>1.3 (± 0.1)</i>
<i>SBA-16</i>	<i>0.05</i>	<i>88 (± 4)</i>	<i>0.9 (± 0.1)</i>
<i>KIT-6</i>	<i>3.84</i>	<i>44 (± 1)</i>	<i>2.5 (± 0.1)</i>
<i>KIT-6</i>	<i>2.22</i>	<i>62 (± 1)</i>	<i>1.8 (± 0.1)</i>
<i>KIT-6</i>	<i>0.78</i>	<i>71 (± 1)</i>	<i>1.6 (± 0.1)</i>
<i>KIT-6</i>	<i>0.46</i>	<i>79 (± 1)</i>	<i>1.4 (± 0.1)</i>
<i>KIT-6</i>	<i>0.13</i>	<i>85 (± 2)</i>	<i>1.2 (± 0.1)</i>
<i>KIT-6</i>	<i>0.05</i>	<i>88 (± 4)</i>	<i>0.9 (± 0.1)</i>

CO titration was used to determine metal dispersions for all 22 catalysts. One area of contention in such use of CO is the Pd:CO stoichiometry so assumed, as CO chemisorbs in atop, bridging or three fold sites.<sup>31</sup> A Pd:CO stoichiometry of 2:1, as commonly employed in the literature, was used for two reasons. First, for particle sizes <2 nm (which XRD suggests dominate at low bulk Pd loadings), bridging sites are reportedly the most common at standard temperature and pressure.<sup>32, 33</sup> Second, adsorption into atop sites only occurs to a maximum coverage of 0.5 monolayers, hence even if such an adsorption mode is favoured, it would result in the same Pd:CO stoichiometry.<sup>26, 34</sup> Metal dispersions were calculated using **Equation 2.6 (Chapter 2)**. Further information regarding average Pd particle size can also be deduced from the total volume of chemisorbed gas and was evaluated using

**Equation 2.7 (Chapter 2).** Metal dispersions and average particle sizes are summarised in **Table 3.4**. All samples display a clear inverse correlation between metal loading and dispersion, and thus direct correlation to particle size. Globally, increasing the support surface area using mesoporous silicas enhances metal dispersion. Within the mesoporous silicas, for a given loading the particle size falls upon moving from SBA-15, to SBA-16 and KIT-6.<sup>35</sup> The latter variations cannot be ascribed to surface area alone, as these are comparable for all three. This may arise due to support interconnectivity, and its possible effect on metal precursor diffusion, adsorption and evaporation/transformation during the various stages of impregnation and processing. The support architecture could thus modulate particle nucleation and subsequent sintering during high temperature calcination and reduction. Even if Pd ions were evenly dispersed through all three supports during impregnation, the interconnecting supports could lower Pd nanoparticle mobility, preventing them crossing pore junctions, or confining them within the narrow entrance pores of SBA-16.<sup>36</sup> In contrast, the straight, non-connected channels of SBA-15 facilitate Ostwald ripening via inter-pore Pd nanoparticle migration and fusion.<sup>37, 38</sup>

### 3.2.2.5 Diffuse reflectance infrared fourier transform

In-situ CO chemisorption by DRIFTS allowed further insight into dispersed Pd nanoparticles spanning 1.3 to 3.4 nm, the samples studied are listed in **Table 3.5**. IR spectra, **Figure 3.12**, reveal two distinct adsorption bands at 2080 and 1960  $\text{cm}^{-1}$ , assigned to atop and bridge sites.<sup>31, 33</sup> The peak maxima for each band shifts to lower wavenumber as Pd loading/particle size declines.

**Table 3.5** –DRIFTS CO adsorption samples and associated Pd particle size

<i>Catalyst</i>	<i>Pd particle size / nm</i>
0.13 wt% Pd/KIT-6	1.2
0.89 wt% Pd/SBA-16	1.6
2.22 wt% Pd/KIT-6	1.8
0.89 wt% Pd/SBA-15	2.3
3.84 wt% Pd/KIT-6	2.50
0.53 wt% Pd/SiO <sub>2</sub>	2.5
4.14 wt% Pd/SBA-15	2.9
3.13 wt% Pd/SiO <sub>2</sub>	3.4

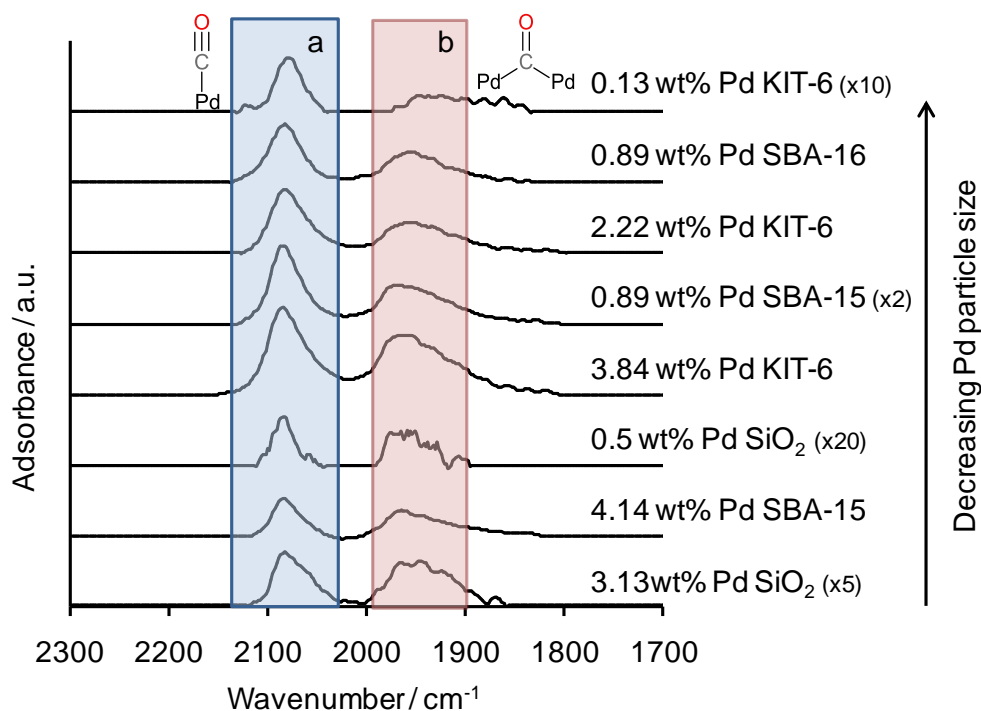


**Figure 3.12** – Offset IR spectra of chemisorbed CO on a range of catalysts

In order to examine possible size-dependent CO adsorption site-switching, both bands were fit across the Pd/silica selection on the basis of a simple model assuming two atop and two bridging CO adsorption sites (with fixed line shape and wavenumber) in accordance with literature methodologies.<sup>31, 39</sup> Fitting of the atop band reveals two features, one at  $2092\text{ cm}^{-1}$  associated with CO bound to Pd(111) facets, and the second at  $2076\text{ cm}^{-1}$  arising from CO bound at low coordination corner and edge sites.<sup>39</sup> The bridging band can also be fit to components at  $1970\text{ cm}^{-1}$  and  $1932\text{ cm}^{-1}$ , previously ascribed to bridging CO on Pd(100) or Pd(111) respectively.<sup>31, 39</sup> There was no evidence for CO bound in three-fold hollow sites<sup>31</sup> over any materials (which typically yields a broad peak at  $1830\text{ cm}^{-1}$ ) reflecting the saturation adsorbate coverage (and associated repulsive lateral interactions) employed in these measurements which disfavors such occupancy.<sup>33</sup>

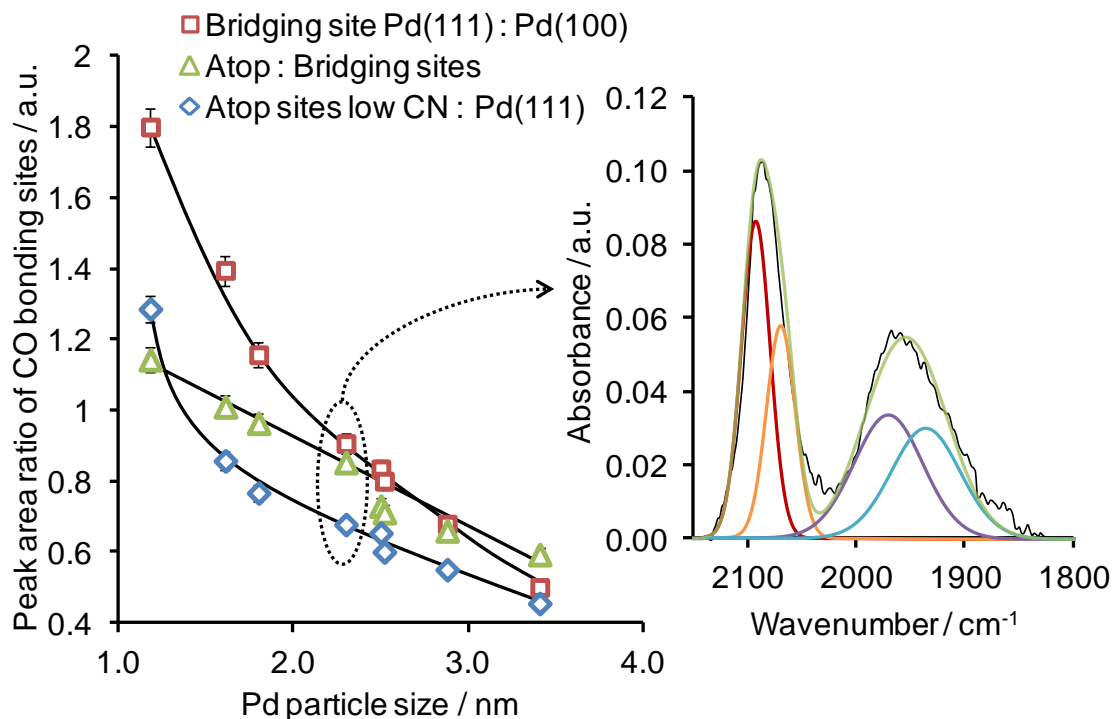


**Figure 3.13** – Relative intensity of varying bonding sites as a function of Pd particle size with deconvolution of 0.89 wt% Pd/SBA-15 illustrated.

**Figure 3.13** reveals the evolution of CO adsorption sites, and thus nanoparticle morphology, with Pd particle size. The overall ratio of atop:bridge sites increases with decreasing particle size, consistent with the loss of high coordination (100) and (111) terraces,<sup>39, 40</sup> although bridge sites dominate for all but the smallest Pd particle sizes. This parallels a rise in the number of low-coordination (defect) Pd sites relative to terraces, as expected for smaller clusters wherein the proportion of corner and edge atoms increases versus terraces.<sup>41</sup> Finally, the bridging (111):(100) site ratio rises as particle size shrinks. This latter observation is consistent with CO adsorption on Pd/Al<sub>2</sub>O<sub>3</sub>, in which particle sintering results in favouring (100) facets,<sup>33</sup> and Pd/microporous silica for which the (111):(100) ratio increases with Pd dispersion,<sup>31</sup> possibly reflecting a size-dependent shape transition from larger cuboctahedra exposing both (100) and (111) facets, to ~1 nm purely (111) terminated icosahedra. Unfortunately support interference prevented atomic-resolution imaging (HAADF STEM) of Pd nanocrystal morphology, which could have confirmed/disproved this.

### 3.2.2.6 Scanning transmission electron microscopy

Imaging of Pd clusters on the mesoporous silica supports was achieved utilising HAADF STEM, which relies on Z-contrast, with heavier elements appearing brighter.<sup>42</sup>

Approximate 1 wt% loadings were selected with representative images, along with bright field images and particle size histograms, shown in **Figure 3.14**. In the associated images, Pd nanoparticles appear as the brightest spots, with the silica and pore structures imaged as grey and dark grey/black areas respectively. The contrast between Pd and silica is hampered by the thickness of the silica supports, which may exceed tens-hundred nanometres resulting in significant high angle scattering, and small size of the Pd particles of <2 nm diameter. The resulting images demonstrate a uniform distribution of Pd throughout each support, and yield average particle sizes of 2.2 ( $\pm$  0.9), 1.6 ( $\pm$  0.6), and 1.5 ( $\pm$  0.7) nm, for SBA-15, SBA-16 and KIT-6 respectively. These are in good agreement with CO chemisorption calculations, supporting the assumed Pd:CO stoichiometry. Such images also indicate significant levels of Pd in-pore, although high-tilt/tomography measurements are required to definitively prove this. Associated bright field images confirm mesopore structure retention, in line with low angle XRD and N<sub>2</sub> porosimetry.

Further imaging was undertaken on the 0.05 wt% Pd/KIT-06 sample; typical images are shown in **Figure 3.15**. This highlights the lower metal loading, from the reduced Pd particles density. Regrettably Pd detection could only be confidently confirmed at the edge and vertices of the support where silica thickness diminishes and thus Pd contrast is greatest. The average Pd particle size of 0.9 ( $\pm$  0.3) nm again agrees well with that from CO titration, with the majority of Pd nanoparticles decorating the mesopore walls. The inability to view lattice fringes and identify specific Pd facets on the 'spherical-like' particles observed renders the ability to distinguish between different literature<sup>43, 44</sup> and in-situ DRIFTS proposed morphologies impossible.

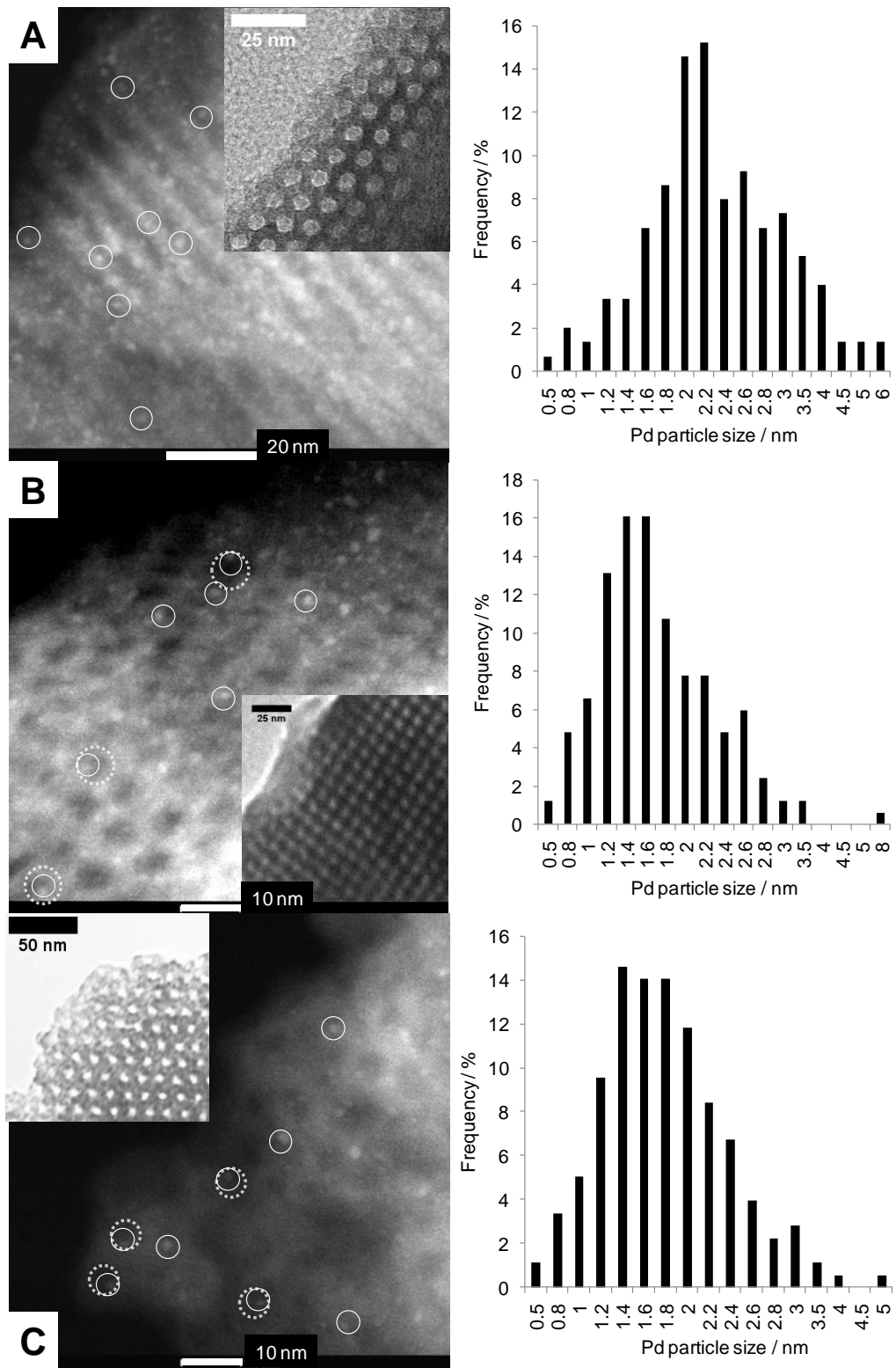


**Figure 3.14** - HAADF HRSTEM images of (A) 0.89 wt% Pd/SBA-15, (B) 0.78 wt% Pd/KIT-6, (C) 0.89 wt% Pd/SBA-16, with Pd (solid) and pores (dashed) circled for clarity, particle size distributions (150-200 particles) and equivalent TEM bright field images are also presented

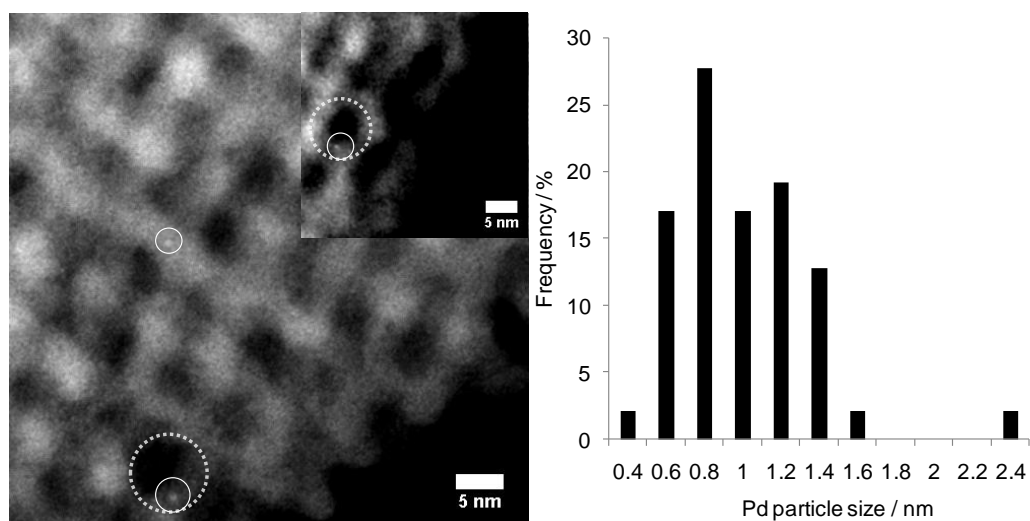


**Figure 3.15** – HAADF STEM images of 0.05 wt% Pd/KIT-6 with Pd (solid) and pores (dashed) circled for clarity and particle size distribution displayed (75 particles)

### 3.2.2.7 X-ray photoelectron spectroscopy

XPS was employed to probe the surface oxidation state of the supported Pd nanoparticles. The resulting Pd 3d XP spectra are shown in **Figure 3.16** for all four supports.

Each Pd X-ray photoelectron spectra, comprising characteristic sets of Pd  $3d_{3/2,5/2}$  doublets ( $\Delta BE = 5.25$  eV),<sup>45</sup> has been energy calibrated to adventitious carbon (at 284.6 eV with this cross checked to SiO<sub>2</sub> 103.4 eV) and background subtracted. Initial inspection of the raw data highlights significant peak broadening with decreasing bulk Pd loading in all cases, which peak fitting shows is the result of a second Pd environment present at higher binding energy. This high binding energy component can be attributed to electron deficient Pd, with a chemical shift consistent with PdO. The relative contributions of metallic Pd at 335.4 eV (indicated by a red dashed line on the SBA-15 plot) and PdO centred at 336.8 eV (indicated by a blue dash dot line on the SBA-15 plot) are shown in **Figure 3.16**. The asymmetric peak shape was determined from fitting of a PdO reference, and subsequently used to fit both surface Pd species.

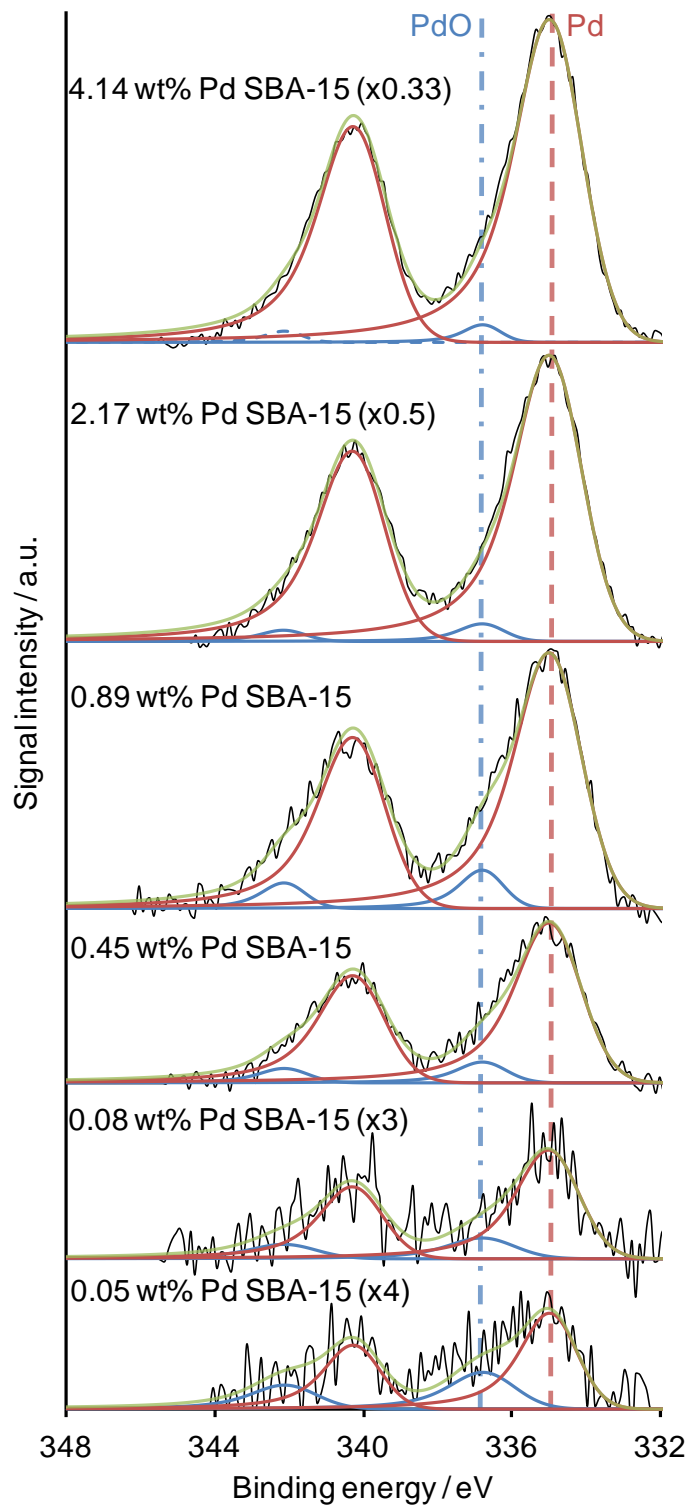


**Figure 3.16 (a)** - Stacked Pd 3d XPS plots of Pd/SBA-15 series

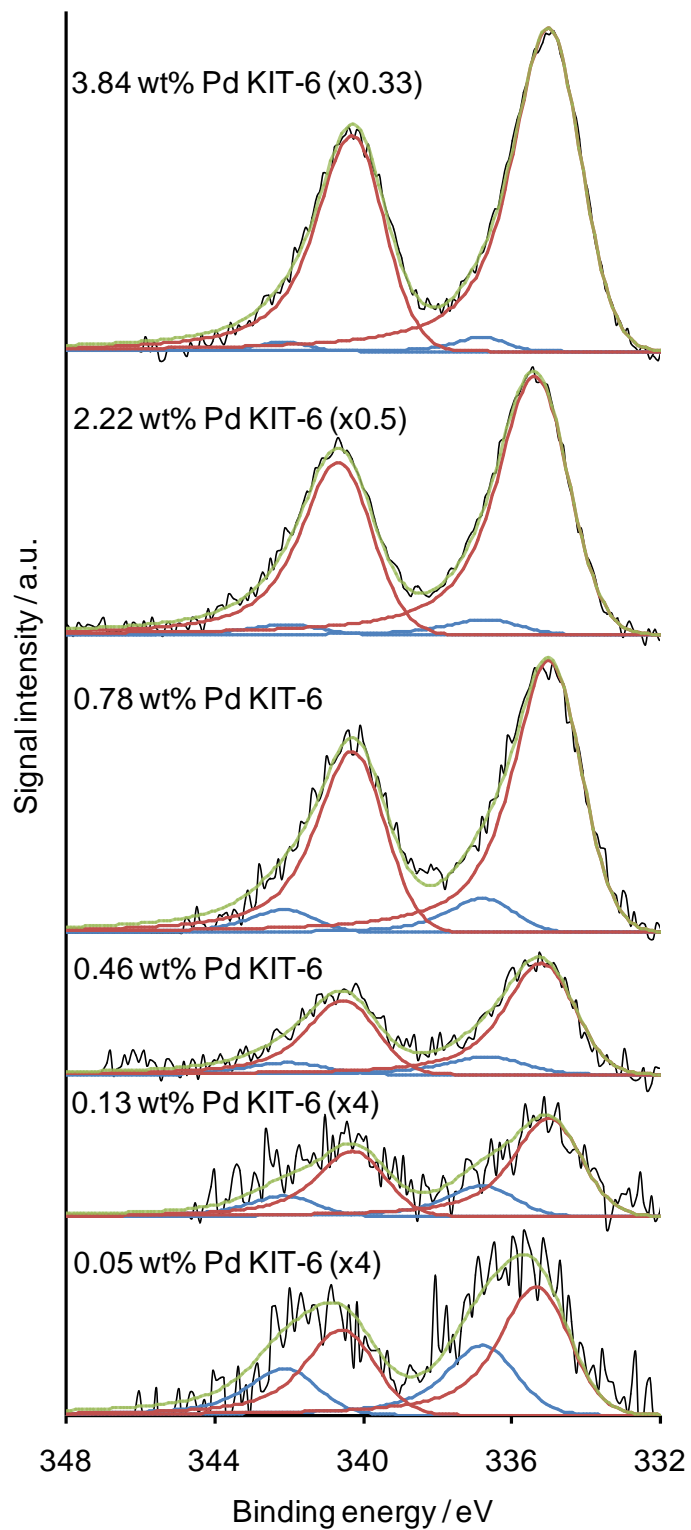


**Figure 3.16 (b)** - Stacked Pd 3d XPS plots of Pd/KIT-6 series

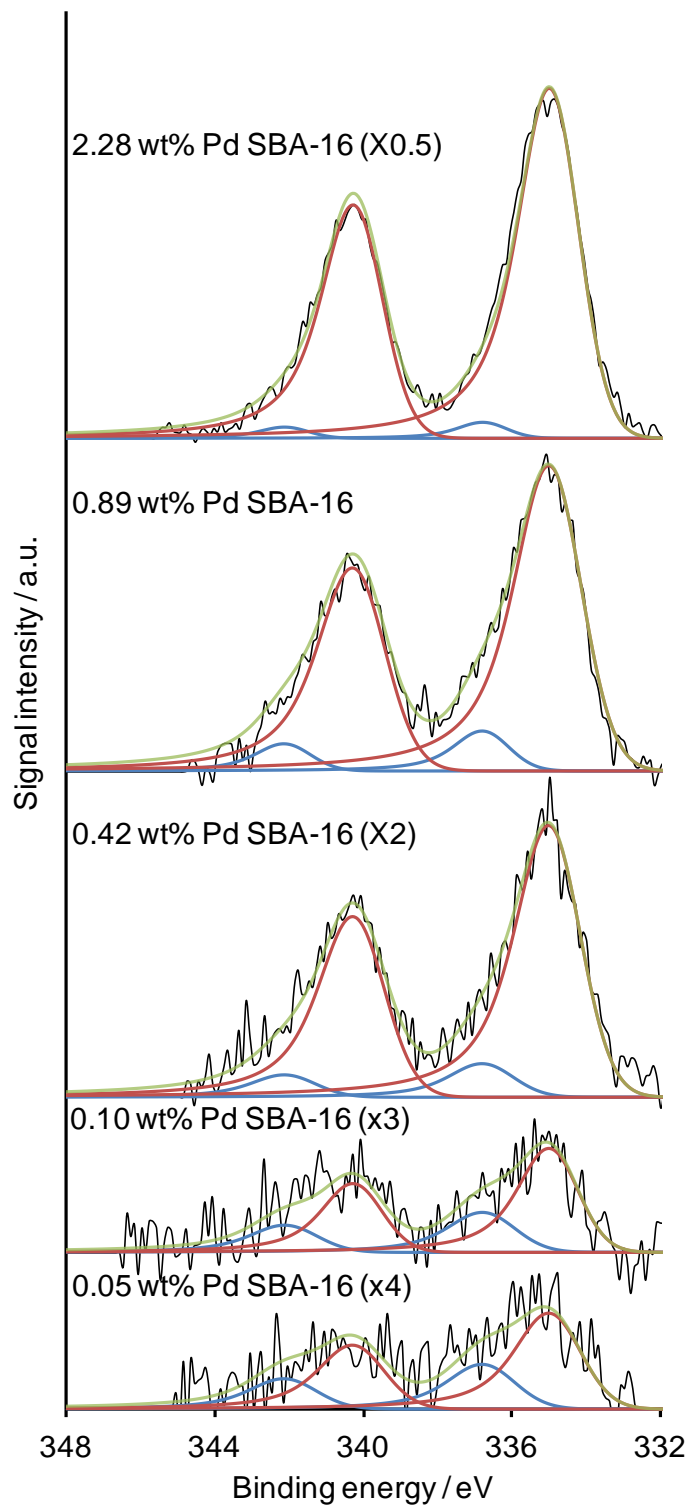
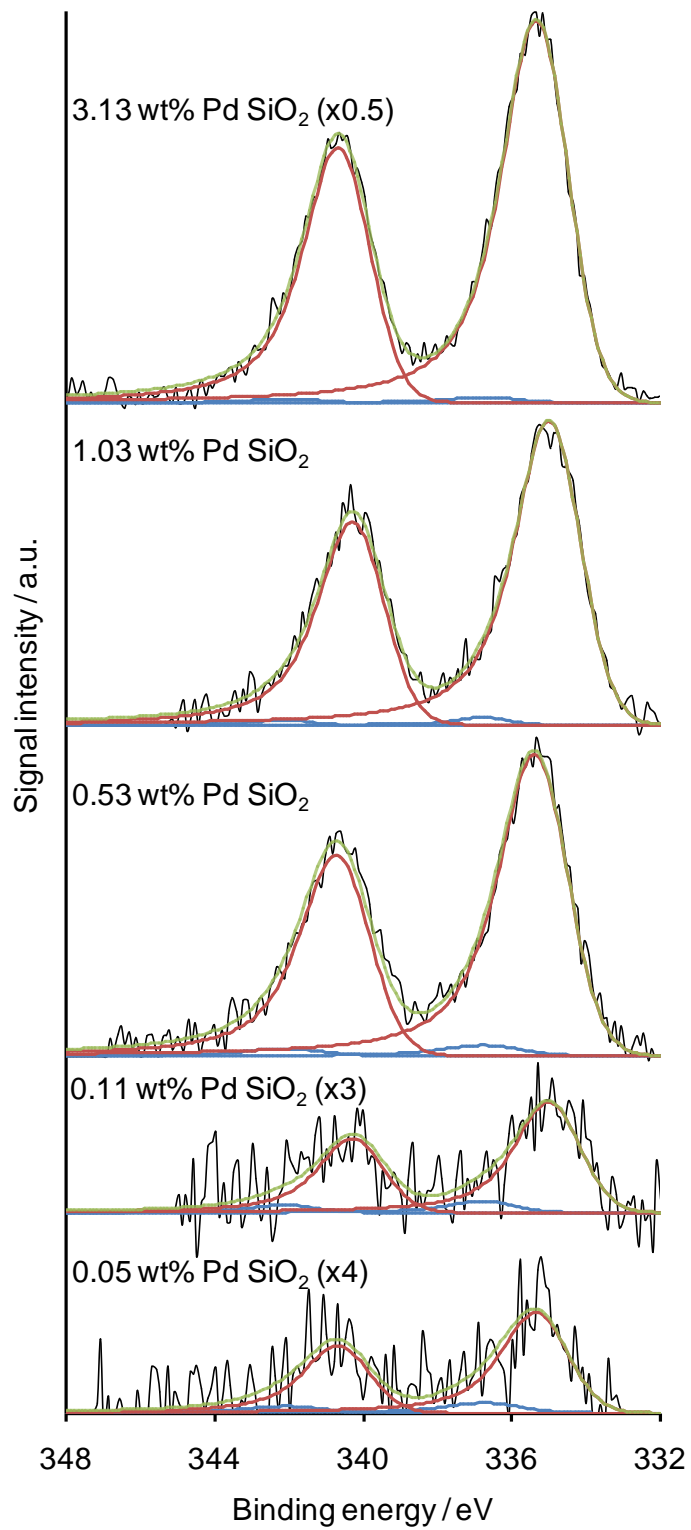
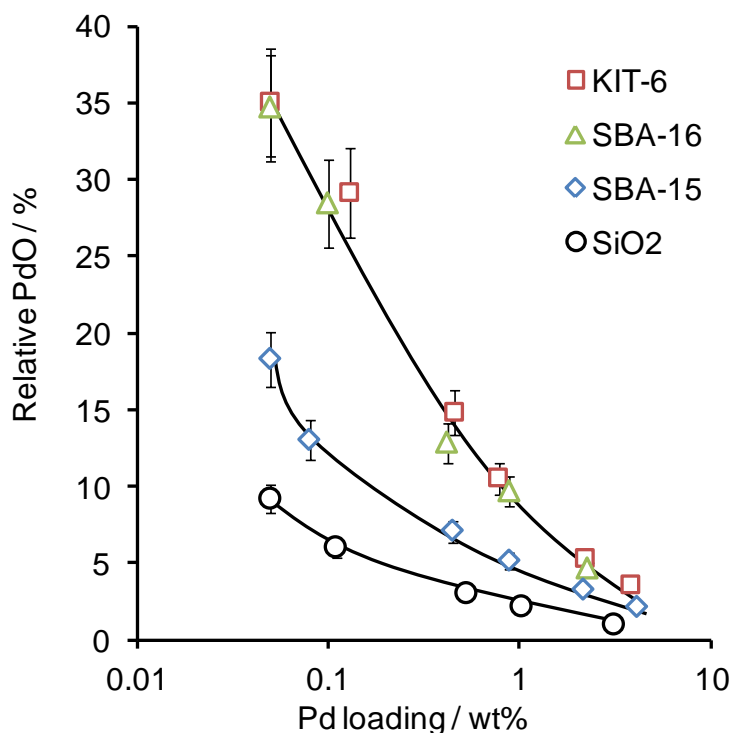


Figure 3.16 (c) - Stacked Pd 3d XPS plots of Pd/SBA-16 series



**Figure 3.16 (d)** - Stacked Pd 3d XPS plots of Pd/commercial silica series

**Figure 3.17** clearly shows that for all four catalyst families there is an inverse relationship between loading and oxide content, as previously reported for both commercial and self-prepared mesoporous alumina supports.<sup>4, 6</sup> This effect is greater for higher surface area supports and enhanced through the use of interconnected architectures. Such an observation is expected, since increasing the support surface area, and thus Pd dispersion, will drive a greater proportion of Pd atoms to adopt the lower surface energy PdO phase.



**Figure 3.17** –Surface PdO as a function of bulk Pd loading and support

The correlation between experimentally-derived surface PdO (from XPS) and Pd dispersion (from CO chemisorption) is confirmed by directly comparing the two, shown in **Figure 3.18**. A common trend is observed for all silica supports, evidencing a common (weak<sup>46</sup>) Pd-support interaction, with surface oxidation state determined solely by Pd particle size.

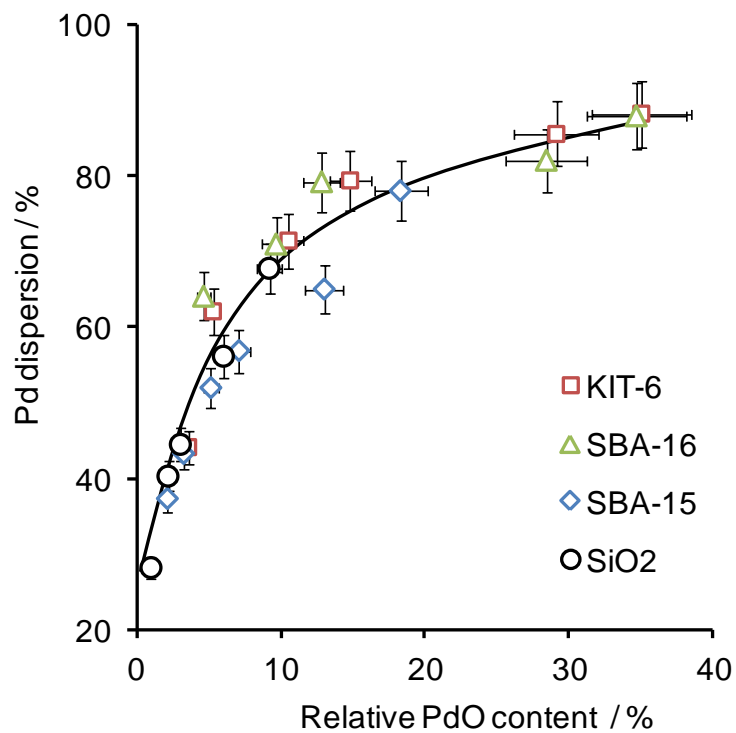


**Figure 3.18** - Relationship between surface PdO and metal dispersion

### 3.2.2.8 X-ray adsorption spectroscopy

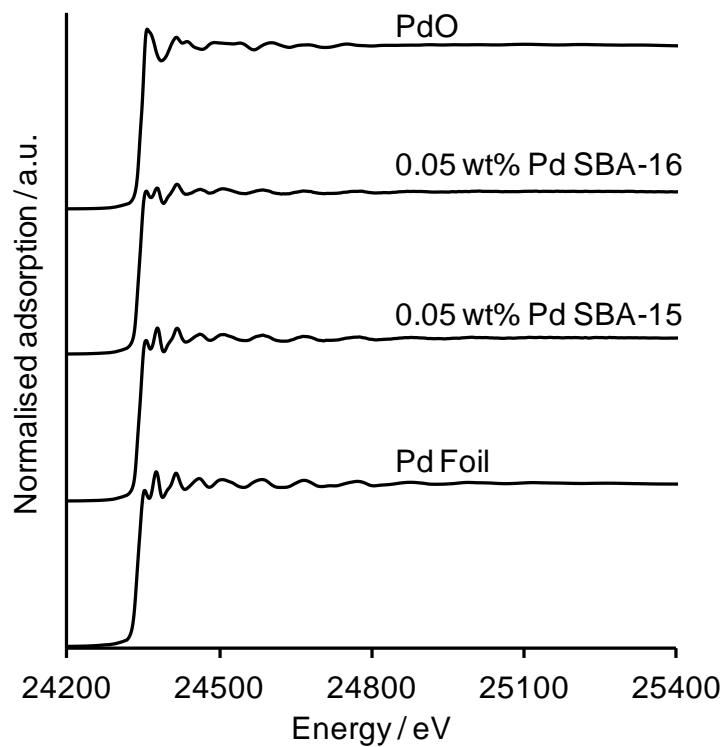


**Figure 3.19** – Stacked XAS normalised Pd K-edge spectra for 0.05 wt% Pd/SBA-16 and Pd/SBA-15

XAS was also utilised to investigate the local Pd properties, in particular low Pd loadings where alternative techniques are less suited. **Figure 3.19** displays the background subtracted Pd K-edge spectra for 0.05 wt% loadings on SBA-15 and SBA-16, along with Pd and PdO standards. These two samples are representative of those possessing the highest proportion of surface PdO (XPS), and smallest average particle sizes (CO chemisorption); recall the many structural similarities of Pd on both SBA-16 and KIT-6. From previous studies, of Pd/mesoporousAl<sub>2</sub>O<sub>3</sub>, activities are likely to be greatest for materials with lowest Pd loadings.<sup>6</sup>

The background subtracted Pd K-edge XANES regions indicate that the two samples are neither fully metallic nor oxidic, but a hybrid of the two. To quantify the oxide/metal contributions, linear combination fitting of the normalised XANES regions was performed. The resulting fits are shown in **Figure 3.20**. These yield overall (i.e. bulk and surface averaged) PdO contents of 34.8 and 17.8 % for SBA-16 and SBA-15 respectively, consistent with the surface sensitive XPS values.

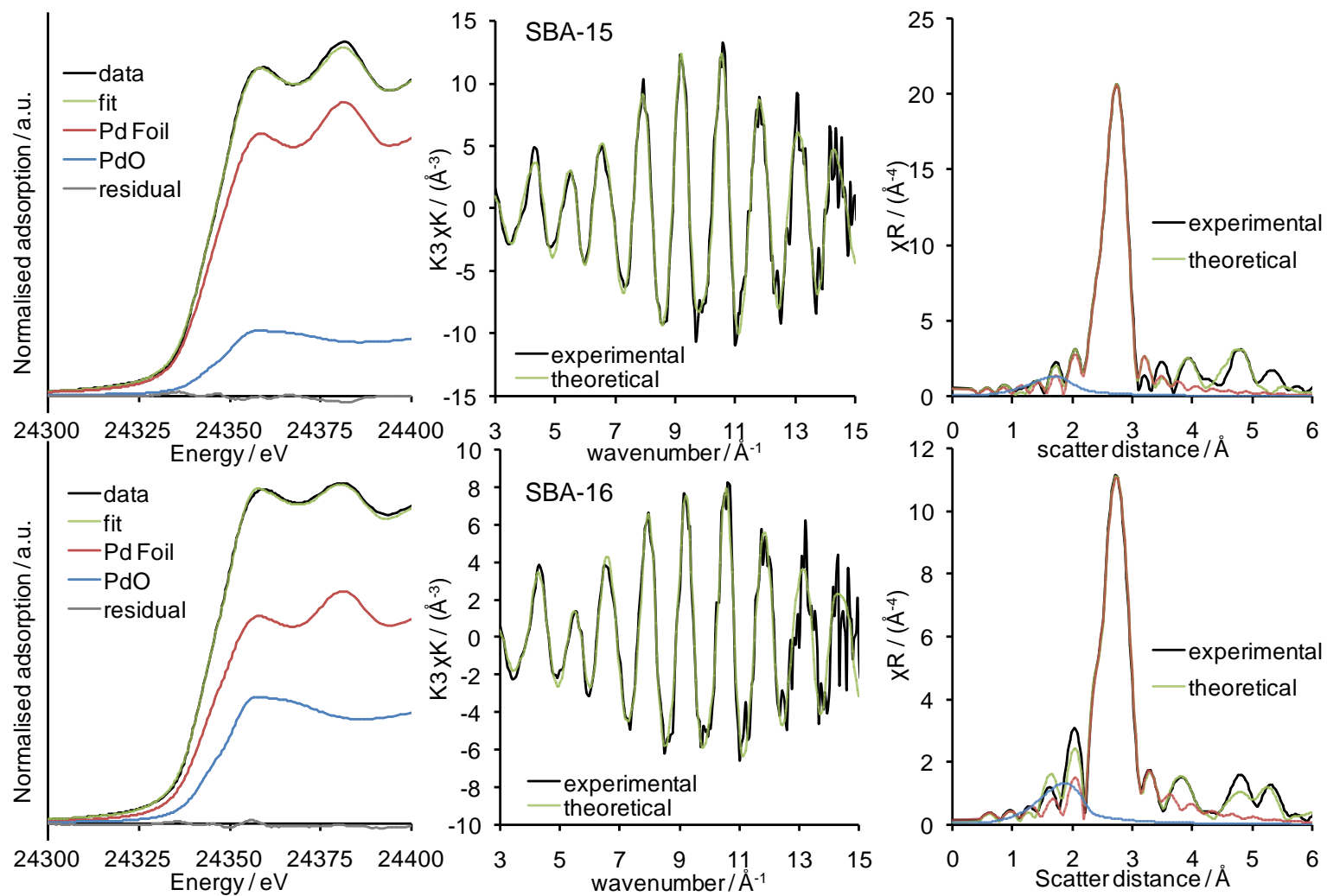


**Figure 3.20** –XANES fitting (left) and EXAFS  $K^3$  weighted data (centre) and Fourier transform data (right) fitting of 0.05 wt% Pd/SBA-15 (top) and SBA-16 (bottom)

The EXAFS regions of Pd foil and PdO standards were fitted to their respective  $Fm\bar{3}m$ <sup>47</sup> and  $P4_2/mmc$ <sup>48</sup> space groups. This enabled amplitude factors, interatomic distances of the neighbouring scatters (coordination shell distances), and Debye-Waller disorder factors to be determined, with the resulting values in **Table 3.6**. EXAFS fitting of the Pd/silica samples was to a model which incorporated the presence on both standards, with the relative contribution of both adjusted to vary between 0 % and 100 %, to obtain the most satisfactory fit. The resulting  $K^3$  weighted and Fourier transform fits are presented in **Figure 3.20**, with their corresponding coordination numbers, interatomic distance and Debye-Waller factors recorded in **Table 3.6**. The fitting revealed a metallic oxidic composite species for both (i.e. the nature of either sample was neither fully metallic nor oxidic), concurring with XANES fitting. Metallic Pd scattering species, which arise due to bulk Pd, are present up to the 2<sup>nd</sup> and 3<sup>rd</sup> coordination shells for the SBA-16 and SBA-15 samples respectively. The degree of Pd population within these shells, and of equal importance the 1<sup>st</sup> coordination shell, is significantly lower than the foil, suggesting small metallic Pd nanoparticles. Pd occupancy within these coordination shells decreases as support morphology changes from non-interconnecting SBA-15 to the interlinked architecture of SBA-16 (further evidence of a decreased Pd particle size on SBA-16 over SBA-15). PdO scattering species are detected solely in the 1<sup>st</sup> coordination shell, with the lack of oxide scatters in further coordination shells (2<sup>nd</sup> and 3<sup>rd</sup> shells) revealing a size limited PdO phase. Therefore the possibility of a second, less abundant, bulk PdO phase is ruled out. These observations being consistent for the presence of small Pd clusters with a metallic core coated in a surface oxide shell. The level PdO scatters increase as support is changed from SBA-15 to SBA-16 (a greater PdO abundance) consistent with a decreasing core shell Pd nanoparticle size, which in turn induces an increase in PdO shell to metallic core ratio.

Average Pd particle size can be deduced from the 1<sup>st</sup> shell coordination number using the method of Jentys.<sup>49</sup> Assuming an equal ratio of (100):(110):(111) facets and a spherical particle shape average Pd particle sizes of 0.8 nm and 1.4 nm are determined for SBA-16 and SBA-15 respectively, which are clearly consistent with alternative techniques.

**Table 3.6** - Pd K-edge EXAFS fitting parameters

<i>Sample</i>	<i>CN1 Pd-Pd</i>	<i>CN2 Pd-Pd</i>	<i>CN3 Pd-Pd</i>	<i>CN4 Pd-Pd</i>	<i>CN1 Pd-O</i>	<i>Amplitude Factor</i>
<i>Pd Foil</i>	12	6	24	12	-	0.8953
<i>0.05 wt% Pd/SBA-15</i>	8.05(±1.50)	2.84(±1.81)	1.72(±2.65)	0	0.93(±1.52)	0.8953/0.6013
<i>0.05 wt% Pd/SBA-16</i>	5.29(±0.97)	1.90(±4.98)	0	0	1.96(±1.48)	0.8953/0.6013
<i>PdO</i>	2	-	-	-	4	0.6013

<i>Sample</i>	<i>R1 Pd-Pd</i>	<i>R2 Pd-Pd</i>	<i>R3 Pd-Pd</i>	<i>R4 Pd-Pd</i>	<i>R1 Pd-O</i>
<i>Pd Foil</i>	2.742	3.878	4.75	5.485	-
<i>0.05 wt% Pd/SBA-15</i>	2.743	3.880	4.751	-	2.012
<i>0.05 wt% Pd/SBA-16</i>	2.743	3.879	-	-	2.012
<i>PdO</i>	2.665	-	-	-	2.030

<i>Sample</i>	<i>σ1 Pd-Pd</i>	<i>σ2 Pd-Pd</i>	<i>σ3 Pd-Pd</i>	<i>σ4 Pd-Pd</i>	<i>σ1 Pd-O</i>	<i>R- Factor %</i>
<i>Pd Foil</i>	0.0052(±0.0003)	0.0096(±0.0027)	0.0055(±0.0003)	0.017(±0.0138)	-	1.86
<i>0.05 wt% Pd/SBA-15</i>	0.0059(±0.0005)	0.0099(±0.0027)	0.0066(±0.0003)	-	0.0089(±0.0019)	3.79
<i>0.05 wt% Pd/SBA-16</i>	0.0063(±0.0009)	0.0109(±0.0013)	-	-	0.0089(±0.0042)	2.78
<i>PdO</i>	0.0062(±0.0003)	-	-	-	0.0015(±0.0010)	1.62

CN = Co-ordination number    R = Interatomic distance from central Pd atom    σ = Debye-Waller factor (accounts for disorder such as thermal disorder in the structure. Lower number = greater order) R-Factor = residual difference between experimental data and theoretical fit

### 3.2.3 Allylic alcohol selox

The selox chemistry of two allylic alcohols were explored. Common reaction conditions of 8.4 mmol alcohol, 10 cm<sup>3</sup> toluene and mesitylene internal standard at 90 °C, were used unless otherwise stated. For full details see **Chapter 2**.

#### 3.2.3.1 Crotyl alcohol selox

Crotyl alcohol (C<sub>4</sub>H<sub>8</sub>O **Chapter 1 Figure 1.1**), was initially investigated as a simple allylic alcohol.

In order that intrinsic reaction kinetics were measured in the absence of external mass-transfer limitations (reactant/product diffusion across either the gas-liquid interface or liquid-solid boundary layer of silica particles) the influence of mixing speed on activity was studied. Representative 1 wt% Pd/silicas were used to determine the optimum stirrer speed for subsequent quantitative evaluation of support effects. The results are presented in **Figure 3.21**.

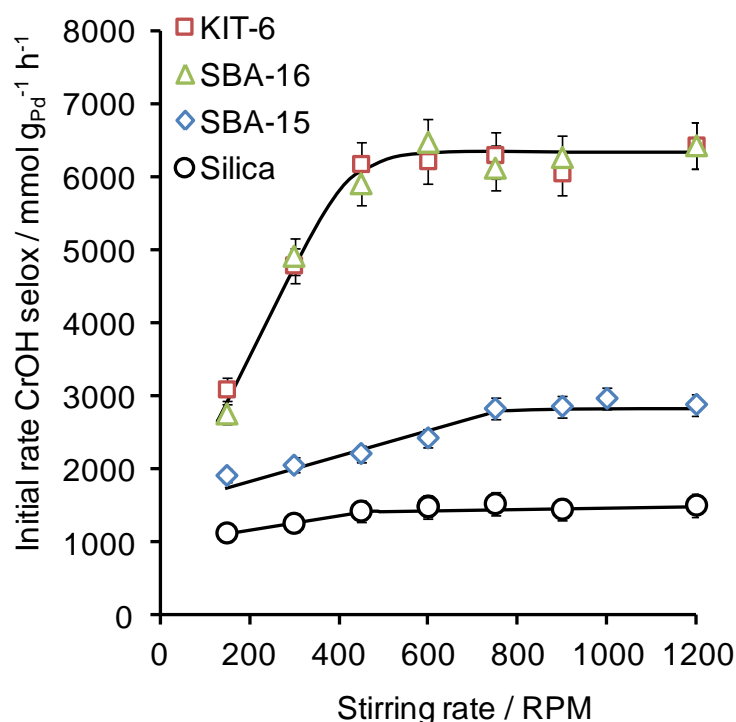


**Figure 3.21** – Effect stirring rate on crotyl alcohol normalised initial rate over approximate 1 wt% metal loading on various silica supports

In all cases, mixing speeds >1000 rpm were sufficient to eliminate external mass transport, which is likely dominated by O<sub>2</sub> solubilisation under our mild conditions (Air atmosphere). Having established an efficient mixing regime, striking differences emerge between the inherent activities of the four distinct Pd/silica catalysts, with Pd/SBA-16 and Pd/KIT-6 giving maximal rates 2-3 times those of Pd/SBA-15, which in turn exhibits a similar magnitude enhancement over the amorphous Pd/SiO<sub>2</sub> catalyst. The relative selox activities are thus intimately linked to support surface area and furthermore the degree of mesopore connectivity (and corresponding Pd dispersion/oxidation state). The latter being in line with previous studies demonstrating the benefits of employing interconnected pore architectures in heterogeneous catalysis.<sup>13, 35, 50-52</sup> As an aside, it is interesting to note that external mass transport to Pd/SBA-16, Pd/KIT-6 and Pd/SiO<sub>2</sub> catalysts is enhanced over Pd/SBA-15, with a maximum constant activity attained at lower stirring speeds (~400-600 rpm for the former versus 800-900 rpm for the latter). The origin of this is not yet understood and may arise from differing surface polarity or roughness.

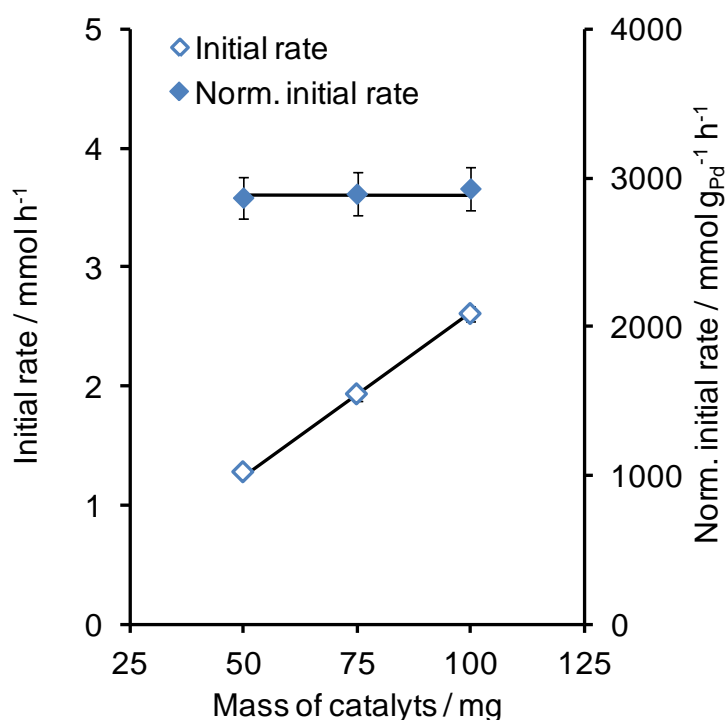


**Figure 3.22** - Influence of catalyst:substrate ratio on crotyl alcohol selox initial rate over 0.89 wt% Pd/SBA-15 at 900rpm

Confirmation that reaction kinetics were measured in the absence of bulk diffusion limitations was obtained by varying the catalyst:substrate ratio. Normalised initial rates were independent of the amount of catalyst for crotyl alcohol selox over 0.89 wt% Pd/SBA-15, as depicted in **Figure 3.22**,<sup>53</sup> confirming the reaction rates are not limited by mixing characteristics.

**Figure 3.23** shows the reaction profiles for all four catalyst series, operating under established bulk mass transfer free conditions for each support.

All catalysts were active for crotyl alcohol selox, with conversions increases with metal loadings. For all catalysts, conversion over the 1<sup>st</sup> 30-40 minutes increased linearly, slowing subsequently (and well before complete conversion was attained), indicating on-stream deactivation.

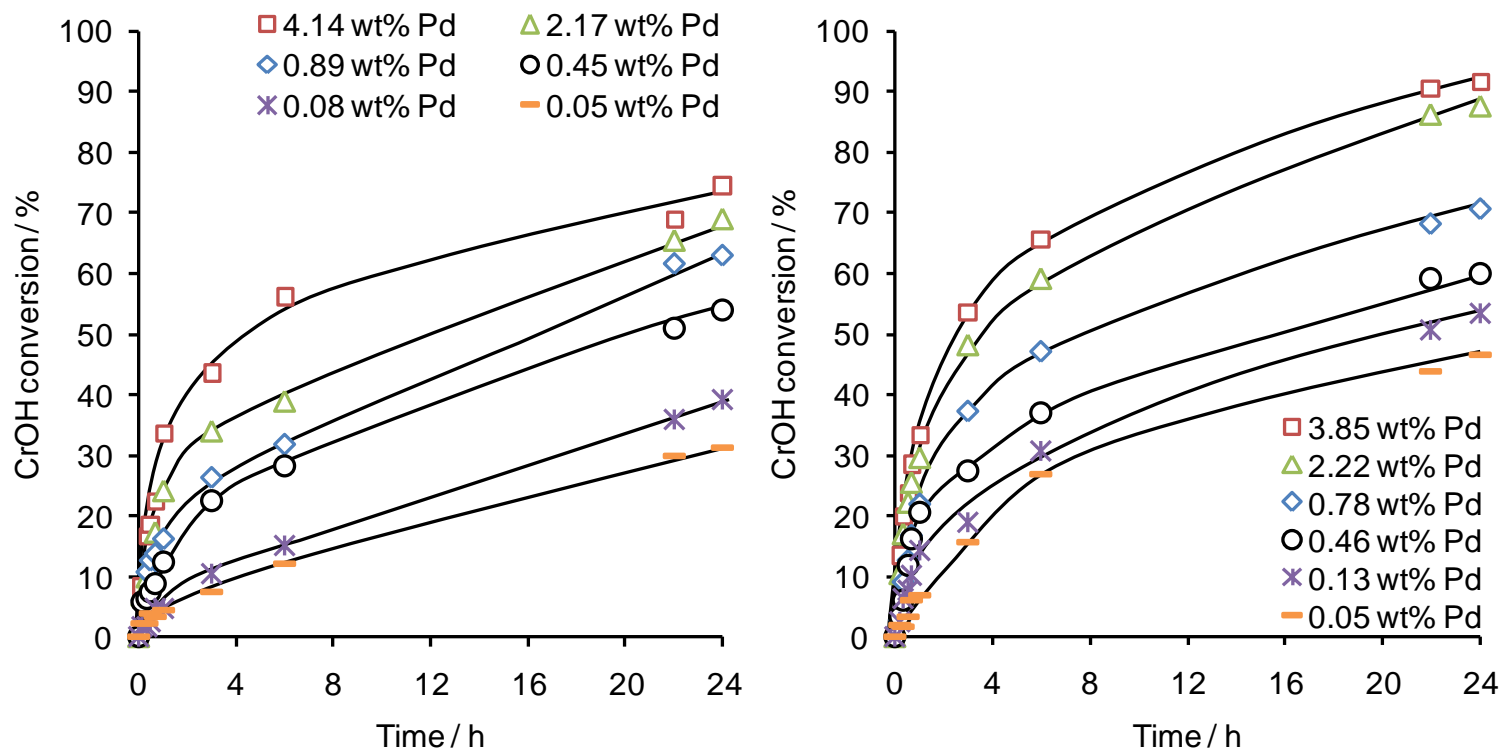


**Figure 3.23 (a)** – Crotyl alcohol reaction profiles for SBA-15 (left) and KIT-6 (right) series

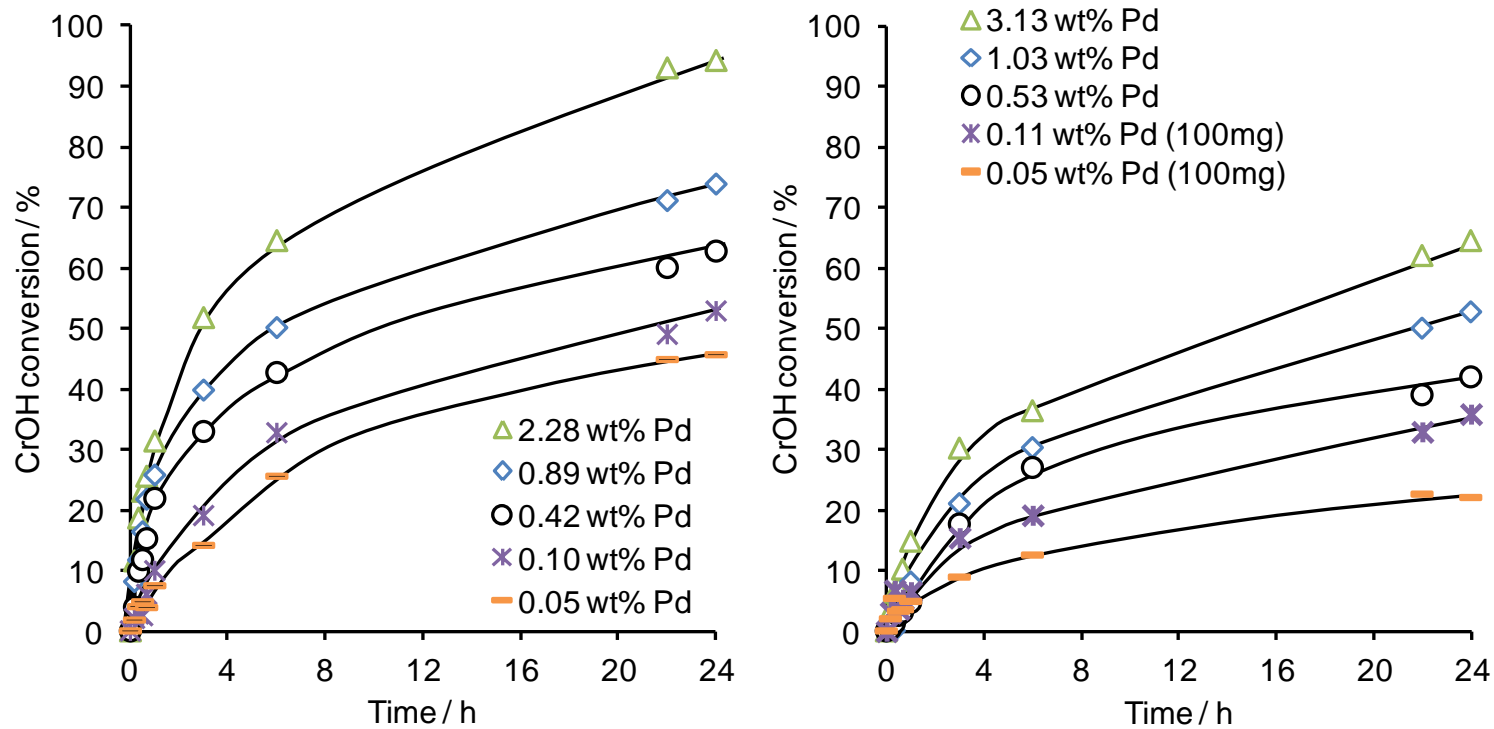


**Figure 3.23 (b)** – Crotyl alcohol reaction profiles for SBA-16 (left) and commercial silica (right) series

The initial rates, derived from the initial linear regime (conversions below 40 %) normalised to the mass of Pd, are shown in **Figure 3.24**. Mass balances here remain above 95 % demonstrating negligible evaporation or reactant/product adsorption.

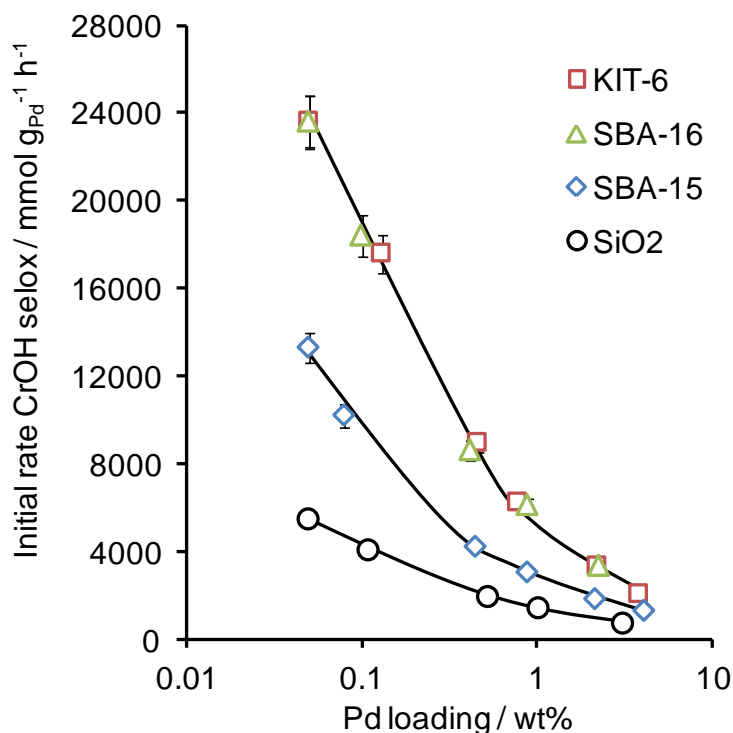


**Figure 3.24** - Dependence of crotyl alcohol aerobic selox activity on bulk Pd loading and silica supports

A striking inverse correlation between activity and metal loading emerges, in accordance with previous reports of supported Pd nanoparticles in allylic and benzyl alcohol selox.<sup>3, 4, 6, 54</sup> Pd dispersion, and thus particle size, is clearly critical in regulating selox activity. While the actual particle size differences across the 0.05-1 wt% loading range for all catalyst families, is relatively small, refer to **Table 3.4** for accurate values, its effect is dramatic, reflecting the rapidly evolving electronic and geometric properties of Pd nanoparticles between ~1-3 nm. For example, the increase in particle size from 1.3 nm to 2.5 nm observed for the KIT-6 family between 0.13-3.84 wt% Pd, represents an increase in cluster size from ~55 to 429 Pd atoms.<sup>49</sup> This in turn would represent a redistribution in the proportion of low coordination atoms (defined as those possessing  $\leq 6$  nearest neighbours) from 55 % to 11 % of all Pd atoms within individual nanoparticles, assuming they exhibited

spherical morphologies. Selox activity is also a strong function of silica support, increasing from  $\sim 6,000 \text{ mmol.g}_{\text{Pd}}^{-1}.\text{h}^{-1}$  over the best commercial low area Pd/SiO<sub>2</sub>, to  $\sim 14,000 \text{ mmol.g}_{\text{Pd}}^{-1}.\text{h}^{-1}$  over the analogous high area mesoporous Pd/SBA-15, and reaching  $\sim 24,000 \text{ mmol.g}_{\text{Pd}}^{-1}.\text{h}^{-1}$  for the interconnected mesoporous Pd/SBA-16 and Pd/KIT-6 variants. Hence support surface area and mesopore architecture both play an important role in controlling selox performance, with (interconnected) mesopores promoting conversion via either improved in-pore diffusion to the active site *or* by increasing the number of such sites.

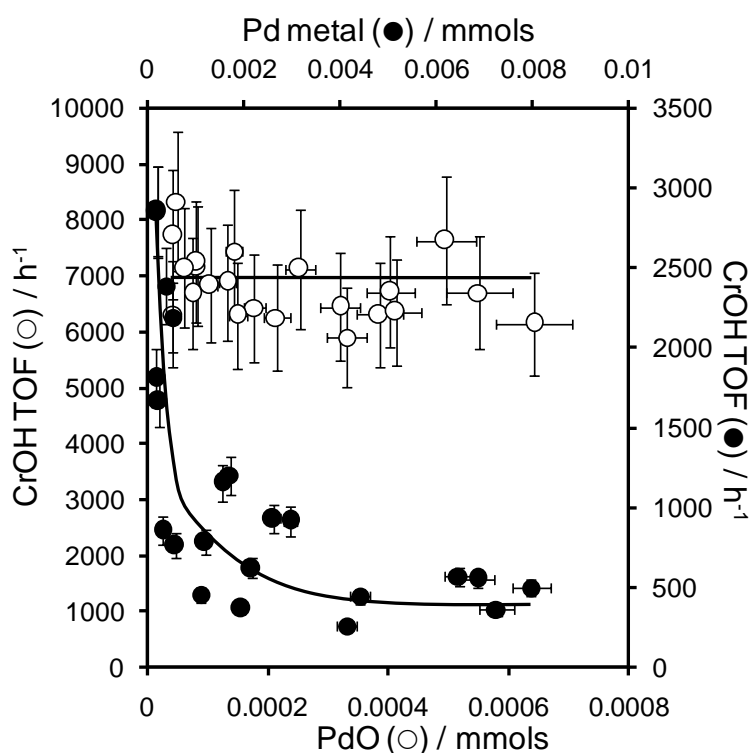


**Figure 3.25** - Crotyl alcohol aerobic selox turnover frequencies as a function of surface PdO or Pd metal content for Pd/SiO<sub>2</sub>, Pd/SBA-15, Pd/SBA-16 and Pd/KIT-6 catalysts.

In order to explore which of these factors is most influential, and to shed insight on the nature of the active Pd species responsible for crotyl selox, TOFs were subsequently calculated for the entire family of twenty two Pd/silica catalysts. The active site in Pd catalysed alcohol selox has been postulated as either Pd(0)<sup>1, 55</sup> or Pd(II),<sup>3-7</sup> the latter proposed as a possible precursor to Pd(0) via in-situ reduction.<sup>55</sup> TOFs were therefore derived for each scenario, by normalising the initial rates to the

concentration of either (i) surface PdO in the as-prepared catalysts (XPS), or (ii) the total surface Pd metal attainable upon reduction (CO chemisorption), and appear in **Figure 3.25**. If crotyl alcohol selox initial activity is solely controlled by the surface density of either Pd species, then the resulting TOF should be constant as activity (i.e. initial rate) is only proportional to the number of such sites. Conversely, if multiple active sites, or in-pore diffusion, are responsible, then complex interdependent interactions between these will result in a fluctuating TOF.

A constant TOF of  $7000 \text{ h}^{-1}$  results from normalisation to surface PdO, while a continuously decaying TOF is obtained from Pd metal. This provides definitive evidence that surface PdO is the catalytic active species for crotyl alcohol selox over Pd/silicas under our mild conditions, as proposed for Pd/aluminas.<sup>3, 6, 7</sup> The invariance of TOF on surface PdO content also indicates the absence of in-pore diffusion restrictions, i.e. the initial rates are solely dependent on the amount of oxide decorating Pd nanoparticles, and not the pore architecture they are confined in. We therefore propose that rate-enhancements on switching supports (SiO<sub>2</sub> to SBA-15 to SBA-16/KIT-6) arise from the stabilisation of more PdO sites, and not improved alcohol diffusion through the support.

Catalyst selectivity towards the desired allylic aldehyde was also investigated. During the 1<sup>st</sup> 40 minutes of reaction, where mass balances are high, selectivity towards crotonaldehyde is ~65 % over all Pd/silicas, with butanal the only other observed product. After the 1<sup>st</sup> hour of reaction, the mass balance falls, eventually to around 70-75 % after 24 hours. Evaporation of both products and starting material may contribute to this low mass balance, however dehydration/decarbonylation side reactions can also occur over Pd, resulting in the formation of gaseous products e.g. butane, propene, carbon monoxide and carbon dioxide,<sup>5, 7</sup> that could not be detected by GC analysis of the liquid phase. In order to reduce evaporation issues, cinnamyl alcohol, the aromatic analogue of crotyl alcohol was also studied in selox.<sup>2</sup>

### 3.2.3.2 Cinnamyl alcohol selox

The effect of stirring rate on cinnamyl alcohol (C<sub>9</sub>H<sub>10</sub>O, **Chapter 1 Figure 1.1**) selox was examined, comparably to crotyl alcohol, in order to confirm conditions which allow intrinsic reaction kinetics to be measured were possible. The results from studies over ~2.5 wt% Pd/silicas are presented in **Figure 3.26**.

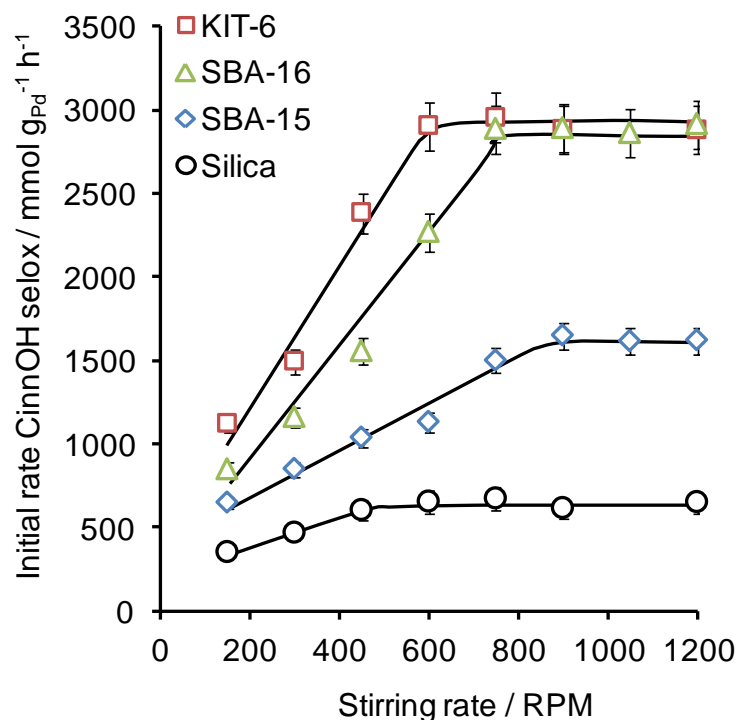


**Figure 3.26** - Effect stirring rate on cinnamyl alcohol normalised initial rate over approximate 2.5 wt% metal loading on various silica supports

Again, mixing speeds >1000 rpm were sufficient to eliminate external mass transport, strengthening the likelihood of O<sub>2</sub> solubilisation are dominating this reaction parameter under our mild conditions. As for crotyl alcohol, under efficient agitation, striking differences in the inherent activities of the four catalysts are apparent. Pd/SBA-16 and Pd/KIT-6 return a two-fold increase relative to Pd/SBA-15, which itself displays a similar elevation over the amorphous Pd/SiO<sub>2</sub> catalyst. Relative activities are once more dependent on support surface area and the degree of mesopore connectivity (and corresponding Pd dispersion/oxidation state). Slower oxidation of cinnamyl versus crotyl alcohol, likewise observed over Pd/Al<sub>2</sub>O<sub>3</sub>,<sup>6</sup> may reflect either more sluggish in-pore molecular diffusion due to its heavier molecular mass, a greater adsorption 'footprint', or a higher activation barrier to rate-determining O-H/C-H cleavage. In the case of cinnamyl alcohol selox, Pd/KIT-6 slightly outperforms Pd/SBA-16, which may reflect the narrower "ink bottle" pore opening of the latter.<sup>10, 56</sup> Concurring with the crotyl alcohol investigation is the lower external mass transport to Pd/SBA-16, Pd/KIT-6 and Pd/SiO<sub>2</sub> catalysts over Pd/SBA-15, although this sheds no further light on the origin of this.

Evidence for the absence of bulk diffusion limitations, at the plateau region, was strengthened by studying O<sub>2</sub> flow rate through the reactor. Normalised initial rates, **Figure 3.27**, are independent of this variable over the 0.46 wt% Pd/KIT-6 catalyst.

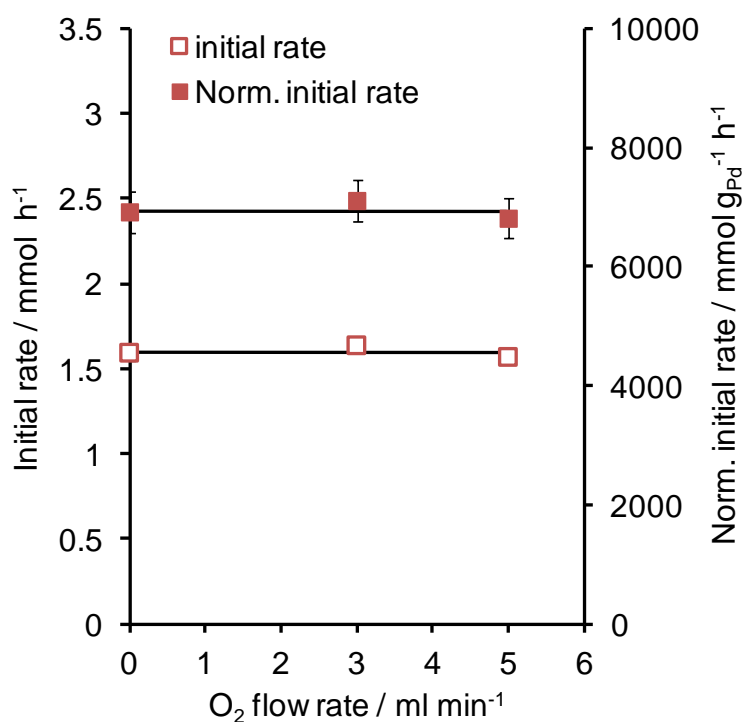


**Figure 3.27** - Influence of O<sub>2</sub> flow rate on cinnamyl alcohol initial reaction rate over 0.46 wt% Pd/KIT-6 at 900rpm

In order to test the solubility of Pd, and thus any possible homogeneous contributions to the observed catalysis, a hot filtration test was instigated for the approximately 0.5 wt% Pd loading Pd/silicas. Filtration of the reaction solution at reaction temperature minimises potential re-adsorption of any dissolved Pd back onto the support.<sup>57</sup> If the reaction is truly heterogeneous, i.e. no Pd leaching occurs, then the filtered reaction solution should subsequently exhibit no activity. **Figure 3.28** shows the results of such a test. Catalyst removal by hot filtration immediately stops further alcohol conversion, confirming a purely heterogeneous reaction pathway. AAS analysis of the hot filtrate validates this. With a Pd detection limit of 0.1 ppm, corresponding to loss of ~0.5 % of the total metal content of the chosen Pd/silicas, no leached Pd was detectable. The deactivation observed beyond the 1<sup>st</sup> hour of reaction cannot thus be attributed to Pd dissolution.

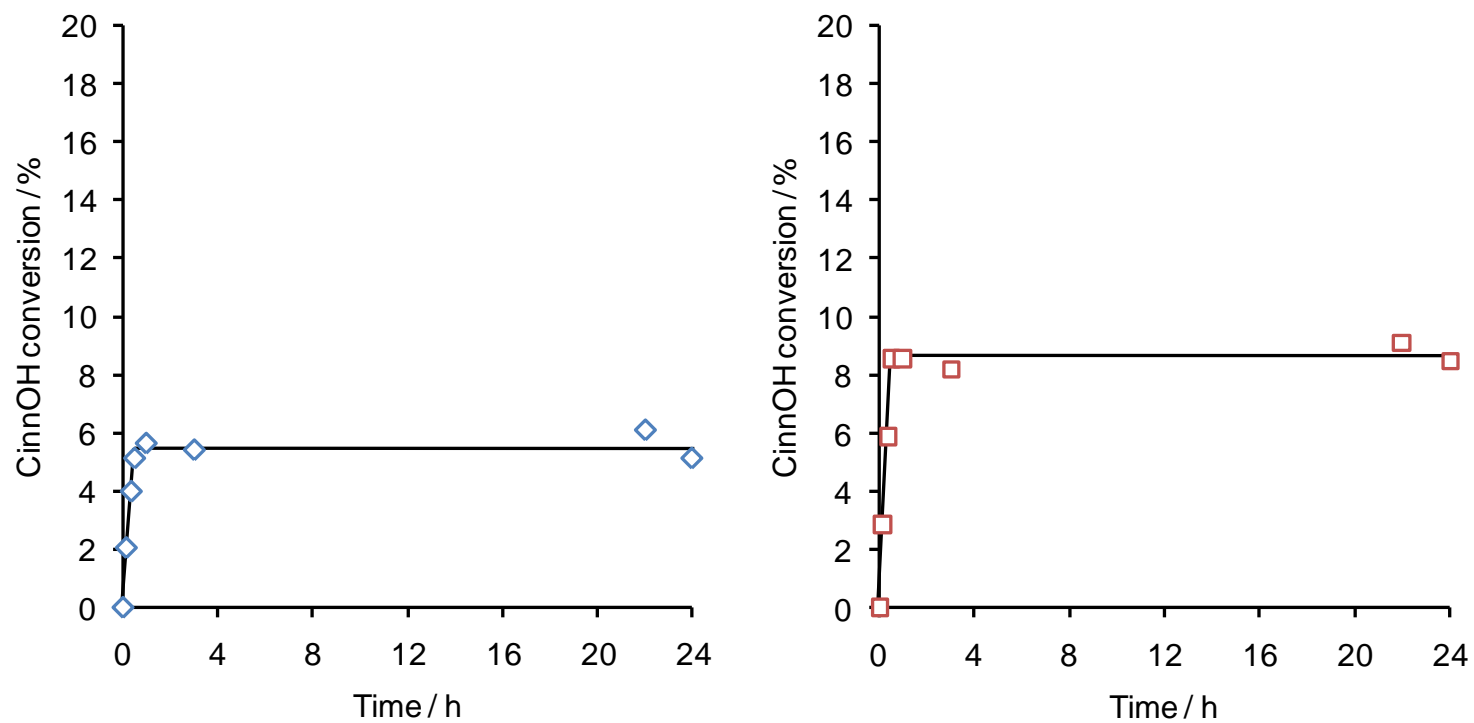


**Figure 3.28 (a)** – Hot filtration tests to assess Pd leaching in cinnamyl alcohol selox over (left) 0.45 wt% Pd/SBA-15 and (right) 0.46 wt% Pd/KIT-6 (catalyst removed after 30 minutes)

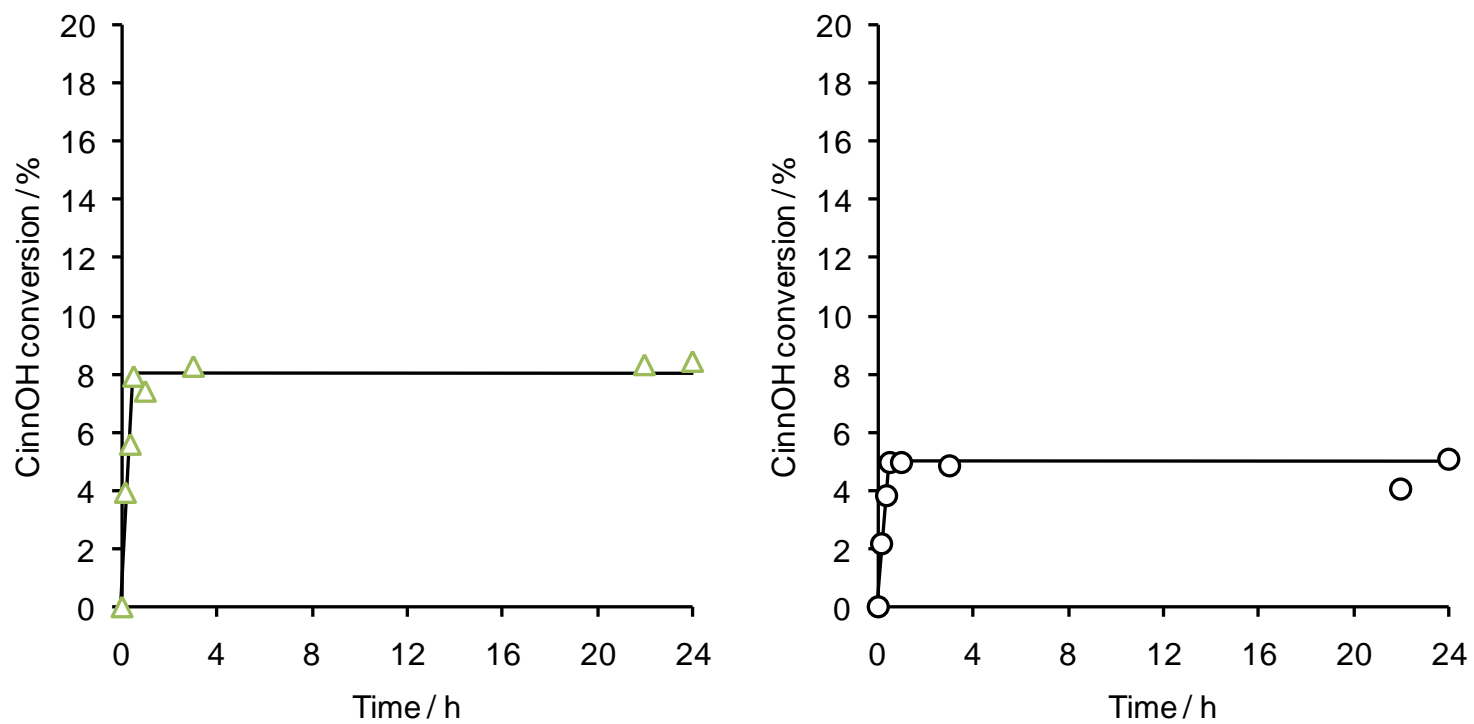


**Figure 3.28 (b)** – Hot filtration tests to assess Pd leaching in cinnamyl alcohol selox over (left) 0.42 wt% Pd/SBA-16 and (right) 0.53 wt% Pd/commercial silica (catalyst removed after 30 minutes)

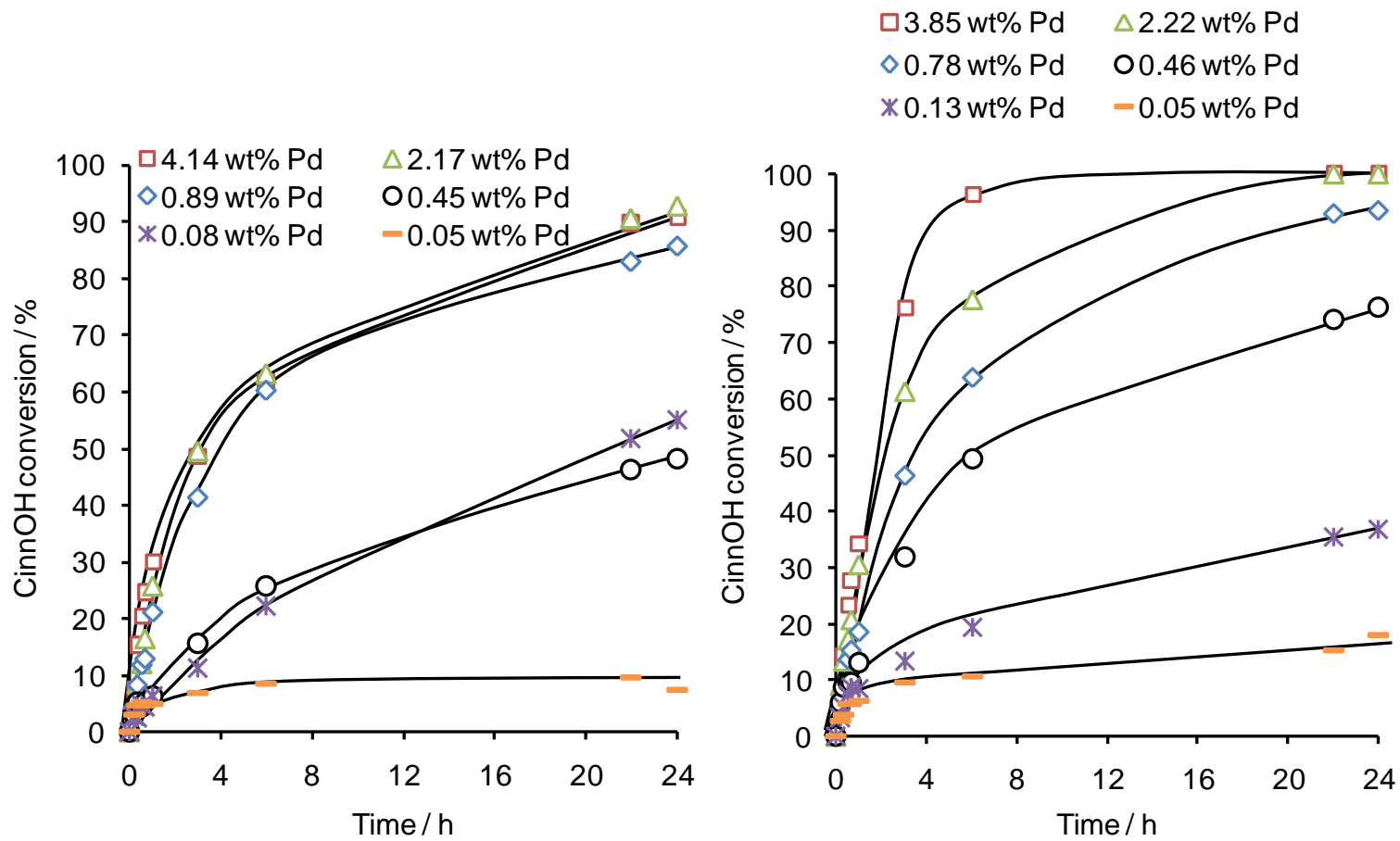


**Figure 3.29 (a)** – Cinnamyl alcohol reaction profiles for SBA-15 (left) and KIT-6 (right) series

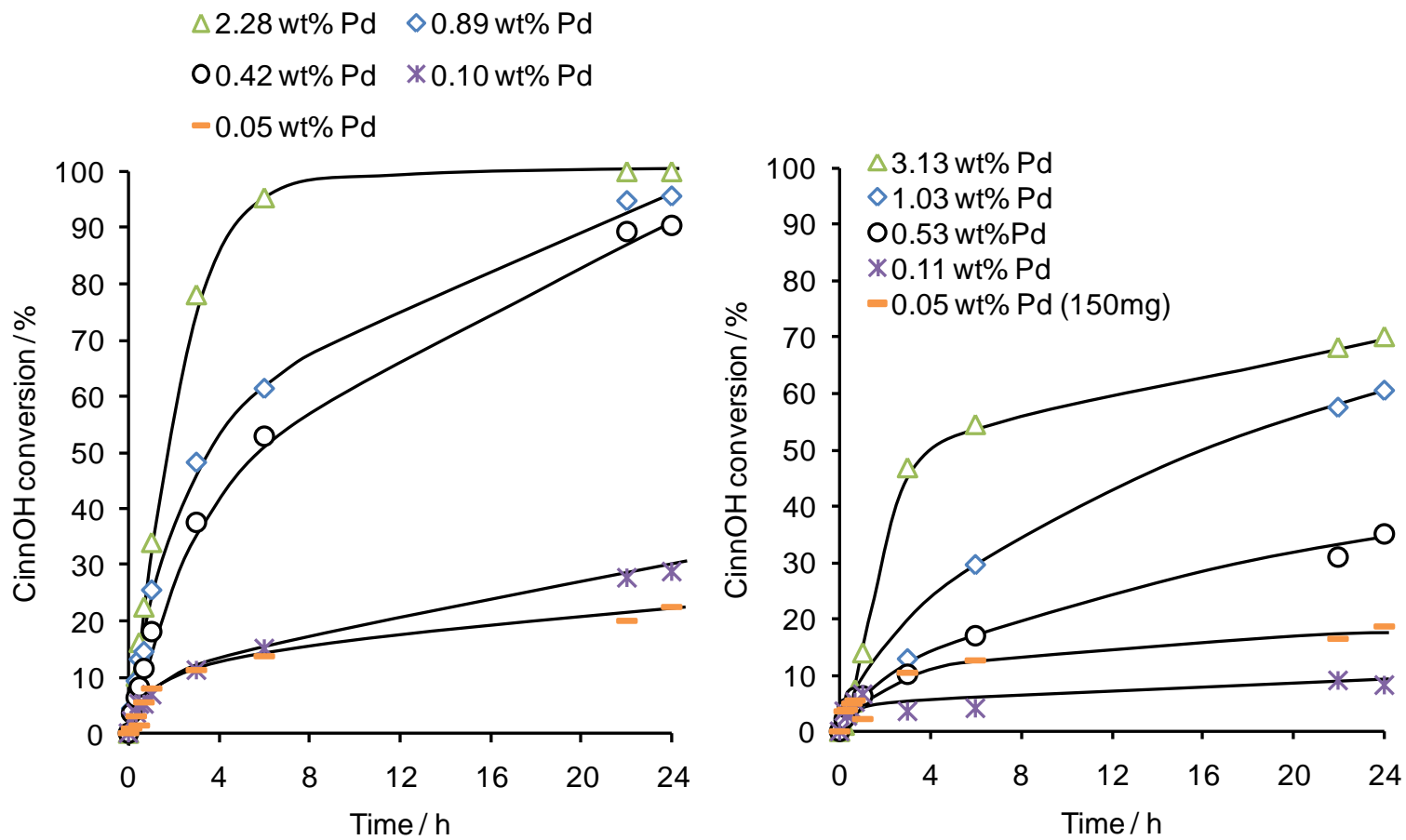


**Figure 3.29 (b)** – Cinnamyl alcohol reaction profiles for SBA-16 (left) and commercial silica (right) series

Cinnamyl alcohol selox reaction profiles, operating under the established non mass transfer limited conditions, for the four series are presented in **Figure 3.29**.

All of the Pd/silicas are active towards cinnamyl alcohol selox, and show similar trends to crotyl alcohol selox regarding increasing conversion with metal loading, and a linear rise in conversion over the 1<sup>st</sup> 30-40 minutes of reaction. Mass balance calculations were greater than 98 % during the 1<sup>st</sup> hour, and remained above 94 % even after 24 hours; once again deactivation after the 1<sup>st</sup> hour of reaction is apparent.

Initial rates, from the linear region over the initial 30 minutes of the reaction, normalised to Pd loading are shown in **Figure 3.30**.

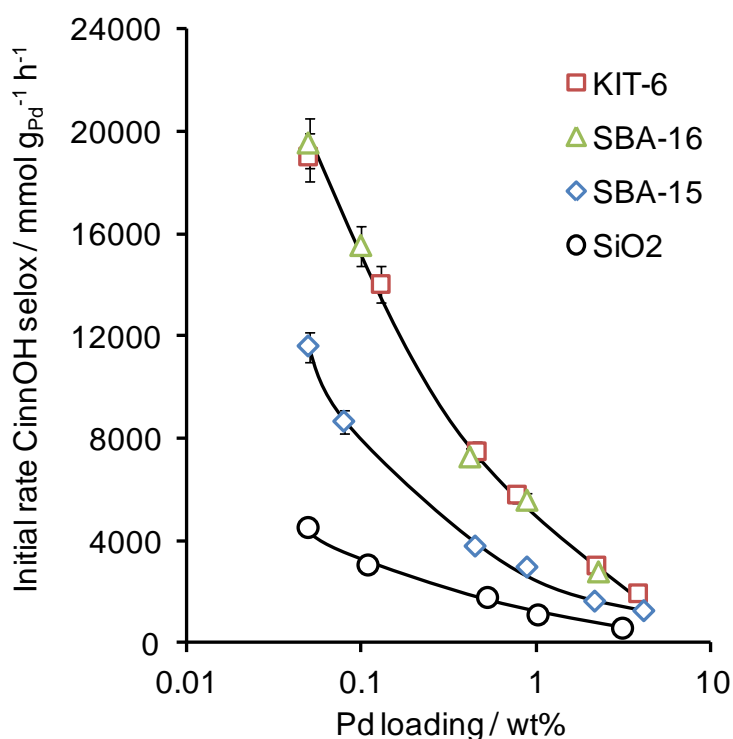


**Figure 3.30** - Dependence of cinnamyl alcohol aerobic selox activity on bulk Pd loading and silica supports

As for crotyl alcohol, and previous reports,<sup>3, 4, 6, 54</sup> a clear inverse correlation between activity and metal loading emerges reinforcing the bearing that Pd dispersion, and thus particle size, has on selox activity. Furthermore, the strong correlation between selox activity and silica support surface area and mesopore architecture is underpinned, with the enhancement again arising from interconnected

supports offering enhanced in-pore diffusion to the active site *or* elevated concentrations of the active site. In line with the external mass transfer investigation, relative to crotyl alcohol the absolute values decrease.

To further strengthen the conclusion that true intrinsic reaction kinetics had been measured, the relative initial rates for both alcohols were compared for all Pd/silica. **Figure 3.31** reveals crotyl alcohol selox is consistently ~20 % faster. This constant result, across the four varying supports, suggests true reaction-rate limited kinetics are being measured, without varying in-pore diffusion limitations.

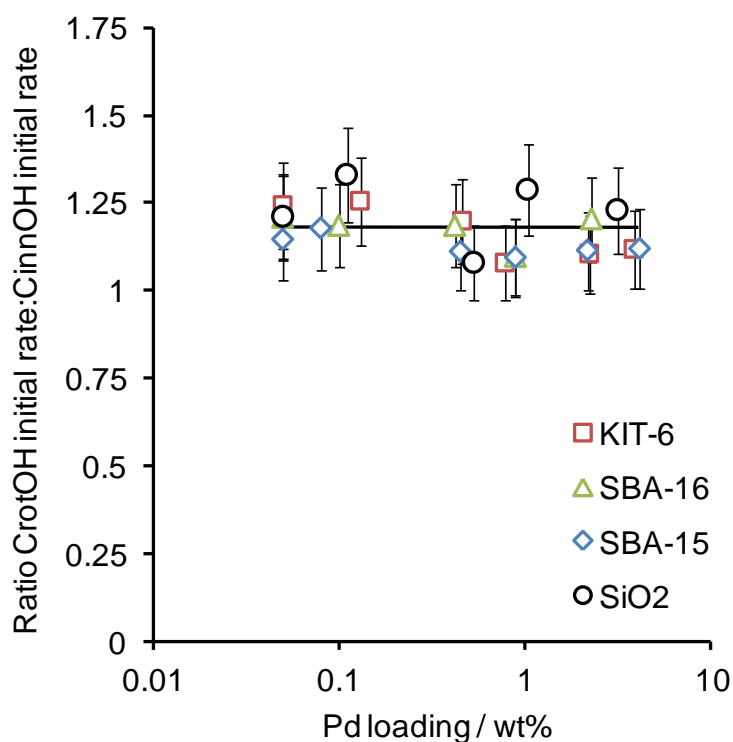


**Figure 3.31** - Ratio of normalised initial rate crotyl alcohol:cinnamyl alcohol for corresponding loadings and supports.

Turnover frequencies, normalised to metallic and oxidic Pd surface concentrations, were calculated as for crotyl alcohol and plotted in **Figure 3.32**. Again the results show strong support for an oxidised active species, with a constant TOF of  $\sim 5800 \text{ h}^{-1}$ , indicating that surface PdO is the generic active species responsible for Pd/silica catalysed allylic alcohol selox. Additionally, it supports the finding regarding the rate of reagent diffusion though the various pore architectures are irrelevant for the conditions studied.

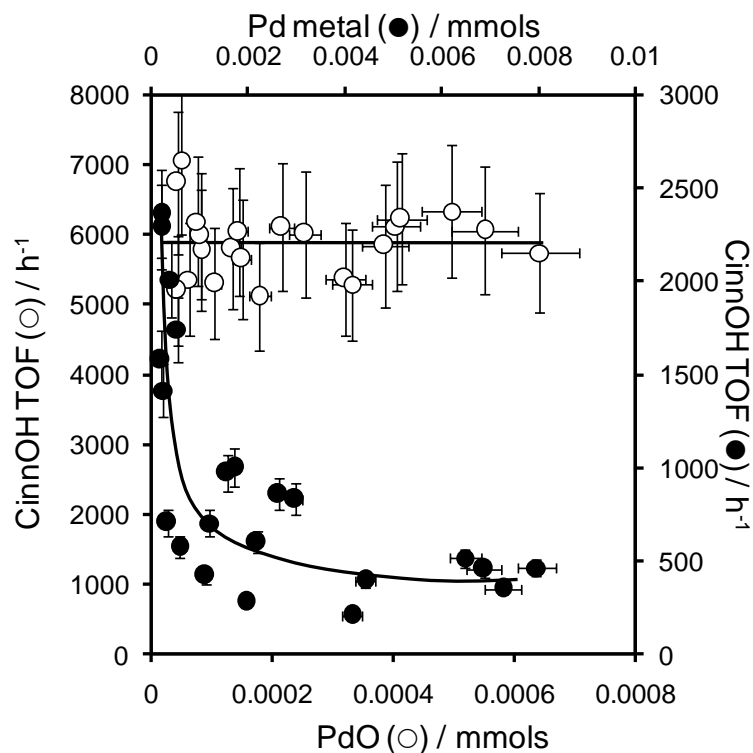


**Figure 3.32** - Cinnamyl alcohol aerobic selox turnover frequencies as a function of surface PdO or Pd metal content for Pd/SiO<sub>2</sub>, Pd/SBA-15, Pd/SBA-16 and Pd/KIT-6 catalysts.

In order to shed insight into surface PdO stability during the 1<sup>st</sup> 30 minutes of reaction, XPS has been conducted on 'spent' Pd/silicas (approximately 0.5 wt% loading). **Figure 3.33** compares the resulting spent KIT-6 catalysts with the fresh sample, and the results are representative of those from the other three silica supports, summarised in **Table 3.7**. These XP spectra show negligible loss of surface PdO during the 1<sup>st</sup> 30 minutes of reaction (the period over which TOFs were determined), although significant longer term catalyst reduction is prevalent across all the Pd/silicas. These observations are consistent with a prior in-situ XAS investigation of Pd on carbon,<sup>3</sup> and are likely to account for the principal mode of catalyst deactivation.

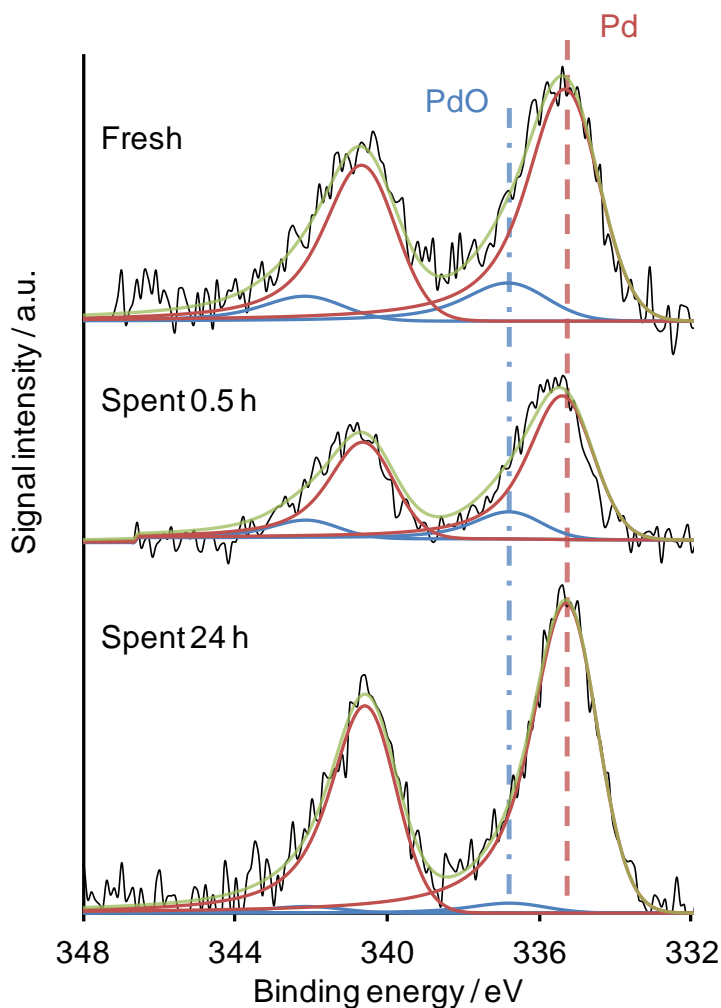


**Figure 3.33-** Pd 3d XPS stacked plot of fresh (top) and spent, 30 minutes (middle) and 24 h (bottom), 0.46 wt% Pd/KIT-6

**Table 3.7** – Comparison of surface PdO content for fresh and spent (0.5 and 24 h) cinnamyl alcohol selox catalysts  $\approx$  0.5 wt% Pd loading

<i>Support</i>	<i>Fresh / %</i>	<i>CinnOH 30 minutes / %</i>	<i>CinnOH 24 h / %</i>
<i>SBA-15</i>	8.5 ( $\pm$ 0.9)	9.2 ( $\pm$ 0.9)	0.3 ( $\pm$ 0.1)
<i>KIT-6</i>	15.2 ( $\pm$ 1.5)	14.9 ( $\pm$ 1.5)	3.3 ( $\pm$ 0.3)
<i>SBA-16</i>	13.8 ( $\pm$ 1.4)	12.8 ( $\pm$ 1.3)	2.9 ( $\pm$ 0.3)
<i>SiO<sub>2</sub></i>	3.8 ( $\pm$ 0.4)	3.5 ( $\pm$ 0.4)	0.0 ( $\pm$ 0.0)

In **Figure 3.34** the corresponding evolution of the major selox products (selectivity) throughout the course of a typical reaction are shown. Highest selectivity is towards the desired cinnamaldehyde, with the other major products being the hydrogenated 3-phenylpropan-1-ol, and the product of C-O bond cleavage of

cinnamyl alcohol, namely *trans*- $\beta$ -methyl styrene. Minor products (<1.5 % of the total) were styrene and ethylbenzene, arising from C-C cleavage of the reactant (cinnamyl alcohol) and of the hydrogenated alcohol (3-phenylpropan-1-ol) product. Significant levels of over-oxidation products (e.g. cinnamic acid) are not observed.

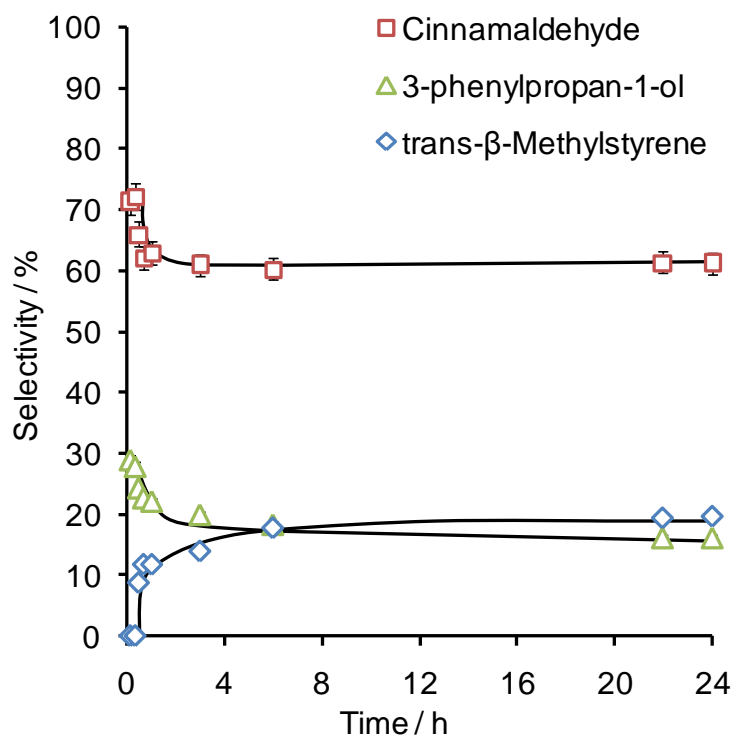


**Figure 3.34** – Representative selectivity profile as a function of time of the major cinnamyl alcohol selox products over 0.46 wt% Pd/KIT-6

The selectivities agree with literature reports for conventional Pd catalysts.<sup>2</sup> Cinnamaldehyde selectivity is constant for the 1<sup>st</sup> 30 minutes of reaction, then decreases rapidly by ~15 % before stabilising, possibly reflecting the transformation from surface Pd oxide to metal.<sup>3, 5, 7</sup> Studies of Pd single crystals and silica supported Pd catalysts, albeit at greatly elevated temperatures, reveal that dehydrogenation reactions also exhibit a decrease in selectivity with reaction time, which has been ascribed to carbon fouling and subsequent Pd carbide formation.<sup>58, 59</sup> The selectivity of 3-phenylpropan-1-ol tracks the cinnamaldehyde trend, suggesting that hydrogen liberated during the oxidative dehydrogenation of cinnamyl alcohol to cinnamaldehyde, also drives parallel cinnamyl alcohol hydrogenation;<sup>2</sup> C=C hydrogenation is widely reported over Pd.<sup>60</sup> It is worth noting that the

cinnamaldehyde:3-phenylpropan-1-ol ratio is well below unity, so the majority of hydrogen liberated in producing cinnamaldehyde is probably removed by O<sub>2</sub> as water.<sup>5</sup> The source of this O<sub>2</sub> may be atmospheric gaseous oxygen, or reduction of the oxide surface, the latter possibly explaining the oxide→metal transformation observed by in-situ XAS.<sup>3</sup> In contrast, selectivity towards trans-β-methylstyrene increases with time, in fact initiation of this side reaction causes the selectivity towards the other major products to decrease, but not through their consumption, i.e. cinnamaldehyde and 3-phenylpropan-1-ol are not precursors to trans-β-methylstyrene. Pd metal is capable of catalysing decomposition,<sup>5, 7</sup> including C-O hydrogenolysis,<sup>61</sup> and in-situ reduction of PdO during reaction could thus account for the onset of trans-β-methylstyrene production.

### 3.2.3.3 Role of oxygen on cinnamyl alcohol selox

Many studies of liquid phase alcohol selox over supported Pd catalysts have been carried out under a continuous flow of O<sub>2</sub> through the reaction solution.<sup>54, 62-64</sup> In the case of benzyl alcohol, this has been shown to enhance selectivity to benzaldehyde.<sup>62</sup> The effect of flowing O<sub>2</sub> on selectivity in cinnamyl alcohol selox was thus investigated.

**Figure 3.35** shows the effect of flowing O<sub>2</sub> (3 cm<sup>3</sup> min<sup>-1</sup>) on the selectivity towards the three major products. Results under static air are also displayed for comparison. O<sub>2</sub> is clearly beneficial, conferring a significant enhancement in selectivity towards the cinnamaldehyde (up to 20 %), as observed for benzyl alcohol selox.<sup>62</sup> Selectivity towards 3-phenylpropan-1-ol no longer tracks cinnamaldehyde, remaining independent of O<sub>2</sub> flow, suggesting the extra hydrogen liberated during cinnamaldehyde formation is not available for cinnamyl alcohol hydrogenation, but exclusively converted to water by the more abundant supply of surface atomic O<sub>2</sub>. The additional cinnamaldehyde is produced at the expense of trans-β-methylstyrene, although the latter's selectivity still increases with time. This suggest additional gas phase oxygen helps stabilise surface PdO/promotes aldehyde desorption, thus suppressing C-O cleavage.<sup>5</sup> Neither conversion nor activity was influenced by flowing O<sub>2</sub>.

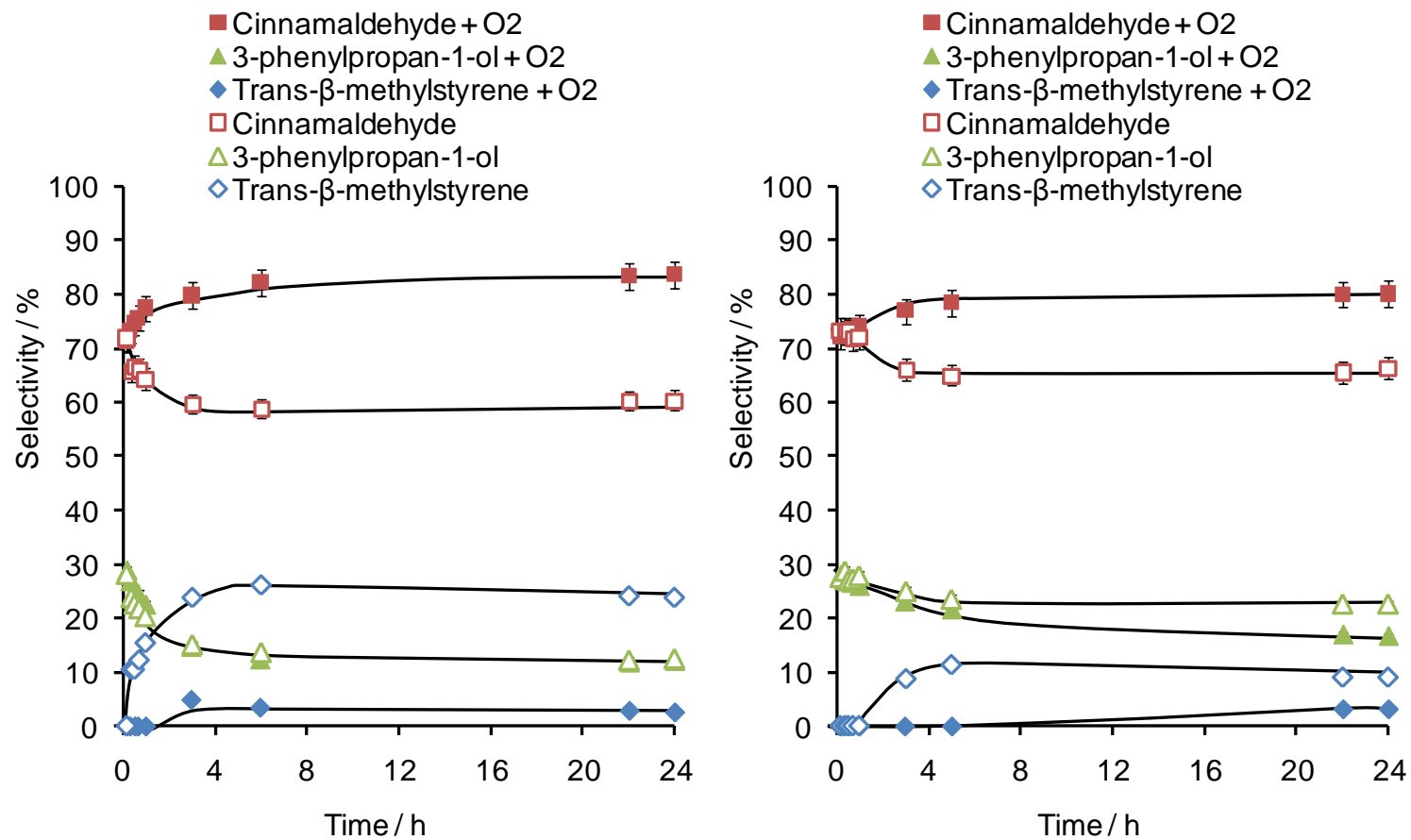


**Figure 3.35-** Representative selectivity profiles as a function of time of the major products from cinnamyl alcohol selox over 2.22 (left) and 0.05 (right) wt% Pd/KIT-6 under static and flowing  $O_2$  ( $3 \text{ cm}^3 \text{ min}^{-1}$ ) conditions

These observations could explain the selectivity trends observed under both static and flowing conditions. Over an oxidised Pd surface, oxidative dehydrogenation to the desired aldehyde product is obtained. If the rate of O<sub>2</sub> supply is low, as under static conditions, Pd reduction occurs over the course of reaction, favouring hydrogenation,<sup>60, 65</sup> and decomposition (hydrogenolysis) products.<sup>5, 7, 61</sup> Metallic Pd in turn then likely cokes, causing a switch to decarbonylation chemistry, which is favoured over hydrogenation on carbon coated Pd surfaces.<sup>58, 59</sup> In contrast, flowing O<sub>2</sub> conditions can stabilise PdO active sites, helping to sustain oxidative dehydrogenation and simultaneously suppressing competing side reactions.

XPS was again employed to further examine the reason behind the selectivity changes. The resulting spectra of spent Pd/KIT-6 catalysts are compared in **Figure 3.36**. The effect of flowing O<sub>2</sub> through the reaction solution on the surface PdO content is obvious; it slows in-situ surface PdO reduction. The addition of O<sub>2</sub> increases the PdO surface concentration of the spent catalysts from 1.1 to 4.6 %, and 7.5 to 17.6 % for the 2.22 and 0.05 wt% Pd/KIT-6 samples respectively, (although these still represent a slight drop relative to their fresh counterparts). The time-dependent selectivity changes from the desired aldehyde to trans- $\beta$ -methylstyrene under static conditions, and the converse under flowing O<sub>2</sub>, can hence be rationalised in terms of the stability of surface PdO.

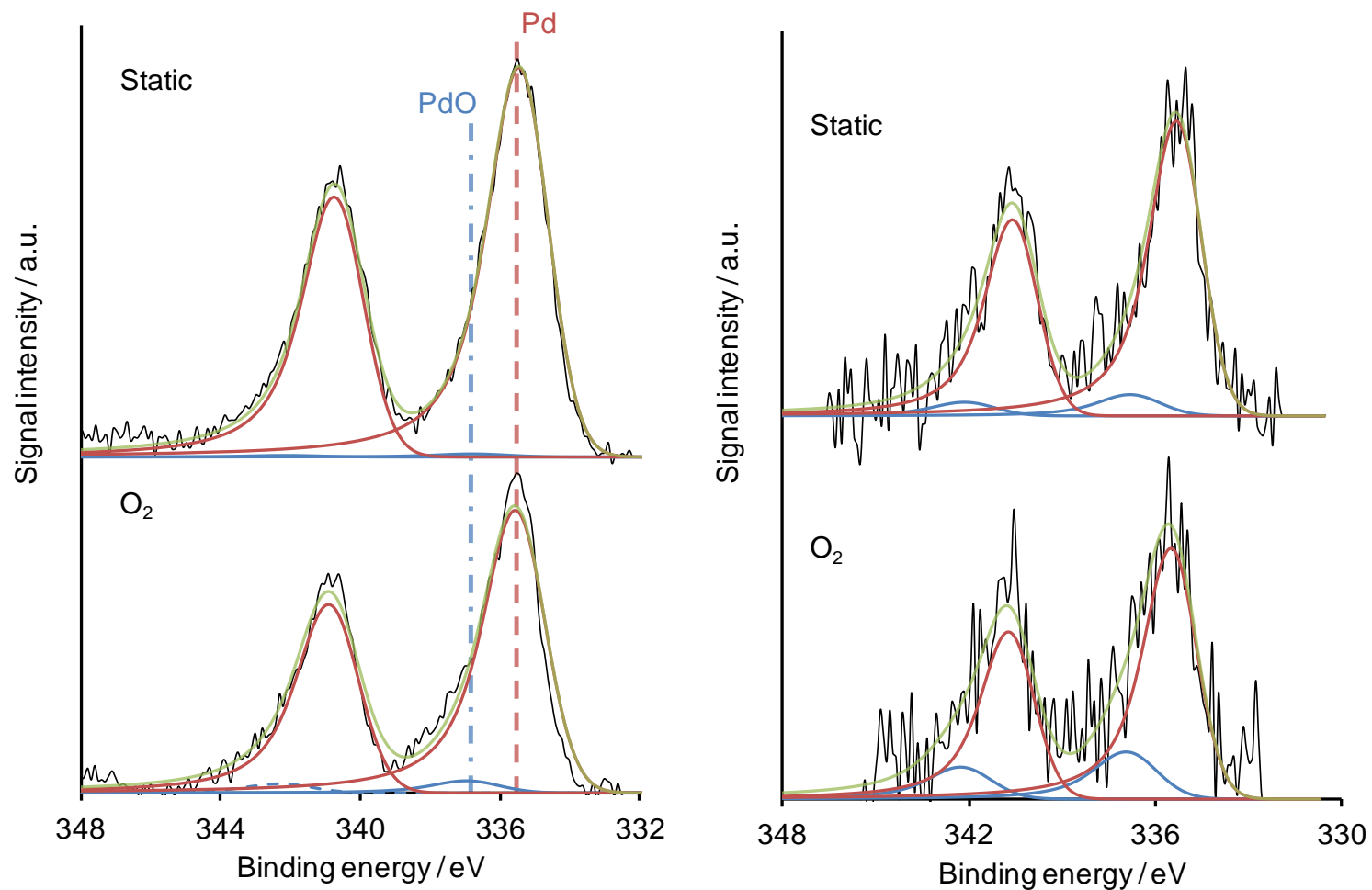


**Figure 3.36** – Pd 3d XPS of spent 2.22 (left) and 0.05 (right) wt% Pd/KIT-6 under static and flowing O<sub>2</sub> (3 cm<sup>3</sup> min<sup>-1</sup>)

### 3.2.3.4 Role of reductive pre-treatment

To further test whether surface PdO is the active site in alcohol selox, the effect of in-situ pre-reduction of Pd/silicas was investigated. This should dramatically *improve* catalytic performance (activity and aldehyde selectivity) if previous hypotheses that Pd metal is the active site are correct.<sup>1</sup>

The effect of pre-reduction on cinnamyl alcohol conversion over 0.46 wt% Pd/KIT-6 is depicted in **Figure 3.37**; please refer to Chapter 2 for a detailed methodology.<sup>62</sup> The reduced catalysts were subsequently tested either under static air or flowing O<sub>2</sub> (3 cm<sup>3</sup> min<sup>-1</sup>). Control samples (referred to as Fresh on the plot), in which N<sub>2</sub> was used instead of H<sub>2</sub> during in-situ reduction, were conducted in parallel.

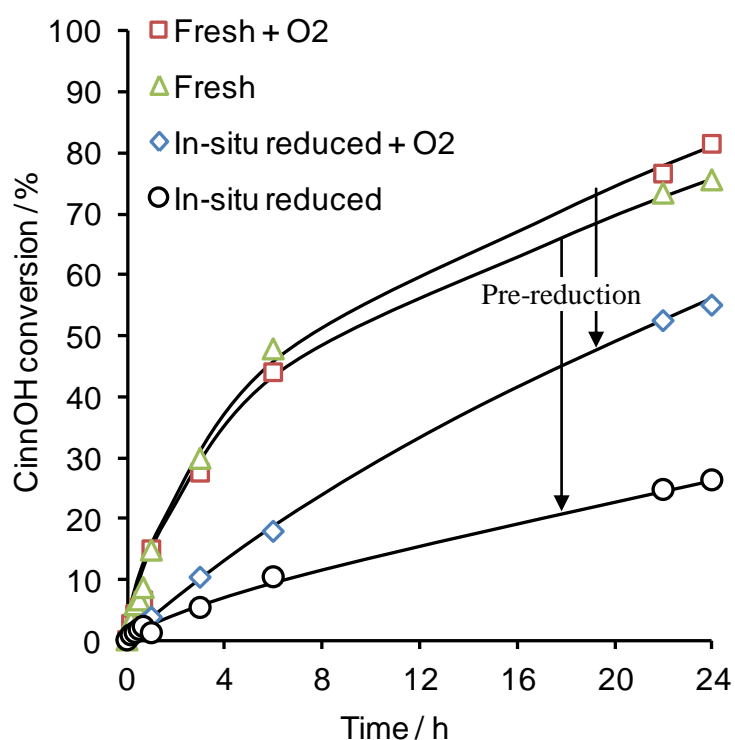


**Figure 3.37**– Cinnamyl alcohol selox reaction profiles over in-situ reduced 0.46 wt% Pd/KIT-6 catalysts under static and flowing O<sub>2</sub> (3 cm<sup>3</sup> min<sup>-1</sup>) and comparable control catalysts

These reaction profiles unequivocally show that in-situ reduction significantly worsens catalyst performance, although flowing O<sub>2</sub> after the reductive pre-treatment slightly mitigates this detrimental effect. Control reactions (Fresh) gave comparable

conversion and selectivity to the original investigation (**Figure 3.29** and **3.44**). The initial rates quantify the negative impact of pre-reduction **Figure 3.38**. The small recovery in rate upon flowing O<sub>2</sub> (reduced catalyst) addition suggests that PdO reduction to metal is essentially not spontaneously reversible under these conditions.

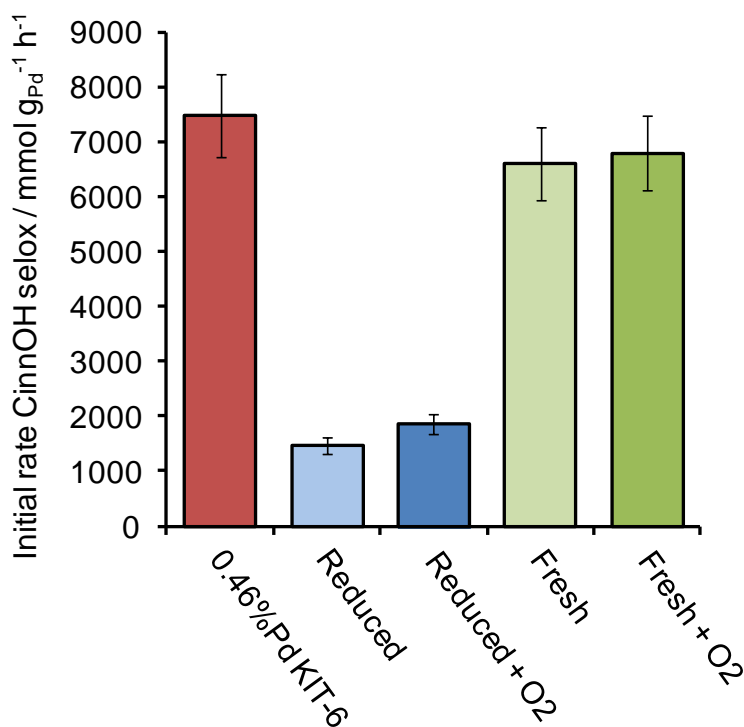


**Figure 3.38** – Effect of in-situ reduction on cinnamyl alcohol selox initial activity over 0.46 wt% Pd/KIT-6 under static and flowing O<sub>2</sub>. Control catalysts under comparable conditions and original catalyst screening data shown for comparison

In-situ pre-reduction also hampers selectivity, revealed in **Figure 3.39**. The resulting product match those from the standard reaction protocol, however the initial selectivities to cinnamaldehyde and 3-phenylpropan-1-ol are substantially reduced, and decrease further over the course of the reaction. Flowing O<sub>2</sub> ameliorates these undesired selectivity losses, eventually returning cinnamaldehyde levels to those observed over a fresh catalyst. Pre-reduction enhances initial selectivity to trans- $\beta$ -methylstyrene, with it detected in the 1<sup>st</sup> data point (after only 10 minutes), with and without O<sub>2</sub> addition. This compares with ~30-40 minutes or 6 hours induction times over the fresh (unreduced) catalysts under static or flowing O<sub>2</sub> respectively. Hydrogenolysis is thus strongly promoted by the formation of metallic Pd.

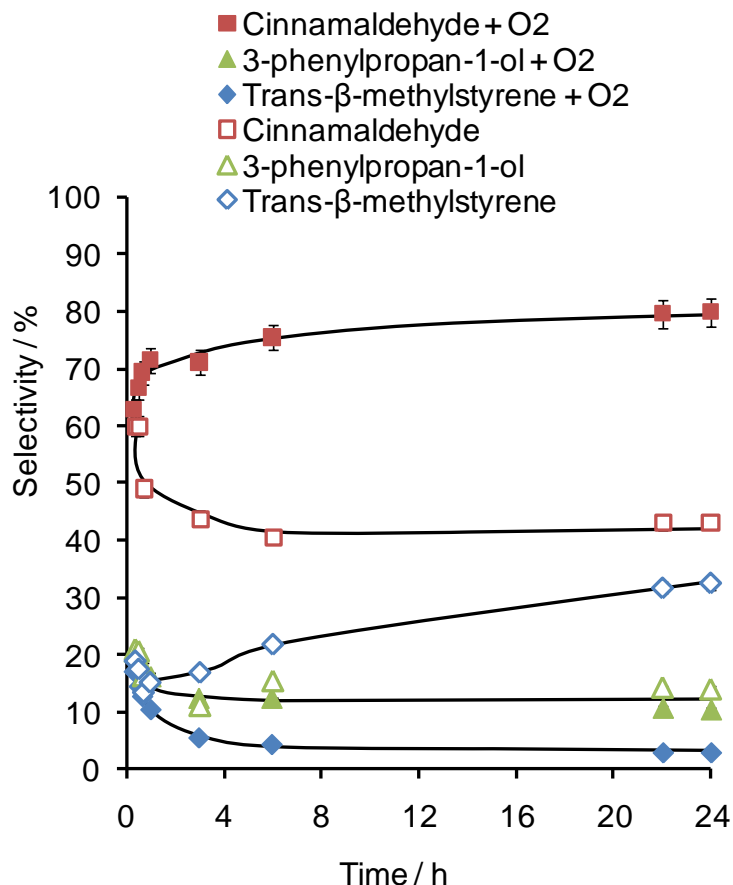


**Figure 3.39** – Selectivity profile as a function of time of the major cinnamyl alcohol select products over in-situ reduced 0.46 wt% Pd/KIT-6 catalysts under static and flowing O<sub>2</sub> (3 cm<sup>3</sup> min<sup>-1</sup>)

In-situ pre-reduction of these Pd/silicas is thus clearly inadvisable, and compromises both activity and selectivity. These experiments also provide compelling evidence that metallic Pd is not the active site in allylic alcohol selox, and in-situ PdO reduction is the likely origin of on-stream catalyst deactivation.

### 3.2.3.5 Recycle testing

Catalyst longevity and recyclability are very important to commercialisation, wherein a short catalyst life and/or problematic on-stream catalyst regeneration will result in unacceptable process downtime and costs.

**Figure 3.40** shows the reaction profiles for three consecutive runs of the 0.42 wt% Pd/SBA-16 catalyst. Between each run the catalyst was reactivated via the same calcination and reduction steps used in the initial synthesis. Initial rates and

selectivity are identical to the fresh catalyst, showing that any in-situ reduction or coking can be readily reversed by high temperature calcination/reduction. The result also confirms that deactivation does not occur through metal leaching, in accordance with the hot filtration experiments, or irreversible Pd sintering.<sup>66, 67</sup>

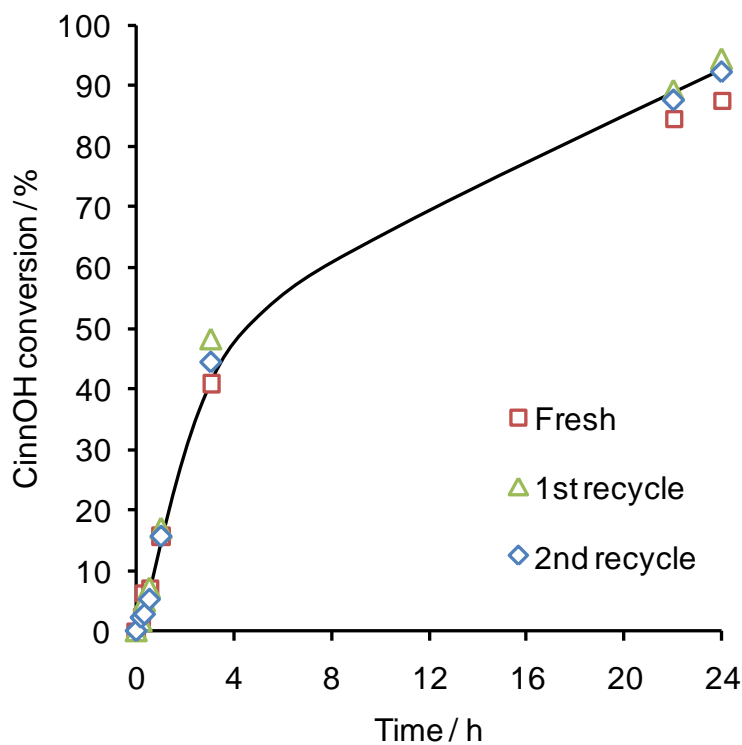


**Figure 3.40**– Comparison of reaction profiles for the fresh and recycled 0.42 wt% Pd/SBA-16 catalysts

Reversibility of the Pd oxide $\leftrightarrow$ metal transition is confirmed by XPS, displayed in **Figure 3.41**. PdO levels of 13.1 and 13.9 % were obtained for a fresh, and twice recycled and subsequently reactivated catalyst respectively.

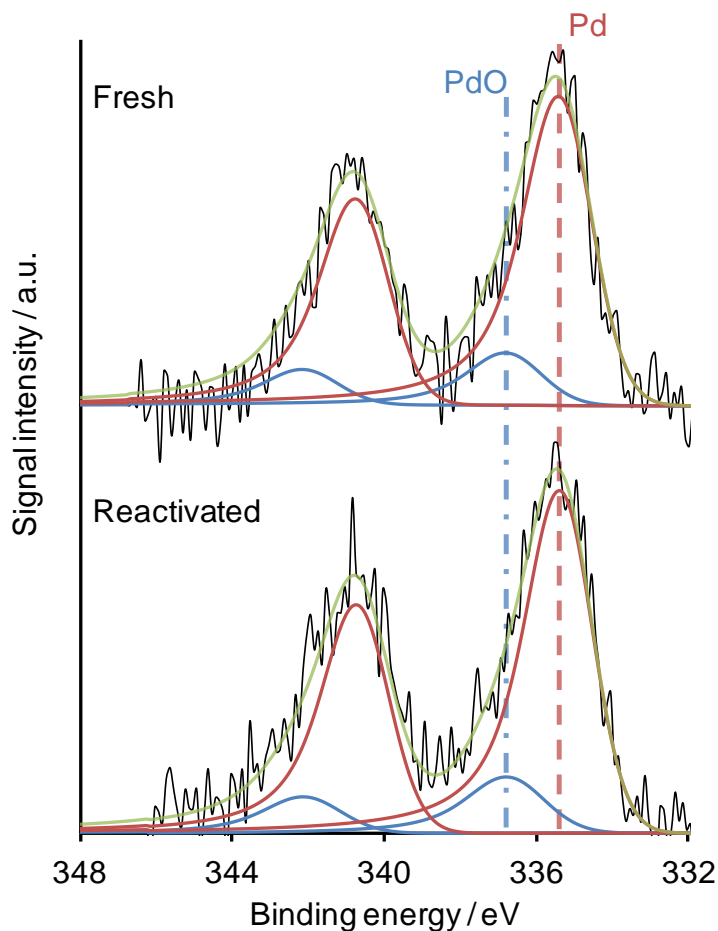


**Figure 3.41** – Stacked Pd 3d XPS of fresh (top) and 2 twice reactivated (bottom) 0.42 wt% Pd/SBA-16

Poisoning of Pd catalysts by CO or strongly bound hydrocarbons was also observed in the XPS of spent catalysts prior to reactivation, illustrated in **Figure 3.42**. Other common Pd catalyst poisons such as Pb, P, Zn, SO<sub>2</sub> and Fe,<sup>66</sup> can be discounted in this study. The concentration of chemisorbed CO increases from 0.3 to 2.1 wt% between fresh and spent catalysts, accompanied by strong hydrocarbon adsorption. Total surface carbon content rises from 1.0 wt% in the fresh Pd/SBA-16, to 10.6 wt% in the spent catalyst.

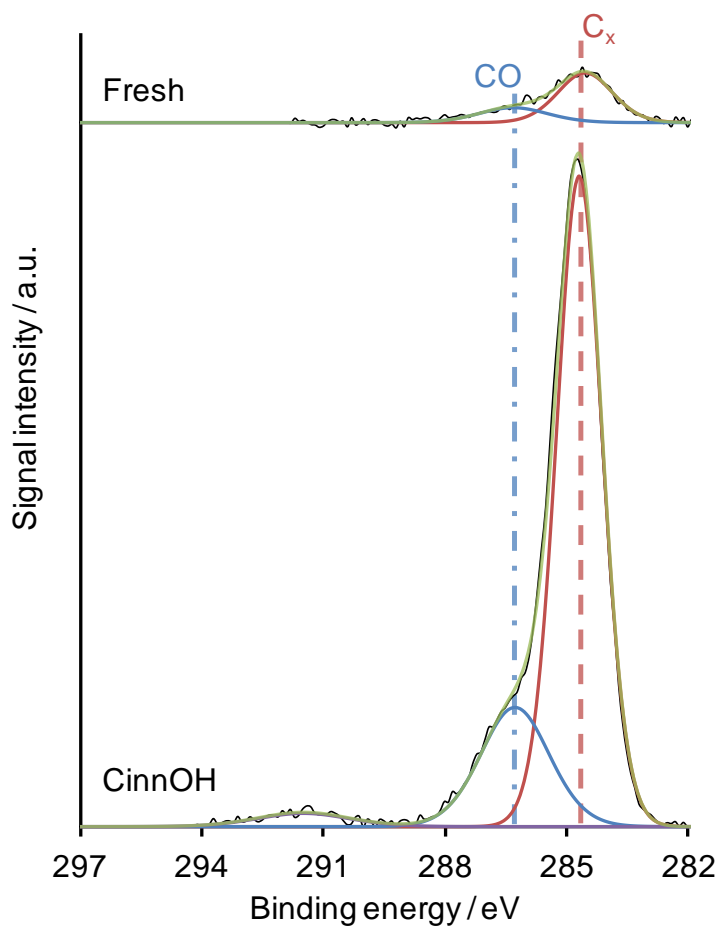


**Figure 3.42**– C 1s XPS of fresh (top) and Cinnamyl alcohol spent (bottom) 0.42 wt% Pd/SBA-16

$N_2$  porosimetry, of spent and reactivated 0.78 wt% Pd/KIT-6 also reveals a significant decrease in BET surface area post-reaction of 20 % (for crotyl alcohol) and 67 % (cinnamyl alcohol). BET surface areas can be easily recovered to the levels of fresh catalysts via calcination, demonstrating this textural change is not a consequence of pore collapse or blockage due to Pd sintering. BJH pore size distributions are compared in **Figure 3.43** for fresh, spent and reactivated catalysts. They show that a small degree of mesopore blocking occurs due to coking during the reaction. This decreases the volume of adsorbed  $N_2$  and shifting the distribution to lower pore diameter. The effect is greatest for cinnamyl alcohol, presumably due its lower volatility and stronger adsorption via the aromatic ring.

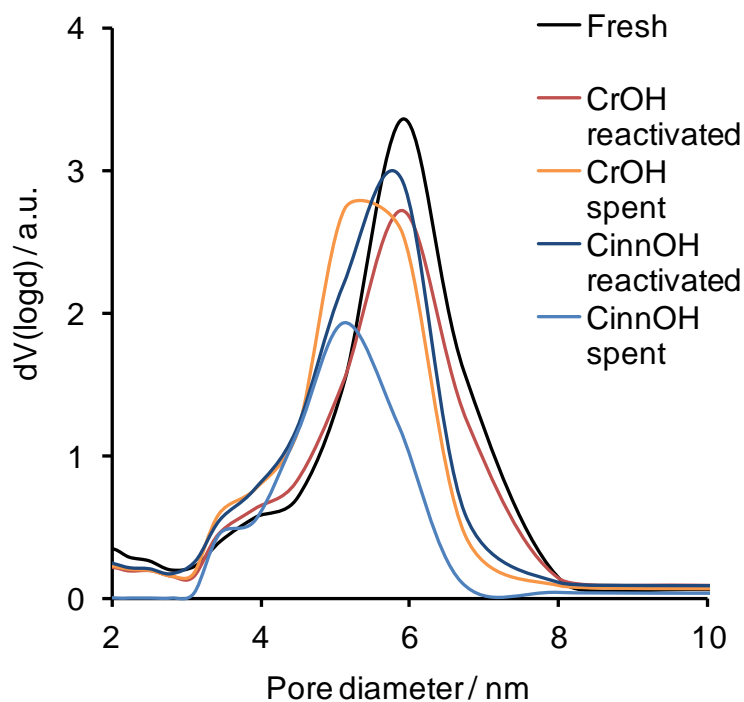


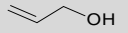
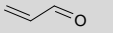
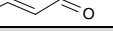
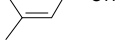
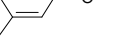
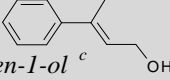
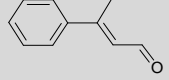
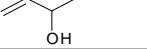
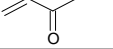
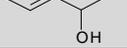
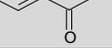
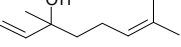
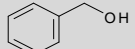
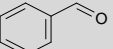
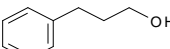
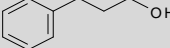
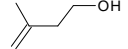
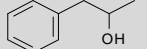
**Figure 3.43**– BJH pore size distribution plots of fresh, spent and reactivated 0.78 wt% Pd/KIT-6

Deactivation during cinnamyl alcohol selox thus appears a combination of PdO surface reduction, CO poisoning of resulting Pd metal sites, and coking of both support and active sites. All of these processes can be easily reversed, offering active, selective and recyclable Pd/silica catalysts.

### 3.2.4 Alternative alcohol selox

To further assess the commercial applicability of these catalysts for alcohol selox, a range of primary, secondary and tertiary allylic alcohols, benzyl alcohol, and non-allylic alcohols were screened using 0.46 wt% Pd/KIT-6. The results are displayed in **Table 3.8**.

**Table 3.8** - Selox performance 0.46 wt% Pd/KIT-6 against allylic and saturated alcohols at 90 °C.

Alcohol	Major Product	Conversion / %	Selectivity / %	Normalised initial rate $\text{mmol.g}_{\text{pd}}^{-1} \cdot \text{h}^{-1}$	
Allyl Alcohol <sup>a</sup>			47	70	11755
Crotyl Alcohol <sup>b</sup>			60	64	8456
Cinnamyl Alcohol <sup>b</sup>			76	59	7575
Prenol Alcohol <sup>c</sup>			27	90	7897
Trans-2-methyl-3-phenyl-2-propen-1-ol <sup>c</sup>			28	76	5309
3-buten-2-ol <sup>a</sup>			70	66	26520
3-penten-2-ol <sup>c</sup>			30	70	7885
Linalool Alcohol <sup>c</sup>		n/a	0	0	0
Benzyl Alcohol <sup>c</sup>			61	96	8054
Hydrocinnamyl Alcohol <sup>c</sup>		n/a	0	0	0
Hydrocinnamyl Alcohol <sup>d</sup>		n/a	0	0	0
3-methyl-3-buten-1-ol <sup>c</sup>		n/a	0	0	0
1-phenylpropen-2-ol <sup>c</sup>		n/a	0	0	0

<sup>a</sup>Catalyst mass 0.025g; T = 90 °C, [Alcohol] = 8.4mmol; conversion and selectivity reported after 3 h; TOF after 30 minutes.

<sup>b</sup>Catalyst mass 0.05g; T = 90 °C; [Alcohol] = 8.4mmol; conversion and selectivity reported after 24 h, TOF after 30 minutes.

<sup>c</sup>Catalyst mass 0.025 g; T = 90 °C, [Alcohol] = 8.4mmol; conversion and selectivity reported after 24 h, TOF after 30 minutes.

<sup>d</sup>Catalyst mass 0.025g; T = 90 °C, [Alcohol] = 8.4mmol; 1 bar flowing O<sub>2</sub> at 3 cm<sup>3</sup> min<sup>-1</sup>; conversion and selectivity after 3 h; TOF after 30 minutes.

The Pd/KIT-6 catalyst is active towards a range of primary and secondary allylic alcohols, and benzyl alcohol. In contrast, linalool alcohol, a tertiary allylic alcohol, and non-allylic alcohols showed no conversion. The stability of tertiary allylic alcohols is proposed to arise from the absence of a  $\beta$ -hydrogen species, and the more difficult methyl/alkyl gamma C–H bond scission.<sup>68</sup> Allylic alcohols are believed to bind through both C=C and alkoxy groups, bringing their  $\beta$ -C-H bonds closer to the Pd surface, facilitating dehydrogenation.<sup>5, 69</sup> The allyl function is also believed to help stabilise the resulting allylic aldehyde/ketone products via conjugation and resonance effects. In the absence of a C=C bond, alkyl chains partially counteract the electron withdrawing effect of the alcohol oxygen, via a positive inductive effect. This partially stabilises the beta C-H species and as a result the  $\beta$ -C-H bond is stronger in non-allylic systems, slowing the rate-determining C-H scission.

### 3.3 Conclusion

Through careful tailoring of the catalyst support structure, via the use of different mesoporous silicas, we have managed to investigate the effect of support architecture on both catalyst preparation and resulting catalytic reactivity. Incorporation of a mesopore network significantly increases support surface area, a highly beneficial property which results in higher metal dispersion compared with equivalent low surface area silica support. This is further enhanced through the creation of interconnecting mesopores to produce ‘3D’ porous architectures. These help stabilise more highly dispersed Pd, which in turn induces escalating surface Pd oxide concentrations. In addition, dispersion and therefore surface PdO concentration can also be controlled through Pd loading, decreasing metal levels gives rise to smaller particles which intrinsically exhibit a higher surface to bulk ratio.

From studying the intrinsic reaction kinetics of allylic alcohol selox, in the presence of flowing O<sub>2</sub> or following pre-reduction, we can conclusively demonstrate that surface PdO is the active catalytic site in allylic alcohol selox. This finding being in strong agreement with a recent multi-technique in operando study, combining XAS, DRIFTS and MS, which showed compelling evidence that PdO is responsible for selox, and reduction to metallic Pd is a generic deactivation route.<sup>7</sup> The simplistic methodology used here to prepare these catalysts; combined with their true

heterogeneous mode of action, facile recyclability without deactivation, and excellent activity towards a wide range of allylic alcohols, indicates these are ideal catalytic systems for allylic alcohol select to their corresponding allylic aldehydes.

### 3.4 References

1. J. D. Grunwaldt, M. Caravati and A. Baiker, *The Journal of Physical Chemistry B*, 2006, **110**, 25586-25589.
2. T. Mallat and A. Baiker, *Chem. Rev.*, 2004, **104**, 3037-3058.
3. A. F. Lee and K. Wilson, *Green Chem.*, 2004, **6**, 37-42.
4. A. F. Lee, S. F. J. Hackett, J. S. J. Hargreaves and K. Wilson, *Green Chem.*, 2006, **8**, 549-555.
5. A. F. Lee, Z. Chang, P. Ellis, S. F. J. Hackett and K. Wilson, *J. Phys. Chem. C*, 2007, **111**, 18844-18847.
6. S. E. J. Hackett, R. M. Brydson, M. H. Gass, I. Harvey, A. D. Newman, K. Wilson and A. F. Lee, *Angew. Chem.-Int. Edit.*, 2007, **46**, 8593-8596.
7. A. F. Lee, C. V. Ellis, J. N. Naughton, M. A. Newton, C. M. A. Parlett and K. Wilson, *J. Am. Chem. Soc.*, 2011, **133**, 5724-5727.
8. C. P. Vinod, K. Wilson and A. F. Lee, *J. Chem. Technol. Biotechnol.*, 2011, **86**, 161-171.
9. C. M. A. Parlett, D. W. Bruce, N. S. Hondow, A. F. Lee and K. Wilson, *ACS Catalysis*, 2011, **1**, 636-640.
10. D. Y. Zhao, J. L. Feng, Q. S. Huo, N. Melosh, G. H. Fredrickson, B. F. Chmelka and G. D. Stucky, *Science*, 1998, **279**, 548-552.
11. T. W. Kim, F. Kleitz, B. Paul and R. Ryoo, *J. Am. Chem. Soc.*, 2005, **127**, 7601-7610.
12. R. Huirache-Acuna, B. Pawelec, E. Rivera-Munoz, R. Nava, J. Espino and J. L. G. Fierro, *Applied Catalysis B: Environmental*, 2009, **92**, 168-184.
13. Y. T. Chen, Z. Guo, T. Chen and Y. H. Yang, *J. Catal.*, 2010, **275**, 11-24.
14. P. A. Webb and C. Orr, *Analytical Methods in Fine Particle Technology*, Micromeritics, Norcross, 1997.
15. S. Brunauer, P. H. Emmett and E. Teller, *J. Am. Chem. Soc.*, 1938, **60**, 309-319.
16. E. P. Barrett, L. G. Joyner and P. P. Halenda, *J. Am. Chem. Soc.*, 1951, **73**, 373-380.
17. Y. Sakamoto, M. Kaneda, O. Terasaki, D. Y. Zhao, J. M. Kim, G. Stucky, H. J. Shim and R. Ryoo, *Nature*, 2000, **408**, 449-453.
18. T. W. Kim, R. Ryoo, M. Kruk, K. P. Gierszal, M. Jaroniec, S. Kamiya and O. Terasaki, *J. Phys. Chem. B*, 2004, **108**, 11480-11489.
19. M. Kruk, M. Jaroniec, C. H. Ko and R. Ryoo, *Chem. Mat.*, 2000, **12**, 1961-1968.
20. C. M. Yang, H. A. Lin, B. Zibrowius, B. Spliethoff, F. Schüth, S. C. Liou, M. W. Chu and C. H. Chen, *Chem. Mat.*, 2007, **19**, 3205-3211.
21. C. M. Yang, B. Zibrowius, W. Schmidt and F. Schüth, *Chem. Mat.*, 2003, **15**, 3739-3741.
22. A. Silvestre-Albero, E. O. Jardim, E. Bruijn, V. Meynen, P. Cool, A. Sepulveda-Escribano, J. Silvestre-Albero and F. Rodriguez-Reinoso, *Langmuir*, 2009, **25**, 939-943.
23. B. C. Lippens and J. H. De Boer, *J. Catal.*, 1965, **4**, 319-323.
24. P. Van der Voort, M. Benjelloun and E. F. Vansant, *J. Phys. Chem. B*, 2002, **106**, 9027-9032.

25. J. F. Shen, X. Z. Liu, S. G. Zhu, H. L. Zhang and J. J. Tan, *Mater. Lett.*, 2011, **65**, 1179-1183.
26. N. Pernicone, *Cattech*, 2003, **7**, 196-204.
27. P. Scherrer, *Gottinger Nachrichten*, 1918, **2**, 98.
28. S. C. Laha and R. Ryoo, *Chem. Commun.*, 2003, 2138-2139.
29. S. Jaenicke, G. K. Chuah, V. Raju and Y. T. Nie, *Catalysis surveys from Asia*, 2008, **12**, 153-169.
30. A. Zukal, H. Siklova and J. Cejka, *Langmuir*, 2008, **24**, 9837-9842.
31. G. C. Cabilla, A. L. Bonivardi and M. A. Baltanas, *Catal. Lett.*, 1998, **55**, 147-156.
32. H. Dropsch and M. Baerns, *Appl. Catal. A-Gen.*, 1997, **158**, 163-183.
33. A. Guerrero-Ruiz, S. W. Yang, Q. Xin, A. Maroto-Valiente, M. Benito-Gonzalez and I. Rodriguez-Ramos, *Langmuir*, 2000, **16**, 8100-8106.
34. P. Canton, F. Menegazzo, S. Polizzi, F. Pinna, N. Pernicone, P. Riello and G. Fagherazzi, *Catal. Lett.*, 2003, **88**, 141-146.
35. K. Soni, K. C. Mouli, A. K. Dalai and J. Adjaye, *Catal. Lett.*, 2010, **136**, 116-125.
36. L. Li, D. L. King, J. Liu, Q. Huo, K. Zhu, C. Wang, M. Gerber, D. Stevens and Y. Wang, *Chem. Mat.*, 2009, **21**, 5358-5364.
37. A. Fukuoka, Y. Sakamoto, T. Higuchi, N. Shimomura and M. Ichikawa, *Journal of Porous Materials*, 2006, **13**, 231-235.
38. H. Araki, A. Fukuoka, Y. Sakamoto, S. Inagaki, N. Sugimoto, Y. Fukushima and M. Ichikawa, *Journal of Molecular Catalysis A: Chemical*, 2003, **199**, 95-102.
39. S. Marx, F. Krumeich and A. Baiker, *J. Phys. Chem. C*, 2011, **115**, 8195-8205.
40. A. F. Lee, C. V. Ellis, K. Wilson and N. S. Hondow, *Catal. Today*, 2010, **157**, 243-249.
41. R. Van Hardeveld and F. Hartog, *Advances in catalysis and related subjects*, 1972, **22**, 75.
42. S. J. Pennycook and L. A. Boatner, *Nature*, 1988, **336**, 565-567.
43. A. R. Tao, S. Habas and P. Yang, *Small*, 2008, **4**, 310.
44. Y. Xiong, H. Cai, J. Benjamin, J. Wang, M. J. Kim and Y. Xia, *J. Am. Chem. Soc.*, 2007, **129**, 3665-3675.
45. M. Brun, A. Berthet and J. C. Bertolini, *Journal of Electron Spectroscopy and Related Phenomena*, 1999, **104**, 55-60.
46. Q. Fu and T. Wagner, *Surface Science Reports*, 2007, **62**, 431-498.
47. A. W. Hull, *Physical Review*, 1921, **17**, 571.
48. J. Waser, H. A. Levy and S. W. Peterson, *Acta Crystallographica*, 1953, **6**, 661-663.
49. A. Jentys, *Physical Chemistry Chemical Physics*, 1999, **1**, 4059-4063.
50. M. S. Holm, E. Taarning, K. Egeblad and C. H. Christensen, *Catal. Today*, 2011, **168**, 3-16.
51. J. Dhainaut, J. P. Dacquin, A. F. Lee and K. Wilson, *Green Chem.*, 2010, **12**, 296-303.
52. Z. C. Ma, H. Q. Yang, Y. Qin, Y. J. Hao and G. A. Li, *J. Mol. Catal. A-Chem.*, 2010, **331**, 78-85.
53. A. F. Lee, J. J. Gee and H. J. Theyers, *Green Chem.*, 2000, **2**, 279-282.
54. C. L. Li, Q. H. Zhang, Y. Wang and H. L. Wan, *Catal. Lett.*, 2008, **120**, 126-136.
55. K. Mori, T. Hara, T. Mizugaki, K. Ebitani and K. Kaneda, *J. Am. Chem. Soc.*, 2004, **126**, 10657-10666.
56. D. Y. Zhao, Q. S. Huo, J. L. Feng, B. F. Chmelka and G. D. Stucky, *J. Am. Chem. Soc.*, 1998, **120**, 6024-6036.

57. A. Corma, D. Das, H. García and A. Leyva, *J. Catal.*, 2005, **229**, 322-331.
58. M. Bowker, L. Cookson, J. Bhanoo, A. Carley, E. Hayden, L. Gilbert, C. Morgan, J. Counsell and P. Yaseneva, *Applied Catalysis A: General*, 2011, **391**, 394-399.
59. M. Bowker, L. Gilbert, J. Counsell and C. Morgan, *The Journal of Physical Chemistry C*, 2010, **114**, 17142-17147.
60. A. Corma, H. Garcia and A. Leyva, *Journal of Molecular Catalysis A: Chemical*, 2005, **230**, 97-105.
61. H. Y. Lee, S. Ryu, H. Kang, Y. Jun and J. Cheon, *Chem. Commun.*, 2006, 1325-1327.
62. T. Yasu-eda, R. Se-ike, N. O. Ikenaga, T. Miyake and T. Suzuki, *J. Mol. Catal. A-Chem.*, 2009, **306**, 136-142.
63. F. Li, Q. H. Zhang and Y. Wang, *Appl. Catal. A-Gen.*, 2008, **334**, 217-226.
64. J. Chen, Q. H. Zhang, Y. Wang and H. L. Wan, *Adv. Synth. Catal.*, 2008, **350**, 453-464.
65. S. Miao, C. Zhang, Z. Liu, B. Han, Y. Xie, S. Ding and Z. Yang, *The Journal of Physical Chemistry C*, 2008, **112**, 774-780.
66. C. H. Bartholomew, *Applied Catalysis A: General*, 2001, **212**, 17-60.
67. P. Albers, J. Pietsch and S. F. Parker, *Journal of Molecular Catalysis A: Chemical*, 2001, **173**, 275-286.
68. X. Y. Liu, R. J. Madix and C. M. Friend, *Chem. Soc. Rev.*, 2008, **37**, 2243-2261.
69. J. Naughton, A. Pratt, C. W. Woffinden, C. Eames, S. P. Tear, S. M. Thompson, A. F. Lee and K. Wilson, *J. Phys. Chem. C*, 2011, **115**, 25290-25297.

## *Chapter 4*

*The selective oxidation of  
allylic alcohols over  
palladium supported on  
SBA-15 – the role of  
complementary pore  
architectures*

## 4.1 Introduction

As **Chapter 3** highlighted, support physical characteristics can drastically alter the resulting catalytic activity <sup>[1]</sup> of dispersed Pd, evidencing the importance of surface PdO.

This chapter builds upon these investigations by comparing two SBA-15 variants with the conventionally prepared material. The effect of incorporating macropores, to form a macroporous-mesoporous SBA-15 (MM-SBA-15) is first explored: this should result in a more open structure, possibly aiding internal mass diffusion <sup>[2]</sup> with shorter length mesopore domains, probably leading to enhanced metal dispersion. Second, an alternative synthetic route utilising true liquid crystal templating (TLCT-SBA-15), has been investigated to observe any impact on resulting support porosity and associated reactivity. It is hoped that these additional catalysts will bear out the predictions from **Chapter 3**, namely that controlling the surface PdO content permits tuning of Pd catalysts allylic alcohol selox.

## 4.2 Results and discussion

### 4.2.1 Characterisation of polystyrene spheres

Mono-dispersed polystyrene spheres were prepared using the emulsion polymerisation method of Vaudreuil and co-workers <sup>[3]</sup> for use as hard macropore templates. The work in relation to the MM-SBA-15 support and subsequent catalyst series in this chapter was performed in conjunction with Ms Pooja Keshwalla, under the supervision of the author.

#### 4.2.1.1 Scanning electron microscopy

SEM was used to confirm the synthesis of mono-dispersed polystyrene spheres and quantify their size distribution. **Figure 4.1** confirms the desired synthesis of only spherical morphologies, and reveals a high degree of mono-dispersity with mean bead diameters of 270 ( $\pm 20$ ) nm, in accordance with literature values for comparable synthesis conditions.<sup>[2]</sup>

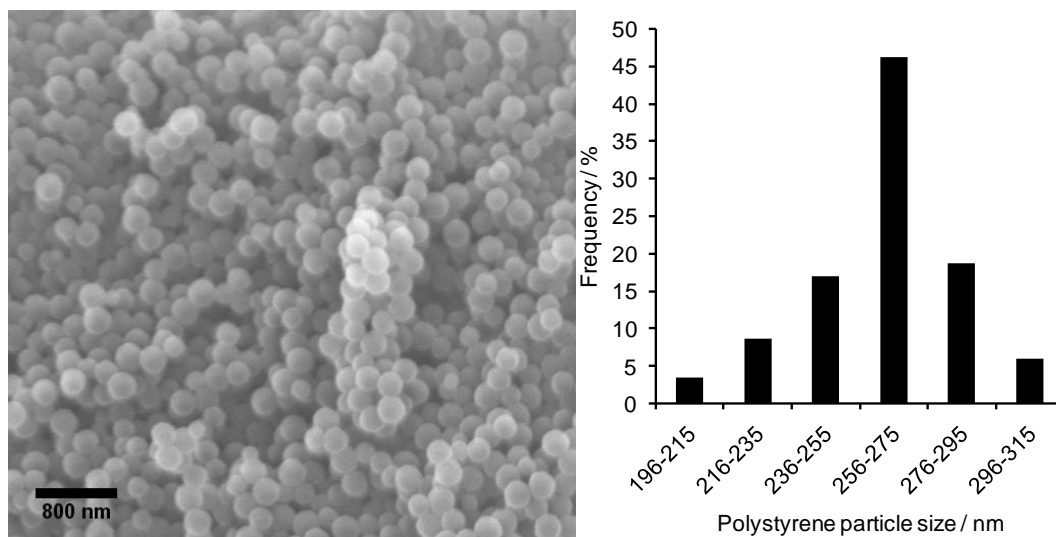


**Figure 4.2** - Representative SEM image of polystyrene spheres and associated particle size distributions (350 particles)

## 4.2.2 Characterisation of parent silica supports

The two mesoporous silicas, MM-SBA-15 and TLCT-SBA-15 were synthesised using the respective methods of Lee and co-workers<sup>[2]</sup> and Bruce and co-workers, the latter based on the modified method of Attard et al.<sup>[4]</sup> The TLCT-SBA-15 was kindly supplied by Dr Stephen G. Wainwright and Prof. Duncan W. Bruce at the University of York. The successful synthesis of these two supports was verified as detailed below. These new supports have been compared to the conventionally prepared SBA-15 (SBA-15) support materials described in **Chapter 3**.

### 4.2.2.1 Powder X-Ray diffraction

The expected  $p6mm$  space group for both MM-SBA-15 and TLCT-SBA-15 was observed via low angle powder XRD, as displayed in **Figure 4.2**. The expected weaker peaks positions are calculated, using the dominant reflection, and concur with their actual values. As for SBA-15, the strongest peak is indexed as the d(10) reflection. Weaker peaks can be assigned as the d(11) and d(20) respectively, which is characteristic of the  $p6mm$  space group and thus confirms successful synthesis. With regard to the macropores of MM-SBA-15, even if these exhibited a high degree of order, this would be undetectable by conventional low angle powder diffraction due to the vast repeat distances (~30 times that of the mesopores), and would require Small Angle X-ray Scattering.

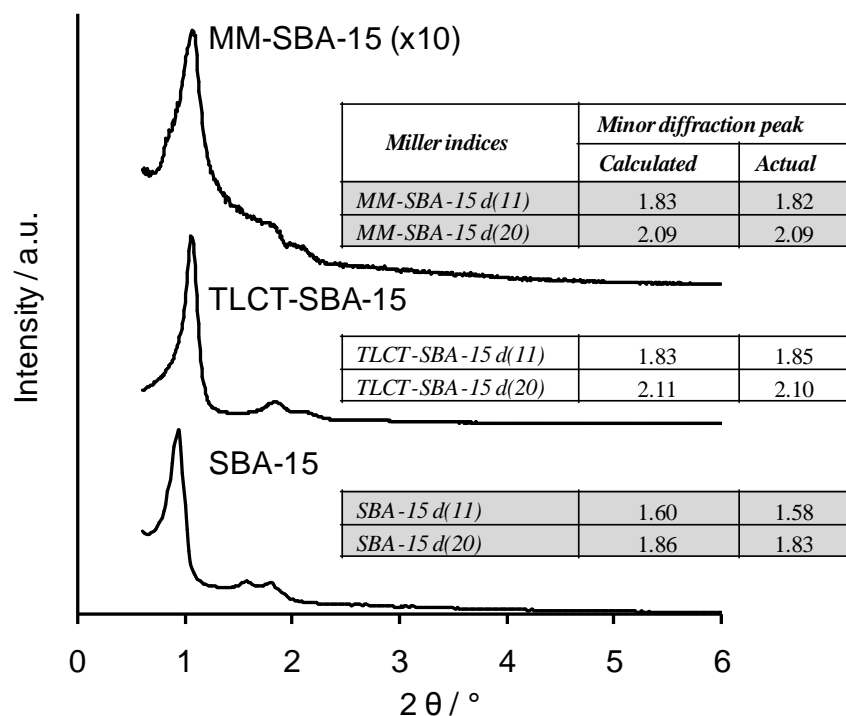


**Figure 4.2** - Stacked Low Angle XRD patterns of MM-SBA-15, TLCT-SBA-15 and SBA-15

**Table 4.1** - Textural properties of parent silica supports

Sample	Surface area / $m^2 g^{-1(a)}$	Micropore surface area / $m^2 g^{-1(b)}$	Mesopore Diameter / $nm^{(c)}$	Cell parameter / $nm^{(d)}$
MM-SBA-15	576 ( $\pm 57$ )	191 ( $\pm 19$ )	3.8	7.2 ( $\pm 0.2$ )
TLCT-SBA-15	528 ( $\pm 53$ )	103 ( $\pm 13$ )	5.1	7.3 ( $\pm 0.2$ )
SBA-15	950 ( $\pm 95$ )	465 ( $\pm 47$ )	5.7	9.4 ( $\pm 0.2$ )

<sup>(a)</sup>  $N_2$  BET, <sup>(b)</sup>  $N_2$  t-plot, <sup>(c)</sup> BJH desorption branch of isotherm, <sup>(d)</sup> Low angle XRD

Cell parameters for both supports were determined from the strongest reflection using Bragg's Law (**Chapter 2 Equation 2.1**) and the results presented in **Table 4.1**. The first order reflection is shifted to higher angle for MM-SBA-15 and TLCT-SBA-15 with respect to SBA-15, indicating a decrease in  $d(10)$  spacing and corresponding contraction in both the cell parameter and pore spacing. This decrease could reflect a drop in pore diameter and/or pore wall thickness. Peak intensities for MM-SBA-15

are much weaker than for TLCT-SBA-15 and SBA-15, due to the lower number of pore repeat units, a consequence of the macropores disrupting the mesopore framework.

#### 4.2.2.2 Nitrogen porosimetry

Textural differences between the supports were explored by N<sub>2</sub> porosimetry, with the resulting isotherms shown in **Figure 4.3**. As seen for SBA-15, both TLCT-SBA-15 and MM-SBA-15 exhibit type 4 isotherms with H1 hysteresis,<sup>[5]</sup> characteristic of mesoporous supports with uniform mesopore diameters. Furthermore, MM-SBA-15 displays a second hysteresis at elevated relative pressures reflecting partial filling/emptying of the macropore network.

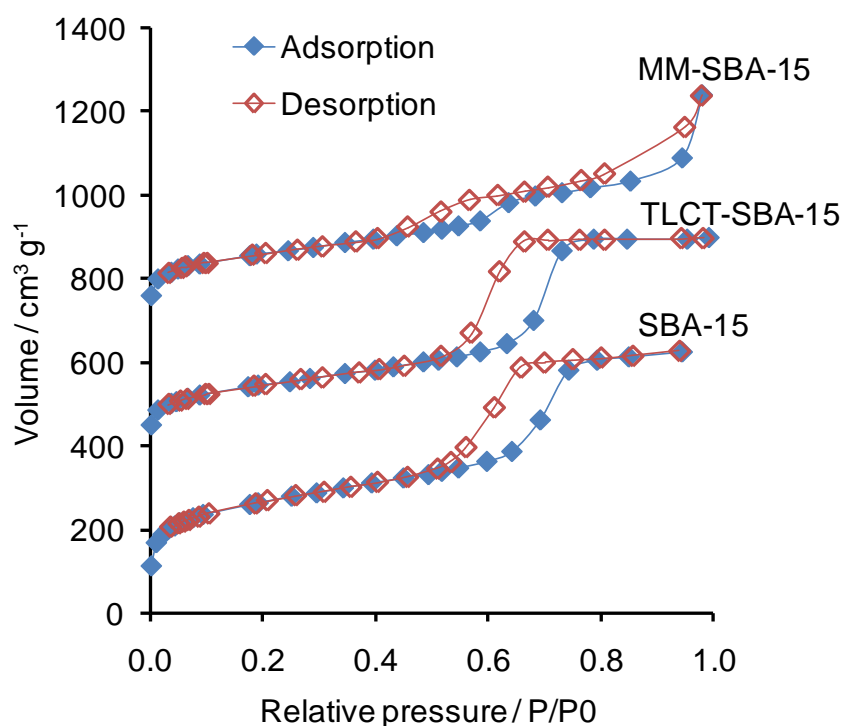


**Figure 4.3** – Stacked isotherm of MM-SBA-15 (offset by 700 cm<sup>3</sup> g<sup>-1</sup>), TLCT-SBA-15 (offset by 400 cm<sup>3</sup> g<sup>-1</sup>) and SBA-15

The BET<sup>[6]</sup> and BJH<sup>[7]</sup> methods were used to determine respective surface areas and average mesopore diameters, with the results presented in **Table 4.1**. The BET surface areas for MM-SBA-15 and TLCT-SBA-15 are significantly lower than for SBA-15, which appears to result from a decrease in their microporosity, as

determined by the t-Plot method.<sup>[8]</sup> Another interesting observation is the apparent decrease in mesopore diameter of MM-SBA-15 relative to the other two samples. This appears initially surprising since all three silicas are synthesised from the same surfactant template. However, during hydrothermal treatment, in which pore swelling occurs,<sup>[9]</sup> confinement of the mesopore phase in voids between the polystyrene macropore bead template may restrict this swelling process. This in turn could account for the smaller cell parameter (low angle XRD). Pore size distributions, calculated from the desorption branch of the isotherm, are presented in **Figure 4.4**, and evidence narrow mesopore distributions for TLCT-SBA-15 and MM-SBA-15.

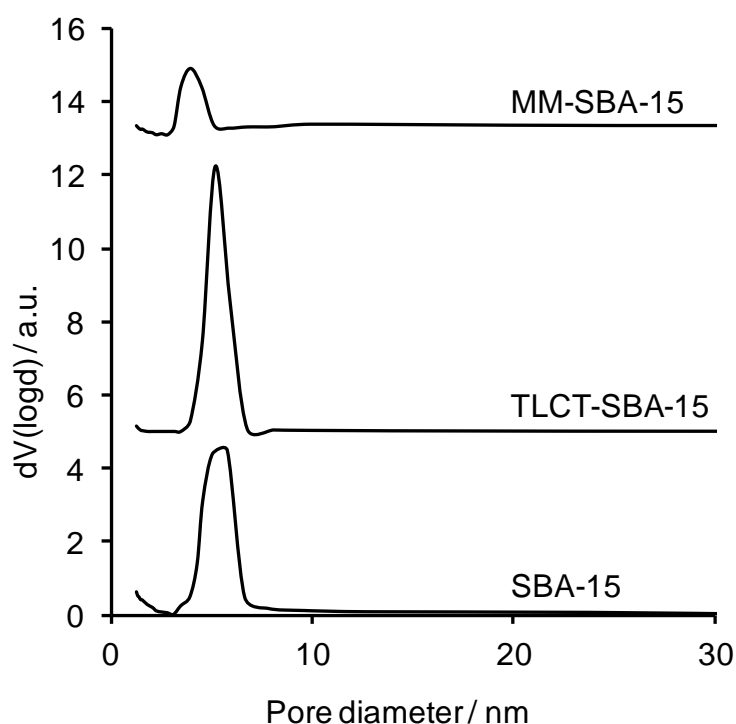


**Figure 4.4** – Stacked BJH pore size distribution plots (MM-SBA-15 and TLCT-SBA-15 offset by 13 and 5 respectively)

$N_2$  porosimetry at high vacuum ( $\sim 0.6$  Pa) was utilised to further study the microporosity of the new silicas. The resulting isotherms were fitted to those on known standards (fitting errors are less than 0.7 %) to enable calculation of micro- and mesopore diameters. These plots and their associated fits are presented in **Figure 4.5** (conventional SBA-15 can be viewed in **Chapter 3 Figure 3.4(a)**). Application

of this approach to determine microporosity was verified in **Chapter 3 (Figure 3.4(e))** for MCM-41 silica, which exhibits only mesoporosity.<sup>[10, 11]</sup>

Comparison of the pore size distribution plots for MM-SBA-15 and SBA-15 reveals that while both contain significant microporosity; MM-SBA-15 possesses less, with micropore surface areas of 379 m<sup>2</sup> g<sup>-1</sup> (SBA-15) and 172 m<sup>2</sup> g<sup>-1</sup> (MM-SBA-15). The reduced microporosity of MM-SBA-15 presumably reflects the hard macroporous template inhibiting micropore formation, unlike the surfactant template throughout the conventional mesoporous SBA-15 network.<sup>[12-14]</sup> Microporosity within SBA-15 materials can be modified through the hydrothermal step<sup>[9, 14]</sup> or the addition of co-surfactants.<sup>[15]</sup> Since identical synthesis conditions were employed for SBA-15 and MM-SBA-15, their differing microporosities cannot be accounted for by such possibilities. The synthesis conditions employed for TLCT-SBA-15 result in greatly reduced microporosity, with a calculated micropore surface area of 98 m<sup>2</sup> g<sup>-1</sup> as anticipated from the t-plot results. This may arise from elimination of the hydrothermal treatment in the conventional preparation: lowering the hydrothermal treatment temperature reportedly decreases the interaction between polyethylene oxide chains of neighbouring micelles in SBA-15 thereby suppressing micropores.<sup>[14]</sup> Omission of the hydrothermal process is also reported to significantly decrease microporosity.<sup>[9]</sup> The average micropore diameters of all three silicas range from 1.0 to 1.4 nm in accordance with the literature,<sup>[14]</sup> however the possibility of micropores ≤0.5 nm cannot be discounted<sup>[10]</sup> as these lie below the analytical detection limit employed. Average mesopore diameters of 4.7 nm (MM-SBA-15) and 6.0 nm (TLCT-SBA-15) concur with the BJH values in **Table 4.1**.

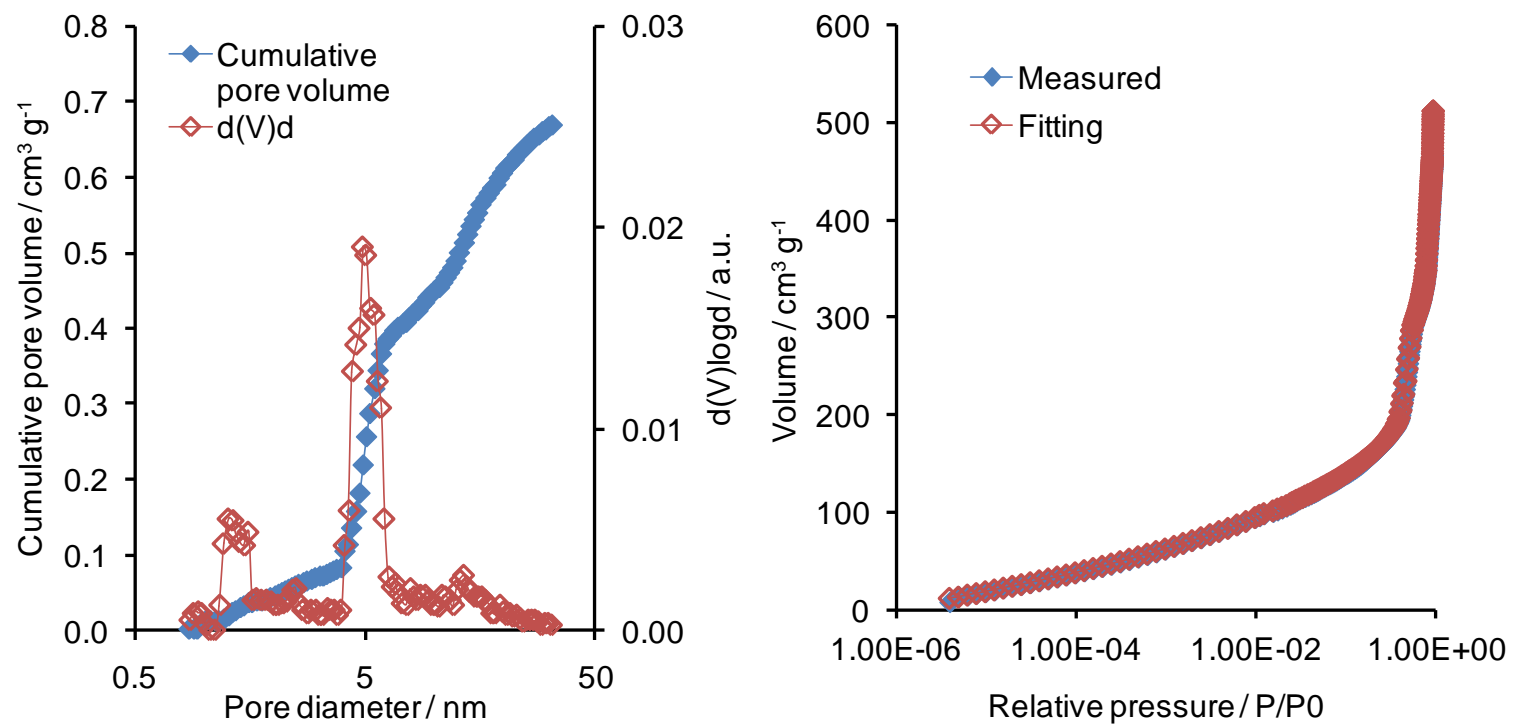


**Figure 4.5 (a)** – Pore size distribution and fitting plots for MM-SBA-15 (fitting error 0.3 %)

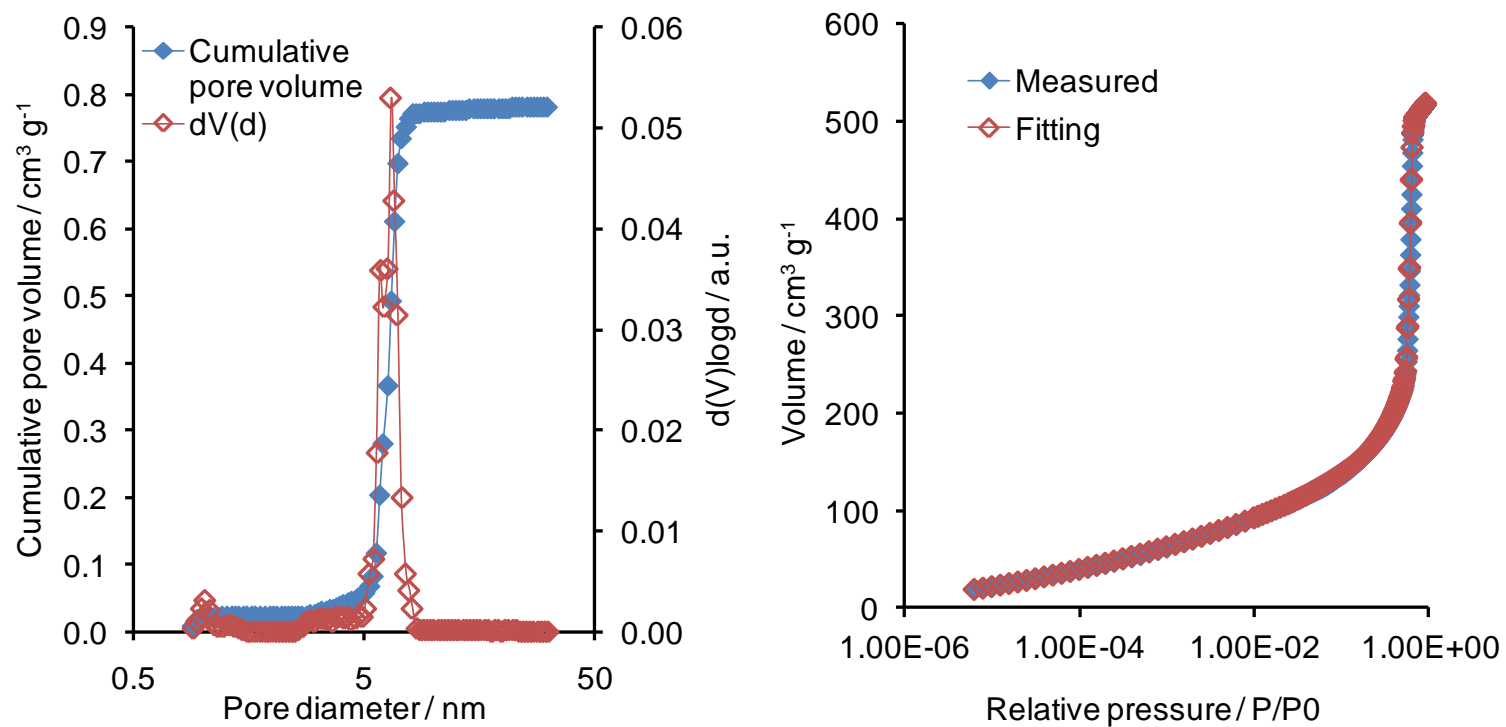


**Figure 4.5 (b)** – Pore size distribution and fitting plots for TLCT-SBA-15 (fitting error 0.7 %)

### 4.2.2.3 Scanning electron microscopy

Support morphology and macropores (where present) were imaged by SEM with **Figure 4.6** showing representative images of the three supports.

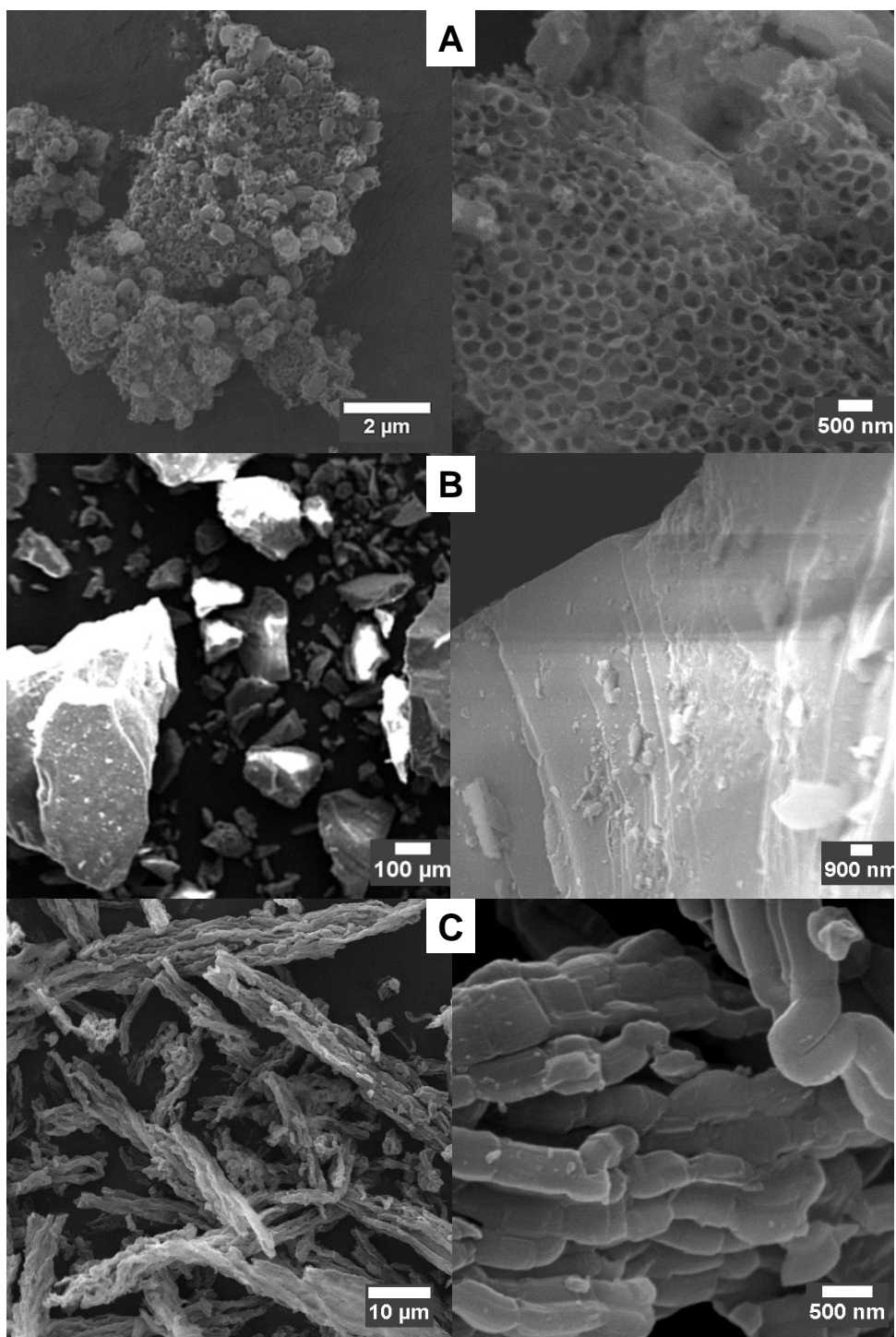


**Figure 4.6** – Representative SEM images of (A) MM-SBA-15, (B) TLCT-SBA-15 and (C) SBA-15

SEM images of MM-SBA-15 demonstrate the successful incorporation of a macropore network throughout silica crystallites,<sup>[2]</sup> which the preceding porosimetry show also contain the characteristic SBA-15 mesopore structure. The average macropore diameter was calculated as 260 ( $\pm 25$ ) nm, comparable to the average polystyrene sphere size, showing neither macropore contraction nor expansion occurs during high temperature calcination. Closer inspection, and comparison with SBA-15, indicates >75-80 % of crystallites exhibit the desired macropore network. In contrast, TLCT-SBA-15 comprises large angular crystallites spanning a very wide particle size distribution from one to hundreds of microns, with a corresponding large distribution of (extremely long) pore lengths expected. In contrast, SBA-15 has a straw like morphology, with crystallites a few hundred microns long. Closer inspection at high magnification reveals curves within the straw-like particles, which in some case double-back on themselves. Similar observations have been made for SBA-15 prepared under comparable conditions.<sup>[16-18]</sup>

#### 3.2.2.4 Transmission electron microscopy

Representative TEM images of MM-SBA-15 and TLCT-SBA-15 are shown in **Figure 4.7** (SBA-15 images are shown in **Chapter 3 Figure 3.5**).

Macropores are clearly incorporated throughout MM-SBA-15, with an average diameter of 280 ( $\pm 18$ ) nm, matching the SEM results. The hexagonal mesopore packing and channel structures of the *p6mm* space group are also evident, confirming successful synthesis of a typical SBA-15 mesopore structure within the framework, and thus successful synthesis of a hierarchical macroporous-mesoporous silica and not two independent phases. TLCT-SBA-15 displays the channel structures typical of SBA-15, although the associated hexagonal packing could not be observed due to crystallite orientation. Average pore spacings of 9.4 ( $\pm 0.3$ ) nm and 9.5 ( $\pm 0.4$ ) nm, and pore diameters of 4.3 ( $\pm 0.3$ ) nm and 5.6 ( $\pm 0.3$ ) nm, were obtained for MM-SBA-15 and TLCT-SBA-15 respectively as predicted by low angle XRD and porosimetry.

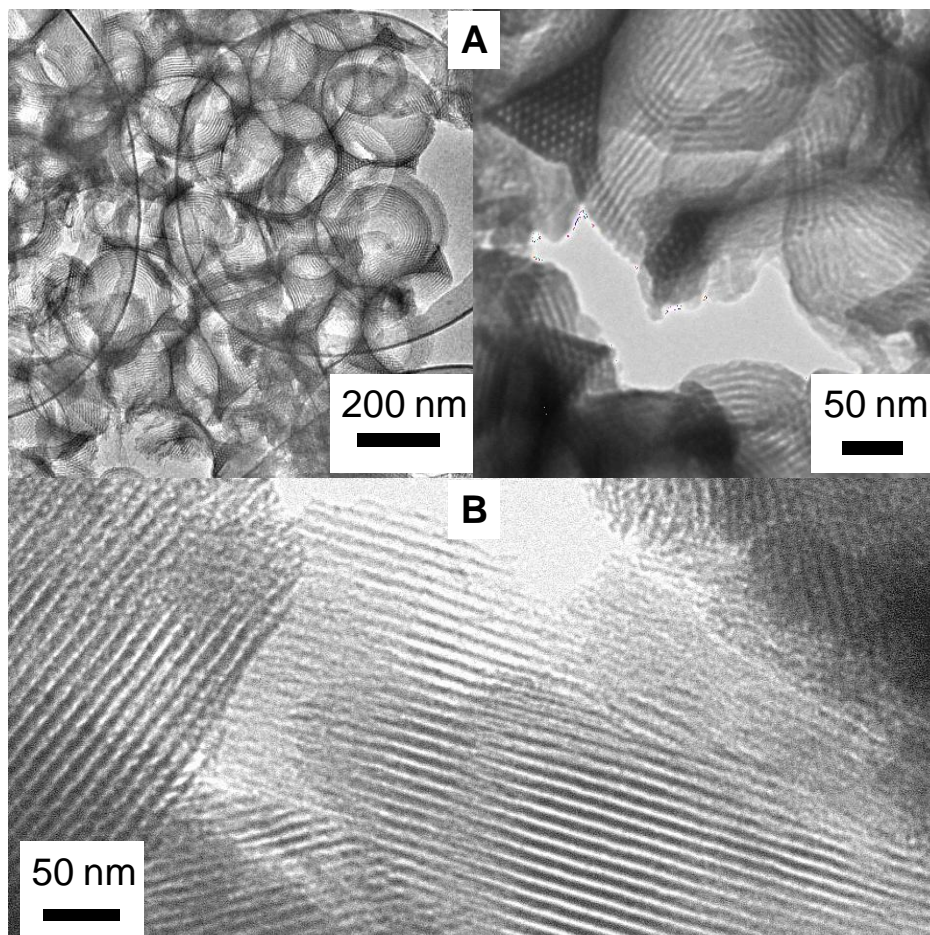


**Figure 4.7** – Representative bright field TEM images of (A) MM-SBA-15 and (B) TLCT-SBA-15

### **4.2.3 Characterisation of Pd impregnated silicas supports**

The incipient wetness technique, as previously used in **Chapter 3**, was utilised to impregnate the two silica supports with desired Pd loadings of 2.5-0.05 wt% (MM-SBA-15) and 5-0.05 wt% (TLCT-SBA-15).

#### **4.2.3.1 Inductively coupled plasma optical emission spectroscopy**

Bulk Pd loadings were determined by Medac analytical services Ltd via ICP-OES, after initial digestion in hydrogen fluoride. **Table 4.2** confirms good agreement between the intended and real loadings for both new silicas.

**Table 4.2** – Comparison of desired and actual bulk metal loadings

<i>Support</i>	<i>Target loading / wt%</i>	<i>Measured loading / wt%</i>
<i>MM-SBA-15</i>	<i>2.5</i>	<i>1.87</i>
<i>MM-SBA-15</i>	<i>1</i>	<i>0.78</i>
<i>MM-SBA-15</i>	<i>0.5</i>	<i>0.43</i>
<i>MM-SBA-15</i>	<i>0.1</i>	<i>0.10</i>
<i>MM-SBA-15</i>	<i>0.05</i>	<i>0.05</i>
<i>TLCT-SBA-15</i>	<i>5</i>	<i>4.89</i>
<i>TLCT-SBA-15</i>	<i>0.5</i>	<i>0.46</i>
<i>TLCT-SBA-15</i>	<i>0.05</i>	<i>0.06</i>

#### 4.2.3.2 Powder X-ray diffraction

**Figure 4.8** shows the low angle XRD patterns for the Pd-impregnated MM-SBA-15 and TLCT-SBA-15 series. Long range pore ordering of the parent supports is preserved, with no evidence for unit cell growth or contraction.

Information on Pd crystalline phases was obtained from analogous wide angle powder diffraction, shown in **Figure 4.9**. As observed for the Pd/silicas in **Chapter 3**, a broad reflection was observed from amorphous silica at angles  $<35^\circ$ .<sup>[19]</sup> No Pd phases were discernible for the MM-SBA-15 series, placing an upper limit of  $\sim 2$  nm for any Pd nanoparticles present within this support,<sup>[20]</sup> as observed for low loadings on SBA-15 in **Figure 3.7(a)**. In contrast, metallic Pd reflections were apparent at  $39.9^\circ$  and  $46.5^\circ$ , corresponding to Pd(111) and Pd(200) reflections, for the highest loading TLCT-SBA-15 samples. An average diameter of  $3.4 (\pm 0.2)$  nm was calculated for these metallic nanoparticles (from **Chapter 2 Equation 2.2**),<sup>[21]</sup> an increase over comparable Pd loadings on SBA-15 (**Table 3.3**).

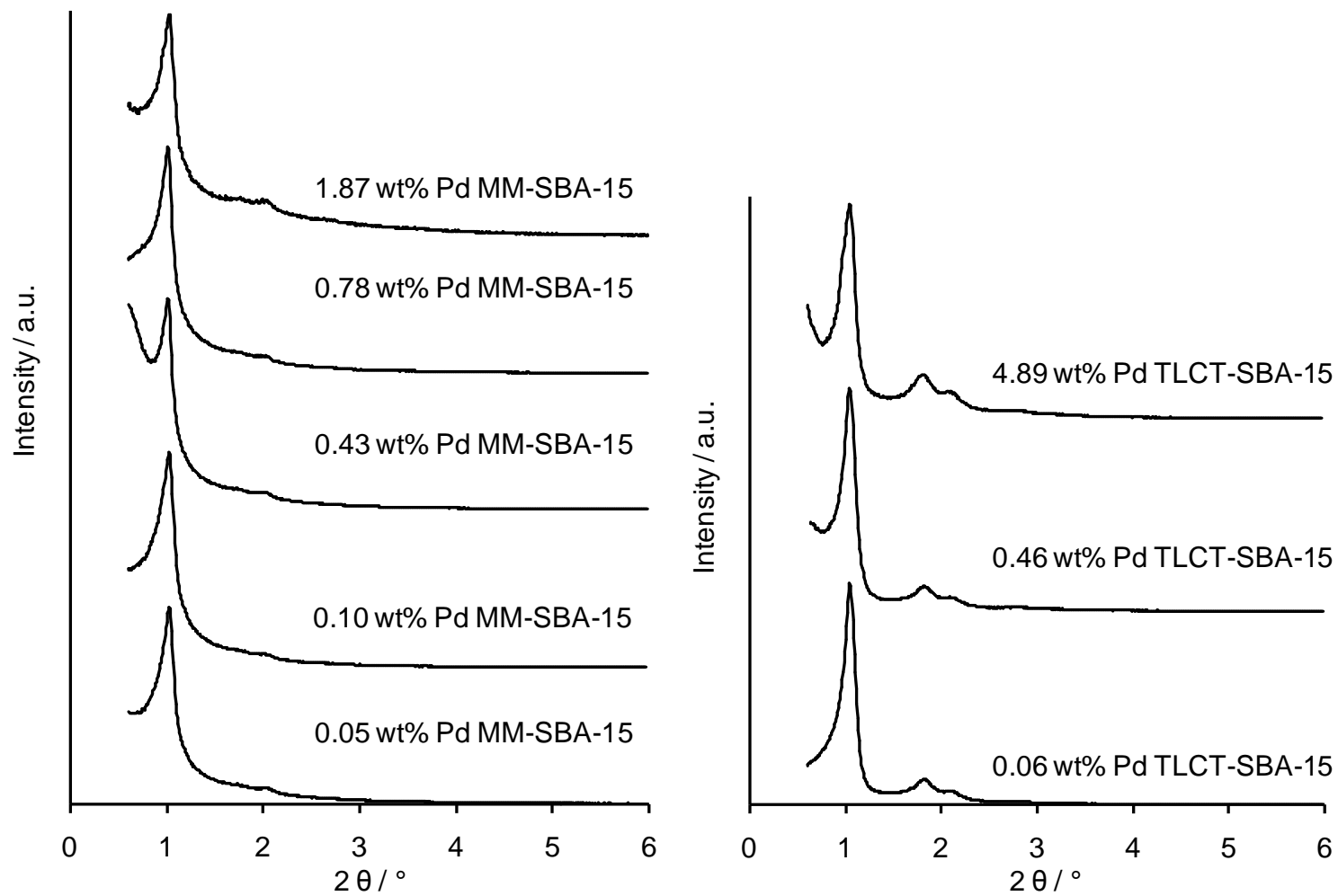


**Figure 4.8** - Stacked low angle XRD plots for Pd/MM-SBA-15 and Pd/TLCT-SBA-15

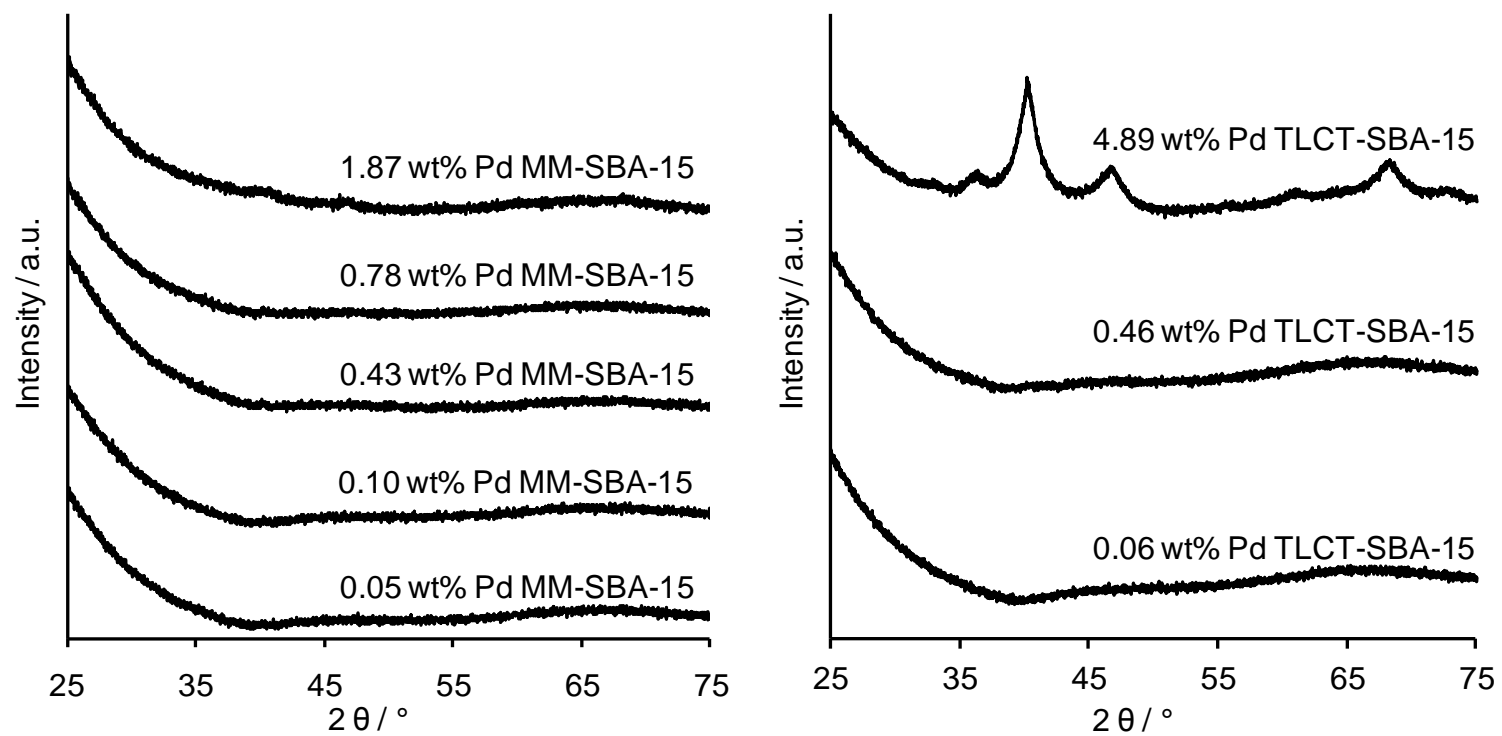


**Figure 4.9** - Stacked wide angle XRD plots for Pd/MM-SBA-15 and Pd/TLCT-SBA-15

### 4.2.3.3 Nitrogen porosimetry

$N_2$  isotherms of the Pd/MM-SBA-15 and Pd/TLCT-SBA-15 series are shown in **Figure 4.10**. The isotherm type and hysteresis of the parent silica support is retained, hence no pore collapse or restructuring occurs during metal impregnation, consistent with the stability of conventional SBA-15 (**Chapter 3 Figure 3.8(a)**).

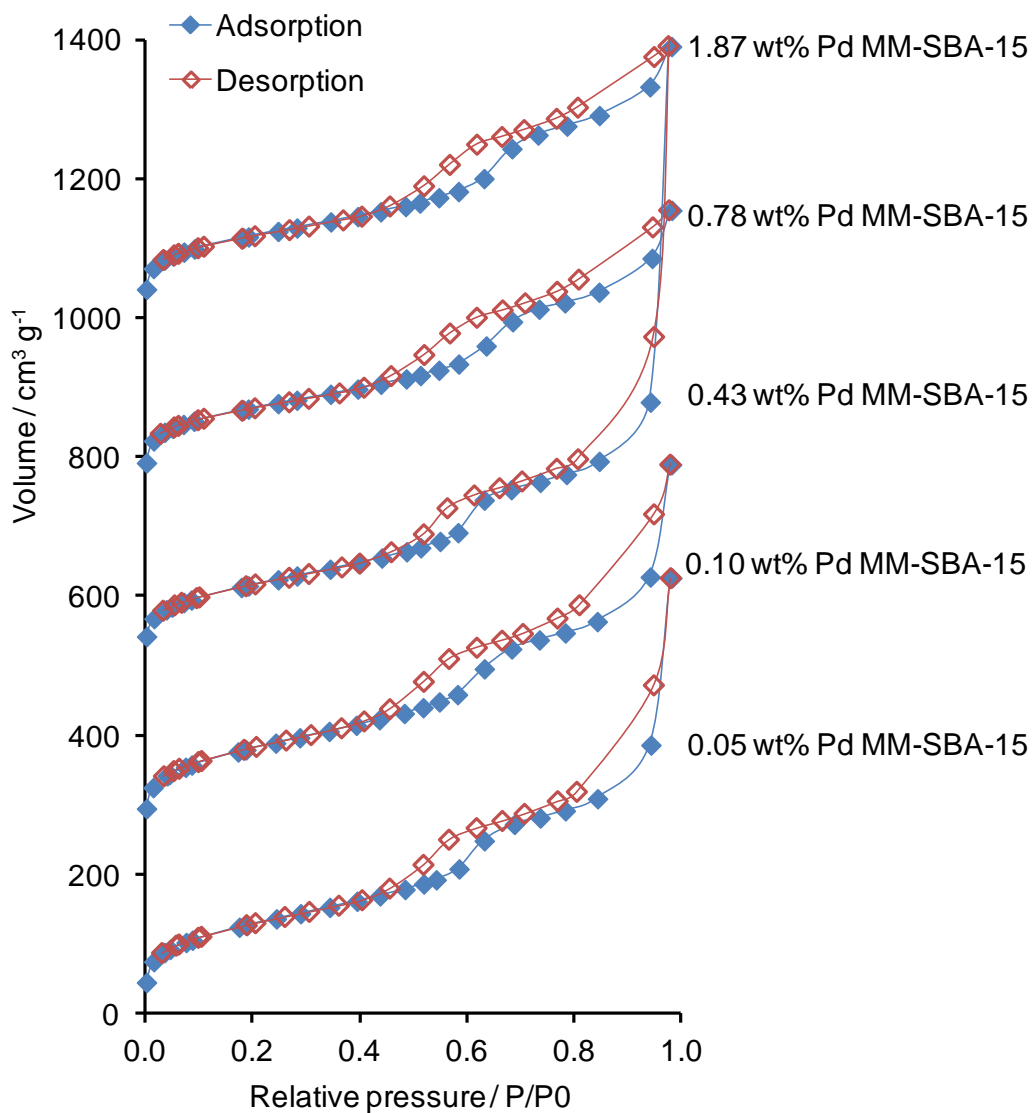


**Figure 4.10 (a)** - Stacked isotherm plots for Pd/MM-SBA-15 (samples consecutively offset by  $250 \text{ cm}^3 \text{ g}^{-1}$  with each increase in metal loading)

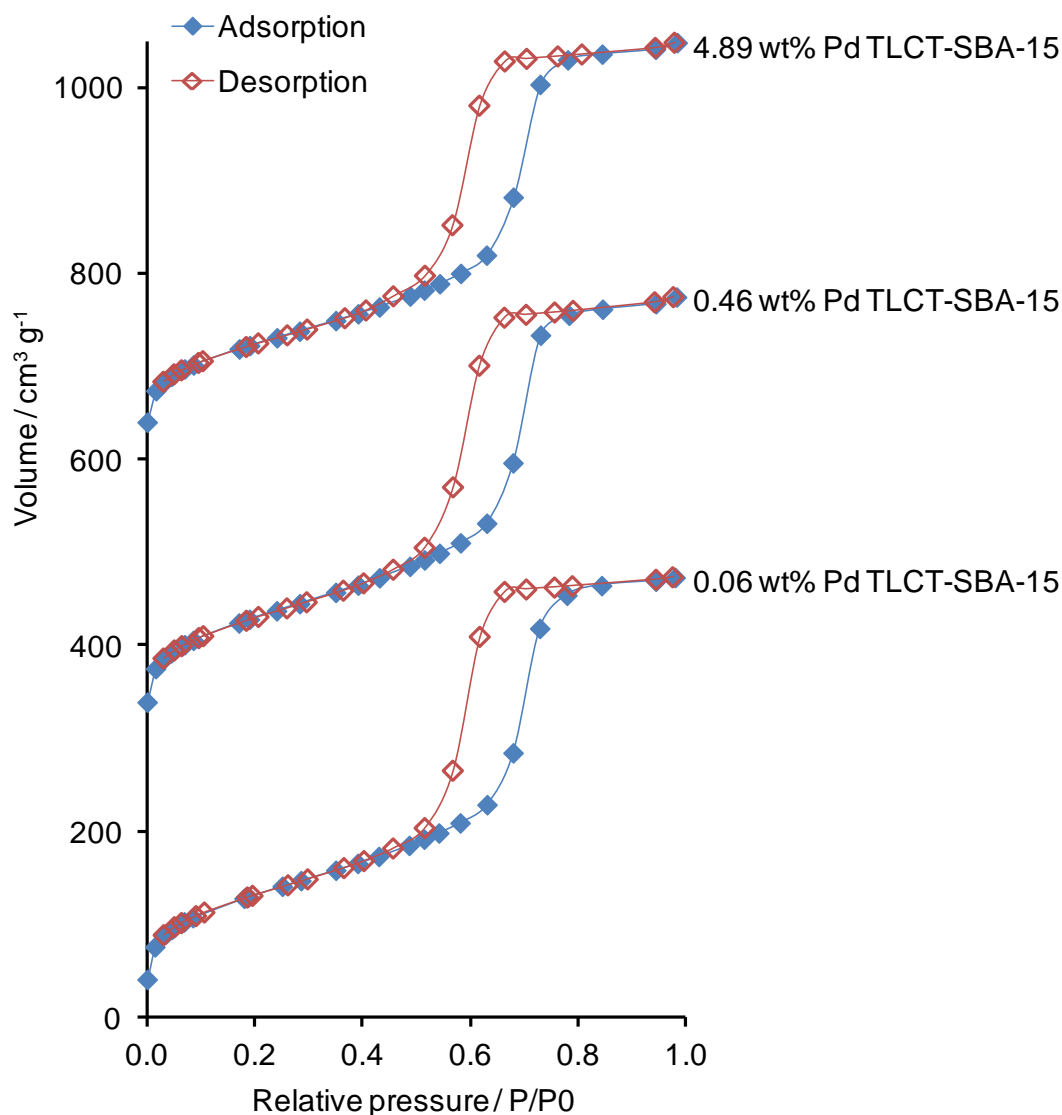


**Figure 4.10 (b)** - Stacked isotherm plots for Pd/TLCT-SBA-15 (samples consecutively offset by  $300 \text{ cm}^3 \text{ g}^{-1}$  with each increase in metal loading)

The most striking textural effect of Pd impregnation upon mesoporous silicas noted in **Chapter 3 (Figure 3.9)** was the inverse relationship between loading and BET surface area. The same relationship was thus explored, with the findings reported in **Figure 4.11** revealing this to be greatly suppressed relative to SBA-15. In **Chapter 3** the decreasing surface area was shown to arise from the loss of microporosity (**Figure 3.10**). Micropore surface areas were again measured to investigate any difference between the supports, **Figure 4.12**. An inverse correlation between loading and microporosity is again observed, though the effect is to a lesser extent than before, reflecting the lower degree of microporosity in the parent

supports, **Table 4.1**. The different BET dependency on Pd loading for MM-SBA-15 and TLCT-SBA-15, compared to SBA-15, is thus attributable to the lower microporosity of the parent silicas, which in turn lowers their total surface areas.

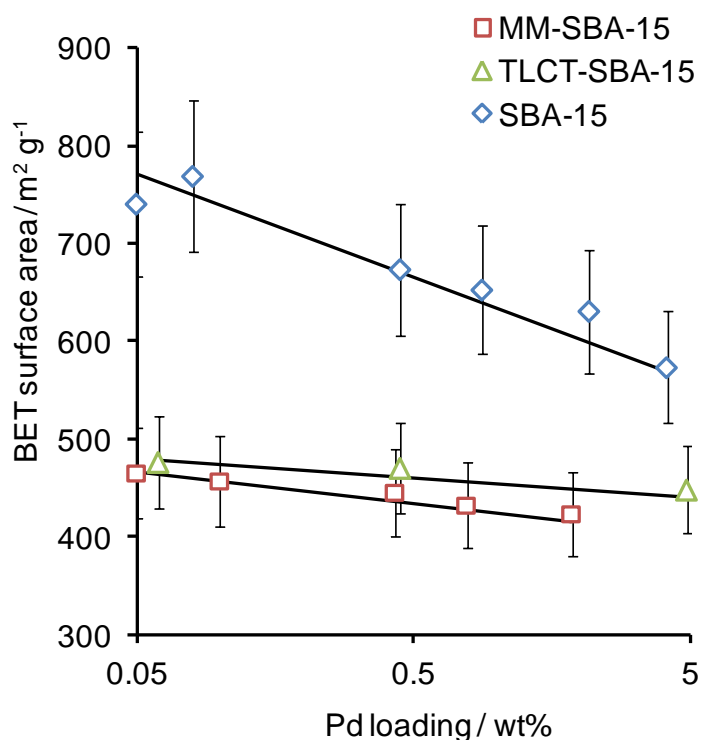


**Figure 4.11** - Effect of metal loading on BET support surface area

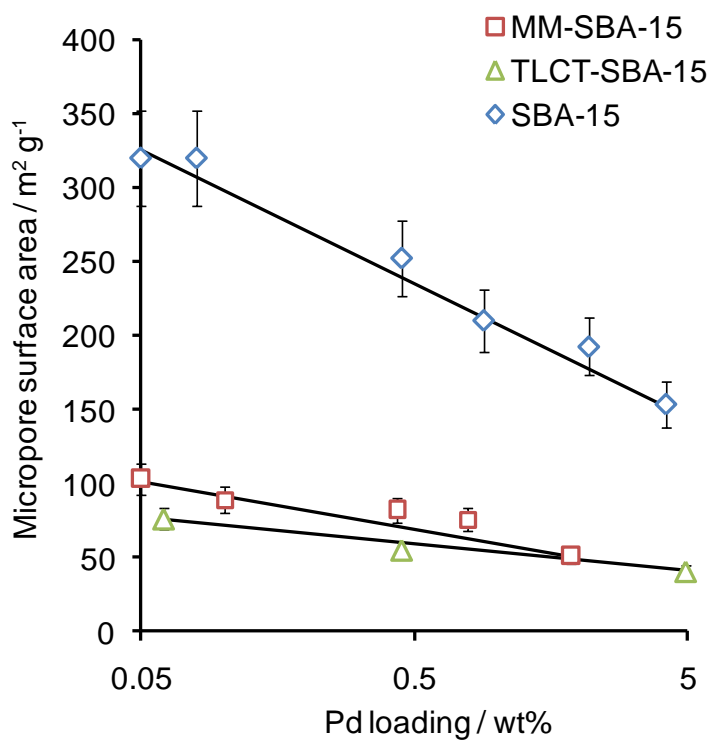


**Figure 4.12** - Effect of metal loading on micropore surface area

**Figure 4.13** shows the BJH pore size distributions for MM-SBA-15 and TLCT-SBA-15, confirming that Pd impregnation does not affect the average pore size or narrow pore size distributions of the resultant new Pd/silicas.

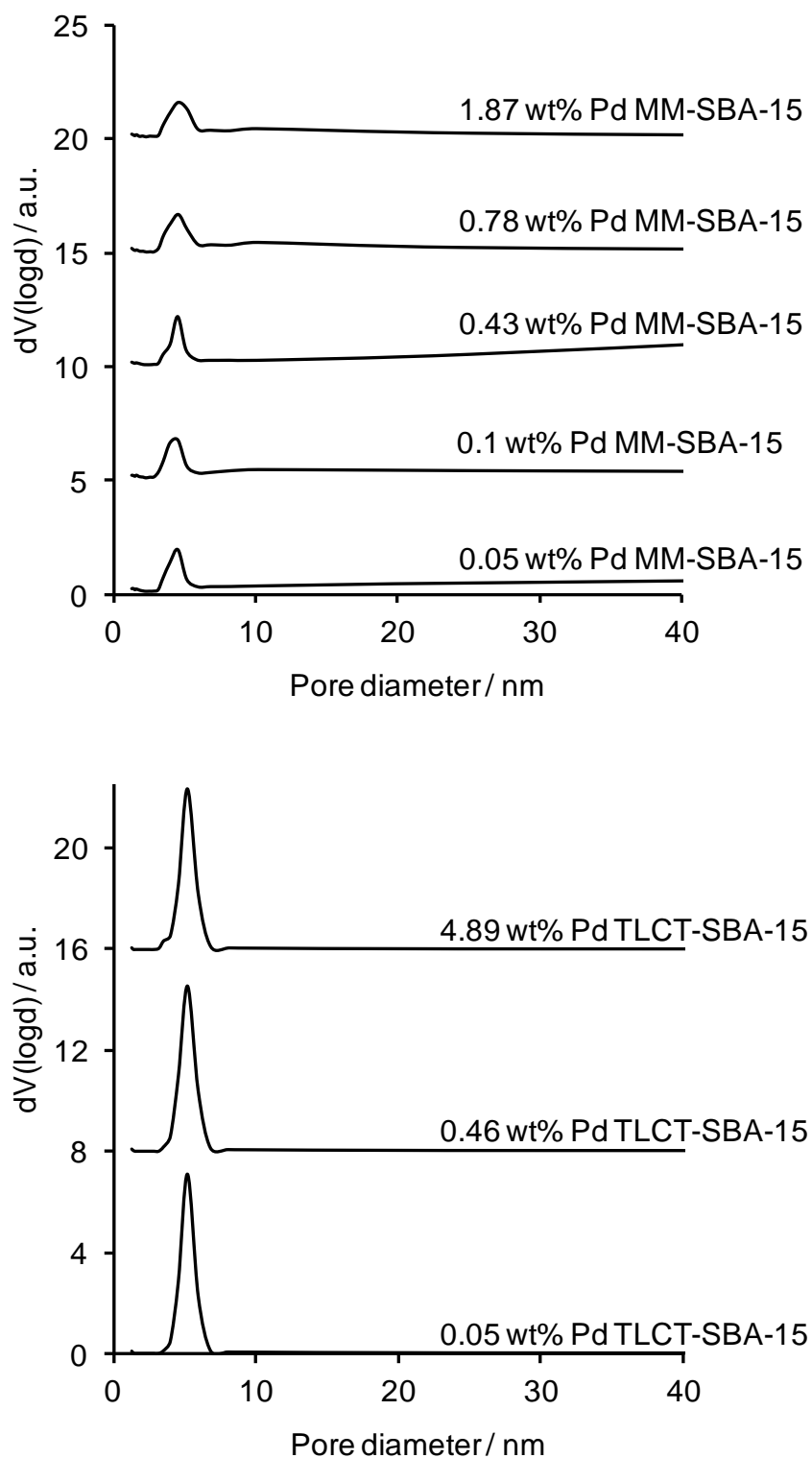


**Figure 4.13** – Stacked BJH plots for Pd/MM-SBA-15 and Pd/TLCT-SBA-15 (samples consecutively offset by 5 (MM-SBA-15) and 8 (TLCT-SBA-15))

#### 4.2.3.4 Carbon monoxide chemisorption

The influence of silica architecture on Pd nanoparticle properties was probed by CO chemisorption, to determine metal dispersion (**Chapter 2 Equation 2.6**) and average Pd particle size (**Chapter 2 Equation 2.7**).

**Table 4.3** – Dispersion and average Pd particle size from CO titrations

<i>Support</i>	<i>Loading / wt%</i>	<i>Dispersion / %</i>	<i>Ave. particle size / nm</i>
<i>MM-SBA-15</i>	<i>1.87</i>	<i>62 (± 1)</i>	<i>1.8 (± 0.1)</i>
<i>MM-SBA-15</i>	<i>0.78</i>	<i>68 (± 1)</i>	<i>1.6 (± 0.1)</i>
<i>MM-SBA-15</i>	<i>0.43</i>	<i>71 (± 1)</i>	<i>1.6 (± 0.1)</i>
<i>MM-SBA-15</i>	<i>0.10</i>	<i>78 (± 2)</i>	<i>1.4 (± 0.1)</i>
<i>MM-SBA-15</i>	<i>0.05</i>	<i>83(± 4)</i>	<i>1.2 (± 0.1)</i>
<i>TLCT-SBA-15</i>	<i>4.89</i>	<i>32 (± 1)</i>	<i>3.0 (± 0.1)</i>
<i>TLCT-SBA-15</i>	<i>0.46</i>	<i>54 (± 1)</i>	<i>2.1 (± 0.1)</i>
<i>TLCT-SBA-15</i>	<i>0.06</i>	<i>72 (± 4)</i>	<i>1.5 (± 0.1)</i>
<i>SBA-15</i>	<i>4.14</i>	<i>37 (± 1)</i>	<i>2.9 (± 0.1)</i>
<i>SBA-15</i>	<i>2.17</i>	<i>43 (± 1)</i>	<i>2.6 (± 0.1)</i>
<i>SBA-15</i>	<i>0.89</i>	<i>52 (± 1)</i>	<i>2.3 (± 0.1)</i>
<i>SBA-15</i>	<i>0.45</i>	<i>56 (± 1)</i>	<i>1.9 (± 0.1)</i>
<i>SBA-15</i>	<i>0.08</i>	<i>64 (± 1)</i>	<i>1.7 (± 0.1)</i>
<i>SBA-15</i>	<i>0.05</i>	<i>78 (± 4)</i>	<i>1.4 (± 0.1)</i>

Pd dispersion (particle size) increases (decreases) with falling metal loading for both Pd/TLCT-SBA-15 and Pd/MM-SBA-15, as observed over the mesoporous silicas in **Chapter 3**. Closer examination of the data in **Figure 4.11** and **Table 4.3** reveal that BET surface area is not the sole parameter regulating metal dispersion, since the lower surface area MM-SBA-15 affords more highly dispersed Pd nanoparticles than the higher area conventional SBA-15, attaining dispersion levels comparable to those Pd/SBA-16 and Pd/KIT-6 from **Chapter 3**. This likely reflects the greater mesopore accessibility and more uniform precursor distribution during Pd impregnation, due to the complementary interpenetrating macropore network and resulting shorter mesopore channel length, within Pd/MM-SBA-15, akin to the enhanced dispersion observed using interconnected mesoporous silica supports. Higher cobalt and molybdenum dispersions have also been reported over macroporous-mesoporous carbons than mesoporous carbon.<sup>[22]</sup> In contrast, the Pd/

TLCT-SBA-15 series exhibits much poorer metal dispersion. This may arise from the genesis of large metallic Pd crystallites during impregnation, and associate poor blockage, which could hinder permeation of the Pd precursor solution through the pore network. A related phenomenon has been observed during CO<sub>2</sub> adsorption into different SBA-15 materials.<sup>[23]</sup> In the case of metal nanoparticles, Co dispersion has been shown to decrease with SBA-15 pore length due to enhanced sintering driven by longer NO<sub>x</sub> and H<sub>2</sub>O residence times during calcination and reduction pre-treatments;<sup>[24]</sup> these such aggressive procedures are known to increase particle size.<sup>[25]</sup>

#### 4.2.3.5 Scanning transmission electron microscopy

HAADF-STEM was utilised to visualise supported Pd clusters. **Figure 4.14** shows representative micrographs of 0.78 wt% Pd/MM-SBA-15 and 0.46 wt% Pd/TLCT-SBA-15 samples. Corresponding bright field images and particle size histograms are also shown.

Pd particles in the HAADF-STEM images appear as bright spots due to their high atomic number,<sup>[26]</sup> with silica walls and pores appearing as grey and dark grey/black areas. Pd nanoparticles supported on MM-SBA-15 appear well distributed over the support, whereas the TLCT-SBA-15 exhibits clustering near the support perimeter (and possibly pore entrances). Resulting mean particle sizes of 1.6 and 2.2 nm for MM-SBA-15 and TLCT-15 respectively are in good agreement with CO chemisorption. The particle size distributions reveal a significantly wider distribution for 0.46 wt% Pd/TLCT-SBA-15 than the comparable Pd/MM-SBA-15, and the three conventional mesoporous silicas in **Chapter 3 (Figure 3.14)**, demonstrating poorer Pd impregnation. Bright-field images show the underlying new silica support structures were retained during impregnation in accordance with XRD and porosimetry.

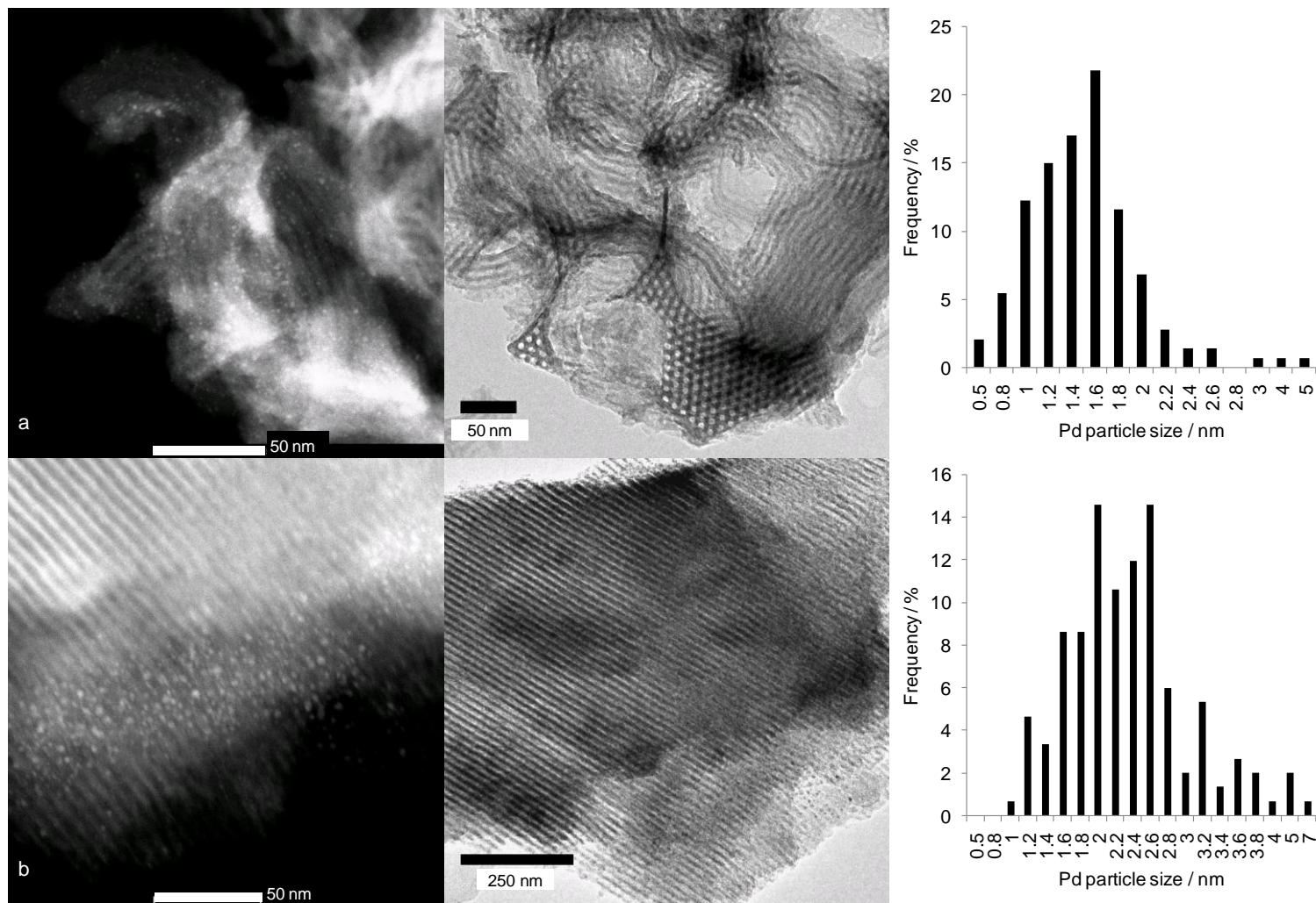


**Figure 4.14** - HAADF-STEM images (left) of (A) 0.78 wt% Pd/MM-SBA-15 and (B) 0.46 wt% Pd/TLCT-SBA-15 with particle size distributions (right) (150-200 particles) and equivalent TEM bright field images (centre).

### 4.2.3.6 X-ray photoelectron spectroscopy

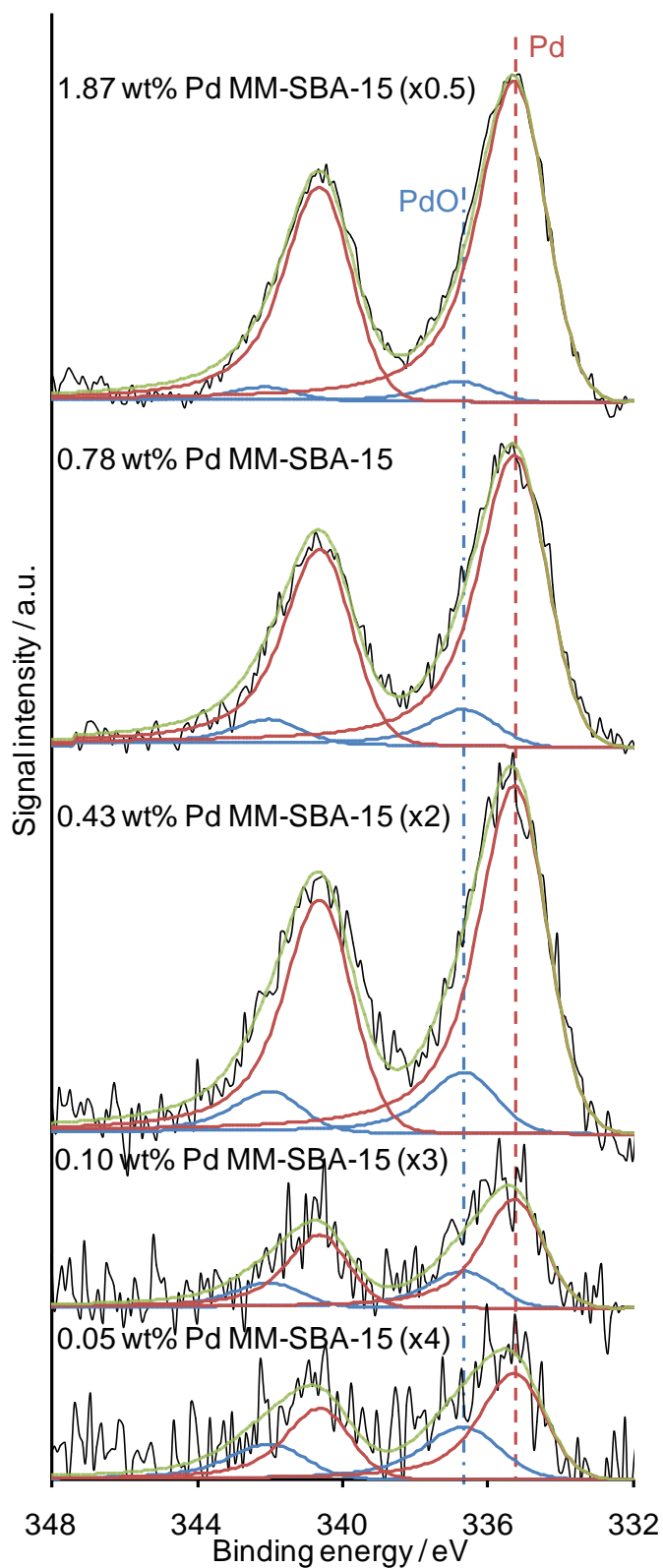


**Figure 4.15 (a)** - Stacked Pd 3d XPS plots of Pd/MM-SBA-15. PdO fit shown in blue; Pd metal fit in red.

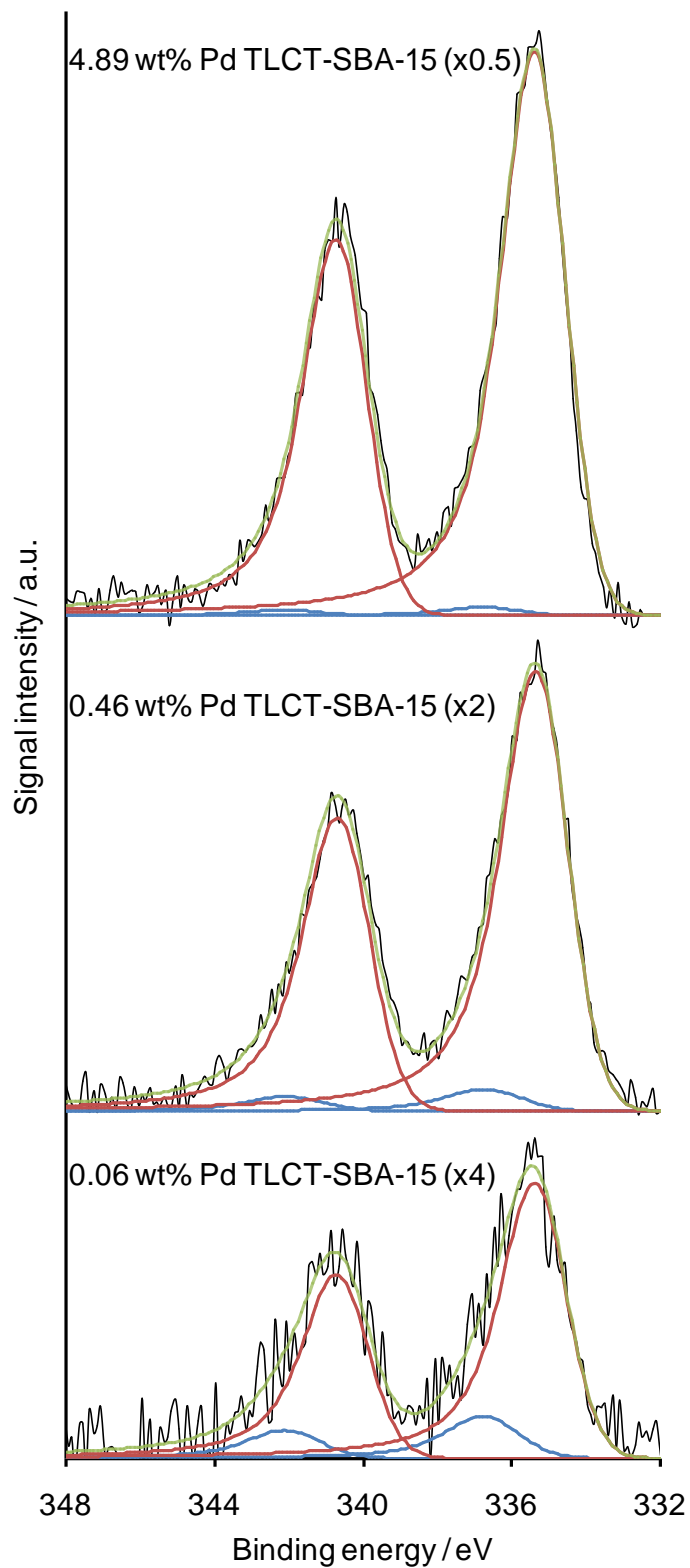


**Figure 4.15 (b)** - Stacked Pd 3d XPS plots of Pd/TLCT-SBA-15 series. PdO fit shown in blue; Pd metal fit in red

The surface oxidation state of supported Pd nanoparticles was evaluated using XPS. Energy referenced (to adventitious carbon at 284.6 eV and cross check to SiO<sub>2</sub> at 103.4 eV) and background subtracted Pd XP spectra for the MM-SBA-15 and TLCT-SBA-15 series are presented in **Figure 4.15**. The characteristic Pd 3d<sub>3/2,5/2</sub> spin-orbit components ( $\Delta BE = 5.25$  eV)<sup>[27]</sup> were detected in all samples, with peak broadening observed with falling metal loadings, arising from the emergence of surface PdO at 336.8 eV and concomitant loss of metallic Pd at 335.4 eV. Peak fitting enables these species to be quantified as in **Chapter 3**.

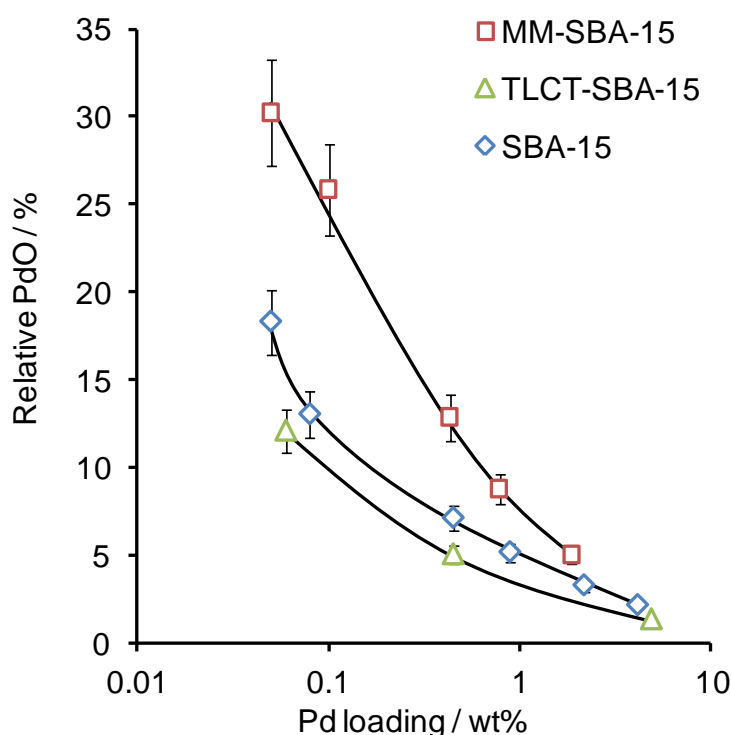


**Figure 4.16** – Relative PdO content as a function of Pd loading and support

**Figure 4.16** shows a strong inverse correlation between Pd loading and oxide content, in accordance with **Chapter 3** and the literature for Pd on related supports.<sup>[1, 28, 29]</sup> This dependence was greater for the MM-SBA-15 than TLCT-SBA-15 families, mirroring the sensitivity of their associated Pd dispersions (believed to drive the metal→oxide transition) on loading. The absolute PdO content of Pd/TLCT-SBA-15s was also lower than that for comparable Pd/SBA-15 materials, also comprehensible in terms of their respective low Pd dispersions. Since **Chapter 3** uncovered a striking relationship between selox activity (normalised per gram Pd)

and surface PdO content (from XPS), then in the absence of mass-transport limitations, one would anticipate that the Pd/MM-SBA-15 series should outperform both Pd/SBA-15 and Pd/TLCT-SBA-15 counterparts. It is interesting to note that despite a total surface area only half that of KIT-6 or SBA-16, the surface PdO content within Pd/MM-SBA-15 is almost as high as these interconnected silicas, demonstrating the importance of support accessibility in achieving small and uniformly distributed integrated nanoparticles.

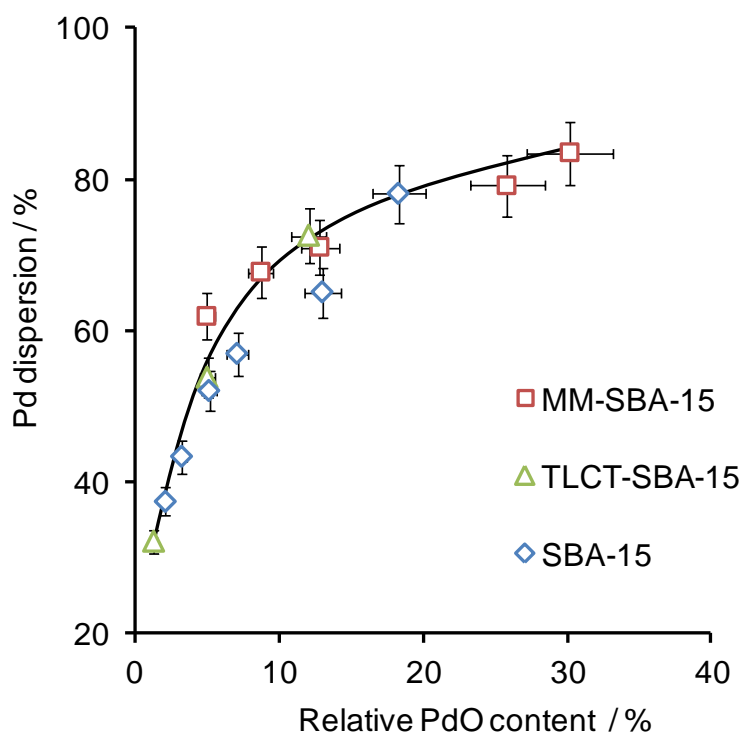


**Figure 4.17** - Relationship between surface PdO and metal dispersion

Surface PdO (evaluated by XPS) content rises monotonically with Pd dispersion as shown in **Figure 4.17** as expected on the basis of the relative metal and oxide surface energies, and as observed for Pd/mesoporous silica (**Figure 3.18**). The identical dependences seen across the differing architectures in **Figure 4.17** suggests that (in the case of the present weakly-interacting, non-reducible silica supports) surface PdO content is solely controlled by Pd dispersion.

## 4.2.4 Allylic alcohol selox

The performance of TLCT-SBA-15 and MM-SBA-15 were screened towards crotyl alcohol and cinnamyl alcohol selox under common test conditions (8.4 mmol alcohol in 10 cm<sup>3</sup> toluene with an internal standard at 90 °C) which are used throughout this chapter unless otherwise stated.

### 4.2.4.1 Crotyl alcohol selox

As discussed in the previous chapter, the influence of stirrer rate on initial catalyst activity was first investigated to confirm mass-transfer limitations (arising from reactant/product diffusion across either the gas-liquid interface or liquid-solid boundary layer of silica particles) we eliminated. The results are shown **Figure 4.18**.

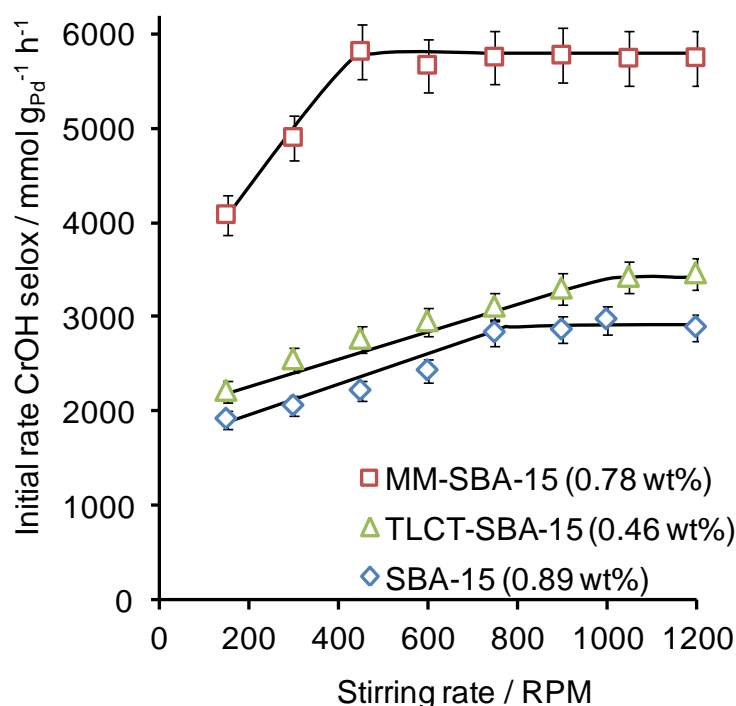


**Figure 4.18** – Effect of stirring rate on crotyl alcohol normalised initial rate

Again, mixing speeds >1000 rpm were sufficient to eliminate external mass transport, with O<sub>2</sub> solubilisation under our mild conditions (air atmosphere) likely to be the dominating factor. Under efficient agitation it is clear that Pd/MM-SBA-15 is ~2 times more active than Pd/SBA-15. The relative selox activity is therefore severely influenced by the additional macroporosity, which is speculated to aid

diffusion via funneling reagents towards the mesopores and decreasing the mesopore domain size,<sup>[2]</sup> which in turn has been already shown to aid Pd dispersion/oxidation state. It is also worth noting the similarity in external mass transport of Pd/MM-SBA-15 to Pd/SBA-16, Pd/KIT-6 and Pd/SiO<sub>2</sub> catalysts (**Figure 3.21**). Pd/TLCT-SBA-15 also exhibits a slight increase in selox activity over Pd/SBA-15, although this is likely to result from the significantly lower metal loading. The higher external mass transport of the Pd/TLCT-SBA-15 sample is the greatest of the systems studied, in both this and the previous chapter, although as mentioned in **Chapter 3** the reason for this is not clear.

Reaction profiles for the MM-SBA-15 and TLCT-SBA-15 series are presented in **Figure 4.19**; the analogous profiles for SBA-15 appear in **Figure 3.24**.

All materials were active for crotyl alcohol selox, with conversion increasing with metal loading which more than compensates for the simultaneous decline in fractional surface PdO. After a period of high initial activity during the first 30-40 min reaction, all catalysts exhibit some degree of deactivation, as observed for the Pd/mesoporous silicas in **Chapter 3**.

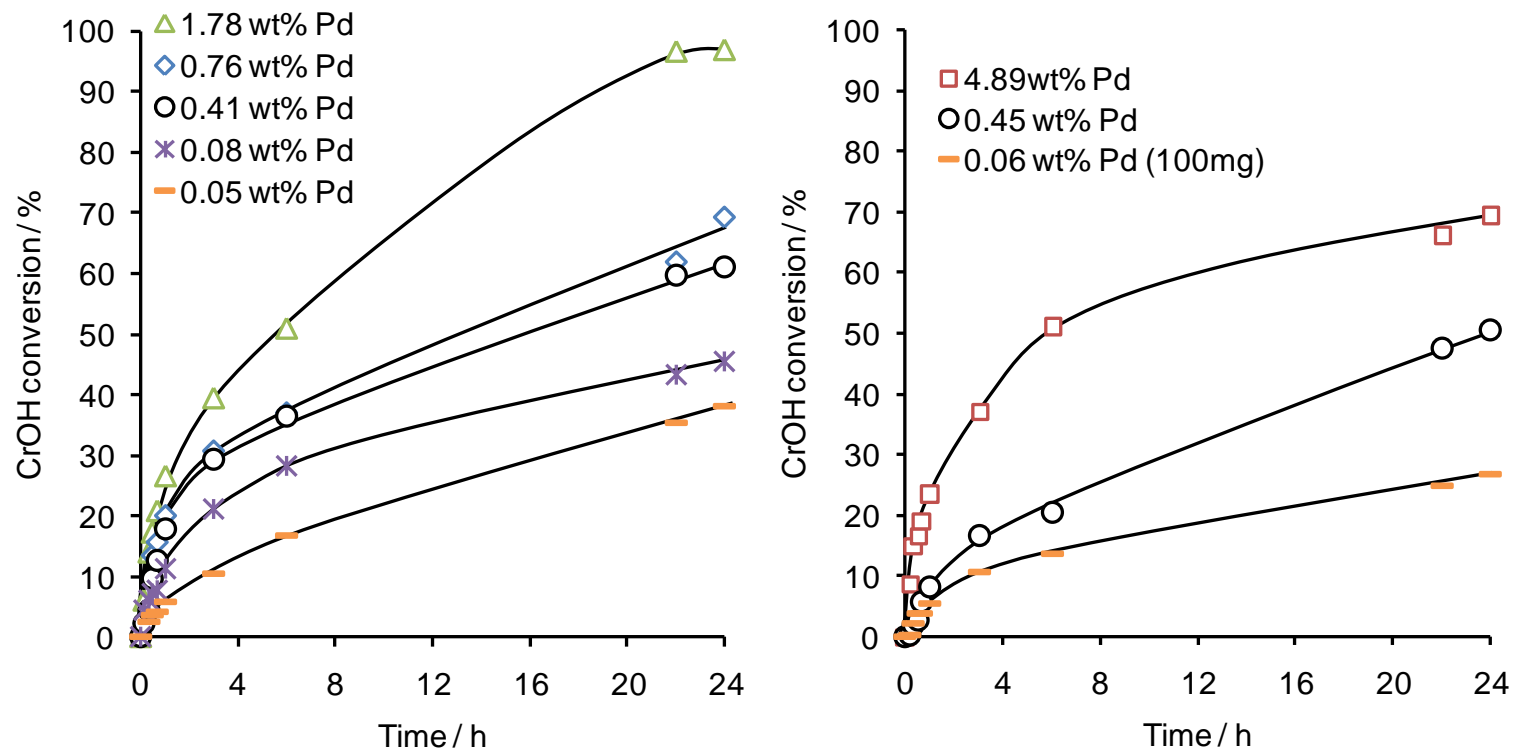


**Figure 4.19** – Crotyl alcohol reaction profiles for MM-SBA-15 (left) and TLCT-SBA-15 (right) series

To more quantitatively compare catalyst performance, their mass normalised initial rates (per gram Pd) were calculated as a function of metal loading for the first 30 minutes of the reaction (mass balances exceed 95 %) are shown in **Figure 4.20**.

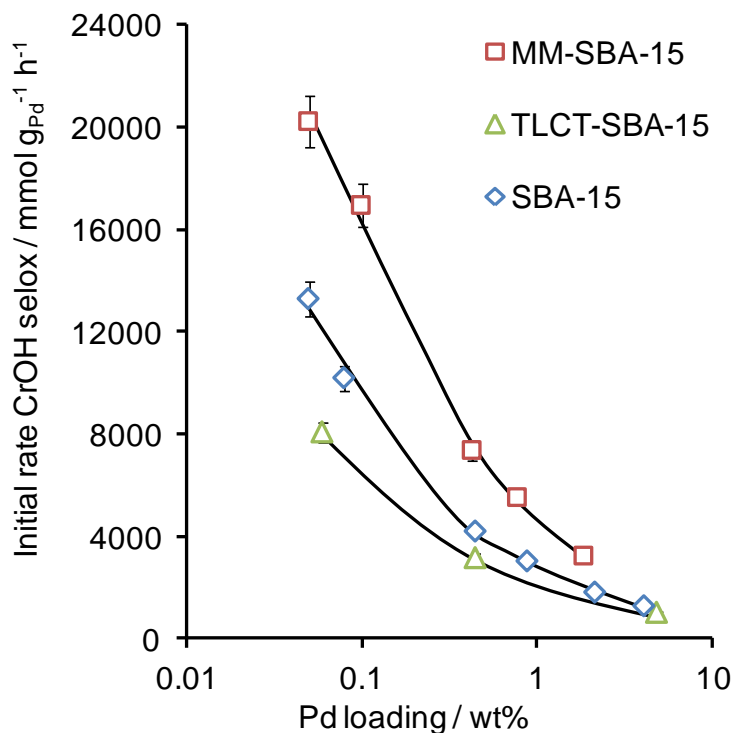


**Figure 4.20** - Dependence of crotyl alcohol aerobic selox activity on bulk Pd loading and nature of SBA-15 support

An inverse relationship between activity and metal loading is apparent for both MM-SBA-15 and TLCT-SBA-15, in agreement with the literature and **Chapter 3** for supported Pd catalysed allylic and benzyl alcohol selox.<sup>[1, 28-31]</sup> As in Chapter 3 a strong dependence of activity is observed to both Pd loading and silica support. The hierarchical macroporous-mesoporous structure of MM-SBA-15 facilitates the highest activity, whereas the TLCT-SBA-15 catalysts actually performed worse than their LCT-derived conventional SBA-15 counterparts. This order of reactivity correlates with their relative surface PdO content (assessed from XPS), supporting the hypothesis advanced in **Chapter 3** that Pd dispersion, and hence surface oxide concentration, control selox activity. MM-SBA-15 catalysts are almost as active as those obtained from interconnected mesoporous KIT-6 and SBA-16 supports in **Chapter 3**. Due to the significantly lower surface area of MM-SBA-15 this could

appear counterintuitive, but in fact it upholds the earlier conclusion that as import as high surface areas are for achieving well dispersed Pd nanoparticles, an open support structure equally important.

Confirmation that PdO and not Pd metal is the active site responsible for selox catalysis in MM-SBA-15 and TLCT-SBA-15 was obtained by normalising initial oxidation rates to the surface concentrations of each of these Pd species (determined by CO chemisorption and XPS). Resulting TOFs are shown as a function of surface Pd metal or PdO content in **Figure 4.21**.

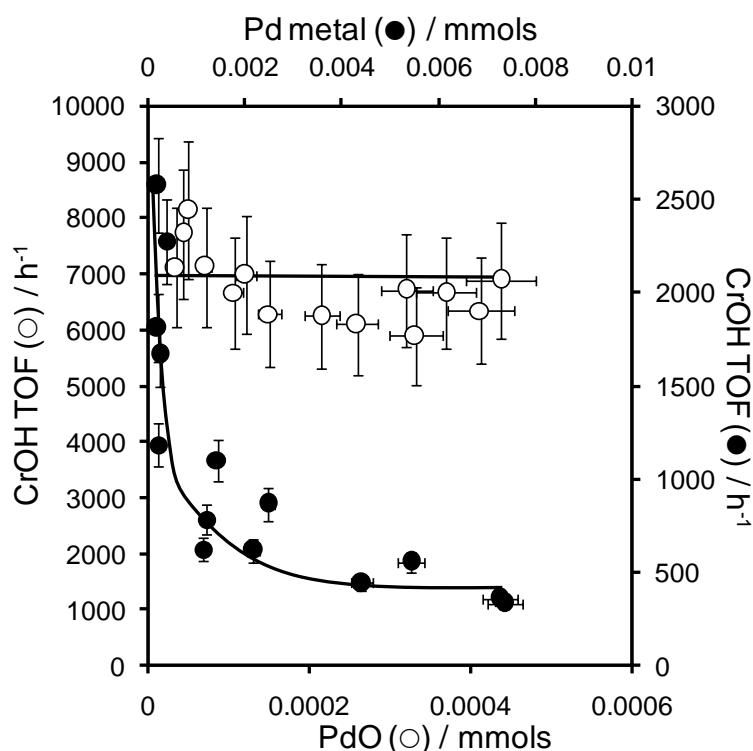


**Figure 4.21** - Crotyl alcohol aerobic selox turnover frequencies as a function of surface PdO or Pd metal content for Pd/MM-SBA-15, Pd/TLCT-SBA-15 and Pd/SBA-15 catalysts.

A strong variation is observed for the Pd metal normalised TOFs for both MM-SBA-15 and TLCT-SBA-15. In contrast, normalisation to the surface PdO concentration yields an almost constant value of  $\sim 7000 \text{ h}^{-1}$ , close to published values<sup>[1]</sup> and the results from **Chapter 3**. This conclusion supports previous operando studies on dispersed catalysts<sup>[32]</sup> and in-situ studies on Pd single crystals.<sup>[33]</sup> The common TOF values obtained for diverse Pd nanoparticle sizes across six different

supports, from this and the previous chapter, lends confidence that intrinsic reaction kinetics have been measured.

As discussed in **Chapter 3**, selectivity measurements for these reactions proved problematic due to the low mass balances at the end of the 24 h reaction (partially associated with solution evaporation), hence these will not be discussed in detail. However, all Pd/MM-SBA-15 and Pd/TLCT-SBA-15 catalysts exhibit similar selectivities of ~65 % towards crotonaldehyde during the first hour of reaction (similar to that obtained for Pd/SBA-15) when mass balances exceeded 90 %, with butanal being the only side-product.

#### **4.2.4.2 Cinnamyl alcohol selox**

Cinnamyl alcohol selox was investigated to provide comparative catalytic results for a bulkier/heavier aromatic allylic alcohol, wherein internal mass transport may be more challenging, and to overcome the selectivity issues encountered during crotyl alcohol selox.

The effect of stirrer speed on activity was again studied to ensure bulk mass transfer diffusion, from either the gas liquid interface or the liquid silica support interface were eliminated. As before stirring rate above 1000 RPM are adequate to eliminate this concern and once operating under this regime the same enhancement of Pd/MM-SBA-15 over Pd/SBA-15 is witnessed. Slower cinnamyl alcohol oxidation relative to crotyl alcohol is apparent again and reflects results for Pd/Al<sub>2</sub>O<sub>3</sub> catalysts.<sup>[28]</sup>

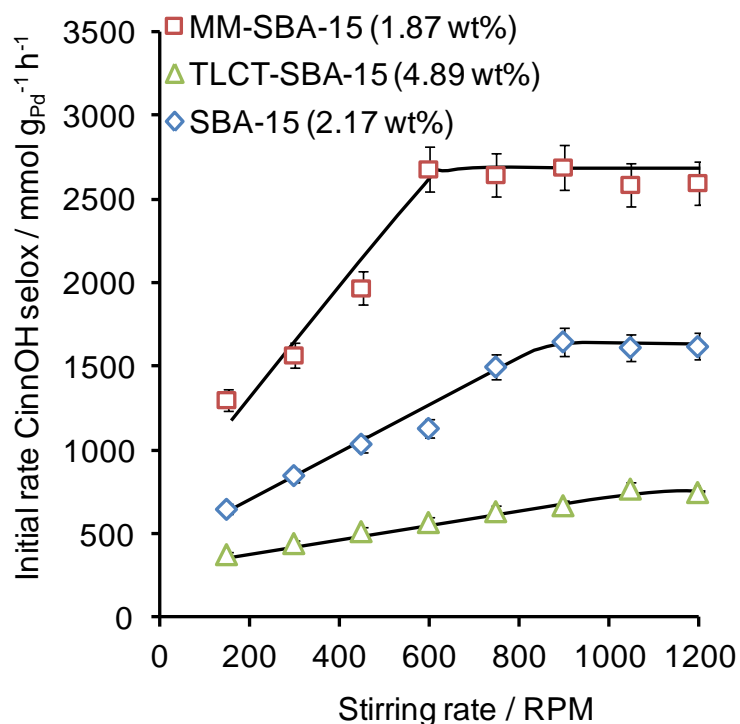


**Figure 4.22** - Effect of stirring rate on cinnamyl alcohol normalised initial rate

**Figure 4.23** depicts the cinnamyl alcohol selox reaction profiles for Pd/MM-SBA-15 and Pd/TLCT-SBA-15 catalyst series, carried out under the optimum stirrer speeds for efficient mixing (>1000 rpm). The Pd/SBA-15 profiles are shown in **Chapter 3 Figure 29**.

Cinnamyl alcohol conversion is proportional to Pd loading for Pd/MM-SBA-15 and Pd/TLCT-SBA-15, and increases linearly with time during the first hour of reaction before deactivating. Mass balances were greater than 98 % (throughout the first hour) and remained above 93 % over the 24 h reaction period.

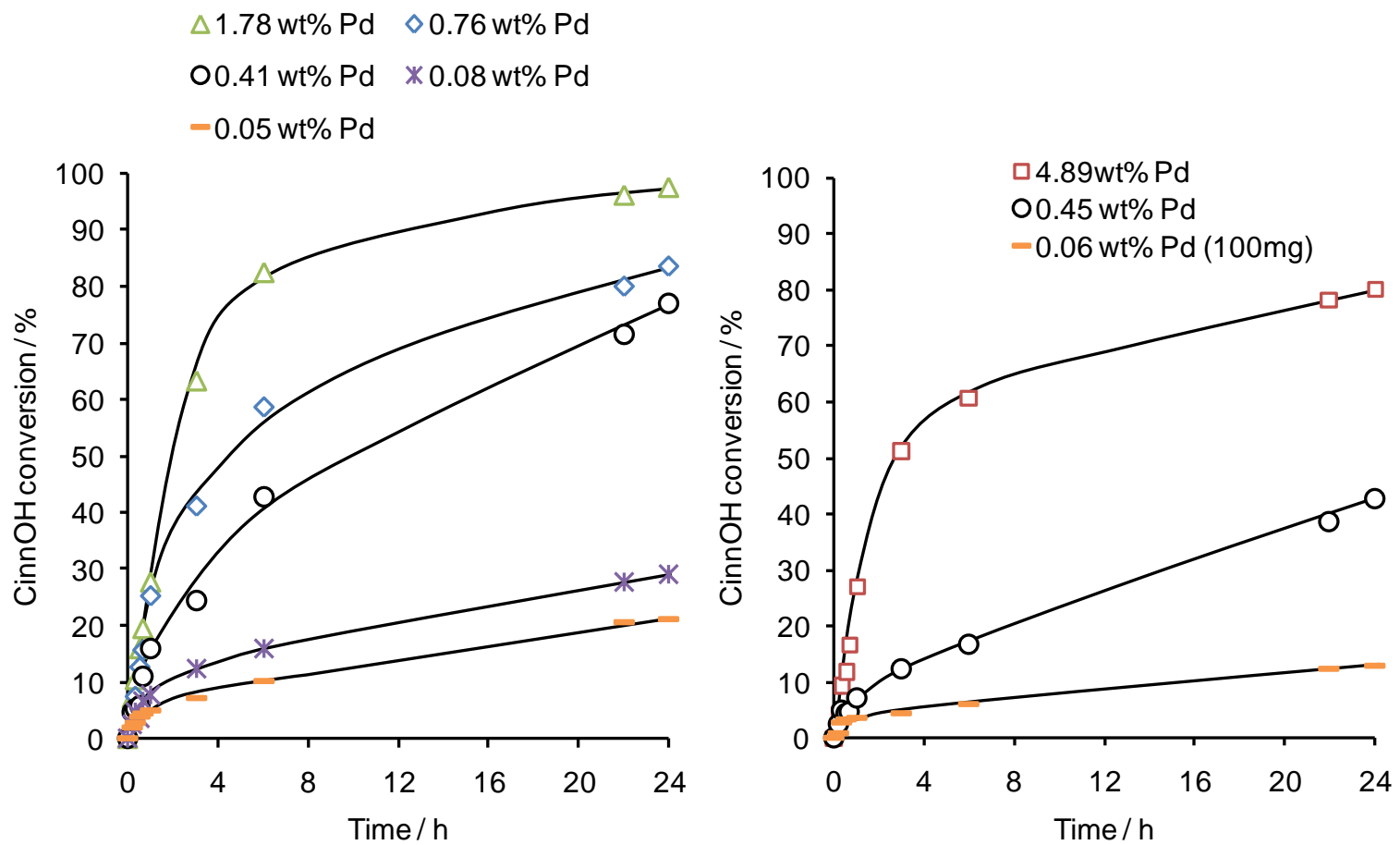


**Figure 4.23** – Cinnamyl alcohol reaction profiles for MM-SBA-15 (left) and TLCT-SBA-15 (right) series

Normalisation of the initial rates to Pd loading allows comparison of the three different SBA-15 supports, depicted in **Figure 4.24**. Similar trends are observed as seen for crotyl alcohol, with MM-SBA-15 again offering a superior support to SBA-15 and the poorly performing TLCT-SBA-15 with its long pore channels. In all cases, high metal dispersions dramatically enhance cinnamyl alcohol conversion, although the absolute rates are ~20-25 % lower than obtained for crotyl alcohol (also seen in **Chapter 3**). The activity of Pd/MM-SBA-15 is comparable with that achievable using the interconnected mesoporous silica supports in **Chapter 3**.

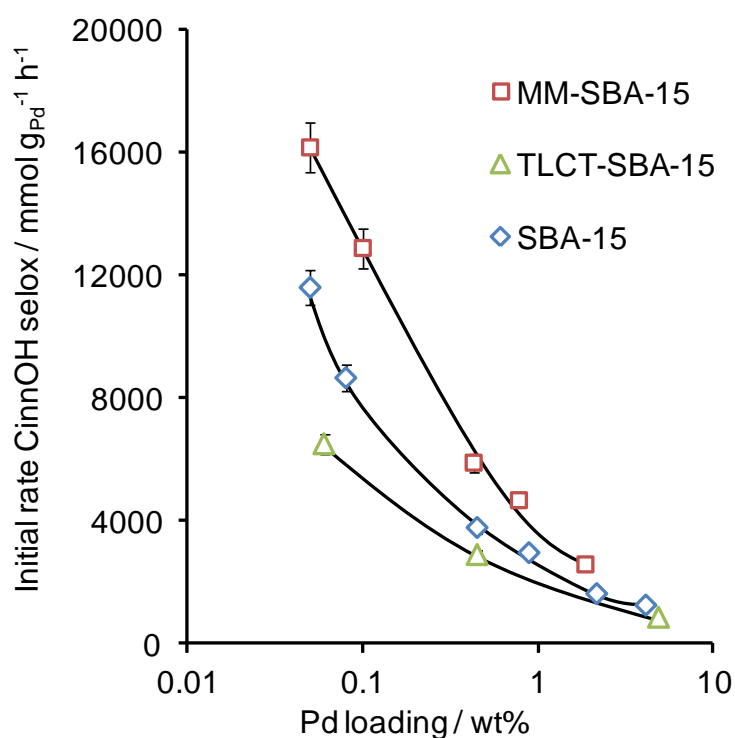


**Figure 4.24** - Dependence of cinnamyl alcohol aerobic selox activity on bulk Pd loading and nature of SBA-15 support

Evidence that the true reaction kinetics were measured was obtained by comparing the initial rates of crotyl alcohol versus cinnamyl alcohol conversion over identical catalysts. This ratio should be constant if the rate-controlling factor is a common difference e.g. intrinsic activation energy for O-H or C-H scission between the two alcohols, independent of Pd particle size or support type, as indeed seen in **Figure 4.25**. A constant ratio of 1.19 is in quantitative agreement with the corresponding value from **Chapter 3** for Pd/mesoporous silicas. The lack of

distinguishable difference between the six supports rules out varying internal mass diffusion variations.

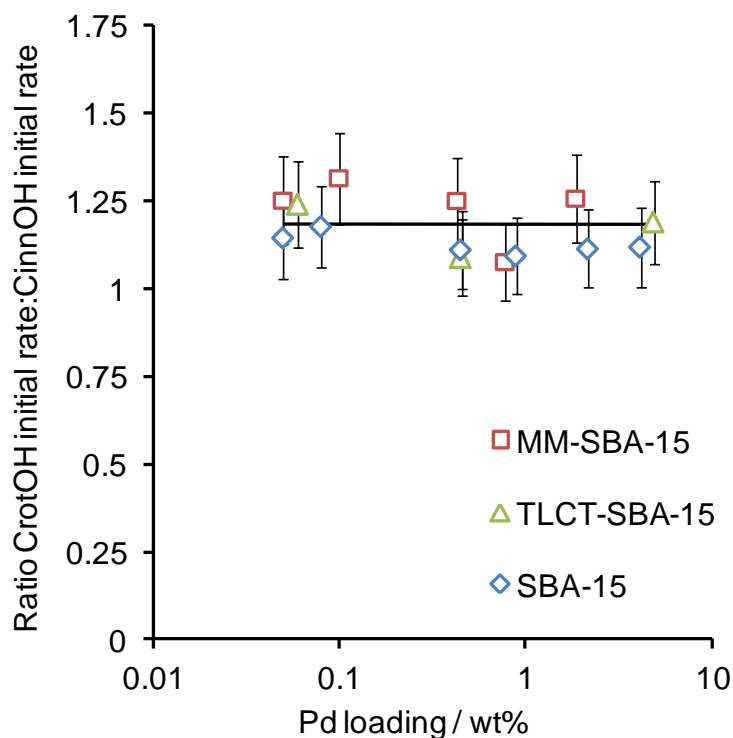


**Figure 4.25** - Ratio of normalised initial rate crotyl alcohol:cinnamyl alcohol for corresponding loadings and supports.

Turnover frequencies, calculated by the normalising initial rates in **Figure 4.24** to either the surface Pd metal (CO chemisorption) or PdO (XPS) concentrations are shown in **Figure 4.26**, and are entirely consistent with observations reported in **Chapter 3**.

Normalisation to surface PdO obtains a constant TOF of  $\sim 5800 \text{ h}^{-1}$ , as expected if the true active site has been identified, whereas a continuously decreasing TOF (with increasing Pd content) was obtained considering metallic Pd active centres. This corroborates the hypothesis from **Chapter 3** that surface PdO is indeed the active catalytic site in allylic alcohol selox. Constant TOFs, across six supports, confirm that the rate of reagent diffusion though the varying pore architectures, being predominately non-porous, mesoporous or macroporous-mesoporous, are irrelevant under the investigation conditions studied.

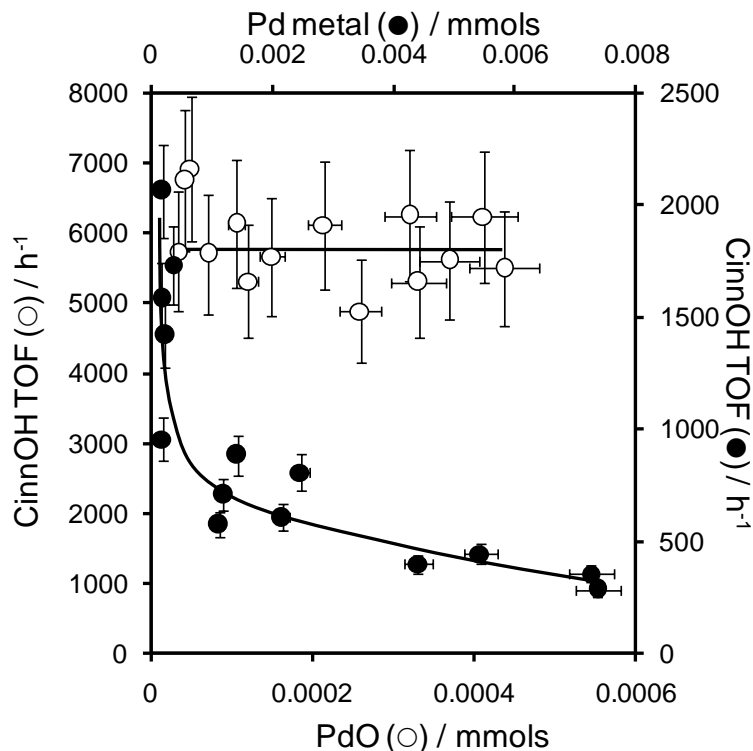


**Figure 4.26** - Cinnamyl alcohol aerobic selox turnover frequencies as a function of surface PdO or Pd metal content for Pd/MM-SBA-15, Pd/TLCT-SBA-15 and Pd/SBA-15 catalysts.

Representative selectivity reaction profiles for major products (contribution greater than 1.5 %), are shown for high and low Pd loading MM-SBA-15 in **Figure 4.27**. These are consistent with **Figure 3.35-6**, and literature reports.<sup>[1, 34]</sup> cinnamaldehyde selectivity decreases with time due to in-situ reduction of surface PdO<sup>[30, 32, 33]</sup> and genesis of metallic sites which drive decarbonylation chemistry.<sup>[35]</sup>

The dependence of initial selectivity (after 30 min reaction) upon relative PdO content (determined from XPS) is explored in **Figure 4.28**. Higher selectivity to cinnamaldehyde is achieved over more oxidic catalysts. Thus elevating Pd surface oxidation state promotes both high activity and selectivity towards the desirable reaction.

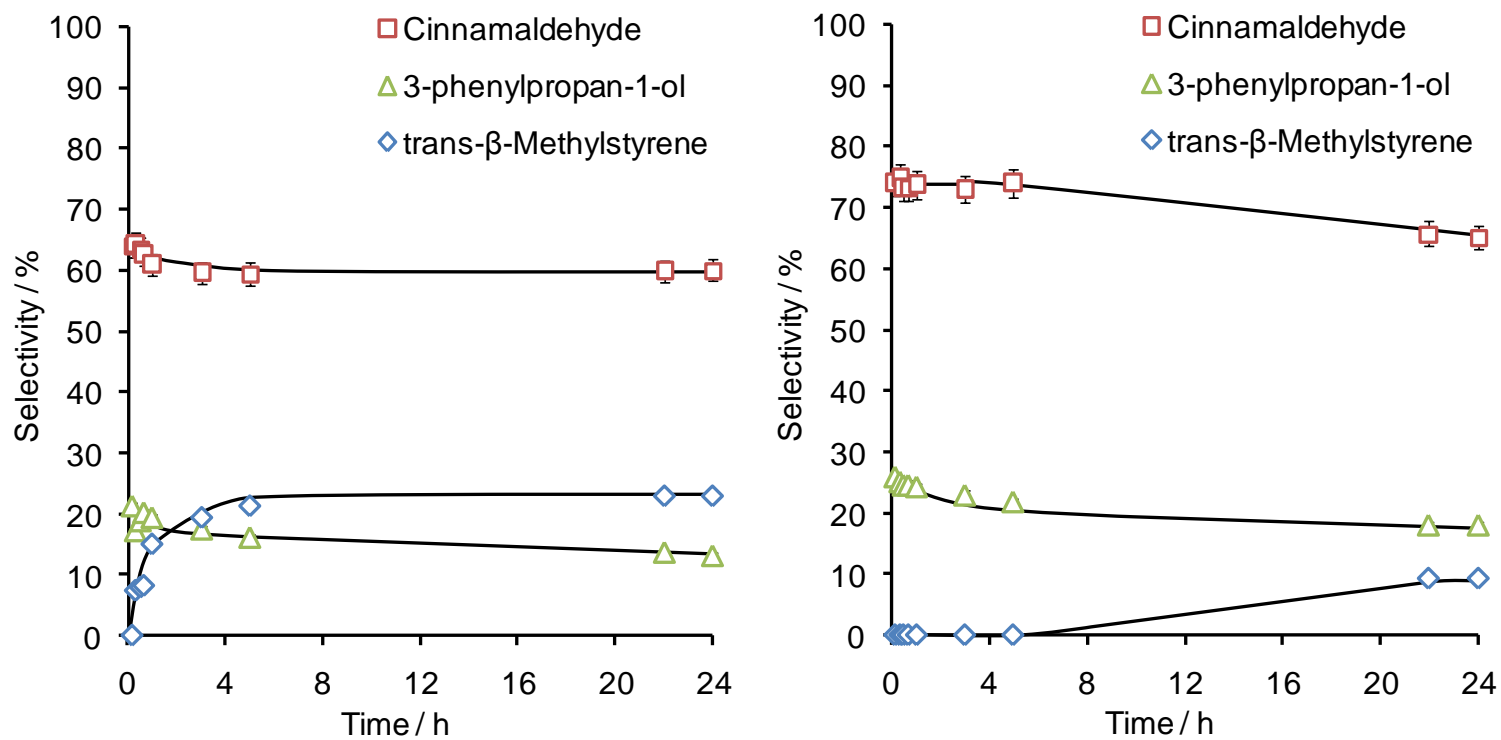


**Figure 4.27** - Representative selectivity profiles as a function of time of the major products from cinnamyl alcohol selox over 1.87 (left) and 0.05 (right) wt% Pd/MM-SBA-15 under static O<sub>2</sub> conditions

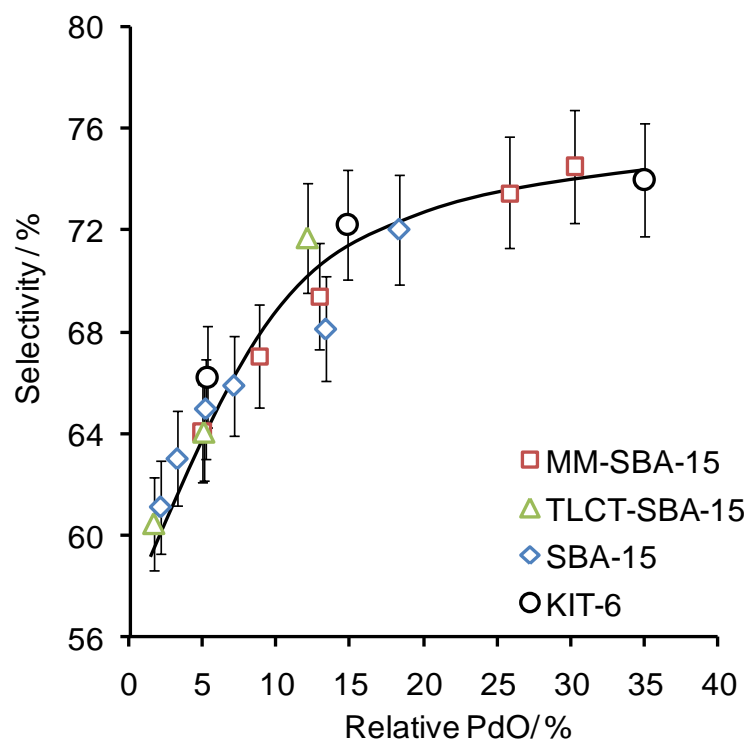


**Figure 4.28** – Surface PdO content and cinnamylaldehyde selectivity correlation after 0.5 hours. (Pd/KIT-6 values from **Chapter 3** included)

### 4.3 Conclusion

The morphology and textural properties of silica supports strongly influence Pd catalysed crotyl and cinnamyl alcohol selox. Macropore incorporation, whilst lowering the total surface area, decreases average mesopore length (reduced domain size) and thus it is reasonable to expect increased accessibility. This is shown to be critical during Pd impregnation and subsequent calcination reduction processes, promoting higher metal dispersion and thus surface PdO concentrations over conventional SBA-15. In contrast, the true liquid crystal template synthesis conditions increased average silica particle sizes relative to conventional SBA-15. This results in longer mesopores, rendering them less accessible and thus favouring production of larger Pd nanoparticles.

The integration of a macropore network into SBA-15 offers catalysts with activities almost comparable to the interconnected mesoporous Pd/SBA-16 and Pd/KIT-6 materials in **Chapter 3**. This advantageous catalytic property is solely a result of increasing metal dispersion (surface PdO species), and not due to enhanced

internal mass diffusion properties. This is in contradiction to when the same support is used in biodiesel production,<sup>[2]</sup> although this can easily be accounted for due to the relatively small reactant size studied here compared with larger bulky triglyceride. The resulting TOF, for both new series, and associated selectivities provide yet more compelling evidence of a surface PdO active species. Finally, further tuning of both macro and mesopore dimensions, and/or the incorporation of macroporosity into 3D mesopore architectures (**Chapter 3**) may afford even greater catalytic performance.

## 4.4 References

1. Parlett, C.M.A., D.W. Bruce, N.S. Hondow, A.F. Lee, and K. Wilson, *Acs Catalysis*, 2011. **1**: p. 636.
2. Dhainaut, J., J.P. Dacquin, A.F. Lee, and K. Wilson, *Green Chemistry*, 2010. **12**: p. 296.
3. Vaudreuil, S., M. Bousmina, S. Kaliaguine, and L. Bonneviot, *Advanced Materials*, 2001. **13**: p. 1310.
4. Attard, G.S., J.C. Glyde, and C.G. Goltner, *Nature*, 1995. **378**: p. 366.
5. Webb, P.A. and C. Orr, *Analytical Methods in Fine Particle Technology*. Journal of the Chemical Society-Faraday Transactions II. 1997, Norcross: Micromeritics.
6. Brunauer, S., P.H. Emmett, and E. Teller, *Journal of the American Chemical Society*, 1938. **60**: p. 309.
7. Barrett, E.P., L.G. Joyner, and P.P. Halenda, *Journal of the American Chemical Society*, 1951. **73**: p. 373.
8. Lippens, B.C. and J.H. De Boer, *Journal of Catalysis*, 1965. **4**: p. 319.
9. Kruk, M., M. Jaroniec, C.H. Ko, and R. Ryoo, *Chemistry of Materials*, 2000. **12**: p. 1961.
10. Silvestre-Albero, A., E.O. Jardim, E. Bruijn, V. Meynen, P. Cool, A. Sepulveda-Escribano, J. Silvestre-Albero, and F. Rodriguez-Reinoso, *Langmuir*, 2009. **25**: p. 939.
11. Galarneau, A., H. Cambon, F. Di Renzo, and F. Fajula, *Langmuir*, 2001. **17**: p. 8328.
12. Yang, C.M., H.A. Lin, B. Zibrowius, B. Spliethoff, F. Schüth, S.C. Liou, M.W. Chu, and C.H. Chen, *Chemistry of Materials*, 2007. **19**: p. 3205.
13. Yang, C.M., B. Zibrowius, W. Schmidt, and F. Schüth, *Chemistry of Materials*, 2003. **15**: p. 3739.
14. Galarneau, A., H. Cambon, F. Di Renzo, R. Ryoo, M. Choi, and F. Fajula, *New Journal of Chemistry*, 2002. **27**: p. 73.
15. Li, D., X. Guan, J. Song, Y. Di, D. Zhang, X. Ge, L. Zhao, and F.S. Xiao, *Colloids and Surfaces A: Physicochemical and Engineering Aspects*, 2006. **272**: p. 194.
16. Meynen, V., P. Cool, and E.F. Vansant, *Microporous and Mesoporous Materials*, 2009. **125**: p. 170.
17. Janssen, A.H., P. Van Der Voort, A.J. Koster, and K.P. de Jong, *Chemical Communications*, 2002: p. 1632.
18. Che, S., K. Lund, T. Tatsumi, S. Iijima, S.H. Joo, R. Ryoo, and O. Terasaki, *Angewandte Chemie International Edition*, 2003. **42**: p. 2182.
19. Shen, J.F., X.Z. Liu, S.G. Zhu, H.L. Zhang, and J.J. Tan, *Materials Letters*, 2011. **65**: p. 1179.

20. Pernicone, N., *Cattech*, 2003. **7**: p. 196.
21. Scherrer, P., *Gottinger Nachrichten*, 1918. **2**: p. 98.
22. Hussain, M., J.S. Yun, S.K. Ihm, N. Russo, and F. Geobaldo, *Industrial & Engineering Chemistry Research*, 2011. **50**: p. 2530.
23. Heydari-Gorji, A., Y. Yang, and A. Sayari, *Energy & Fuels*, 2011. **25**: p. 4206.
24. Prieto, G., A. Martinez, R. Murciano, and M.A. Arribas, *Applied Catalysis a-General*, 2009. **367**: p. 146.
25. Wang, H.-F., H. Ariga, R. Dowler, M. Sterrer, and H.-J. Freund, *Journal of Catalysis*, 2012. **286**: p. 1.
26. Pennycook, S.J. and L.A. Boatner, *Nature*, 1988. **336**: p. 565.
27. Brun, M., A. Berthet, and J.C. Bertolini, *Journal of Electron Spectroscopy and Related Phenomena*, 1999. **104**: p. 55.
28. Hackett, S.E.J., R.M. Brydson, M.H. Gass, I. Harvey, A.D. Newman, K. Wilson, and A.F. Lee, *Angewandte Chemie-International Edition*, 2007. **46**: p. 8593.
29. Lee, A.F., S.F.J. Hackett, J.S.J. Hargreaves, and K. Wilson, *Green Chemistry*, 2006. **8**: p. 549.
30. Lee, A.F. and K. Wilson, *Green Chemistry*, 2004. **6**: p. 37.
31. Li, C.L., Q.H. Zhang, Y. Wang, and H.L. Wan, *Catalysis Letters*, 2008. **120**: p. 126.
32. Lee, A.F., C.V. Ellis, J.N. Naughton, M.A. Newton, C.M.A. Parlett, and K. Wilson, *Journal of the American Chemical Society*, 2011. **133**: p. 5724.
33. Lee, A.F., Z. Chang, P. Ellis, S.F.J. Hackett, and K. Wilson, *Journal of Physical Chemistry C*, 2007. **111**: p. 18844.
34. Mallat, T. and A. Baiker, *Chemical Reviews*, 2004. **104**: p. 3037.
35. Lee, H.Y., S. Ryu, H. Kang, Y. Jun, and J. Cheon, *Chemical Communications*, 2006: p. 1325.

## *Chapter 5*

*The selective oxidation of  
allylic alcohols over  
palladium supported on  
mesoporous alumina*

## 5.1 Introduction

Chapters 3 and 4 have highlighted the influence that support materials can exert upon supported metal nanoparticle catalysts. Altering support properties can induce considerable changes in the physical and chemical nature of such nanoparticles, and in turn control their catalytic performance. A major discovery from both chapters is evidence for the previously hypothesised surface PdO active site,<sup>[1, 2]</sup> which corroborates in-situ/operando studies.<sup>[3, 4]</sup> In addition to its architecture, the chemical composition of a support can also modify catalysis via metal-support interactions, which may change nanoparticle morphology, oxidation state and/or electronic properties.<sup>[5-8]</sup>

High metal dispersion, and thus small highly oxidised Pd nanoparticles are desired for allylic alcohol selox, hence this chapter explores the effect of changing the support from silica to alumina on nanoparticle properties. Pure mesoporous alumina supports have previously shown significantly higher surface oxidation states for comparable metal loadings than their equivalent mesoporous silica supports,<sup>[1, 4]</sup> however it is unclear whether this reflects the Pd-alumina interaction, or the different support architectures. This question will be decoupled by studying mesoporous aluminas synthesised either using a comparable solvothermal methodology to that employed for SBA-15,<sup>[9]</sup> or via grafting alumina thin films onto a pre-formed SBA-15 (Diagram 5.1).<sup>[10]</sup>

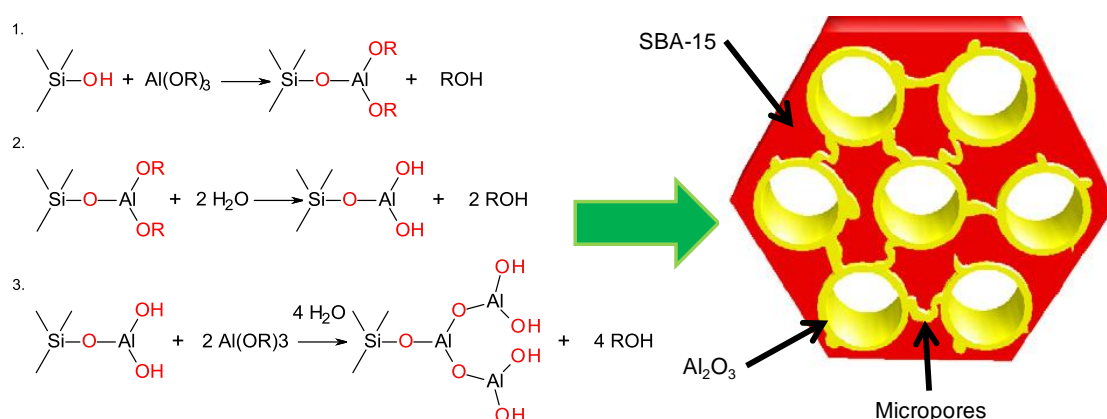


**Diagram 5.1** – Reaction schemes for multiple alumina grafting on SBA-15 and graphical representation of final Al grafted SBA-15(reproduced from ref 11) <sup>[10, 11]</sup>

## 5.2 Results and discussion

### 5.2.1 Characterisation of parent supports

Two mesoporous aluminas were prepared by different methods. First, adopting the method of Yuan et al.,<sup>[9]</sup> a purely mesoporous alumina (mesoAl<sub>2</sub>O<sub>3</sub>) was synthesised using Pluronic P123 as a template via the evaporative induced self-assembly (EISA) method. Alternatively alumina was grafted onto SBA-15 (Al-SBA-15) using the method developed by Landau and co-workers,<sup>[10]</sup> with SBA-15 produced by the method of Zhao and co-workers<sup>[12]</sup> which also uses Pluronic P123 but via the cooperative self-assembly method.<sup>[13]</sup> In the latter preparation, the hydrothermal treatment for SBA-15 was increased to 100 °C to increase the pore diameter and spacing relative to the material described in **Chapter 3**.<sup>[14]</sup> Four grafting cycles, each targeted to give a loading of ~5 wt% alumina, were performed to obtain a surface mimicking the chemistry of pure alumina.<sup>[10, 11, 15]</sup> Multiple grafting cycles were employed with the aim to ensure a more uniform covering of the parent SBA-15, and assess the evolution of alumina surface characteristics with film thickness. The resulting materials were used as catalyst supports for Pd, and compared to the analogous silica SBA-15 (SBA-15) catalyst series in **Chapter 3**.

#### 5.2.1.1 Powder X-ray diffraction

Low angle powder XRD was applied to verify successful formation of the *p6mm* space group of the mesoAl<sub>2</sub>O<sub>3</sub>, and confirm that alumina grafting did not damage the parent SBA-15. Resulting patterns along with expected and actual position values for the minor reflections, a necessity to identify the mesopore space group, are displayed in **Figure 5.1**. The mesoAl<sub>2</sub>O<sub>3</sub> pattern indicates less regular pore packing than SBA-15, apparent from broadening of the main d(10) peak and less resolved d(11) and d(20) peaks. This negative effect is reported for EISA SBA-15, due to more rapid mesophase formation and less uniform micelles.<sup>[13]</sup> This said the presence of d(11) and d(20) peaks in mesoAl<sub>2</sub>O<sub>3</sub> reveals improved periodicity over other ordered mesoporous aluminas.<sup>[16-18]</sup> The grafting approach shows no detrimental effect on mesostructure, with d(11) and d(20) resolution increased, suggesting higher ordering. Similar results are known when a second hydrothermal treatment/recrystallisation step is used in SBA-15 synthesis, albeit on an as-synthesised sample.<sup>[13]</sup>

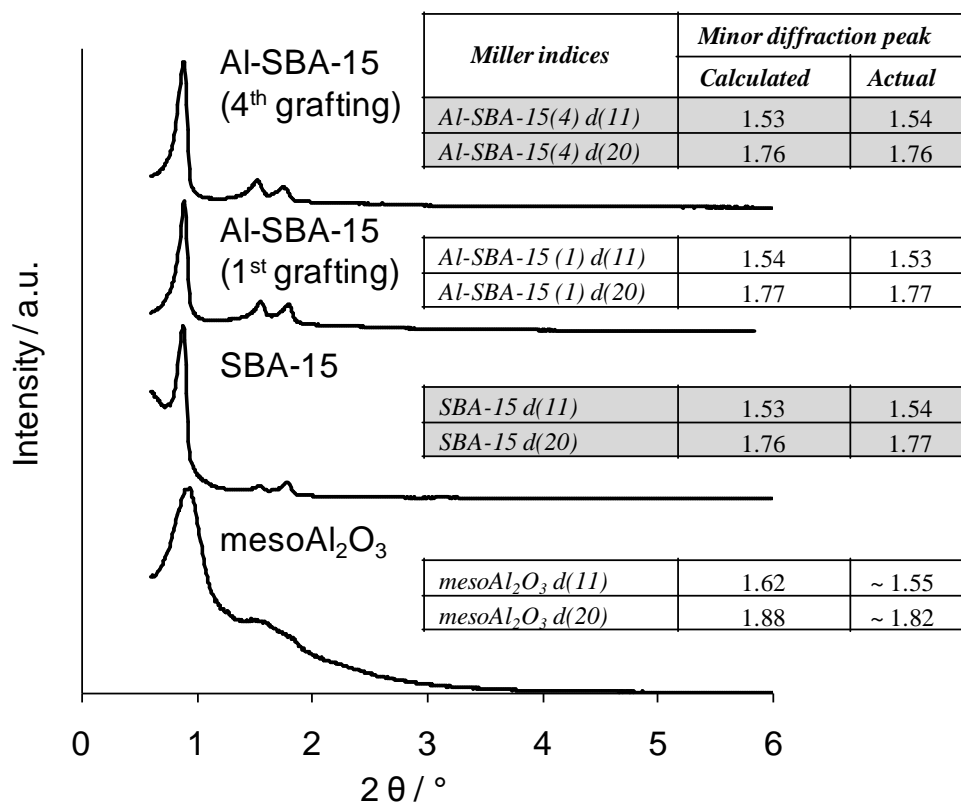


**Figure 5.1** - Offset low angle XRD patterns of mesoAl<sub>2</sub>O<sub>3</sub>, parent SBA-15 and Al-SBA-15 after 1<sup>st</sup> and 4<sup>th</sup> grafting

Using Bragg's Law (**Chapter 2 Equation 2.1**) the cell parameters for all materials have been calculated, shown in **Table 5.1** and **Figure 5.6**; for the mesoAl<sub>2</sub>O<sub>3</sub> good agreement is observed with the literature.<sup>[19]</sup> The main peak position for the grafted Al-SBA-15 samples is consistent with that of the parent SBA-15, another clear indication that parent pore structure is retained after grafting.

**Table 5.1** - Textural properties of support materials

Sample	Surface area / m <sup>2</sup> g <sup>-1(a)</sup>	Micropore surface area / m <sup>2</sup> g <sup>-1(b)</sup>	Mesopore Diameter / nm <sup>(c)</sup>	Cell parameter / nm <sup>(d)</sup>
MesoAl <sub>2</sub> O <sub>3</sub>	276 (± 28)	19 (± 2)	6.6	9.2 (± 0.2)
SBA-15	979 (± 98)	440 (± 44)	6	10.0 (± 0.2)
Al-SBA-15 (1 <sup>st</sup> )	583 (± 58)	107 (± 11)	5.9	9.9 (± 0.2)
Al-SBA-15 (2 <sup>nd</sup> )	405 (± 40)	46 (± 5)	5.8	10.0 (± 0.2)
Al-SBA-15 (3 <sup>rd</sup> )	323 (± 32)	33 (± 3)	5.6	10.0 (± 0.2)
Al-SBA-15 (4 <sup>th</sup> )	254 (± 25)	28 (± 3)	5.4	10.0 (± 0.2)

<sup>(a)</sup> N<sub>2</sub> BET, <sup>(b)</sup> N<sub>2</sub> t-plot, <sup>(c)</sup> BJH desorption branch of isotherm, <sup>(d)</sup> Low angle XRD

### 5.2.1.2 Nitrogen porosimetry

Textural properties of the supports were characterised by  $N_2$  porosimetry. Isotherms for meso $Al_2O_3$ , parent SBA-15 and the 1<sup>st</sup> and 4<sup>th</sup> grafting for Al-SBA-15 are shown in **Figure 5.2**. All are type 4 isotherms with H1 hysteresis, <sup>[20]</sup> characteristic of constant diameter channel pores. The possibility of narrowed channel regions in the Al-SBA-15 samples can also be discounted, as these would exhibit an additional broad hysteresis region, at the lower end of the original hysteresis, due to localised smaller mesopores.<sup>[21, 22]</sup> Surface areas and average pore diameters, **Table 5.1**, were calculated using the BET <sup>[23]</sup> and BJH <sup>[24]</sup> methods respectively. The surface area of meso $Al_2O_3$  concurs with the literature,<sup>[19]</sup> although the average pore diameter is slightly larger. Relative to the SBA-15 series (Chapter 3) the meso $Al_2O_3$  exhibits an increased pore diameter, this combined with its lower cell parameter dimensions indicates thinner support walls. The microporosity of meso $Al_2O_3$ , determined using the t-plot method,<sup>[25]</sup> is significantly less than for pure silica SBA-15. In the case of Al-SBA-15, and in agreement with published reports, the average surface area and mesopore diameter decreases with increasing alumina grafting cycles.<sup>[10, 11, 26]</sup>

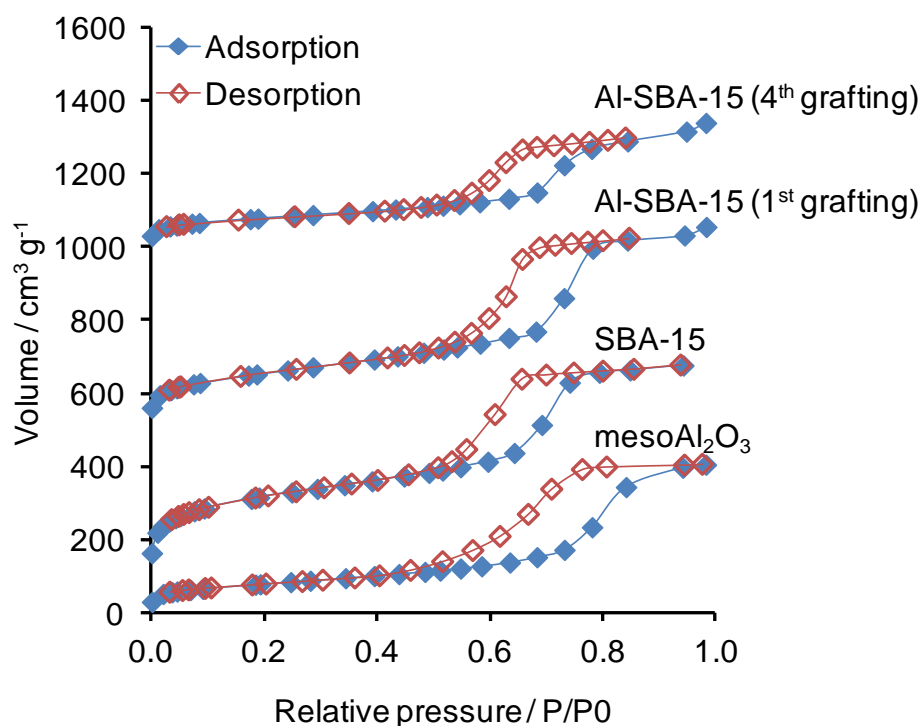


**Figure 5.2** – Isotherms of meso $Al_2O_3$ , SBA-15 (offset  $50 \text{ cm}^3 \text{ g}^{-1}$ ), Al-SBA-15 (1<sup>st</sup> grafting offset  $500 \text{ cm}^3 \text{ g}^{-1}$ ) and Al-SBA-15 (4<sup>th</sup> grafting offset  $1000 \text{ cm}^3 \text{ g}^{-1}$ )

The effect of alumina grafting on the total, mesopore and micropore surface area is shown in **Figure 5.3**. A sharp decrease in total surface area after the 1st cycle is reflected by a similar magnitude loss of micropore surface area (probably due to rapid micropore filling).<sup>[11, 27]</sup> Subsequent graftings show a slower drop in total and micropore surface areas, presumably since the latter can accommodate only a restricted number (one/two) of alumina monolayers. Thus they are almost completely filled after 2 grafting, with ~90 % of the original microporosity is lost after the 2<sup>nd</sup> grafting. The rate of mesopore surface area decrease is obviously slower due to their greater diameter, allowing accommodation of multiple alumina layers without significant pore constriction. A control grafting process, in which the alumina precursor was omitted, was also investigated. Stable surface areas and mesopore diameters confirmed that the original decreases were a direct consequence of alumina grafting onto SBA-15 and not due to silica support restructuring.

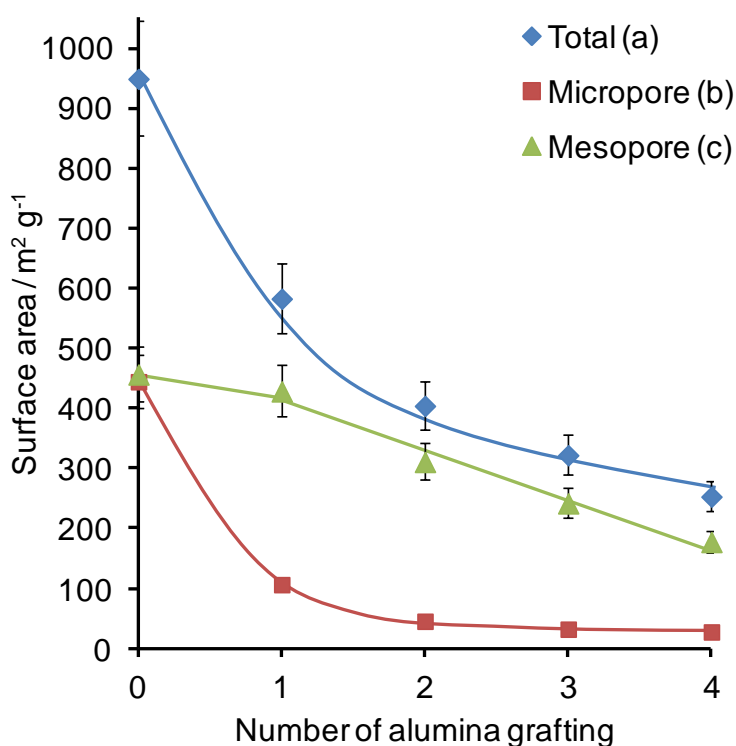


**Figure 5.3** – Effect of alumina grafting cycles on Al-SBA-15 surface area <sup>(a)</sup> N<sub>2</sub> BET, <sup>(b)</sup> N<sub>2</sub> t-plot, <sup>(c)</sup> BET - ( t-plot + external surface area)

**Figure 5.4** shows the corresponding mesopore size distributions. All are relatively narrow, although the mesoAl<sub>2</sub>O<sub>3</sub> is significantly broader than its grafted counterparts.

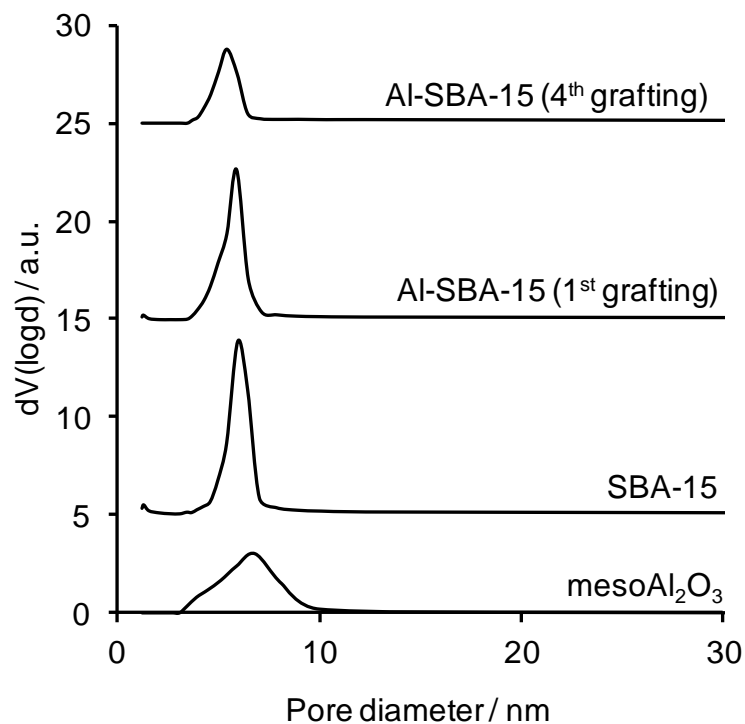


**Figure 5.4** – BJH pore size distributions of mesoAl<sub>2</sub>O<sub>3</sub>, SBA-15 (offset by 5), Al-SBA-15 (1<sup>st</sup> grafting) (offset by 15) and Al-SBA-15 (4<sup>th</sup> grafting) (offset by 25)

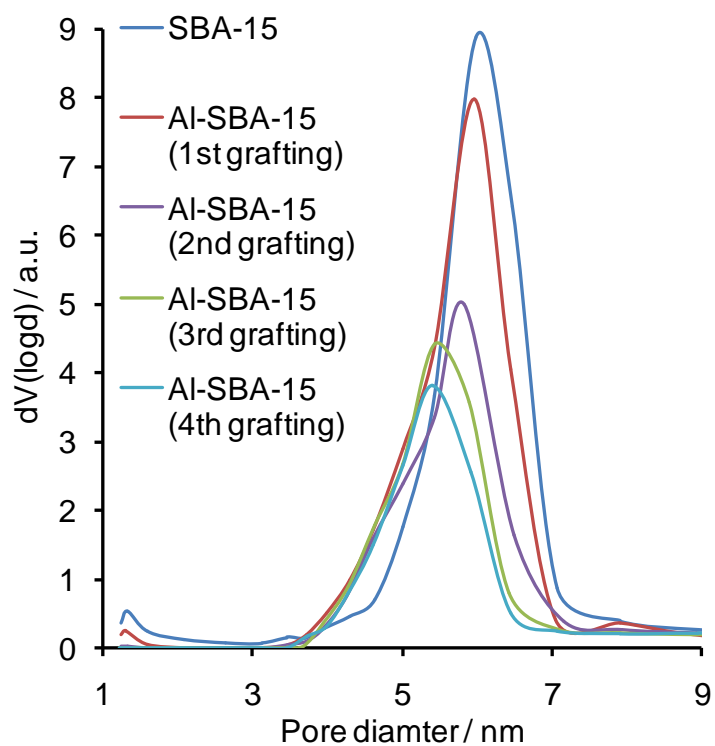


**Figure 5.5** – Pore size distributions of parent SBA-15 and Al-SBA-15

The pore size distributions from successive alumina graftings onto SBA-15 reveals a systematic shift to smaller pores with a corresponding decrease in mesopore volume. This trend is clearer in **Figure 5.5** and demonstrates that mesopore diameter (and volume) is inversely proportional to the number of alumina grafting cycles and thus as anticipated alumina layer thickness.

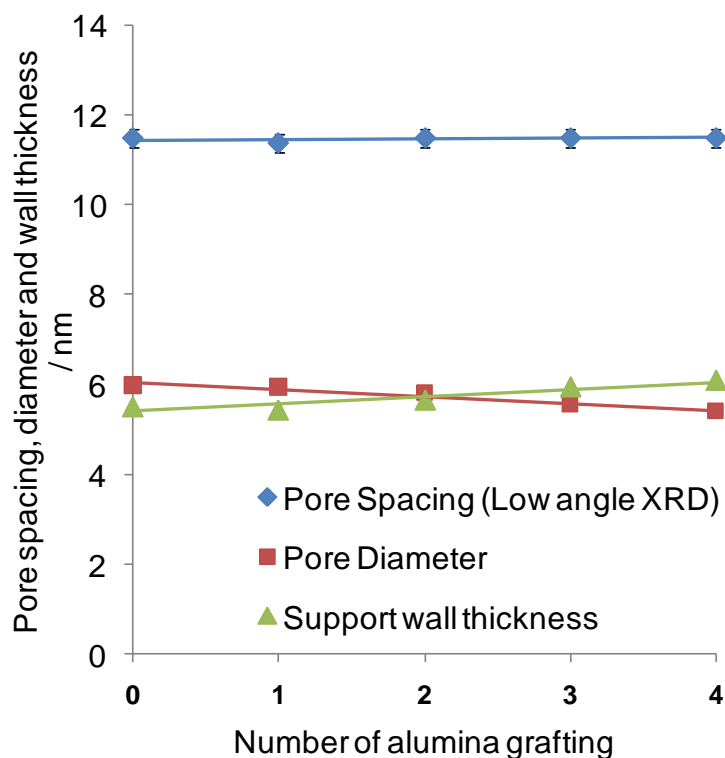


**Figure 5.6** – Influence of alumina grafting cycle on pore spacing, mesopore diameter and wall thickness on Al-SBA-15

From the low angle XRD and N<sub>2</sub> porosimetry results it is possible to determine the pore wall thickness of these alumina supports. The evolution of pore spacing, wall thickness, and average pore diameter, as a function of grafting number for the Al-SBA-15, is shown in **Figure 5.6**. Pore wall thickness (difference between pore spacing and diameter) is proportional to grafting cycles for the Al-SBA-15 with this arising solely from the decreasing pore diameter. The control exhibited a constant pore wall thickness. This, combined with the surface area and pore diameter effects, is persuasive evidence that alumina is deposited onto SBA-15 during grafting, and not precipitated as a separate phase. It also strongly discredits the possibility that the

altered physical properties are due to high temperature processing of the parent SBA-15 support during the grafting protocol.

### 5.2.1.3 X-ray photoelectron spectroscopy

The surface sensitivity of XPS renders it ideal to investigate the formation of alumina adlayers by the grafting route, wherein subtle differences in the binding energies of both the silica and alumina regions may occur with respect to pure SBA-15 and mesoAl<sub>2</sub>O<sub>3</sub> reference materials.

Aluminium 2p XP spectra of the Al-SBA-15 series are depicted in **Figure 5.7** (background subtracted and energy referenced to adventitious carbon at 284.6 eV). Comparison against the mesoAl<sub>2</sub>O<sub>3</sub> material reveals Al peaks are significantly shifted to higher binding after only 1st grafting cycle (74.8 eV versus 73.9 for the pure mesoAl<sub>2</sub>O<sub>3</sub>). Additional grafting cycles induce a progressive shift towards lower binding energy, evolving towards bulk alumina, reaching 74.2 eV after the 4<sup>th</sup> cycle. The higher binding energies observed for grafted alumina may be explained by coordination to a more electronegative oxygen anion than that present within pure Al<sub>2</sub>O<sub>3</sub> species. This is expected at the silica-alumina interface due to the higher Pauling electronegativity of Si (1.9) versus Al (1.6), resulting in additional electron density drawn away from aluminium.<sup>[28]</sup> This effect of hetero-atoms bonded via an oxygen linkage is visually represented in **Diagram 5.2**. The contribution from such polarised aluminium atoms at the interface with SBA-15 is expected to dominate after only 1<sup>st</sup> grafting cycle, and subsequently diminish as less perturbed alumina multilayers evolve upon additional grafts.

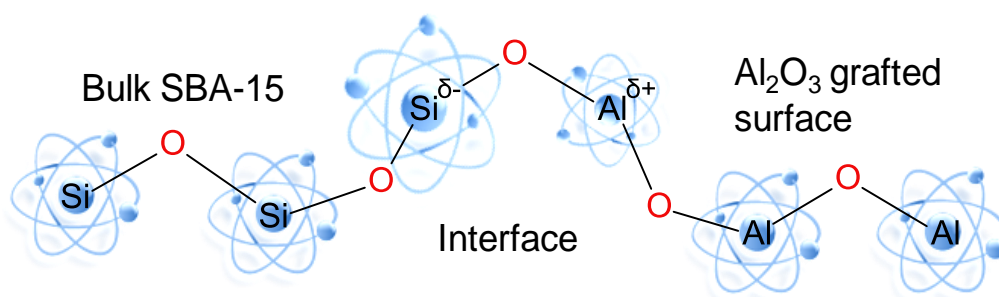


**Diagram 5.2** – Cartoon of electron re-distribution at silica-alumina interface relative to bulk silica and alumina environments

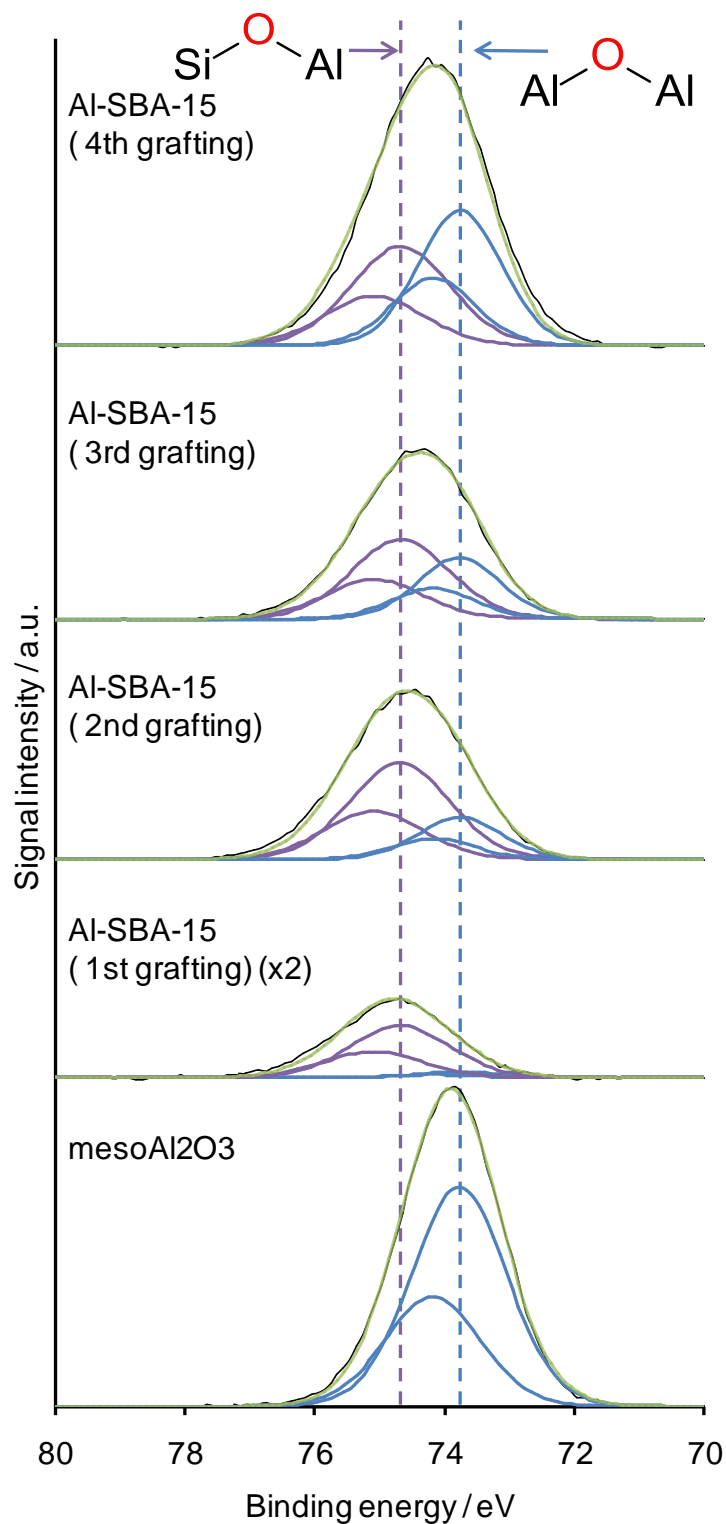


**Figure 5.7** – Fitted Al 2p XP spectra of Al-SBA-15 and mesoAl<sub>2</sub>O<sub>3</sub>

This is confirmed from the required fitting of two distinct set of doublets for the Al spectra in Al-SBA-15 ( $\Delta BE = 0.41$  eV).<sup>[29]</sup> The first at 73.8 eV is attributed to

bulk alumina (blue dashed line), and is the sole species present at the surface of mesoAl<sub>2</sub>O<sub>3</sub>. The second at 74.7 eV is attributed to aluminium atoms at the silica-alumina interface (purple dashed line). The presence of this interfacial species is further proof against the formation of two distinct support phases, one of pure alumina and one of pure silica. The emergence of a pure alumina species with elevating grafting cycle number is also evident, and suggests the formation of alumina multilayers growing on top of an alumina capping monolayer contacting the silica-alumina interface (**Diagram 5.1**). Around 90 % of the Al signal originates from the interfacial species for the 1<sup>st</sup> grafting, declining to 45 % after the 4<sup>th</sup> cycle.

The corresponding Si 2p XP spectra are shown in **Figure 5.8(a)**. The binding energy of the overall envelope decreases from 103.6 eV for pure SBA-15 by ~0.3 eV for each of the 1<sup>st</sup> three grafting cycles, and an additional ~0.2 eV after the 4<sup>th</sup> graft, to a final value of 102.5 eV. This binding energy shift is in the opposite direction to that observed for the aluminium signal, precisely as expected if the contribution from bulk silica is progressively screened by thicker alumina adlayers. This leads to the emergence of the silica environment at the interface, in which silicon atoms are linked via oxygen to less electronegative aluminium.

These Si spectra likewise fit well to two distinct chemical environments with  $\Delta BE = 0.61$  eV.<sup>[29]</sup> The state at 103.4 eV is attributed to the pure silica (red dashed line), and is the only species in SBA-15. An additional peak at 102.3 eV (purple dashed line) is only present in the Al-SBA-15 samples. This assigned to silicon atoms at the silica-alumina interface, yet more reinforcement for the conclusion against the formation of two separate support phases. The interface layer eventually becomes the dominate silica species, ~96 % after the 4<sup>th</sup> cycle (24 % after the 1<sup>st</sup>), with the pure silica signal decreases with grafting cycle. This results from the suppression of the bulk silica signal, from the growing alumina coating (remembering the short electron escape depth of this technique).<sup>[30]</sup> Comparative spectra for the control sample (in which no Al precursor was added during the grafting) are shown in **Figure 5.8(b)**, and only comprise the single state characteristic of pure SBA-15.

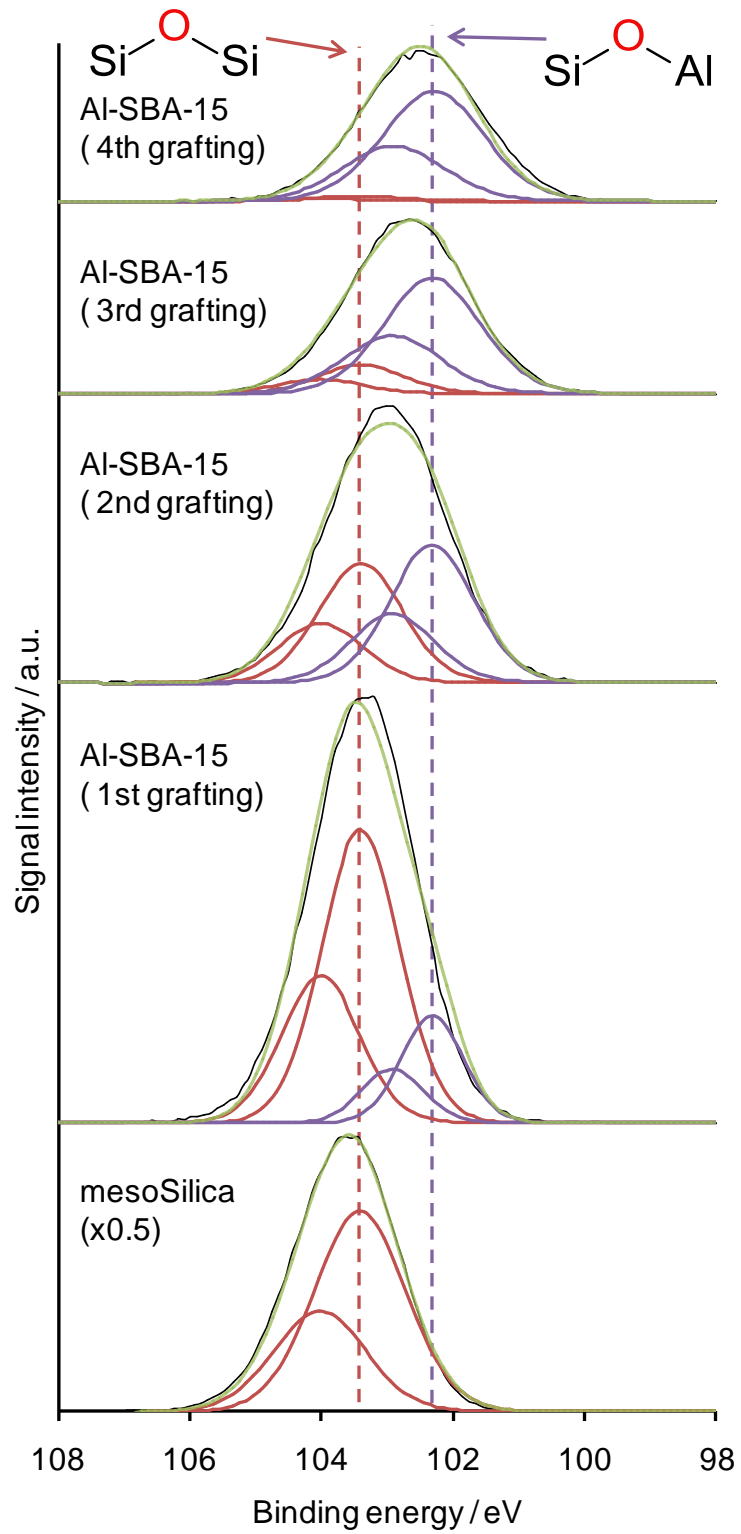


**Figure 5.8(a)** – Offset Si 2p XP spectra of Al-SBA-15 and SBA-15

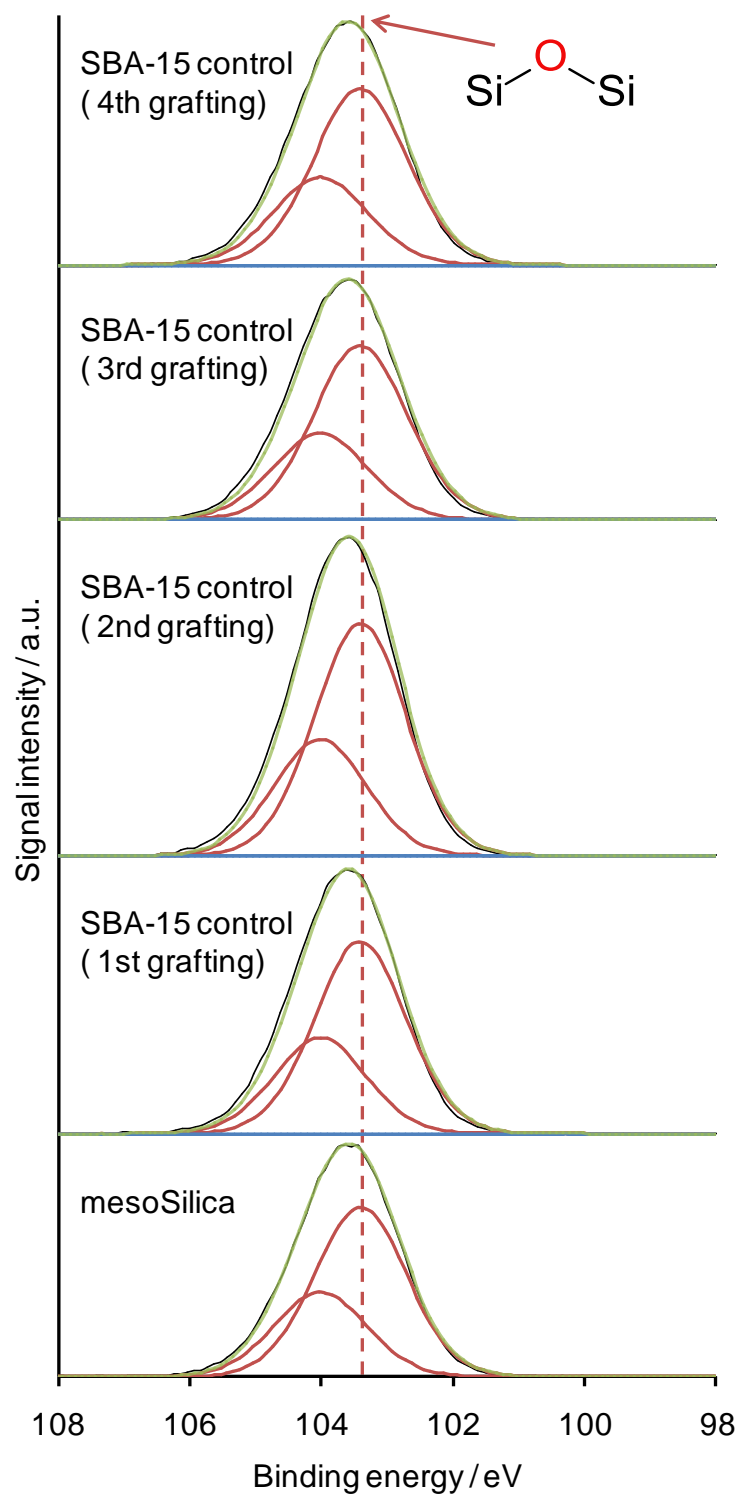


**Figure 5.8(b)** – Offset Si 2p XP spectra of control and SBA-15

#### 5.2.1.4 Scanning electron microscopy

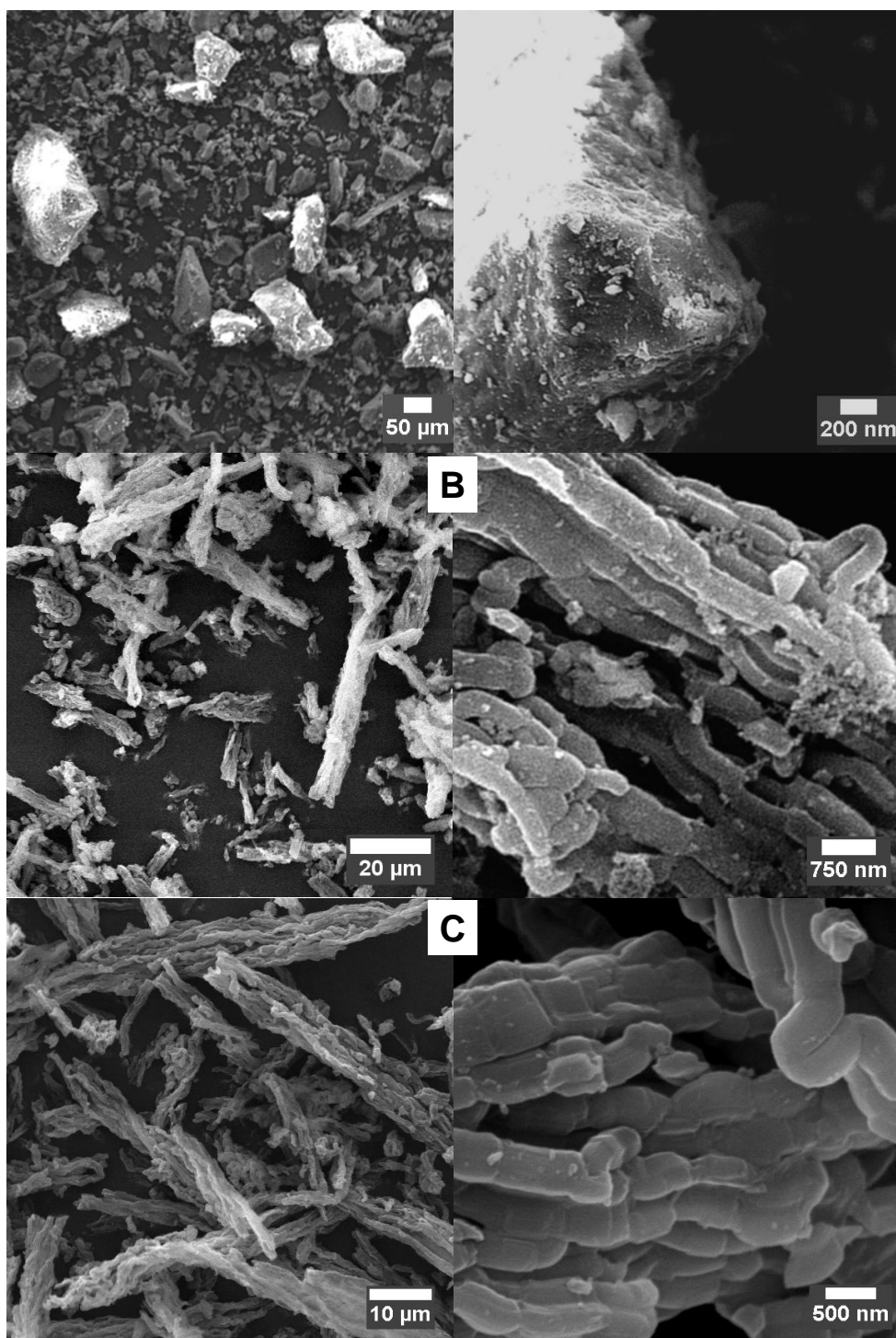


**Figure 5.9** – Representative SEM images of (A) mesoAl<sub>2</sub>O<sub>3</sub>, (B) Al-SBA-15 (4<sup>th</sup> grafting) and (C) SBA-15

SEM was used to visualise the mesoAl<sub>2</sub>O<sub>3</sub> and Al-SBA-15 (4<sup>th</sup> grafting) materials. The images in **Figure 5.9** of mesoAl<sub>2</sub>O<sub>3</sub> reveal a very broad particle size distribution

spanning tens to several hundreds of microns of angular crystallites. High magnification images show a rough surface decorated with nanocrystallites three orders of magnitude smaller. The morphology and particle size range of Al-SBA-15 (4<sup>th</sup> grafting) are comparable to the parent SBA-15. As seen for the mesoAl<sub>2</sub>O<sub>3</sub> support, at high magnification the surface appears rough and covered in small particles, although to a lesser extent. This surface roughening is not observed for SBA-15, suggesting very small agglomerates of alumina form on the external surface of Al-SBA-15.

### 5.2.1.5 Transmission electron microscopy

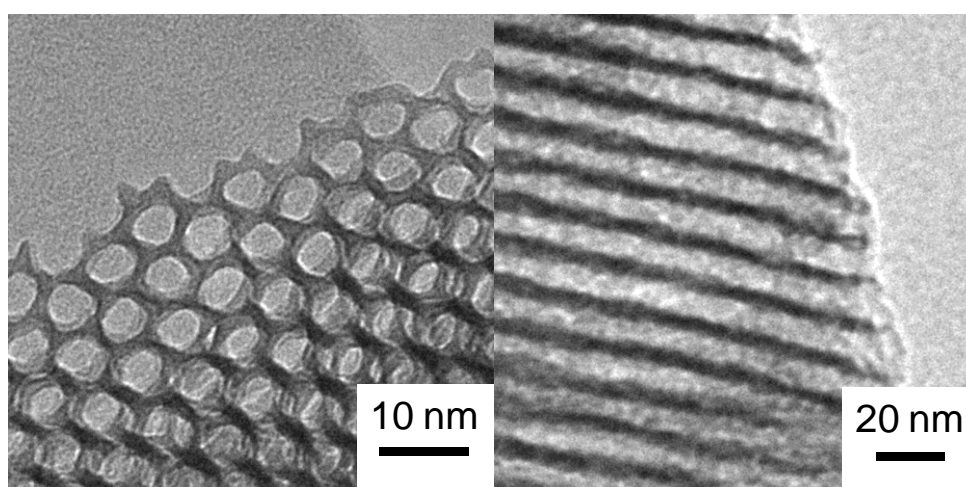


**Figure 5.10** – Bright field TEM images of mesoAl<sub>2</sub>O<sub>3</sub>

Representative TEM images of mesoAl<sub>2</sub>O<sub>3</sub> are presented in **Figure 5.10**. These confirm the presence of hexagonally close-packed, parallel channels typical of the *p6mm* space group in agreement with low angle XRD. Values for the average pore diameter and spacing of 6.3 ( $\pm$  0.6) and 10.3 ( $\pm$  0.6) nm respectively agree with porosimetry and low angle XRD.

### 5.2.2 Characterisation of Pd impregnated alumina supports

A Pd/mesoAl<sub>2</sub>O<sub>3</sub> series was prepared by the incipient wetness impregnation, with nominal Pd loadings between 5 and 0.05 wt%. A nominal 1 wt% Pd/Al-SBA-15 catalyst was also synthesised by the same methodology, using SBA-15 that had been subjected to 4 alumina grafting cycles.

### 5.2.2.1 Inductively coupled plasma optical emission spectroscopy / Atomic adsorption spectroscopy

Actual total Pd loadings were assessed by AAS (mesoAl<sub>2</sub>O<sub>3</sub> series) or ICP-OES (Al-SBA-15) after nitric acid or hydrogen fluoride digestion. These are given in **Table 5.2** and show close agreement with the nominal values.

**Table 5.2** – Comparison of desired and actual bulk metal loadings.

<i>Support</i>	<i>Target loading / wt%</i>	<i>Measured loading / wt%</i>
<i>mesoAl<sub>2</sub>O<sub>3</sub></i>	5	4.11
<i>mesoAl<sub>2</sub>O<sub>3</sub></i>	2.5	1.75
<i>mesoAl<sub>2</sub>O<sub>3</sub></i>	1	0.74
<i>mesoAl<sub>2</sub>O<sub>3</sub></i>	0.5	0.44
<i>mesoAl<sub>2</sub>O<sub>3</sub></i>	0.1	0.07
<i>mesoAl<sub>2</sub>O<sub>3</sub></i>	0.05	0.05
<i>Al-SBA-15</i>	1	0.77

### 5.2.2.2 Powder X-Ray diffraction

Low angle XRD patterns for representative Pd/mesoAl<sub>2</sub>O<sub>3</sub> series and the Pd-Al-SBA-15 sample are illustrated in **Figure 5.11**, with the parent mesoAl<sub>2</sub>O<sub>3</sub> shown for comparison. Pd impregnation of mesoAl<sub>2</sub>O<sub>3</sub> is clearly detrimental to mesopore periodicity, shown by the complete loss of the d(10), d(11) and d(20) reflections. This indicates a loss of pore ordering and/or complete mesopore collapse. In contrast, the 0.77 wt% Pd/Al-SBA-15 sample retained the high ordering of the parent SBA-15, with no discernable change in unit cell (pore spacing), reported in **Table 5.3**.

**Table 5.3** – Support textural properties of catalysts and parent supports

<i>Support</i>	<i>Pd Loading / wt%</i>	<i>Surface area / m<sup>2</sup> g<sup>-1(a)</sup></i>	<i>Micropore surface area / m<sup>2</sup> g<sup>-1(b)</sup></i>	<i>Mesopore Diameter / nm<sup>(c)</sup></i>	<i>Cell parameter / nm<sup>(d)</sup></i>
<i>MesoAl<sub>2</sub>O<sub>3</sub></i>	<i>n/a</i>	276 (± 28)	19 (± 2)	6.6	9.2 (± 0.2)
<i>MesoAl<sub>2</sub>O<sub>3</sub></i>	4.11	282 (± 28)	0	3.5	<i>n/a</i>
<i>MesoAl<sub>2</sub>O<sub>3</sub></i>	1.75	299 (± 30)	0	3.4	<i>n/a</i>
<i>MesoAl<sub>2</sub>O<sub>3</sub></i>	0.74	303 (± 30)	0	3.4	<i>n/a</i>
<i>MesoAl<sub>2</sub>O<sub>3</sub></i>	0.44	303 (± 30)	0	3.4	<i>n/a</i>
<i>MesoAl<sub>2</sub>O<sub>3</sub></i>	0.07	308 (± 31)	0	3.4	<i>n/a</i>
<i>MesoAl<sub>2</sub>O<sub>3</sub></i>	0.05	300 (± 30)	0	3.4	<i>n/a</i>
<i>Al-SBA-15 (4<sup>th</sup>)</i>	<i>n/a</i>	254 (± 25)	28 (± 3)	5.4	10.0 (± 0.2)
<i>Al-SBA-15</i>	0.77	236 (± 24)	25 (± 3)	5.4	10.0 (± 0.2)

<sup>(a)</sup> N<sub>2</sub> BET, <sup>(b)</sup> N<sub>2</sub> t-plot, <sup>(c)</sup> BJH desorption branch of isotherm, <sup>(d)</sup> Low angle XRD

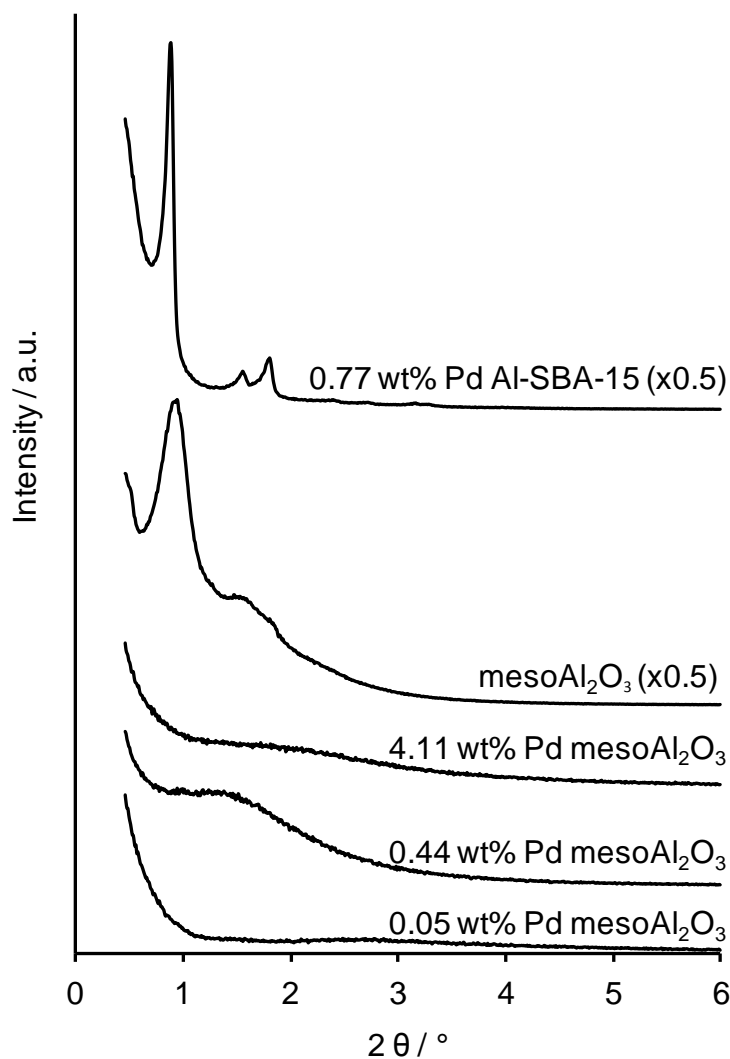


**Figure 5.11** - Offset low angle XRD patterns for representative Pd/mesoAl<sub>2</sub>O<sub>3</sub> samples and Pd/Al-SBA-15 catalyst

Wide angle XRD was also employed to investigate the chemical nature and size of any crystalline Pd and alumina phases. The resulting diffraction patterns are shown in **Figure 5.12**.

The dominant Pd(111) reflection at 39.9°, which would indicate metallic nanoparticles > 2 nm,<sup>[31]</sup> is absent over both supports, even for the highest 4.11 wt% loading. There were also no other phases attributable to Pd. This suggests that Pd is even more highly dispersed over the mesoAl<sub>2</sub>O<sub>3</sub> and Al-SBA-15 supports than any of the previously studied mesoporous silicas, for which reflections due to fcc Pd emerge at loadings > 3 wt%. However, Pd impregnation did perturb the mesoAl<sub>2</sub>O<sub>3</sub> support, inducing a phase transition in the amorphous parent alumina framework to gamma

alumina evidenced by reflections at  $46.0^\circ$ ,  $59.8^\circ$  and  $66.5^\circ$ .<sup>[17, 32]</sup> This restructuring demonstrates the as-prepared mesoAl<sub>2</sub>O<sub>3</sub> support is less stable than comparable silica supports.

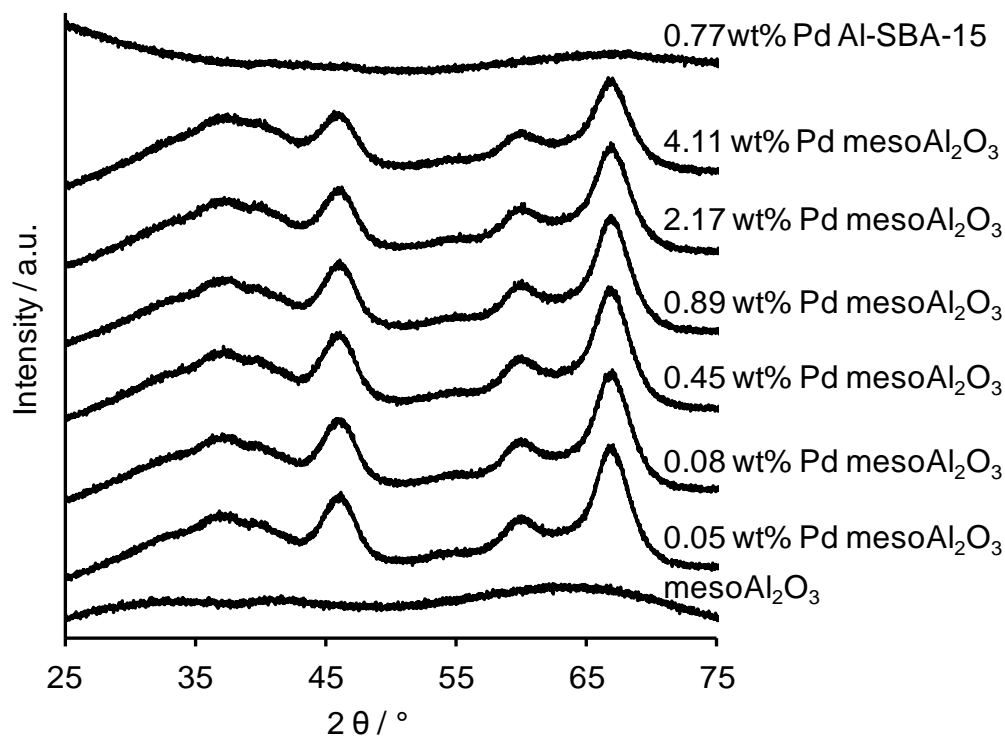


**Figure 5.12** - Offset wide angle XRD patterns for Pd/mesoAl<sub>2</sub>O<sub>3</sub> and 0.77 wt% Pd/Al-SBA-15

### 5.2.2.3 Nitrogen porosimetry

**Figure 5.13** shows N<sub>2</sub> isotherms for both the Pd/Al-SBA-15 and Pd/mesoAl<sub>2</sub>O<sub>3</sub> series. The isotherm of 0.77 wt% Pd/Al-SBA-15 is comparable to of the pre-impregnated Al-SBA-15 parent. Conversely, the hysteresis loops of Pd/mesoAl<sub>2</sub>O<sub>3</sub> samples are shifted to lower relative pressure when compared with the as-prepared mesoAl<sub>2</sub>O<sub>3</sub>, indicative of decreased pore diameter. Textural properties were evaluated using the BET,<sup>[23]</sup> t-plot,<sup>[25]</sup> and BJH methods.<sup>[24]</sup> The results reported in **Table 5.3**. The mesoAl<sub>2</sub>O<sub>3</sub> samples show a significant reduction in the average mesopore diameter following impregnation, although their BET surface areas are little affected. By comparison, the 0.77 wt% Pd/Al-SBA-15 shows no change in BET or micropore surface areas, or mesopore diameter. Thus, the pore wall thickness is also unchanged and it seems reasonable to assume that the grafted alumina surface coating remains intact.

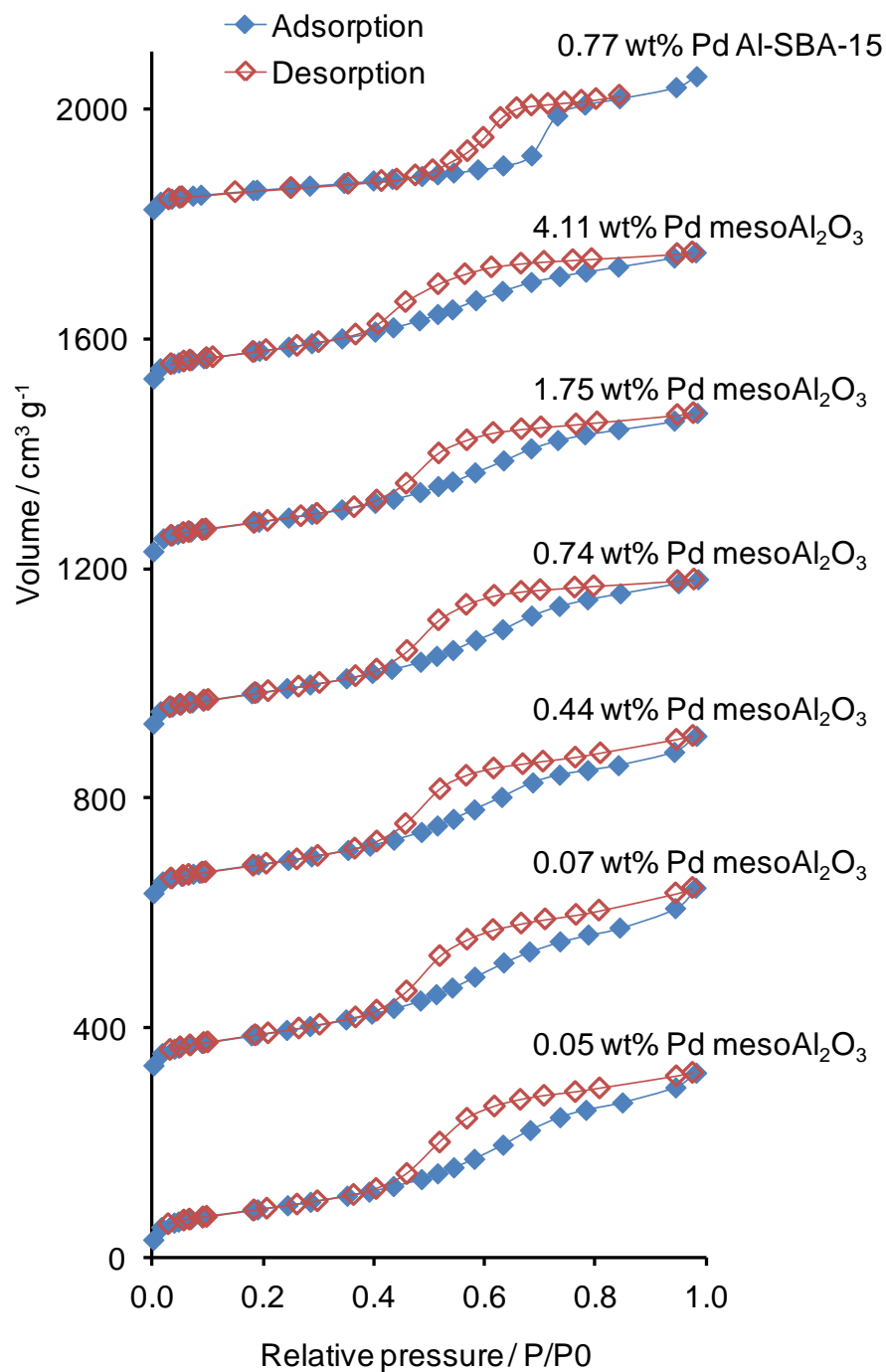


**Figure 5.13** - Offset isotherms of 0.77 wt% Pd/Al-SBA-15 and Pd/mesoAl<sub>2</sub>O<sub>3</sub> series (samples consecutively offset by 300 cm<sup>3</sup> g<sup>-1</sup>)

The BJH pore size distribution for all 7 catalysts is shown in **Figure 5.14**. This visualises the decrease in mesopore diameter for all members of the Pd/mesoAl<sub>2</sub>O<sub>3</sub> series relative to Pd/Al-SBA-15 catalyst, which is little changed (**Figure 5.15**). Even

though the mesopore diameter is significantly modified across the Pd/mesoAl<sub>2</sub>O<sub>3</sub> series, they still exhibit a narrow size distribution.

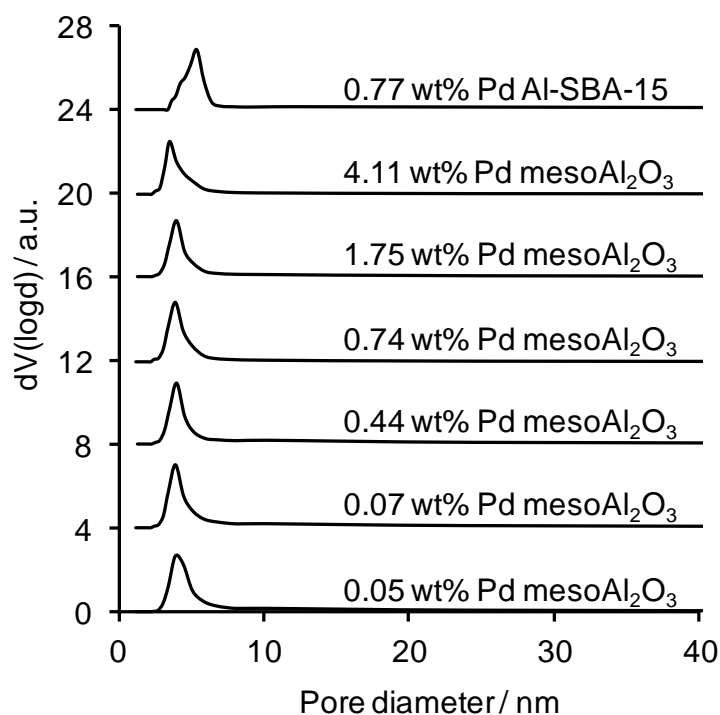


**Figure 5.14** – BJH size distributions of 0.77 wt% Pd/Al-SBA-15 and Pd/mesoAl<sub>2</sub>O<sub>3</sub> series (samples consecutively offset by 4)

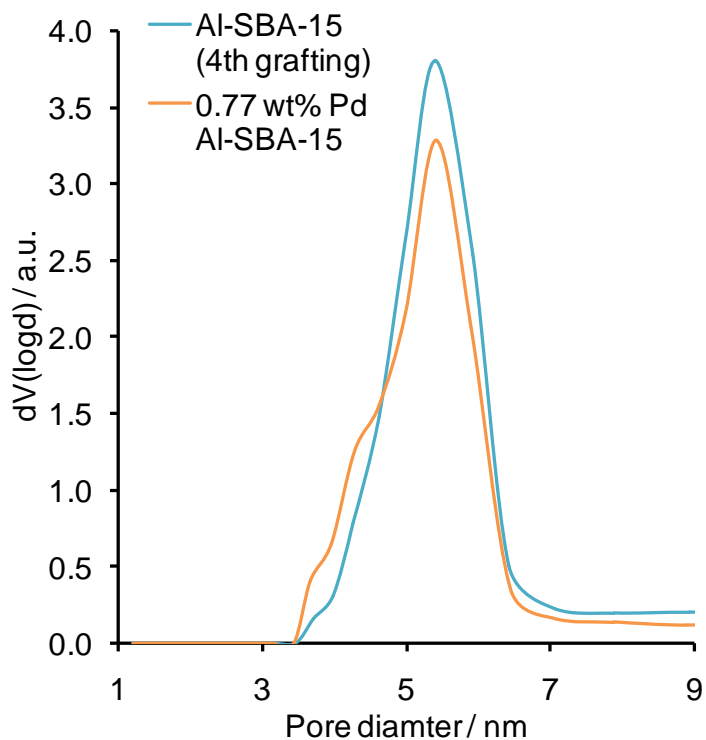


**Figure 5.15** – Pd/Al-SBA-15 and parent support pore size distributions

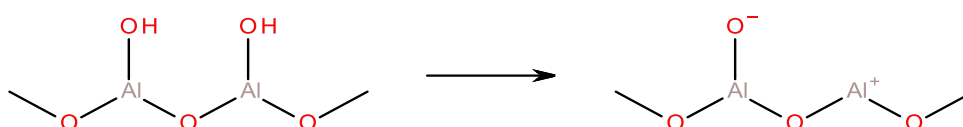
### 5.2.2.4 Carbon monoxide chemisorption

Palladium dispersion (**Chapter 2 Equation 2.6**) and average particle size (**Chapter 2 Equation 2.7**) of the Pd/mesoAl<sub>2</sub>O<sub>3</sub> series and Pd/Al-SBA-15 sample were estimated via CO titration and the results shown in **Table 5.4**.

**Table 5.4** – Dispersion and average Pd particle size from CO titrations

<i>Support</i>	<i>Loading / wt%</i>	<i>Dispersion / %</i>	<i>Ave. particle size / nm</i>
<i>MesoAl<sub>2</sub>O<sub>3</sub></i>	<i>4.11</i>	<i>63 (± 1)</i>	<i>1.8 (± 0.1)</i>
<i>MesoAl<sub>2</sub>O<sub>3</sub></i>	<i>1.75</i>	<i>67 (± 1)</i>	<i>1.7 (± 0.1)</i>
<i>MesoAl<sub>2</sub>O<sub>3</sub></i>	<i>0.74</i>	<i>74 (± 1)</i>	<i>1.5 (± 0.1)</i>
<i>MesoAl<sub>2</sub>O<sub>3</sub></i>	<i>0.44</i>	<i>84 (± 1)</i>	<i>1.2 (± 0.1)</i>
<i>MesoAl<sub>2</sub>O<sub>3</sub></i>	<i>0.07</i>	<i>88 (± 2)</i>	<i>0.1 (± 0.1)</i>
<i>MesoAl<sub>2</sub>O<sub>3</sub></i>	<i>0.05</i>	<i>93 (± 5)</i>	<i>0.9 (± 0.1)</i>
<i>Al-SBA-15</i>	<i>0.77</i>	<i>87 (± 01)</i>	<i>1.1 (± 0.1)</i>

As observed with the silica supports investigated in **Chapters 3 and 4**, the lower metal loadings induce higher dispersions and smaller particle sizes for the mesoAl<sub>2</sub>O<sub>3</sub> series. Quantitative comparison shows palladium is more dispersed over the mesoAl<sub>2</sub>O<sub>3</sub> than over any of the silicas, despite the lower surface area and lack of pore interconnectivity, evidencing a stronger metal-support interaction.<sup>[33]</sup> [6, 7, 34] This enhanced dispersion was also seen for the Pd/Al-SBA-15<sup>[35]</sup> versus pure SBA-15, indicating the critical importance of the support surface layer compared with support texture and architecture. Such strong metal-support interactions may restrict particle sintering during high temperature activation calcination/reduction. Enhanced metal dispersion has been previously reported over alumina-grafted mesoporous silica,<sup>[35, 36]</sup> and attributed to greater support acidity. Grafted Al-mesoporous silicas have shown high surface acid site densities<sup>[11, 35, 36]</sup> arising from both Lewis and Brønsted sites.<sup>[37, 38]</sup> The origin of this acidity is still debated, but the consensus is that Lewis acidity arises from co-ordinatively unsaturated Al cations<sup>[36]</sup> possibly via surface dehydroxylation as illustrated in **Scheme 5.1** <sup>[10, 37]</sup>



**Scheme 5.1** – Al<sub>2</sub>O<sub>3</sub> surface Lewis acidity (water not depicted for clarity)

Brønsted acidity is a consequence of tetrahedral-coordinated Al atoms forming bridging groups,<sup>[36, 38]</sup> (**Chapter 1 Figure 1.6**), via their incorporation into the silica matrix during high temperature treatments.<sup>[39, 40]</sup> Such acid sites have been observed to withdraw charge from supported PGM clusters via electron donation to Lewis acid sites or protons at Brønsted acid sites.<sup>[6]</sup> Although consecutive grafting cycles were utilised with the aim of mimicking the surface properties of bulk alumina,<sup>[10, 11]</sup> it is likely that the residual support acidity present at the Al-SBA-15 surface is important in achieving the higher dispersions relative to the mesoAl<sub>2</sub>O<sub>3</sub> support.

#### 5.2.2.5 Scanning transmission electron microscopy

HAADF-STEM was employed to probe palladium within the 0.74 wt% Pd/mesoAl<sub>2</sub>O<sub>3</sub> and 0.77 wt% Pd/Al-SBA-15 samples, shown in **Figure 5.16**. Corresponding bright field images and particle size histograms are also shown.

Under HAADF-STEM configuration Pd nanoparticles appear as bright spots due to the techniques sensitivity to heavier atoms.<sup>[41]</sup> For the mesoAl<sub>2</sub>O<sub>3</sub>, Pd appears well-distributed with a narrow size distribution and average size of 1.1 (±0.5) nm, slightly lower than that by CO chemisorption. However, the ordered pore structure of the parent alumina was not visible (bright field TEM or HAADF STEM), concurring with low angle XRD and porosimetry. This indicates significant support restructuring, which may result in Pd entrainment within enclosed pores or support walls. Such nanoparticles would be visible by HAADF STEM but not CO titratable. The Al-SBA-15 supported catalysts also shows well-dispersed Pd nanoparticles with a mean particle size of 1.9 (±1) nm, representing an increase on CO chemisorption. Particle size analysis suggests this reflects the presence of a significant number of larger particles, and indeed a bimodal distribution is apparent in **Figure 5.16** with maxima centred at 1.0 and 3.0 nm. The larger particles are predominately on areas of the support wherein the underlying SBA-15 pore structure is absent (and of similar morphology to the disordered mesoAl<sub>2</sub>O<sub>3</sub>). This suggests that a small proportion of the support comprises amorphous, low surface area alumina, which favours poorer Pd dispersion. The difficulty in imaging small (<1 nm) clusters over silica supports, described for the 0.05 wt% Pd/KIT-6 (**Chapter 3 Figure 3.15**), could also artificially skew the size distribution towards larger nanoparticles, whereas the thinner walled mesoAl<sub>2</sub>O<sub>3</sub> support facilitates more facile detection of small Pd clusters.

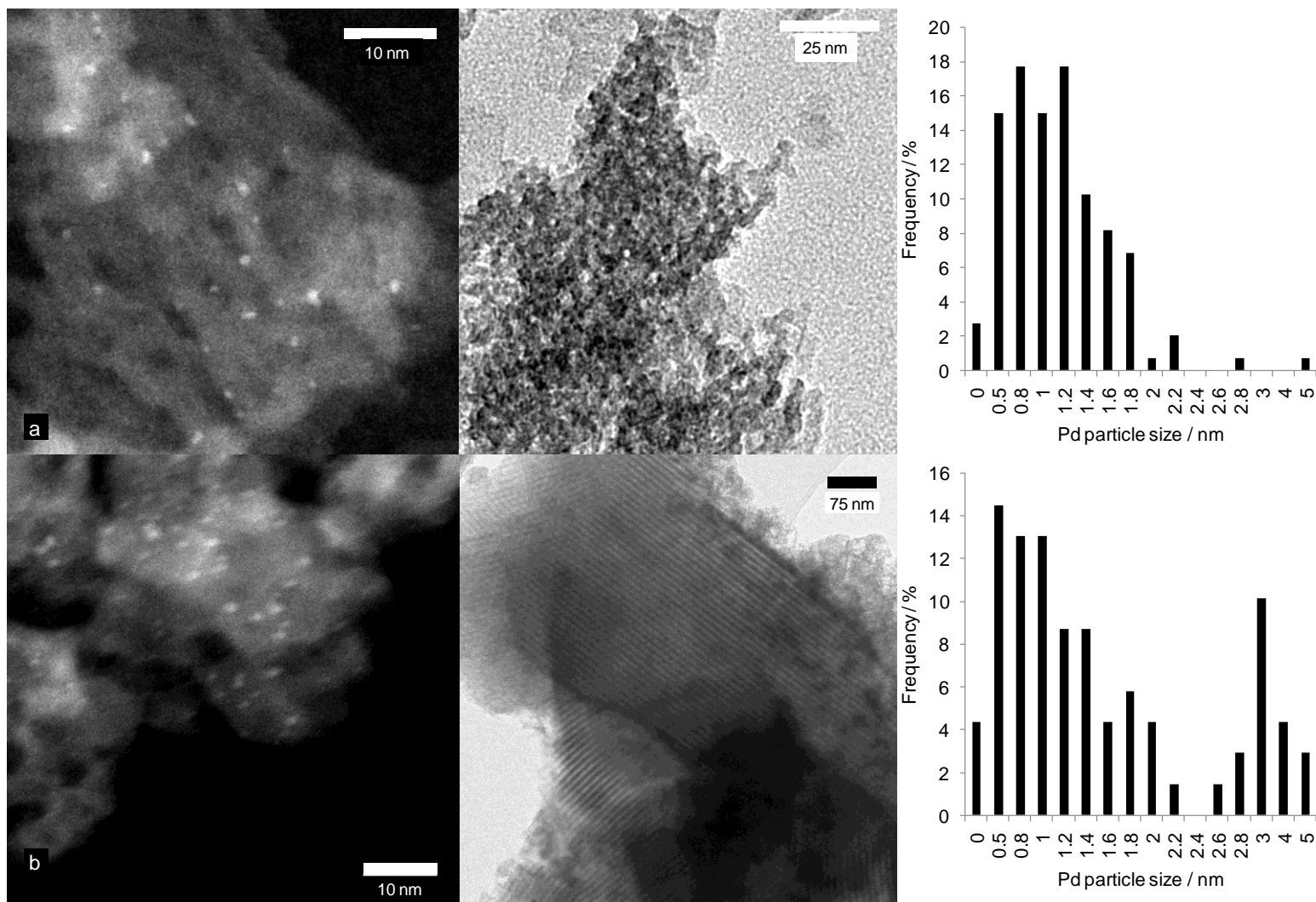


**Figure 5.16** - HAADF-STEM images (left) of (A) 0.74 wt% Pd/mesoAl<sub>2</sub>O<sub>3</sub> and (B) 0.77 wt% Pd/Al-SBA-15 with particle size distributions (right) (100-150 particles) and equivalent bright field TEM images (centre).

### 5.2.2.6 X-ray photoelectron spectroscopy

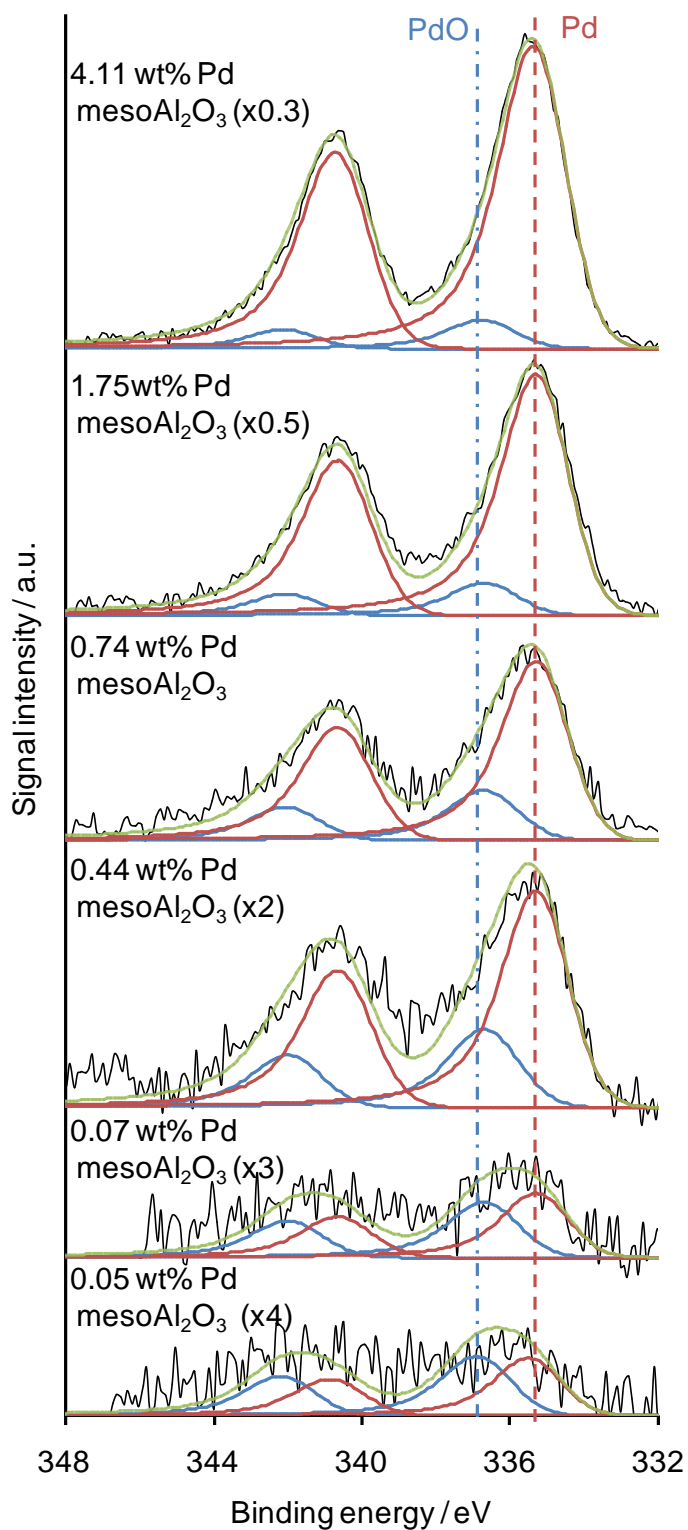
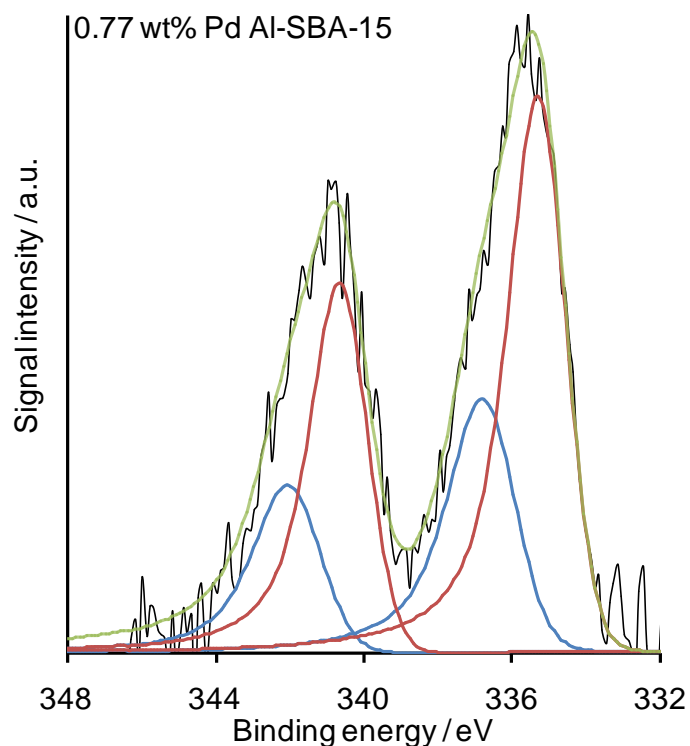
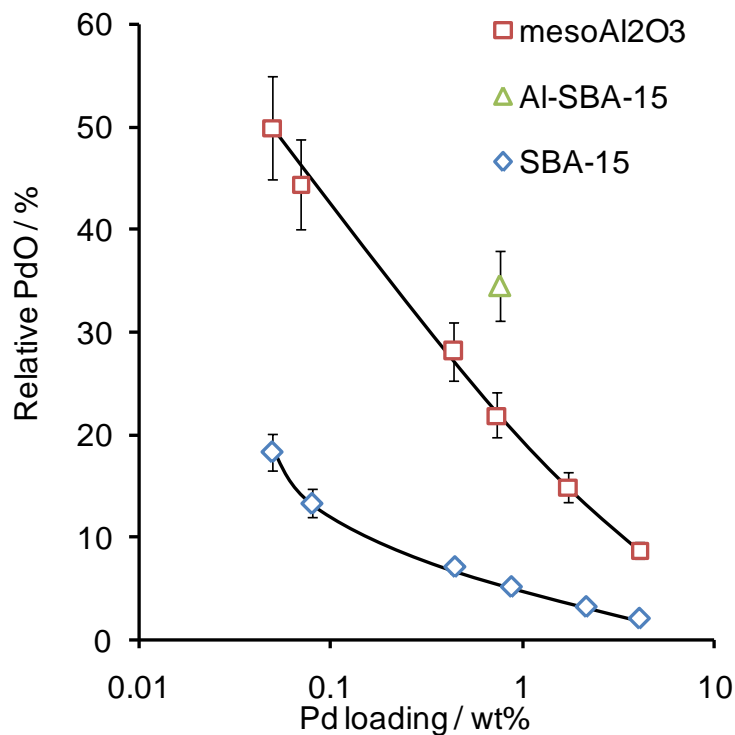


Figure 5.17 (a) - Pd 3d XP spectra of Pd/mesoAl<sub>2</sub>O<sub>3</sub>



**Figure 5.17 (b)** - Pd 3d XP spectra of 0.77 wt% Pd/Al-SBA-15

**Figure 5.17** shows Pd 3d XP spectra of the Pd/mesoAl<sub>2</sub>O<sub>3</sub> series and Pd/Al-SBA-15 samples which all exhibit the characteristic set of Pd 3d<sub>3/2,5/2</sub> doublets ( $\Delta BE = 5.25$  eV).<sup>[42]</sup> For the Pd/mesoAl<sub>2</sub>O<sub>3</sub> series, a major peak is observed at 335.4 eV due to Pd(0) (red dashed line), with the overall envelope broadening with falling loading due to the growth of a second Pd species, assigned to Pd(II) oxide at 336.8 eV (blue dash dot line). No significant shift in the binding energies of either species was apparent between the two different alumina supports.



**Figure 5.18** – Relative PdO content as a function of Pd loading and support

The relative surface PdO concentrations of the Pd/mesoAl<sub>2</sub>O<sub>3</sub> series and Pd/Al-SBA-15 samples are compared with that obtained for Pd/SBA-15 in **Figure 5.18**. The Pd/mesoAl<sub>2</sub>O<sub>3</sub> series exhibit the previously reported inverse correlation between metal loading and surface oxide,<sup>[1, 2, 4]</sup> attributed to the associated change in Pd dispersion. In the case of 0.77 wt% Pd/Al-SBA-15, which exhibits the highest dispersion of any support examined for its given metal loading, the surface PdO content is also the greatest of any material investigated.

The Si and Al 2p XP spectra of the Pd/Al-SBA-15 sample show no change following impregnation (**Figure 5.19**), evidencing excellent support stability, and resistance to formation of separate Pd/silica and Pd/alumina domains.

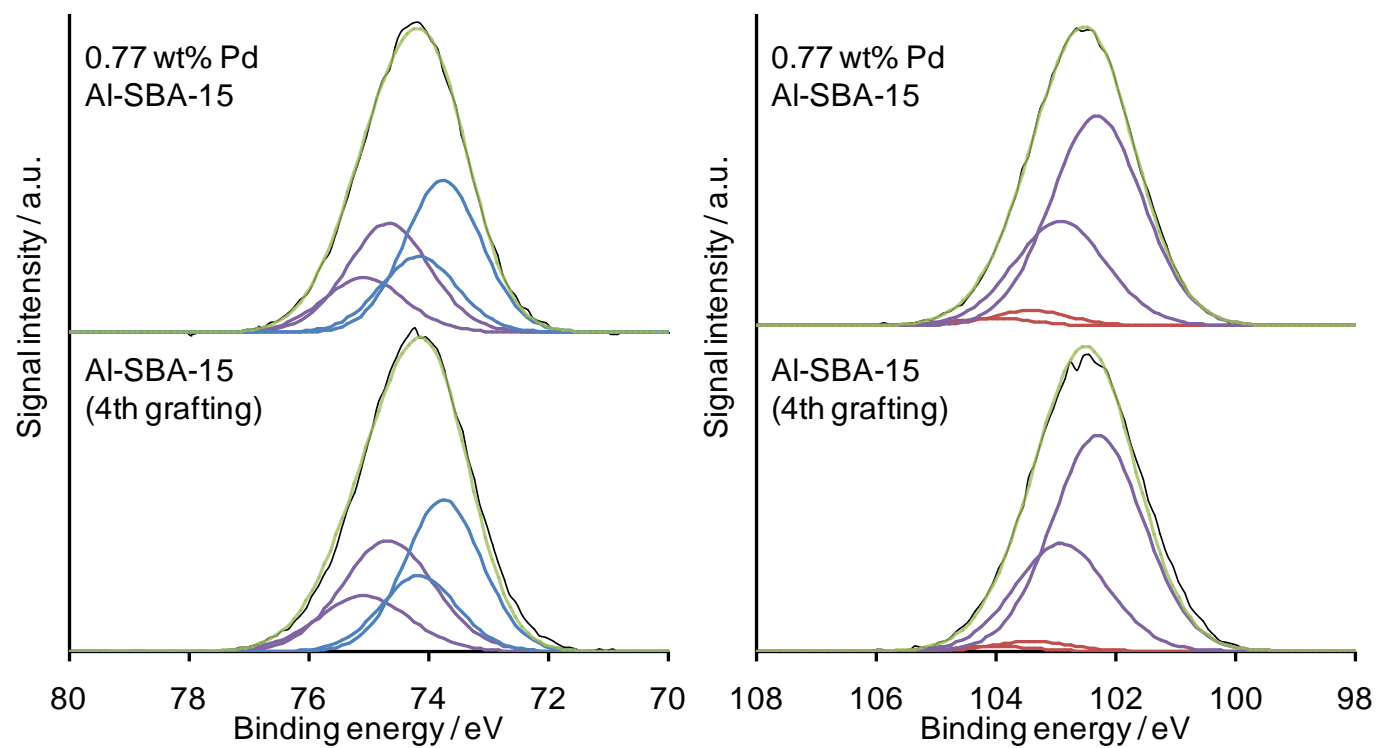


**Figure 5.19** - Al 2p (left) and Si 2p (right) XP spectra for Pd impregnated and parent Al-SBA-15 support

### 5.2.3 Allylic alcohol selox

Crotyl and cinnamyl alcohol selox were subsequently conducted over Pd/mesoAl<sub>2</sub>O<sub>3</sub> and Pd/Al-SBA-15 to investigate their performance in comparison with Pd/silicas. Full reaction conditions are described in **Chapter 2**.

#### 5.2.3.1 Crotyl alcohol selox

Initial screening of Pd/mesoAl<sub>2</sub>O<sub>3</sub> for crotyl alcohol selox under analogous conditions to those previously used (8.4 mmol alcohol in 10 cm<sup>3</sup> toluene with an internal standard at 90 °C), revealed rapid deactivation compared with the Pd/silicas studied in **Chapters 3** and **4**, apparent after only 10 min. in **Figure 5.20**.

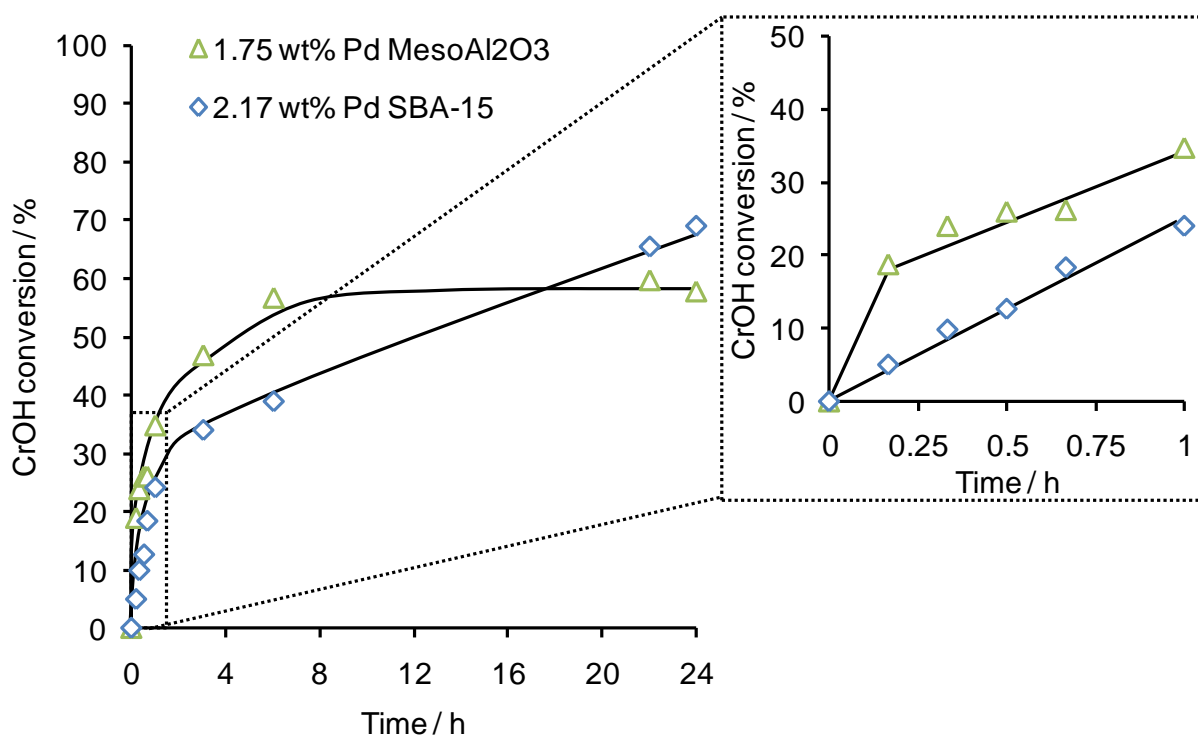


**Figure 5.20** – Representative crotyl alcohol reaction profiles highlighting rapid catalyst deactivation (shown inset) for Pd/mesoAl<sub>2</sub>O<sub>3</sub> compared to Pd/SBA-15

This rapid deactivation hampered attempts to measure initial rates. One of the observed deactivation routes for the Pd/silicas in **Chapters 3** was reduction of surface palladium oxide. Hence flowing O<sub>2</sub> was introduced in an effort to overcome this deactivation, however deteriorating mass balances resulted and attention thus shifted to cinnamyl alcohol.

### 5.2.3.2 Cinnamyl alcohol selox

The effect of catalyst:substrate ratio on initial rates was first examined to ensure that bulk mass transfer limitations (oxygen transfer at the gas liquid interface and reagent transfer at the liquid solid interface at the support surface) were not present at 1000 rpm stirrer speed under  $5 \text{ cm}^3 \text{ min}^{-1}$  flowing  $\text{O}_2$ . The results are shown in **Figure 5.21** for one loading of the Pd/mesoAl<sub>2</sub>O<sub>3</sub> series and the Pd/Al-SBA-15 catalyst.

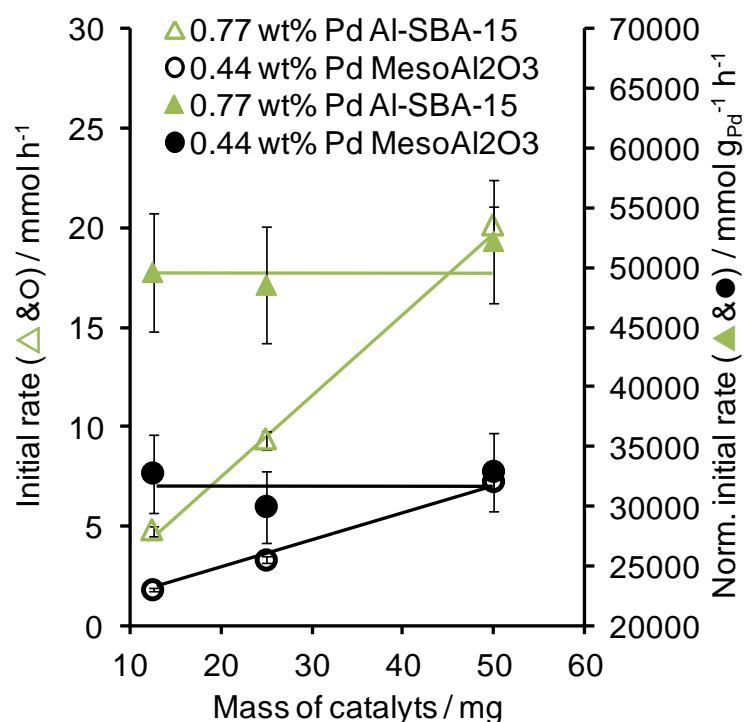


**Figure 5.21** – Effect of catalyst:substrate ratio on cinnamyl alcohol selox

Initial rates were directly proportional to the mass of both catalysts, and the resulting mass normalised initial rates therefore constant, indicating selox was free of bulk mass transport limitations.

Cinnamyl alcohol reaction profiles are displayed in **Figure 5.22** for the Pd/mesoAl<sub>2</sub>O<sub>3</sub> series and 0.77 wt% Pd/Al-SBA-15. Rapid deactivation was observed for all catalysts in the absence of flowing  $\text{O}_2$ .

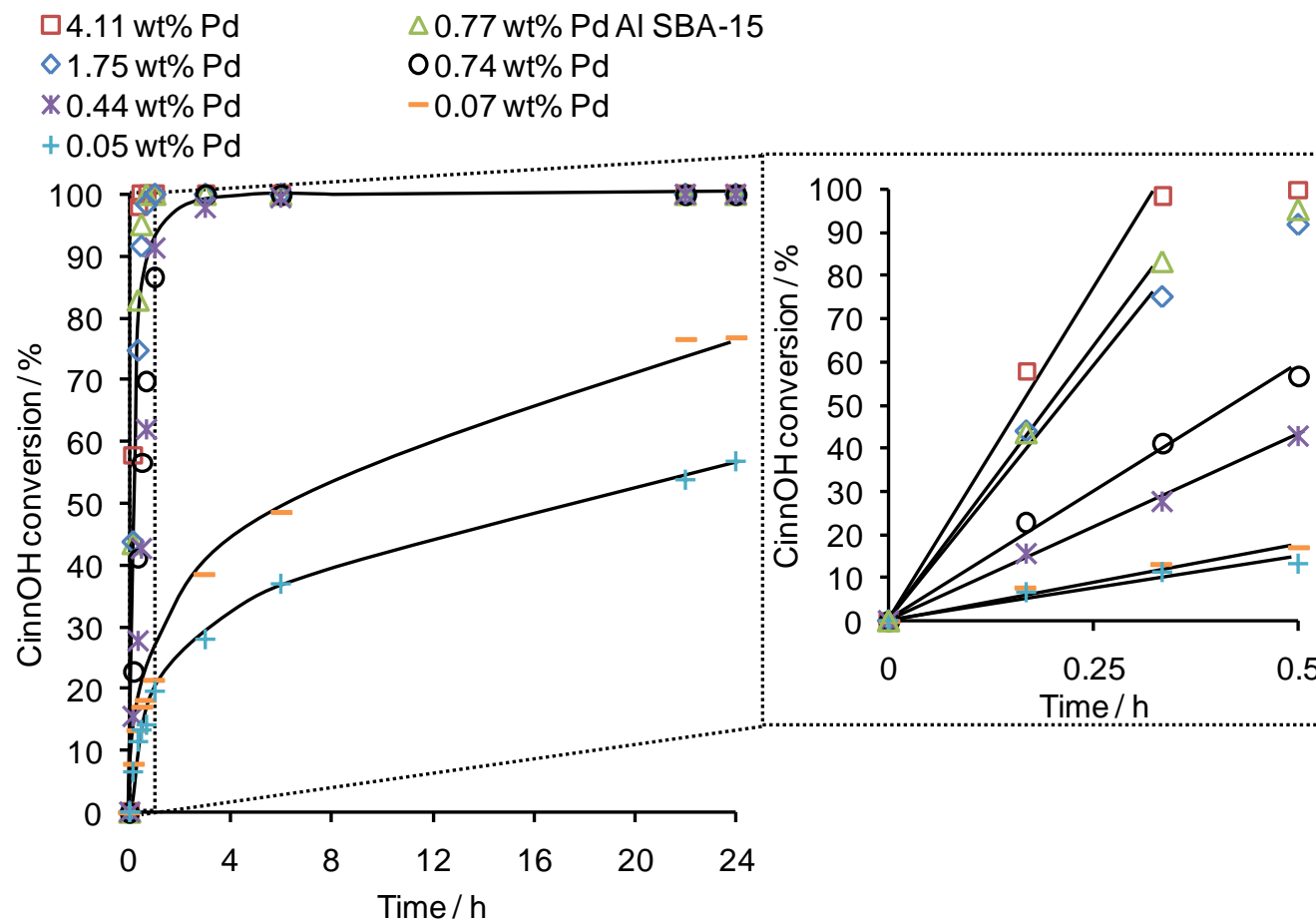


**Figure 5.22** - Cinnamyl alcohol reaction profiles under flowing O<sub>2</sub> (inset shows initial 30 min of reaction).

All catalysts were extremely active for cinnamyl alcohol selox, with their rates proportional to metal loading. Conversion was linear in time for at least the first 20 minutes in all cases, and mass balances determined either during the first hour of reaction (or up to 95 % conversion levels), were  $\geq 95$  %, falling to 85 % and 80 % respectively for Pd/mesoAl<sub>2</sub>O<sub>3</sub> and Pd/Al-SBA-15 after 24 h. The lower mass balances result from the formation of high molecular weight species, apparent as long retention time peaks in the GC traces that could not be easily identified. Comparison of equivalent loadings on the two supports revealed significantly faster conversion for the Pd/Al-SBA-15 versus counterpart Pd/mesoAl<sub>2</sub>O<sub>3</sub> sample, possibly reflecting the pore collapse and Pd encapsulation suggested by the preceding structural characterisation of the Pd/mesoAl<sub>2</sub>O<sub>3</sub> series. Blank reactions using the pure parent supports resulted in negligible conversion during the initial hour and only low conversions after 24 h (9 % for mesoAl<sub>2</sub>O<sub>3</sub> and 14 % for Al-SBA-15).

The fast catalyst deactivation, observed under static O<sub>2</sub>, could result from rapid surface reduction. This could be increased relative to the previously studied silica supports (**Chapter 3 and 4**), due to elevated hydrogen generation from their enhanced catalytic activity. As a result it would be reasonable to expect that lowering the mass of catalyst used, and thus lower hydrogen generation, should decrease the level of dissolved oxygen required to stabilise the PdO active site. That is to say, the rate of PdO reduction is offset by re-oxidising, which could open the possibility of reactions under static O<sub>2</sub> conditions. The effect of varying catalyst mass between 5-20 mg (5 mg for Pd loading of 4.11 - 1.75 wt%, 10 mg for Pd loadings of 0.77 - 0.44 wt% and 20 mg for Pd loading of 0.07 - 0.05 wt%) on cinnamyl alcohol selox is shown in **Figure 5.23**. The 0.77 wt% Pd/Al-SBA-15 catalyst exhibits significantly higher initial activity over all loadings on Pd/mesoAl<sub>2</sub>O<sub>3</sub>. Mass balances are greater than 97 % for over the first hour and remain above 92 % or 86 % after 24 hours for Pd/mesoAl<sub>2</sub>O<sub>3</sub> and Pd/Al-SBA-15 respectively. Examination of conversion over the initial 30 minutes of the reaction reveals a linear increase in conversion. Thus the rapid deactivation, time taken for initial rate to half, witnessed after only 10 minutes when using using 50 mg of catalysts (**Figural 5.20**) is not an issue. This shows that decreasing the amount of catalyst allows deactivation to be slowed, by reducing oxygen demand. The absence of this detrimental issue for the Pd/silica series (**Chapter 3 and 4**) is accredited to their lower activity, which slows H<sub>2</sub> production.

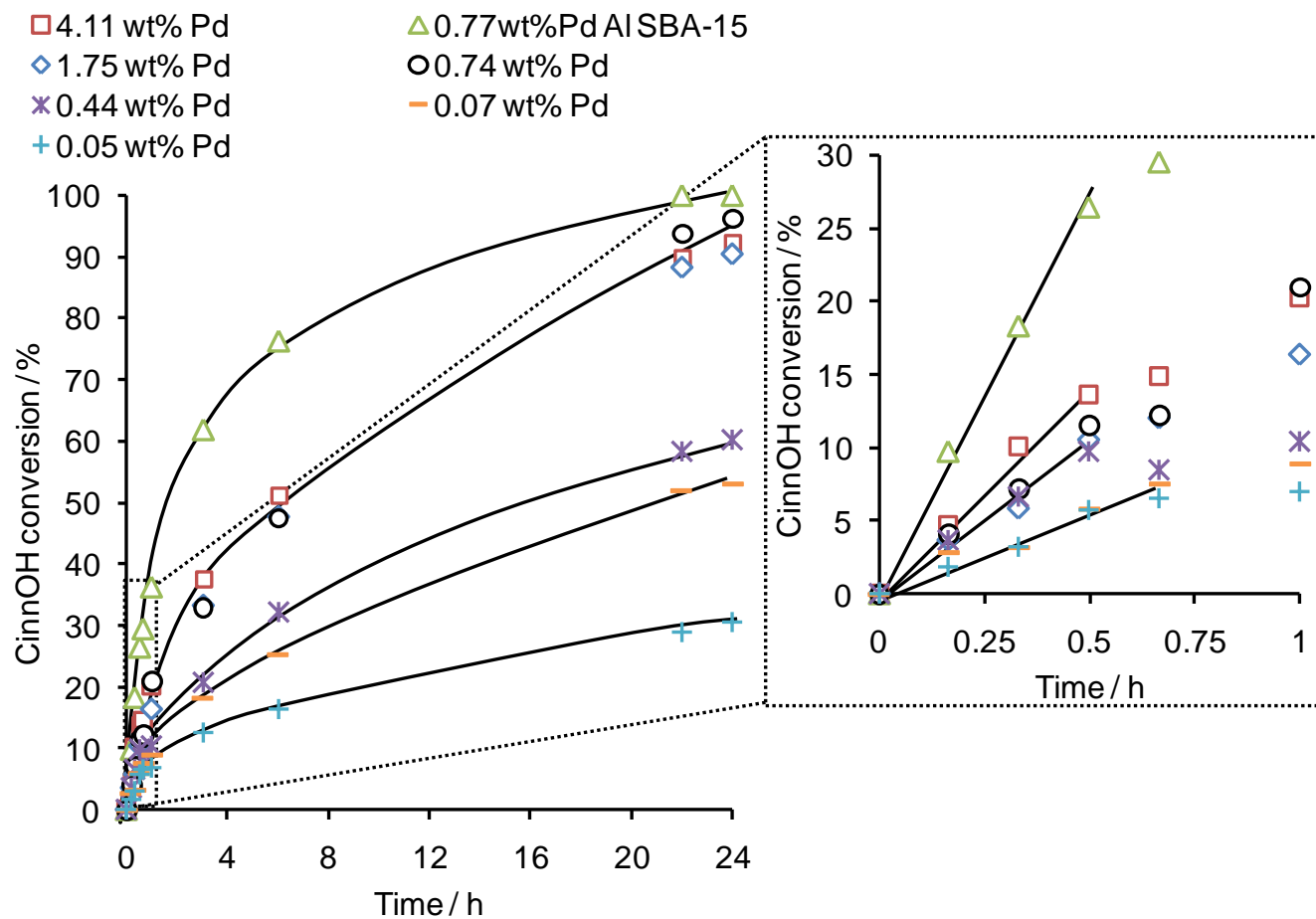


**Figure 5.23** - Cinnamyl alcohol reaction profiles acquired from using reduced catalyst masses (5 mg for Pd loading > 1 wt%, 10 mg for Pd loadings 1- 0.1 wt% and 20 mg for Pd loading < 0.1 wt%)(inset shows the first hour of reaction)

Mass-normalised initial rates for a range of Pd/alumina catalysts are compared in **Figure 5.24** as a function of Pd loading, alongside those for Pd/SBA-15.

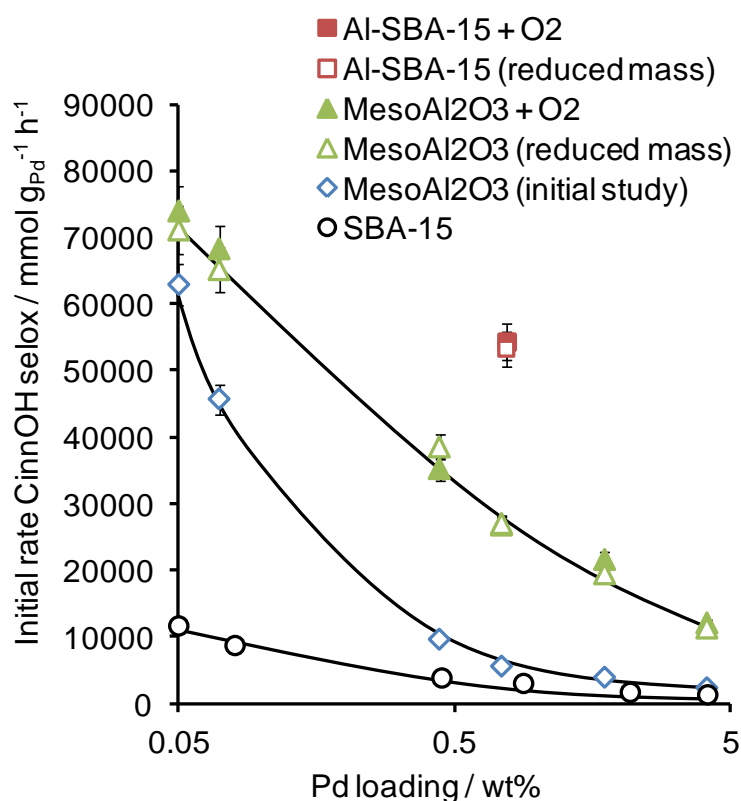


**Figure 5.24** – Consequence of bulk loading and reaction conditions on cinnamyl alcohol aerobic selox activity (5 mg for Pd loading above 1 wt%, 10 mg for Pd loadings 1- 0.1 wt% and 20 mg for Pd loading below 0.1 wt%)(initial study was with 50 mg of each catalyst under static O<sub>2</sub> conditions)

The general trend for the Pd/ mesoAl<sub>2</sub>O<sub>3</sub> series is similar to that observed for Pd/ silicas, with activity inversely proportional to metal loading (and thus directly proportional to surface PdO concentration). However, the absolute activities of all Pd/aluminas (whether pure alumina or Al-SBA-15) surpass those of their Pd/SBA-15 counterparts, with this alumina-induced enhancement increasing dramatically at lower loadings, as PdO concentrations increase and become the dominate Pd species.

Turnover frequencies, calculated by normalisation to either surface Pd metal or oxide as described in earlier chapters, are presented in **Figure 5.25**.

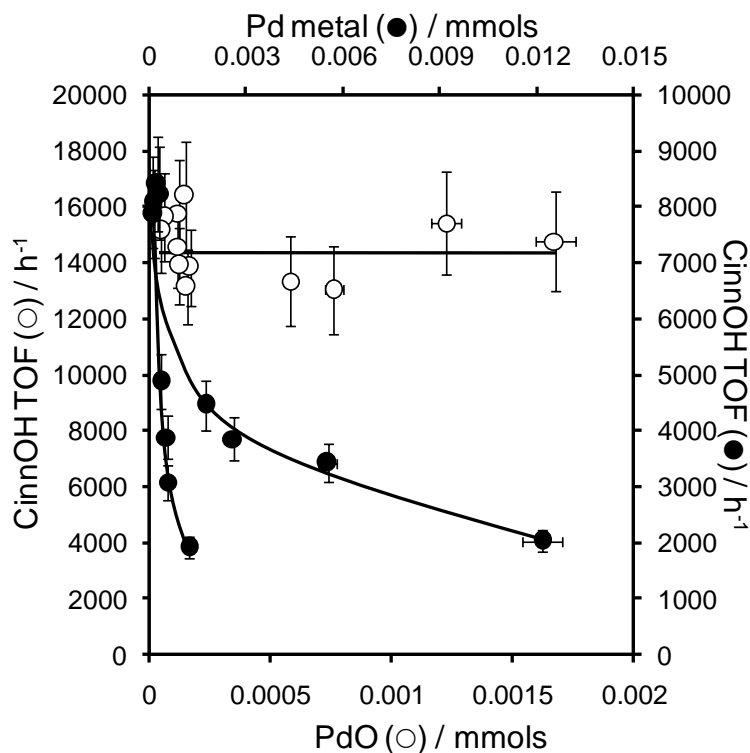


**Figure 5.25** - Cinnamyl alcohol aerobic selox turnover frequencies as a function of surface PdO or Pd metal content for Pd/mesoAl<sub>2</sub>O<sub>3</sub>.

A constant TOF is derived only upon normalisation to the concentration of surface PdO, precisely as observed for Pd/silicas, and confirms the existence of a common active site in Pd-catalysed alcohol selox for both alumina and silica supports. However, the actual TOF value of 14,100 h<sup>-1</sup> is substantially greater than that of 5,800 h<sup>-1</sup> calculated for Pd/silicas, evidencing some influence of metal-support interaction on the absolute performance of surface PdO.<sup>[6, 7]</sup> The calculated TOF for 0.77 wt% Pd/Al-SBA-15 is ~17000 h<sup>-1</sup> (not included in **Figure 5.25**) is yet a further enhancement. This could suggest that the notion of a 'common' alumina surface, for both pure mesoAl<sub>2</sub>O<sub>3</sub> and Al-SBA-15 supports, with comparable interaction between support surface and oxidised Pd nanoparticles is only an approximation. Alternatively, partial Pd encasement within the mesoAl<sub>2</sub>O<sub>3</sub> walls, resulting from pore collapse during Pd impregnation, could evoke this difference. These entrapped sites being inaccessible to cinnamyl alcohol would result in a slight (and thus artificial) lowering of the apparent TOF relative to Pd/Al-SBA-15 catalyst.

Selectivity profiles for major products (> 1.5 %) from representative high and low loaded Pd/mesoAl<sub>2</sub>O<sub>3</sub> catalysts under flowing O<sub>2</sub> are depicted in **Figure 5.26**.

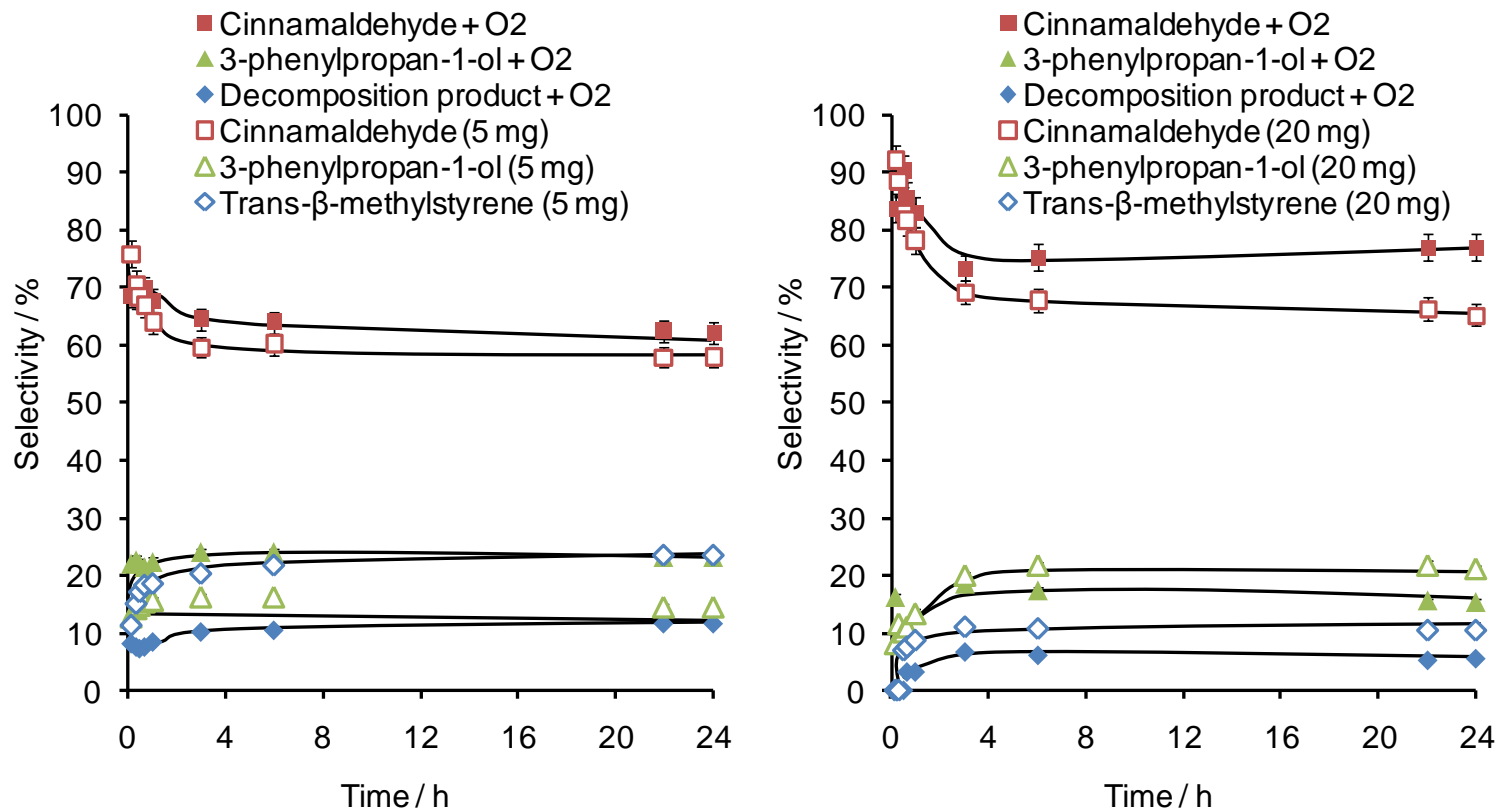


**Figure 5.26** - Representative selectivity profiles for the major products of cinnamyl alcohol selox over 1.75 (left) and 0.05 (right) wt% Pd/mesoAl<sub>2</sub>O<sub>3</sub> under flowing O<sub>2</sub> and reduced mass ( 5mg for 1.75 wt% Pd and 20 mg for 0.05 wt% Pd).

The principal product was cinnamaldehyde under all reaction conditions, with smaller amounts of 3-phenylpropan-1-ol detected, via reactant hydrogenation, and ethylbenzene, styrene and trans- $\beta$ -methylstyrene via hydrogenolysis.<sup>[43]</sup> Under flowing O<sub>2</sub>, these three product classes form in a 1:1:1 ratio, whereas under static O<sub>2</sub> using the reduced catalyst mass (5 mg Pd loading 1.75 wt% and 20 mg for Pd loading 0.05 wt%) trans- $\beta$ -methylstyrene was the only decomposition product observed. In all cases, cinnamaldehyde selectivity decreases with time as both hydrogenation and decomposition side reactions contributions increase. Under static conditions, Pd/silica and Pd/alumina exhibit comparable selectivities (see for example the Pd/KIT-6 series in **Chapter 3** and literature<sup>[44]</sup>). Flowing O<sub>2</sub> suppresses the decomposition products, albeit to a lesser degree than observed with Pd/ KIT-6, suggesting that an elevated O<sub>2</sub> flow rate (or higher pressure operation) may be necessary to maintain high selectivity alongside the superior intrinsic activity of Pd/mesoAl<sub>2</sub>O<sub>3</sub>. For further details on the observed side reactions please refer to **Chapter 3** sections 3.2.3.2 & 3.2.3.3.

### 5.2.3.3 Effect of reaction temperature on cinnamyl alcohol selox

Cinnamyl alcohol selox was studied over ~1 wt% Pd/mesoAl<sub>2</sub>O<sub>3</sub> and Pd/Al-SBA-15 at reaction temperatures of 55 and 75 °C, and the resulting normalised initial rates and TOFs (normalised to surface PdO) reported in **Table 5.5**. Apparent activation energies for each catalyst were determined applying the Arrhenius equation.<sup>[45]</sup>

**Table 5.5** – Comparison of catalyst activity and TOF as a function of reaction temperature with associated activation energies of each catalyst

<i>Catalysts</i>	<i>Norm. initial rate / mmol g<sub>Pd</sub><sup>-1</sup> h<sup>-1</sup> (<math>\pm 5</math> %)</i>			<i>TOF (PdO) / h<sup>-1</sup> (<math>\pm 10</math> %)</i>			<i>Activation energy / kJ mol<sup>-1</sup></i>
	<i>55 °C</i>	<i>75 °C</i>	<i>90 °C</i>	<i>55 °C</i>	<i>75 °C</i>	<i>90 °C</i>	
<i>0.74 wt% Pd/mesoAl<sub>2</sub>O<sub>3</sub></i>	<i>3181</i>	<i>5077</i>	<i>26986</i>	<i>1549</i>	<i>2472</i>	<i>13143</i>	<i>57</i>
<i>0.77 wt% Pd/Al-SBA-15</i>	<i>12457</i>	<i>16527</i>	<i>54363</i>	<i>3843</i>	<i>5584</i>	<i>16769</i>	<i>41</i>

The Pd/Al-SBA-15 catalyst was more active than the comparable Pd/mesoAl<sub>2</sub>O<sub>3</sub> at all temperatures examined. It is worth noting that the 55 °C TOF for the Pd/Al-SBA-15 catalyst is close to that obtained for atomically-dispersed Pd on mesoporous

alumina ( $4400 \text{ h}^{-1}$ ),<sup>[1]</sup> suggesting that the Al-SBA-15 support is indeed a good mimic of a structurally robust pure alumina framework containing sub-1nm PdO clusters.

Activation energy values for both alumina supports are in good agreement with published values for crotyl alcohol selox over Pd/ mesoporous alumina ( $45 \text{ kJ mol}^{-1}$ )<sup>[1]</sup> and Pd(111) single crystals ( $45\text{-}54 \text{ kJ mol}^{-1}$ ),<sup>[3]</sup> benzyl alcohol utilising Pd/mesoporous silica ( $44\text{-}54 \text{ kJ mol}^{-1}$ )<sup>[46]</sup> and 1-phenylethanol using Pd/carbon nanotubes ( $72 \text{ kJ mol}^{-1}$ ).<sup>[47]</sup> Significantly lower activation energies have been reported for benzyl alcohol selox catalysed by Pd supported on amine functionalised SBA-16 ( $12 \text{ kJ mol}^{-1}$ )<sup>[48]</sup> and polyvinylpyrrolidone stabilised AuPd nanoparticles ( $14 \text{ kJ mol}^{-1}$ ).<sup>[49]</sup> In both cases the lower activation energies observed are concluded to an indication that they are proceeding under mass transfer limited regimes.<sup>[50, 51]</sup> Amine functionalisation of SBA-16 significantly decreases porosity and may account for such diffusion limitations, that are absent from the study conducted in **Chapter 3**. Thus these activation energies are likely to reflect a common surface rate-limiting step.

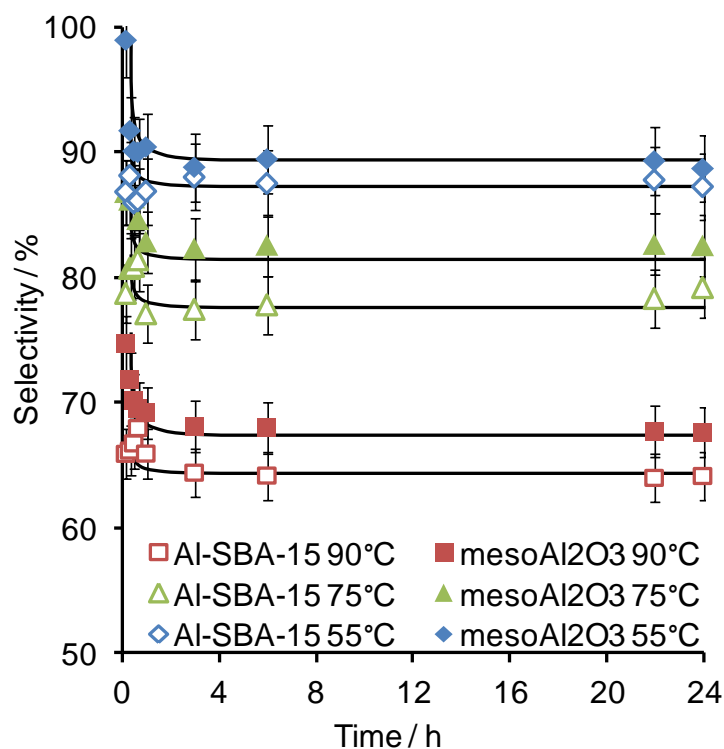


**Figure 5.27** - Cinnamaldehyde selectivity profiles as a function of reaction temperature for 0.74 wt% Pd/mesoAl<sub>2</sub>O<sub>3</sub> and 0.77 wt% Pd/Al-SBA-15

**Figure 5.27** shows cinnamaldehyde selectivity profiles for 0.74 wt% Pd/mesoAl<sub>2</sub>O<sub>3</sub> and 0.77 wt% Pd/Al-SBA-15 catalysts at the three reaction temperatures. Although the desired aldehyde is the major product formed at all reaction temperatures, lower temperatures systematically favour its selective production, with ~90 % selectivity possible at 55 °C (albeit at slower rates). The Pd/Al-SBA-15 catalyst was slightly less selective than the equivalent Pd/mesoAl<sub>2</sub>O<sub>3</sub> sample, possibly reflecting its superior activity, and thus greater tendency to reduce on-stream leading to undesired side reactions.

### 5.3 Conclusion

Mesoporous alumina supports, produced via surfactant templating, or grafting of pre-formed silica architectures enhance Pd dispersion over their silica analogues, despite their lower surface areas. Unfortunately the Pd/mesoAl<sub>2</sub>O<sub>3</sub> exhibits poorer stability, and is prone to pore collapse during impregnation which results in loss of active sites accessibility. Fortuitously the beneficial properties of an alumina support, enhanced metal dispersion, can be combined with the high support stability of silica supports by grafting of an alumina surface onto preformed mesoporous silica. This composite outperforms both pure silica and alumina in its ability to stabilise highly dispersed Pd nanoparticles with enhanced surface PdO content and accessibility.

Catalytic activity for cinnamyl alcohol selox over Pd supported on both mesoporous aluminas outperforms that possible using any nanoporous silica from **Chapters 3** or **4**, attributable to the higher concentration of surface PdO. However, the lower stability (seemingly higher rates of surface PdO reduction) of the PdO active sites necessitates careful regulation of the rate of O<sub>2</sub> supply during selox to prevent rapid deactivation. A support consisting of an alumina surface deposited on mesoporous silica outperforms its equivalent bulk alumina support; reflected in the resulting activity and TOFs, likely due to pore collapse and Pd encapsulation for the latter. However, we cannot dismiss possible differences in the strength of Pd-alumina interaction between this pure alumina and silica-supported alumina bi-layer, or associated surface acidity. Further investigation into the atomic-level uniformity and composition of alumina monolayers grown on SBA-15 is needed in order to fully understand the exceptional catalytic activity of Pd/Al-SBA-15.

## 5.4 References

1. Hackett, S.E.J., R.M. Brydson, M.H. Gass, I. Harvey, A.D. Newman, K. Wilson, and A.F. Lee, *Angewandte Chemie-International Edition*, 2007. **46**: p. 8593.
2. Lee, A.F., S.F.J. Hackett, J.S.J. Hargreaves, and K. Wilson, *Green Chemistry*, 2006. **8**: p. 549.
3. Lee, A.F., Z. Chang, P. Ellis, S.F.J. Hackett, and K. Wilson, *Journal of Physical Chemistry C*, 2007. **111**: p. 18844.
4. Parlett, C.M.A., D.W. Bruce, N.S. Hondow, A.F. Lee, and K. Wilson, *Acs Catalysis*, 2011. **1**: p. 636.
5. Hayek, K., R. Kramer, and Z. Paal, *Applied Catalysis a-General*, 1997. **162**: p. 1.
6. Stakheev, A.Y. and L.M. Kustov, *Applied Catalysis a-General*, 1999. **188**: p. 3.
7. Dropsch, H. and M. Baerns, *Applied Catalysis a-General*, 1997. **158**: p. 163.
8. Somorjai, G.A. and J.Y. Park, *Angewandte Chemie-International Edition*, 2008. **47**: p. 9212.
9. Yuan, Q., A.X. Yin, C. Luo, L.D. Sun, Y.W. Zhang, W.T. Duan, H.C. Liu, and C.H. Yan, *Journal of the American Chemical Society*, 2008. **130**: p. 3465.
10. Landau, M.V., E. Dafa, M.L. Kaliya, T. Sen, and M. Herskowitz, *Microporous and Mesoporous Materials*, 2001. **49**: p. 65.
11. Baca, M., E. de la Rochefoucauld, E. Ambroise, J.M. Krafft, R. Hajjar, P.P. Man, X. Carrier, and J. Blanchard, *Microporous and Mesoporous Materials*, 2008. **110**: p. 232.
12. Zhao, D.Y., J.L. Feng, Q.S. Huo, N. Melosh, G.H. Fredrickson, B.F. Chmelka, and G.D. Stucky, *Science*, 1998. **279**: p. 548.
13. Wan, Y. and D. Zhao, *Chemical Reviews*, 2007. **107**: p. 2821.
14. Zhao, D.Y., Q.S. Huo, J.L. Feng, B.F. Chmelka, and G.D. Stucky, *Journal of the American Chemical Society*, 1998. **120**: p. 6024.
15. Goldbourn, A., M.V. Landau, and S. Vega, *The Journal of Physical Chemistry B*, 2003. **107**: p. 724.
16. Vaudry, F., S. Khodabandeh, and M.E. Davis, *Chemistry of Materials*, 1996. **8**: p. 1451.
17. Aguado, J., J.M. Escola, M.C. Castro, and B. Paredes, *Microporous and Mesoporous Materials*, 2005. **83**: p. 181.
18. Cejka, J., *Applied Catalysis a-General*, 2003. **254**: p. 327.
19. Dacquain, J.P., J. Dhainaut, D. Duprez, S. Royer, A.F. Lee, and K. Wilson, *Journal of the American Chemical Society*, 2009. **131**: p. 12896.
20. Webb, P.A. and C. Orr, *Analytical Methods in Fine Particle Technology*. Journal of the Chemical Society-Faraday Transactions II. 1997, Norcross: Micromeritics.
21. Meynen, V., P. Cool, and E.F. Vansant, *Microporous and Mesoporous Materials*, 2009. **125**: p. 170.
22. Van Bavel, E., P. Cool, K. Aerts, and E.F. Vansant, *The Journal of Physical Chemistry B*, 2004. **108**: p. 5263.
23. Brunauer, S., P.H. Emmett, and E. Teller, *Journal of the American Chemical Society*, 1938. **60**: p. 309.
24. Barrett, E.P., L.G. Joyner, and P.P. Halenda, *Journal of the American Chemical Society*, 1951. **73**: p. 373.
25. Lippens, B.C. and J.H. De Boer, *Journal of Catalysis*, 1965. **4**: p. 319.
26. Liang, X., N.H. Li, and A.W. Weimer, *Microporous and Mesoporous Materials*, 2012. **149**: p. 106.

27. Zukal, A., H. Siklova, and J. Cejka, *Langmuir*, 2008. **24**: p. 9837.
28. Richards, R., ed. *Surface and Nanomolecular Catalysis*. Surface and Nanomolecular Catalysis. 2006, CRC Press: Boca Ranton.
29. NIST X-Ray Photoelectron spectroscopy database, 2003. *NIST Standard Reference Database 20, Version 3.5.*: p. [online] Available at: < <http://srdata.nist.gov/xps/>> [Accessed January 2012].
30. Chorkendorff, I. and J.W. Niemantsverdriet, *Concepts of modern catalysis and kinetics*. 2003, Mörlenbach: Wiley-VCH.
31. Pernicone, N., *Cattech*, 2003. **7**: p. 196.
32. Yuan, X., S. Xu, J. Lu, X. Yan, L. Hu, and Q. Xue, *Microporous and Mesoporous Materials*, 2011. **138**: p. 40.
33. Chen, J., Q.H. Zhang, Y. Wang, and H.L. Wan, *Advanced Synthesis & Catalysis*, 2008. **350**: p. 453.
34. Bartholomew, C.H., *Applied Catalysis A: General*, 2001. **212**: p. 17.
35. Kanda, Y., T. Aizawa, T. Kobayashi, Y. Uemichi, S. Namba, and M. Sugioka, *Applied Catalysis B: Environmental*, 2007. **77**: p. 117.
36. Venezia, A.M., R. Murania, V. La Parola, B. Pawelec, and J.L.G. Fierro, *Applied Catalysis a-General*, 2010. **383**: p. 211.
37. Iengo, P., M. Di Serio, A. Sorrentino, V. Solinas, and E. Santacesaria, *Applied Catalysis A: General*, 1998. **167**: p. 85.
38. Bhange, P., D.S. Bhange, S. Pradhan, and V. Ramaswamy, *Applied Catalysis A: General*, 2011. **400**: p. 176.
39. Li, Y., D. Pan, C. Yu, Y. Fan, and X. Bao, *Journal of Catalysis*, 2012. **286**: p. 124.
40. Hensen, E.J.M., D.G. Poduval, P. Magusin, A.E. Coumans, and J.A.R. Veen, *Journal of Catalysis*, 2010. **269**: p. 201.
41. Pennycook, S.J. and L.A. Boatner, *Nature*, 1988. **336**: p. 565.
42. Brun, M., A. Berthet, and J.C. Bertolini, *Journal of Electron Spectroscopy and Related Phenomena*, 1999. **104**: p. 55.
43. Mallat, T. and A. Baiker, *Chemical Reviews*, 2004. **104**: p. 3037.
44. Yasu-eda, T., R. Se-ike, N.O. Ikenaga, T. Miyake, and T. Suzuki, *Journal of Molecular Catalysis a-Chemical*, 2009. **306**: p. 136.
45. Atkins, P., *The Elements of Physical Chemistry*. 3rd ed. 2001, Oxford: Oxford University Press.
46. Chen, Y.T., Z. Guo, T. Chen, and Y.H. Yang, *Journal of Catalysis*, 2010. **275**: p. 11.
47. Chen, Y.T., L.L. Bai, C.M. Zhou, J.M. Lee, and Y.H. Yang, *Chemical Communications*, 2011: p. 6452.
48. Chen, Y.T., H.M. Lim, Q.H. Tang, Y.T. Gao, T. Sun, Q.Y. Yan, and Y.H. Yang, *Applied Catalysis a-General*, 2010. **380**: p. 55.
49. Hou, W.B., N.A. Dehm, and R.W.J. Scott, *Journal of Catalysis*, 2008. **253**: p. 22.
50. Tang, Q., Q. Zhang, H. Wu, and Y. Wang, *Journal of Catalysis*, 2005. **230**: p. 384.
51. Groppo, E., G. Agostini, A. Piovano, N.B. Muddada, G. Leofanti, R. Pellegrini, G. Portale, A. Longo, and C. Lamberti, *Journal of Catalysis*, 2012. **287**: p. 44.

# *Chapter 6*

## *Conclusions*

## 6.1 Conclusion

The goal at the beginning of this project was to investigate the use of mesoporous silicas as catalyst support materials; in particular for the application of stabilising deposited Pd nanoparticles, which find employment as heterogeneous catalysts for allylic alcohol selox.<sup>[1, 2]</sup> Individual tuning of mesoporous silicas, to produce both 2D non-interconnecting SBA-15 and 3D interpenetrating mesopore structures SBA-16 and KIT-6,<sup>[3, 4]</sup> allowed the role of mesoporosity, including varying architectures to be studied. Mesopore incorporation results in a substantial elevation in surface areas, over a non-porous commercial silica, with this being beneficial towards the goal of achieving highly dispersed metal (Pd) catalytically active species. This desirable effect is further escalated when 3D structures (SBA-16 and KIT-6) are used over 2D non-interconnecting architectures (SBA-15). This indicates the importance of porosity receptiveness during metal impregnation for the generation of catalytic species. Pd activity towards allylic alcohol selox shows a direct correlation with metal dispersion. Pd loaded series of SBA-16 and KIT-6 outperform SBA-15, with all three showing significantly greater productivity than a series generated using a low surface area commercial support. To date there is still debate over the active Pd state responsible for these industrially relevant organic transformations, with the main candidates being metallic<sup>[5, 6]</sup> or oxidic<sup>[7-9]</sup> Pd surfaces. Both were tested as possible active sites with the resulting non-fluctuating TOF for surface PdO providing categorical proof of a size and structure independent active species (**Figure 6.1** taken from **Chapter 3**). Variations in catalyst activity, with loading, can be attributed solely to changes in active site density. A surface PdO active species is further apparent from reactions under flowing oxygen conditions, which show greater allylic aldehyde production, and from the catastrophic effect of in-situ pre-reduction on both activity and selectivity. This destructive pre-treatment resulted in increasing favourability towards hydrogenation and decarbonylation chemistry.

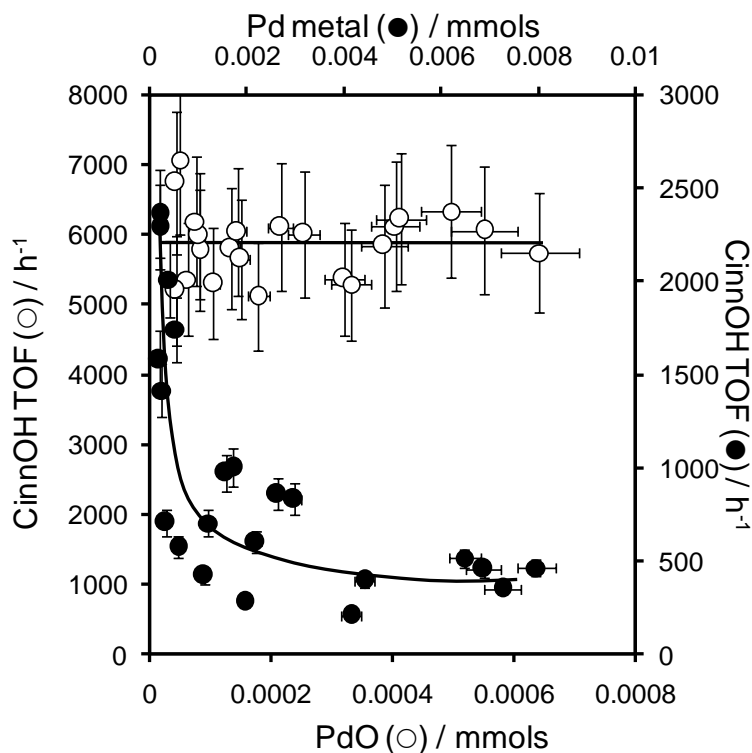


**Figure 6.1** – Cinnamyl alcohol aerobic selox turnover frequencies as a function of surface PdO or Pd metal content for Pd/SiO<sub>2</sub>, Pd/SBA-15, Pd/SBA-16 and Pd/KIT-6 catalysts (crotyl alcohol selox exhibited identical trends).

Having observed the critical nature of mesopore accessibility in **Chapter 3**, for promoting Pd dispersion, the aim of the subsequent chapter was to probe whether the conventional SBA-15 could be improved. The incorporation of a second macropore structure, thus producing a hierarchical mesomacroporous composite,<sup>[10]</sup> was hoped to remedy the reduced mesopore receptiveness of conventional SBA-15. Even with a resulting loss in support surface area, approximately 40%, Pd dispersion was significantly enhanced. This corresponded to a marked increase in catalyst activity, shown in **Figure 7.2** (taken from **Chapter 4**). The value of support openness was further highlighted when the larger particle sized TLCT-SBA-15 support was explored. This resulted in decreased catalyst activity. Again, normalisation to surface PdO validated a surface PdO active species, with constant TOFs of  $\sim 7000 \text{ h}^{-1}$  (crotyl alcohol) and  $\sim 5800 \text{ h}^{-1}$  (cinnamyl alcohol) concurring with findings in **Chapter 3**.

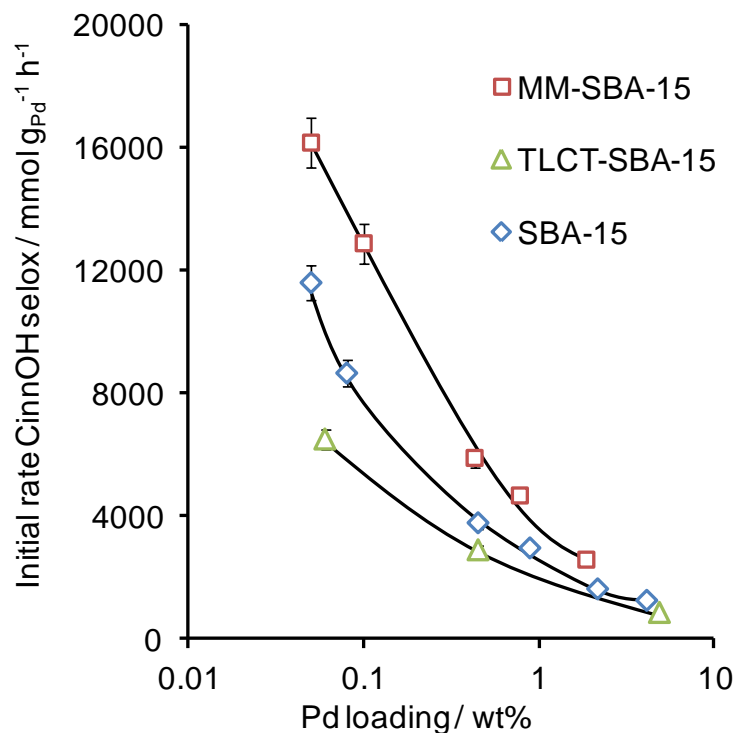


**Figure 7.2** – Dependence of cinnamyl alcohol aerobic selox activity on bulk Pd loading and nature of SBA-15 support (crotyl alcohol selox revealed comparable observation)

Finally mesoporous aluminas were scrutinised to see if the nature of the support surface plays a role. A 2D mesoporous alumina ( $\text{mesoAl}_2\text{O}_3$ ),<sup>[11]</sup> comparable in architecture to SBA-15, but with a considerable lower surface area, resulted in significantly higher metal dispersions. This resulting catalyst series displayed a tremendous enhancement in catalyst activity over the silica series. Unfortunately though, the alumina exhibited lower stability, with pore contraction and loss of mesopore ordering, during active site generation. An alumina surface silica shell composite material, produced by grafting alumina onto SBA-15 (Al-SBA-15),<sup>[12]</sup> overcame this issue and resulted in yet another increase in catalytic activity. The  $\text{mesoAl}_2\text{O}_3$  series revealed uniform TOF values, when normalised to surface PdO, albeit with a values of  $\sim 14100 \text{ h}^{-1}$  (cinnamyl alcohol) being a notable increase over silica series. Therefore it is apparent that the chemical nature of the support material is critical in relation to a catalysts activity. The Al-SBA-15 support showed greater TOFs still although the exact reason for this cannot be established. It could arise due to the differences in the support surfaces of the two aluminas, such as acid strength,

or due to the possibility of pore collapse/contraction accompanied by active site encapsulation with regard to the pure mesoAl<sub>2</sub>O<sub>3</sub>.

Studying a range of catalyst supports has indicated the importance of both open high surface area materials and surface chemical composition. The production of highly dispersed Pd centres, with greater surface PdO density, is a critical requirement. These showed excellent activity towards allylic alcohol selox, with kinetic and selectivity investigations communicating compelling evidence towards a surface PdO active species.

## 6.2 References

1. Hackett, S.E.J., R.M. Brydson, M.H. Gass, I. Harvey, A.D. Newman, K. Wilson, and A.F. Lee, *Angewandte Chemie-International Edition*, 2007. **46**: p. 8593.
2. Vinod, C.P., K. Wilson, and A.F. Lee, *Journal of Chemical Technology and Biotechnology*, 2011. **86**: p. 161.
3. Zhao, D.Y., J.L. Feng, Q.S. Huo, N. Melosh, G.H. Fredrickson, B.F. Chmelka, and G.D. Stucky, *Science*, 1998. **279**: p. 548.
4. Kleitz, F., S.H. Choi, and R. Ryoo, *Chemical Communications*, 2003: p. 2136.
5. Grunwaldt, J.D., C. Keresszegi, T. Mallat, and A. Baiker, *Journal of Catalysis*, 2003. **213**: p. 291.
6. Grunwaldt, J.D., M. Caravati, and A. Baiker, *The Journal of Physical Chemistry B*, 2006. **110**: p. 25586.
7. Lee, A.F., C.V. Ellis, J.N. Naughton, M.A. Newton, C.M.A. Parlett, and K. Wilson, *Journal of the American Chemical Society*, 2011. **133**: p. 5724.
8. Lee, A.F., Z. Chang, P. Ellis, S.F.J. Hackett, and K. Wilson, *Journal of Physical Chemistry C*, 2007. **111**: p. 18844.
9. Lee, A.F. and K. Wilson, *Green Chemistry*, 2004. **6**: p. 37.
10. Dhainaut, J., J.P. Dacquin, A.F. Lee, and K. Wilson, *Green Chemistry*, 2010. **12**: p. 296.
11. Yuan, Q., A.X. Yin, C. Luo, L.D. Sun, Y.W. Zhang, W.T. Duan, H.C. Liu, and C.H. Yan, *Journal of the American Chemical Society*, 2008. **130**: p. 3465.
12. Landau, M.V., E. Dafa, M.L. Kaliya, T. Sen, and M. Herskowitz, *Microporous and Mesoporous Materials*, 2001. **49**: p. 65.